Silicon nanocrystals as light sources: optical analysis and realisation of microcavities

Mathias Grün

Nancy-Université
Université Henri Poincaré

IJL – Institut Jean Lamour – UMR 7198
Matériaux-Métallurgie-Nanosciences-Plasmas-Surfaces

Thèse

présentée pour l'obtention du titre de

Docteur de l'Université H. Poincaré, Nancy 1

en Physique par

Mathias Grün

Les nanocristaux de silicium comme source de lumière : analyse optique et réalisation de microcavités

Soutenance publique devant la commission d'examen : 15 octobre 2010

Membres du Jury :

Président :

Dr. G. LERONDEL	Professeur, Université de Technologies de Troyes (Rapporteur)

Examinateurs :

Dr. S. CALLARD	Professeur, Ecole Centrale de Lyon (Rapporteur)
Dr. A. EN NACIRI	MCF, Université Paul Verlaine, Metz
Dr. M. VERGNAT	Professeur, Université Henri Poincaré, Nancy 1 (Directeur de thèse)
Dr. P. MISKA	MCF, Université Henri Poincaré, Nancy 1 (Co-directeur de thèse)

Ecole Doctorale EMMA
Département de Formation Doctorale de Physique et Chimie de Matière et des Matériaux

Remerciements

Je tiens à remercier à Michel Vergnat pour m'avoir accueilli dans le département en plus d'avoir accepté de diriger ma thèse.

Ce travail doit beaucoup à Patrice Miska qui a également encadré cette thèse. Il a toujours été là – jour et nuit, en semaine comme pendant les weekends – quand j'avais « juste une petite question » dont l'explication, parfois, nous occupait des heures. Je lui exprime ma gratitude pour tout ce qu'il a fait pour moi pendant ces années à Nancy.

Je remercie les membres du Jury d'avoir accepté d'évaluer ce travail : M. Lérondel, Mme. Callard, et M. EnNaciri. Je remercie également M. Bouazaoui et M. Gilliot qui, malgré leur impossibilité à venir participer au Jury, ont manifesté un grand intérêt pour ce travail.

Je remercie Hervé Rinnert pour son soutien soit administratif, soit moral.

Pour le soutien technique pendant ma thèse je tiendrai remercier du fond du cœur : François Mouginet, Juan Arocas-Garcia et Alexandre Bouché pour la réalisation des échantillons, Xavier Devaux et Pascal Martin pour les nombreuses lames minces fabriquées et analysées, Sylvie Robert pour les analyses en rayons X, Christian Senet pour le soutien informatique ainsi que Hamid M'Jahed pour avoir réparé plus qu'une fois nos alimentations.

Pour le soutien moral, je tiens remercier : Martine (les deux !!), Damien, Michel Hehn, Daniel Lacour, bref le cercle qui se rassemblait régulièrement autour d'un bon café souvent très fort au quatrième étage. Je remercie également les autres doctorants et étudiants avec lesquels j'ai eu le plaisir de collaborer : Ganye Wora-Adéola, avec lequel j'ai partagé le bureau en arrivant, Joël Briones, Luis Cardenas-Arellano et Emilie Steveler. Pour la bonne collaboration un grand merci également à Nader Kozhaja, Nguyen Thi Dinh, Anne-Laure Pointel et Aurélie Thiel.

Cet énorme travail n'aurait pas été possible sans plusieurs collaborations fructueuses pour lesquelles je voudrais remercier : Manuel Dossot et Jérôme Grausem de nous avoir donné accès à leur spectromètre Raman, J.-F. Pierson pour l'accès au spectromètre UVVIS, l'équipe de M. Blas Garrido pour nous avoir accueillis très chaleureusement à Barcelone et pour nous avoir facilité l'accès au microscope EFTEM et M. EnNaciri pour les mesures d'ellipsométrie.

Le dernier paragraphe va être dédié à ceux auxquels je dois tout parce qu'ils m'ont toujours encouragés pendant ce temps parfois très dur de séparation de ma chère famille : mes beaux-parents, ma sœur, mes deux frères et mes parents. Et la dernière ligne est réservée aux deux femmes dans ma vie : Myriam et Elisa, ma petite famille à moi. Merci pour tout ce que Vous me donnez ! Je Vous aime !!!

Table of Contents

Chapitre 1

Nous présentons dans ce chapitre l'état de l'art de l'élaboration et de l'analyse de nanocristaux de silicium présentés dans la littérature. Dans un premier temps, nous détaillons les principales propriétés issues du confinement quantique des paires électron-trous à l'intérieur de ces nanostructures. Dans un deuxième temps, nous donnons les motivations et les moyens utilisés et présentés dans la littérature afin d'isoler et d'analyser, par spectroscopie optique, un nanocristal unique. Nous présentons ensuite rapidement les principes physiques des microcavités. Celles-ci sont utilisées afin de modifier les propriétés d'émission spontanée de la lumière issue des nanocristaux de silicium. Dans quelques cas récemment décrits dans la littérature, elles permettent également d'évaluer l'élargissement homogène des nanocristaux de silicium sans réaliser l'analyse optique d'un nanocristal unique. Nous présentons succinctement les principes physiques du couplage entre la lumière et les nanocrisatux de silicium en microcavités. Nous discutons ensuite rapidement les différents résultats issus de la littérature concernant la réalisation et l'analyse de microcavités optiques à base de nanocristaux de silicium. Nous donnons également, au regard de la littérature, les pistes que nous nous proposerons de suivre dans ce travail.

Les nanocristaux de silicium sont intensivement analysés depuis le début des années 1990. Depuis la publication des résultats de Canham montrant la forte luminescence du silicium poreux, de nombreuses études ont été consacrées aux propriétés optiques des nanocristaux de silicium. Différentes techniques d'élaboration de ces nanostructures ont été développées, parmi lesquelles nous pouvons citer la pulvérisation, l'implantation ionique, le dépôt chimique en phase vapeur, l'évaporation … Des études théoriques ont montré que la diminution de la taille de cristallites de silicium jusqu'à des tailles nanométriques engendrait d'une part une augmentation de la bande interdite des nanocristaux de silicium, et d'autre part une augmentation du rendement radiatif de luminescence de ces nano-objets. Pour expliquer ce phénomène, il est classiquement évoqué une augmentation de l'incertitude sur l'impulsion liée à une réduction de l'incertitude sur la position, celle-ci apparaissant à la suite de la réduction en taille de ces objets. Cette relaxation des règles de sélection engendrerait une augmentation du rendement radiatif des nanocristaux de silicium. Bien que ce phénomène soit encore mal compris, de nombreuses études sur le gain, les propriétés non linéaires et les propriétés de luminescence et d'absorption ont été publiées. Ces différentes études visent d'une part à réaliser des composants optoélectroniques performants sur substrat de silicium et, d'autre part, à mieux comprendre les fondements des propriétés optiques remarquables de ces objets.

La compréhension des processus optiques des nanocristaux de silicium passe par l'analyse d'un nanocristal unique. Ce type d'analyse permet de s'affranchir de l'élargissement inhomogène d'une population d'objets. Ce type d'analyse est désormais courant dans le domaine des semiconducteurs de type III-V. L'expérience historique fut réalisée en gravant des « mesas » de plus en plus petits renfermant des boites quantiques InAs/GaAs.

Sur silicium, ce type d'expérience est plus rarement décrit. Les nanocristaux analysés ont été isolés en pratiquant des étapes de gravure et d'oxydation successives sur des piliers de silicium. Il apparaissait alors, au bout de ce pilier, une particule de silicium. Les largeurs des spectres de photoluminescence observés sont alors de l'ordre de 100-150 meV à température ambiante et de 2 meV à basse température. Si les résultats de spectroscopie réalisés sur ces objets sont intéressants, la nanostructure analysée est, quant à elle, très particulière. Située au sommet du pilier de silicium, elle

est entourée par une coquille d'oxyde dont on ne connaît pas clairement la nature, et elle est probablement couplée à un continuum d'états situés dans le pied du pilier. La deuxième approche concernant l'analyse d'un nanocristal unique et présentée dans la littérature décrit la réalisation de masques opaques percés de trous de tailles nanométriques. L'excitation se fait alors à travers ces ouvertures. Ce type d'analyse est très courant dans le domaine des nanostructures III-V. Sur silicium, des chercheurs ont réalisé l'implantation ionique et la spectroscopie optique à travers un masque opaque. Cette technique a permis de réaliser la spectroscopie de photoluminescence sur une zone localisée de l'espace. Dans notre cas, cette approche semble être la plus simple et nous disposons au laboratoire des technologies de salle blanche permettant la réalisation de tels masques. Nous mettrons en œuvre cette technique au cours de ce travail de thèse.

La réalisation et l'analyse de microcavités optiques couplées à des émetteurs de lumières est bien décrite dans la littérature. Ces systèmes permettent d'obtenir un couplage optique entre les modes optiques confinés de la microcavité et les états électroniques confinés de la nanoparticule. La force de ce couplage est décrite par le facteur de Purcell :

$$F_P = \frac{3Q\left(\frac{\lambda}{n}\right)^3}{4\pi^2 V_0}$$

Ce facteur dépend du facteur de qualité de la microcavité et du volume modal. Si la valeur de ce facteur est supérieure à un, il est possible d'observer une augmentation de l'intensité de photoluminescence des émetteurs de lumière. En utilisant ces dispositifs, certains auteurs décrivent même la possibilité de remonter jusqu'à la signature d'un nanocristal unique.

Différentes géométries des microcavités sont décrites dans la littérature. Celles-ci peuvent être sphériques, planaires, ou cylindriques. Elles peuvent également parfois bénéficier d'un confinement latéral à travers la réalisation de micropiliers ou de microtores. Dans notre cas, nous choisissons de réaliser des microcavités planaires. Nous présentons dans ce manuscrit les différentes étapes de réalisation et d'analyse de ces microcavités.

Chapitre 2

Ce chapitre est consacré à la présentation des différentes techniques expérimentales et des différents moyens de modélisation utilisés lors de cette étude. Les principaux échantillons sont également présentés.

L'ensemble des échantillons est réalisé par évaporation. L'enceinte utilisée permet d'atteindre un vide de l'ordre de 10^{-8} Torr. Les substrats de silicium monocristallin non-dopé [1,0,0], de verre ou de silice fondue sont coupés et scotchés sur un porte-substrat chauffé à 100°C. La température du porte-substrat est contrôlée par une bobine chauffante sur le principe de l'effet Joule. Le monoxyde de silicium (SiO) est évaporé par effet Joule à partir d'un creuset de tantale. Le dioxyde de silicium (SiO_2) quant à lui est évaporé par canon à électrons à partir d'un creuset en graphite. Les épaisseurs déposées sont contrôlées à l'aide de microbalances à quartz et leur évaluation inclut un facteur correctif tenant compte de la géométrie du dispositif. Les évaporations s'effectuent à la vitesse de 0.1 nm/s. Un cache automatisé permet le dépôt d'alternances de couches de SiO et de SiO_2 qui forment la base de la plupart des échantillons étudiés au cours de ce travail.

Les échantillons ainsi obtenus sont ensuite recuits afin de faire apparaître la phase stable de silicium nanostructuré. Un four de recuit rapide a été acquis durant ce travail de thèse (Annealsys). Il permet de pratiquer des recuits rapides (5 minutes) sous atmosphère contrôlée (Azote, Argon…). La mise en place et les tests de recuit à l'aide ce four ont été réalisés durant la thèse.

Les mesures d'épaisseurs ont été réalisées en particulier par réflectométrie de rayons X aux petits angles. L'appareil commercial utilisé est le diffractomètre X'Pert Pro – Philips muni d'un détecteur de technologie PIXcel. Cette technique consiste à envoyer un flux de rayons X provenant d'une anticathode de cuivre (λ= 1,6 Å) sous incidence rasante sur la couche mince à analyser. Une figure d'interférence apparaît alors due à la différence d'indice optique, d'épaisseur et de densité électronique entre la couche mince déposée et le substrat. La simulation de ces spectres nous donne ainsi accès à l'épaisseur de la couche.

Le phénomène de démixtion est à la base de l'apparition des nanocristaux de silicium. Cette réaction, qui modifie les liaisons chimiques à l'intérieur du matériau, peut être suivie et analysée par spectroscopie de transmission infrarouge par transformée de Fourier (spectromètre Nicolet Protégé 460). Cette analyse donne accès, via l'observation de la position spectrale ν des vibrations de la liaison Si-O-Si, à la stœchiométrie x = [O]/[Si] du matériau SiO_x grâce à la relation :

$\nu = 965 + 50\ x\ (cm^{-1})$

Certains échantillons ont été analysés par microscopie électronique à transmission. Les échantillons destinés à ce type d'analyse sont préparés sous forme de lame mince (technique d'amincissement physico-chimique du tripode) ou sont issus d'un microclivage de la surface.

Les échantillons nanostructurés et la formation des nanocristaux de silicium sera suivie par spectroscopie Raman. Cette étude se fait en collaboration avec le Laboratoire de Chimie Physique pour la Microbiologie et l'Environnement (LCPME UMR CNRS 7564) à l'aide d'un dispositif Raman commercial T64000 Jobin-Yvon.

Certains résultats comme la détermination de la densité surfacique de nanocristaux de silicium, ont nécessité l'utilisation d'une technique de microscopie plus pointue : la microscopie électronique à transmission filtrée en énergie (Energy Filtered Transmission Electron Microscopy : EFTEM). Cette technique s'apparente à de la spectroscopie de perte d'énergie, dans ce cas utilise en mode imagerie. En se positionnant sur le pic plasmon du silicium, il est alors possible de ne récupérer que les électrons issus du silicium, et d'obtenir ainsi une imagerie de tous les clusters de silicium. Cette analyse s'est effectuée en collaboration avec l'Université de Barcelone.

Les échantillons luminescents ont été analysés par spectroscopie de photoluminescence résolue en énergie, en temps ou en angle. Le dispositif de photoluminescence résolue en énergie est constitué d'une lampe à mercure, d'un spectromètre TRIAX 190 - Jobin-Yvon constitué d'un réseau à 150 traits/mm, blazé à 500 nm et d'une caméra CCD. Le dispositif de photoluminescence résolue en temps utilise pour excitation la troisième harmonique à 355 nm d'un laser Nd:YAG pulsé au taux de répétition de 10 Hz et d'une durée d'impulsion de 10 ns. La détection se fait à l'aide d'un photomultiplicateur via un monochromateur (TRIAX 190, 600 traits/mm, blazé à 500 nm, Jobin-Yvon). La mise en place du dispositif de photoluminescence résolue en angle a fait partie de ce travail de thèse. Nous utilisons la lampe à mercure et la caméra CCD. Une fibre optique montée sur un support goniométrique réalisé spécialement pour cette étude permet de recueillir le signal à différents angles et de l'acheminer jusqu'au détecteur.

La spectroscopie de transmission s'effectue sur des échantillons déposés sur verre ou sur silice fondue à l'aide d'un spectromètre CARY 5000 - Varian. La transmittance est mesurée à incidence normale sur la gamme de longueur d'onde 175-3300 nm.

La détermination de l'absorption et de l'indice optique des couches revêt un caractère très important dans notre étude. Ces données ont été déterminées à l'aide des spectres de transmission UV-Visible et de deux modèles permettant de décrire les spectres obtenus. Le développement de ces modèles fait partie de ce travail de thèse.

Les deux modèles utilisés sont d'une part un modèle dit formel, et d'autre part le modèle des enveloppes de Swanepoel.

Dans le modèle formel, nous utilisons l'expression complète de la transmission d'une couche mince déposée sur un substrat transparent semi-infini. Cette expression dépend de l'absorption, de l'indice et de l'épaisseur de la couche. Dans cette expression, l'absorption s'exprime de différentes manières selon la zone spectrale :

Zone d'Urbach : $\alpha = \alpha_0 \exp(\frac{E}{E_u})$

Zone de Tauc : $\alpha E = B(E - E_g)^2$

La relation de dispersion de l'indice s'exprime selon une loi de Cauchy :

$$n = n_1 + \frac{n_2}{\lambda^2} + \frac{n_3}{\lambda^4}.$$

1. Les paramètres d'ajustement sont nombreux (il faut ajouter au paramètres précédents, n_1, n_2, n_3, E_u, α, E_g, B, l'épaisseur de la couche). La procédure à suivre doit donc être rigoureuse. L'acquisition des spectres se fait en mode double faisceaux, avec un faisceau de référence. Ceci nous permet d'avoir d'une part la transmission du substrat et d'autre part la transmission du film déposé sur le substrat. La transmission du substrat nous donne accès à son indice. La formule complète est ensuite ajustée en prenant l'ordre suivant :
2. n_1, n_2, n_3
3. E_u et α
4. E_g et B

La détermination de l'indice par la méthode des enveloppes est plus simple dans son principe. L'indice optique du substrat est déterminé comme précédemment. L'indice optique, le coefficient d'absorption et l'épaisseur de la couche se calculent ensuite à l'aide de la position et de l'intensité des maxima et des minima successifs de transmission. La seule intervention de l'expérimentateur consiste à désigner les trois zones décrites par Swanepoel : transparence, faible absorption, forte absorption.

La méthode formelle possède l'avantage de pouvoir obtenir une évaluation correcte de l'absorption près de la bande interdite, à condition toutefois de choisir la bonne expression de l'absorption dans cette zone. Son point faible est la nécessité d'ajuster un grand nombre de paramètres.

La méthode des enveloppes, plus directe, donne des résultats fiables pour l'évaluation de l'absorption et de l'indice dans les zones de transparence et de faible absorption. La détermination du coefficient d'absorption devient plus délicate dès lors que les oscillations dues aux interférences disparaissent, c'est-à-dire dans la zone de forte absorption près de la bande interdite.

Ces deux méthodes semblent complémentaires et seront utilisées conjointement dans ce travail.

Pour terminer, nous décrivons les modèles, également développés durant ce travail de thèse, qui concernent la modélisation des miroirs de Bragg et des microcavités. Les modèles utilisés s'appuient sur la méthode des matrices de transfert. Dans cette méthode, chaque couche de matériau est caractérisée par une matrice de transmission et de réflexion. L'absorption des couches, déterminée comme précédemment décrit sur les couches minces seules, est également prise en compte ainsi que le caractère polarisé ou non de la lumière. La transmission (ou la réflexion) totale du système s'obtient par multiplication des matrices de chaque couche.

Chapitre 3

Ce chapitre est consacré à l'étude du contrôle en taille et en densité surfacique des nanocristaux de silicium. L'objectif final est l'isolation et l'analyse d'un nombre restreint de nanocristaux de silicium, voire d'un nanocristal de silicium unique. Une telle étude revêt un caractère fondamental et ce type d'analyse est peu discuté dans la littérature. La possibilité de s'affranchir de l'élargissement inhomogène du signal de luminescence des nanocristaux de silicium permettrait d'aborder la compréhension des mécanismes de luminescence de ces nano-objets. Les enjeux sont par exemple la compréhension de la nature de la bande interdite et le rôle des phonons dans la relaxation des porteurs de charges à l'intérieur du nanocristal.

Dans notre cas, les agrégats de silicium s'obtiennent par recuit thermique d'une couche de SiO_x selon la relation :

$$SiO_x \rightarrow \frac{x}{2} SiO_2 + \left(1 - \frac{x}{2}\right) Si$$

La phase de silicium pur qui apparaît alors peut être amorphe ou cristalline. Elle constitue les nanostructures de silicium qui sont, dans les études présentées ici, nos émetteurs lumineux. Dans le cas d'une couche initiale de SiO_x enrichie en oxygène, on peut s'attendre à obtenir, à l'issue de la réaction de démixtion, des agrégats de silicium moins nombreux et/ou de plus petite taille. Dans les couches de SiO_x démixées, l'excès de silicium sera noté :

$$excès = \frac{1 - \frac{x}{2}}{1 + x}$$

Dans le but de modifier la quantité de nanocristaux de silicium, une première étude a été réalisée à partir de deux couches, l'une de SiO_1, l'autre de $SiO_{1,5}$. Ces échantillons sont obtenus par co-évaporation de SiO et de SiO_2. Les analyses par spectroscopie d'absorption infrarouge de l'étirement asymétrique de la liaison Si-O-Si en fonction de la température de recuit nous donne accès à la stœchiométrie des couches minces. Celle-ci évolue de 0,9 à 2 dans le cas de la couche de SiO, prouvant ainsi le caractère métastable de ce matériau. Pour la couche de $SiO_{1,5}$, le coefficient de stœchiométrie évolue quant à lui de 1,62 à 1,9, montrant ainsi que le phénomène de démixtion n'est pas complet. Dans les deux cas, la composition globale de la couche évolue vers de la silice stœchiométrique. Ceci tend à prouver que le silicium initialement présent dans la couche mince et issu de cette séparation de phase, reste en excès et s'agglomère pour former des agrégats. La couche de $SiO_{1,5}$ présente cependant, pour une température de recuit équivalente, un retard à ce phénomène de démixtion.

Pour les échantillons non recuits, l'analyse par spectroscopie de photoluminescence montre un pic aux alentours de 550 nm généralement attribué aux défauts de la silice. Avec la température de recuit, ce pic subit un décalage vers le rouge, et se stabilise vers 750 et 900 nm dans le cas des échantillons $SiO_{1,5}$ et SiO. Ces spectres de photoluminescence sont cependant difficilement interprétables. Les analyses de spectroscopie de photoluminescence en fonction de la température d'analyse ne montrent aucune évolution de la bande interdite de type Varshni ou Pässler, typique dans le cas de nanocristaux de silicium. L'analyse par spectroscopie de diffusion Raman révèle, quant à elle, la présence de

silicium amorphe dans le cas de l'échantillon de SiO. L'analyse Raman de l'échantillon $SiO_{1,5}$ n'a rien révélé de probant. Pour conclure, cette première étude révèle la possibilité d'obtenir des centres luminescents par recuit thermique à partir de couches de SiO. Ces centres luminescents peuvent difficilement être attribués à des nanocristaux de silicium et leur rendement optique est faible.

L'étude s'est alors poursuivie avec l'analyse de multicouches SiO/SiO_2. Ce type d'échantillon permet, par rapport aux couches minces étudiées précédemment, de mieux contrôler la taille des nanostructures de silicium. Lors du recuit thermique de la multicouche, comme observé précédemment, le SiO se décompose pour former des agrégats riches en silicium. Les couches de SiO_2, situées de part et d'autre, jouent alors le rôle de barrière thermique, limitant ainsi la coalescence des nanograins de silicium selon la direction de croissance de la multicouche.

Une étude préalable des conditions de recuit est tout d'abord décrite. Elle montre l'effet d'un recuit sous vide primaire, vide secondaire et sous atmosphère d'azote. Il apparaît que les nanocristaux de silicium issus de multicouches recuites à 1100°C sous atmosphère d'azote sont plus luminescents, de taille plus petite (d'après la position en énergie du pic de photoluminescence), avec cependant une largeur à mi-hauteur du pic de photoluminescence plus importante. Ce dernier point peut s'interpréter comme la présence d'une plus grande dispersion en taille pour cet échantillon. Nous choisirons par la suite de recuire les multicouches pendant cinq minutes à 1100°C sous pression atmosphérique d'azote

Les nanocristaux issus du système multicouche SiO/SiO_2 ont été, avant le début de ce travail, bien caractérisés en taille par microscopie électronique à transmission. Leur signal de photoluminescence, quant à lui, est typique de ce genre de structures. Il permet d'évaluer de façon plus ou moins précise la taille moyenne des nanostructures. La spectroscopie de diffusion Raman, en revanche, a été peu mise en œuvre pour étudier les nanocristaux de silicium issus de multicouches SiO/SiO_2. .

Des multicouches SiO/SiO_2 avec des épaisseurs de SiO de 2, 3 et 4 nm ont donc été évaporées et analysées par spectroscopie de photoluminescence et diffusion Raman. Seules les multicouches 4/5 nm ont donné du signal Raman exploitable. Les spectres de photoluminescence de cet échantillon montrent, pour l'échantillon non recuit, un pic de photoluminescence correspondant aux défauts de la silice. Après un recuit à haute température, l'intensité du pic des défauts de la silice diminue fortement au profit d'un signal intense et large aux alentours de 840 nm. L'évolution du maximum du signal de photoluminescence évolue avec la température d'analyse et peut être ajustée par une loi de type Varshni. Ce point nous autorise à attribuer ce signal de photoluminescence à du silicium cristallin. La position spectrale de ce pic de photoluminescence se situe à une énergie supérieure à celle du silicium cristallin massif. Ce point suffit à lui seul pour évoquer un confinement quantique. Nous avons donc, dans le cas des multicouches recuites, des nanocristaux de silicium fortement luminescents.

L'analyse par diffusion Raman de ces structures, bien que rendue délicate par la présence du substrat de silicium, permet néanmoins d'observer un décalage vers les petits nombres d'onde. Ceci est décrit dans la littérature comme le signe d'un confinement de phonons à l'intérieur du nanocristal de silicium. Des modèles ont alors été développés afin d'analyser quantitativement les décalages observés lors de ces expériences de photoluminescence et de diffusion Raman. Le modèle de photoluminescence prend en compte une distribution gaussienne des tailles des nanoparticules, une évolution théorique de l'énergie de la bande interdite en fonction de la taille des nanoparticules ainsi qu'une expression phénoménologique des forces d'oscillateur des transitions dans ces nano-objets. Le modèle Raman, quant à lui, consiste à développer, dans l'espace réciproque, une fonction de Lorentz

sur une base de fonctions de confinement. Celles-ci sont du type sinus cardinal. L'ajustement des courbes à partir de ces deux modèles est bon et donne des résultats compatibles avec notamment une taille de nanocristal de l'ordre de 5 nm.

Le bon contrôle de la taille des nanocristaux de silicium ayant été vérifié par spectroscopie de photoluminescence et diffusion Raman, l'étude s'est orientée vers le contrôle de la densité surfacique de nanocristaux. En nous inspirant de l'étude menée précédemment sur les couches minces de SiO_x, des multicouches SiO_x,/SiO $x \in \{1, 1{,}25, 1{,}5, 1{,}75\}$ d'épaisseurs 3/5 nm ont été élaborées. Plus précisément, il s'agit de couches uniques de SiO_x $x \in \{1, 1{,}25, 1{,}5, 1{,}75\}$ d'une épaisseur de 3,3 nm enchâssées entre des couches de 9 nm de SiO_2. Le choix d'une épaisseur de 9 nm pour les couches de SiO_2 supérieure et inférieure relève d'une optimisation des propriétés de luminescence réalisée au préalable. Les couches de SiO_x, après recuit thermique, conduisent en principe à la formation d'un unique plan de nanocristaux de silicium situé dans une matrice de silice.

L'analyse par photoluminescence de ces échantillons montre un signal de nanocristaux de silicium pour les couches centrales initiales de SiO_1 et $SiO_{1,5}$. Seuls des signaux correspondant à des défauts de la silice sont visibles pour les deux autres compositions. Par ailleurs, le signal de photoluminescence le plus intense est obtenu pour la couche initiale de SiO_1. D'après la position du pic de luminescence, les nanocristaux obtenus à partir de la couche initiale de SiO_1 semblent également être plus gros en moyenne que ce de la couche initiale de $SiO_{1,5}$.

Des lames minces ont été réalisées à partir de ces échantillons et analysées par microscopie électronique à transmission filtrée en énergie. Conformément à nos attentes, il apparaît que la densité surfacique des nanocristaux de silicium augmente avec l'augmentation de l'excès de silicium. Parallèlement à cela, le diamètre des nanocristaux de silicium augmente très légèrement. Ceci prouve que nous avons bien la possibilité de contrôler à la fois le diamètre et la densité surfacique (ou volumique dans le cas d'une multicouche) des nanocristaux de silicium.

Dans nos échantillons, la densité surfacique de nanocristaux de silicium reste néanmoins importante et rend difficile l'obtention d'un nanocristal unique par modification des paramètres d'élaboration. Afin de progresser davantage vers l'isolement de quelques nanocristaux de silicium, des techniques de nanostructuration de surface ont été développées durant ce travail de thèse. Celles-ci requièrent un travail en salle blanche et l'utilisation de la lithographie électronique. Dans un premier temps, des masques ont été dessinés puis reportés sur une couche d'aluminium. L'épaisseur de cette couche a été préalablement choisie de façon à être totalement opaque à la lumière à la longueur d'onde des nanocristaux de silicium. L'ouverture des trous dans la couche d'aluminium s'effectue ensuite par attaque chimique à l'aide d'une solution d'acide phosphorique diluée. La vitesse d'attaque chimique par cette solution acide a été préalablement calibrée, et le temps d'attaque choisi afin de réaliser des ouvertures de tailles minimum 50 à 100 nm. Les masques ainsi réalisés, et observés par microscopie à force atomique et microscopie électronique à balayage, montrent des ouvertures complètes de la couche d'aluminium avec des diamètres de l'ordre de 100 nm. De telles ouvertures, étant données les densités surfaciques évaluées précédemment pour une couche de SiO_1, devraient permettre d'observer aux alentours de 300 nanocristaux de silicium.

La pratique de la spectroscopie de photoluminescence à travers de telles ouvertures nécessite l'utilisation d'un dispositif à microscope confocal que l'on trouve sur le dispositif Raman. Les spectres de photoluminescence obtenus montrent un spectre large pour des ouvertures dans l'aluminium de

l’ordre 2 µm. Ces spectres sont conformes à ceux obtenus en champs lointain. Lorsque le diamètre des ouvertures se réduit, l’intensité du spectre de photoluminescence diminue, mais reste néanmoins large. Il ne permet pas la mise en évidence de la signature optique de nanocristaux individuels.

Les résultats présentés dans ce chapitre sont issus d’un travail très prospectif qui présente de réelles difficultés de mise en œuvre. Il est néanmoins d’un intérêt considérable pour la communauté scientifique travaillant sur les nano-objets en silicium. Quelques autres pistes existent visant à explorer le nanocristal individuel. Parmi celles-ci, nous pouvons évoquer les expériences de photoluminescence à basse température à réaliser à travers les ouvertures d’aluminium. Nous pouvons également travailler sur la croissance et la spectroscopie optique de piliers de diamètres de l’ordre de quelques centaines de nanomètres et contenant des nanocristaux de silicium. Une autre possibilité serait une analyse de spectroscopie par champ proche optique de ces nano-objets.

Chapitre 4

Ce chapitre est consacré à l'étude de l'interaction lumière-nanocristal de silicium via la structuration modale de l'environnement électromagnétique. De façon plus précise, il s'agit de contrôler l'émission de lumière issue des nanocristaux de silicium. Celle-ci, de part son caractère spontané, est par essence non-contrôlable. L'idée est de modifier la répartition spatiale de cette lumière ainsi que son temps d'échappement hors du système. Une telle étude a des visées fondamentales comme la compréhension des mécanismes de couplage lumière-matière ou la réalisation de nano-émetteurs. Mais elle rendrait possible la réalisation d'applications plus concrètes. La réorganisation spatiale du diagramme de rayonnement issu des nanocristaux de silicium permettrait par exemple une injection optique efficace de cette source de lumière dans des fibres optiques. Ce point est d'autant plus important qu'il concerne des émetteurs en silicium et réalisés sur silicium à l'aide de techniques compatibles avec la technologie CMOS.

Au début de ce travail, la réalisation de miroirs de Bragg et à fortiori de microcavités optiques par évaporation n'avait jamais été abordée au laboratoire. Ce chapitre détaille donc les différentes étapes de réalisation et d'analyse de tels objets.

Nous nous posons la question, dans un premier temps, du choix du matériau à utiliser afin de réaliser de telles microcavités. La couche active de la microcavité est constituée de nanocristaux de silicium issus de la démixtion d'une multicouche SiO/SiO_2. Dans la littérature, les matériaux les plus employés pour la réalisation de miroirs de Bragg sont le dioxyde de titane (TiO_2) couplé au dioxyde de silicium (SiO_2). Ce couple de matériaux permet d'obtenir des miroirs de Bragg transparents dans le visible. L'utilisation du silicium en remplacement du TiO_2 est possible, mais ce type de miroir de Bragg, à cause de la présence de silicium, absorbe une partie de la lumière visible. Nous avons également au laboratoire la possibilité de réaliser, par évaporation, des couches de dioxyde d'étain (SnO_2). Une première étude théorique est présentée montrant l'efficacité de différents miroirs de Bragg réalisés à l'aide de ces différents couples de matériaux. Le doublet SiO_2/TiO_2 s'avère être le plus efficace pour la réalisation d'une bande interdite photonique large et de forte réflectivité. Des essais d'élaboration de TiO_2 par évaporation de titane sous oxygène moléculaire ont été réalisés, mais il apparaît difficile, pour des raisons de simplicité et de reproductibilité, d'utiliser le TiO_2 pour la, réalisation des miroirs de Bragg. Nous choisissons donc le doublet Si/SiO_2.

L'apparition de nanocristaux de silicium via la démixtion d'une multicouche SiO/SiO_2 se fait par un recuit thermique rapide aux alentours de 1100°C. La réalisation de la microcavité optique se fait de façon monolithique lors d'un unique processus d'évaporation. Un point important à noter est que les couches minces obtenues par cette technique sont poreuses. Elles subissent donc certainement, durant le recuit thermique, d'importantes modifications de leurs épaisseurs et de leurs indices de réfraction optique car le matériau se densifie. Or la maîtrise de ces deux derniers paramètres, dont le produit constitue l'épaisseur optique de la couche déposée, est cruciale dans le contrôle de la bande interdite optique du miroir de Bragg. Nous présentons donc une étude systématique de propriétés optiques des couches minces de silice et de silicium, des miroirs de Bragg ainsi que des microcavités en fonction de la température de recuit. Une étude de l'influence de l'épaisseur de la couche active est également présentée.

Les propriétés optiques des couches minces de silicium et de silice en fonction de la température de recuit sont présentées dans un premier temps. Celles-ci sont analysées à l'aide de différentes techniques : ellipsométrie spectroscopique, spectroscopie de transmission dans le domaine spectral UV-Visible et réflectométrie X. Concernant la spectroscopie de transmission dans le domaine spectral UV-Visible, deux méthodes ont été développées durant cette thèse: la méthode formelle et la méthode des enveloppes de Swanepoel. La procédure utilisée pour la méthode formelle est donnée en détails. Les analyses en fonction de la température de recuit des couches de silicium déposées sur un substrat de silice fondue donnent des résultats proches. Elles nous permettent de déterminer l'évolution de l'indice optique pris à 800 nm (longueur d'onde d'émission des nanocristaux de silicium) avec la température de recuit. L'évolution obtenue à l'aide de la méthode des enveloppes de Swanepoel montre un saut d'indice entre 500 et 700°C qui pourrait être lié à la cristallisation du silicium initialement amorphe. Les techniques de spectroscopie de transmission dans le domaine spectral UV-visible montrent également une diminution de l'épaisseur de la couche de l'ordre de 10 à 17%. L'observation conjointe de ces deux phénomènes met en évidence un phénomène de densification de la couche mince. Les expériences de réflectométrie de rayons X montrent, quant à elles, une diminution d'épaisseur de l'ordre de 11%. La spectroscopie de transmission UV-visible nous donne également accès au coefficient d'absorption des couches de silicium recuites. Ce paramètre est très important et devra être pris en compte dans la modélisation des miroirs de Bragg et des microcavités optiques. Là encore, les résultats obtenus par la méthode formelle est par la méthode des enveloppes de Swanepoel sont semblables. La méthode formelle, comme présentée au Chapitre 2, nous donne également accès au paramètres α_0 et E_u d'Urbach. Ces paramètres sont proches de ceux obtenus dans la littérature. Cette méthode nous fournit également l'énergie de Tauc E_g ainsi que le paramètre de Tauc B. Là encore, les paramètres obtenus sont cohérents avec ceux de la littérature donnés pour du silicium cristallin. L'évolution de E_u en fonction de B semble témoigner, comme démontré de cette façon dans la littérature, d'une augmentation de l'ordre cristallin dans la couche de silicium. L'ensemble de ces analyses révèle donc une cristallisation et une densification de la couche de silicium avec le recuit.

L'indice optique de la couche de SiO_2 a été déduit d'analyses d'ellipsométrie spectroscopique. L 'épaisseur de la couche, quant à elle, a été tirée d'analyses par ellipsométrie et réflectométrie de rayons X. Nous observons une diminution d'épaisseur de l'ordre de 11% après un recuit de la couche à 1100°C ainsi qu'une légère augmentation de l'indice optique. Celui-ci peut être considéré constant étant donné la faible variation observée.

Finalement, les propriétés optiques de la couche active sont finalement analysées par spectroscopie de transmission UV-visible et à l'aide des deux méthodes citées ci-dessus. Une telle étude reste forcément approximative car un tel système constitué de multicouches puis de nanocristaux de silicium est fort complexe et nécessite, afin d'être bien compris, une étude plus poussée. Elle nous donne néanmoins un ordre de grandeur sur lequel nous nous appuierons lors de la modélisation des microcavités otiques. Les deux méthodes d'analyse nous donnent des ordres de grandeur de l'indice optique et du coefficient d'absorption équivalent.

Les résultats obtenus lors de la caractérisation des couches minces formant la brique de base du miroir de Bragg et de la microcavité optique sont ensuite utilisés pour l'étude des miroirs de Bragg. Dans un premier temps, une série de miroirs de Bragg non recuits et contenant de deux à cinq doublets

sont analysés par transmission UV-visible. Cette étude permet dans un premier temps de valider le modèle optique développé durant cette thèse. Nous observons qu'il nous permet de modéliser les spectres de transmission des miroirs de Bragg en tenant compte de paramètres d'absorption eux même déduits précédemment (paramètres d'Urbach α_0, E_u et de Tauc B et E_u). Cette étude nous permet également d'évaluer l'influence du nombre de doublets Si/SiO_2 sur la formation de la bande interdite photonique du miroir de Bragg. Les résultats expérimentaux sont cohérents avec ceux obtenus par modélisation.

Le comportement des miroirs de Bragg sont ensuite analysés en fonction de la température de recuit. Les paramètres utilisés dans ces simulations correspondent à ceux déterminés auparavant pour chaque température de recuit. Dans ces conditions, le décalage expérimental de la bande interdite photonique avec la température de recuit est reproductible par simulation. L'évolution des épaisseurs et des indices utilisés lors de ces simulations avec la température de recuit témoigne du processus de densification du miroir de Bragg. Les épaisseurs diminuent de l'ordre de 17 et 20% pour la silice et le silicium. Les indices optiques, quant à eux, augmentent de 7 et 9% pour ces mêmes matériaux.

Les microcavités sont ensuite analysées. D'un point de vue technique, il nous est difficile de réaliser des microcavités d'épaisseur totale supérieure au micromètre, le procédé d'élaboration n'étant pas adapté à la réalisation d'échantillons épais. Cette limitation en épaisseur déduit la possibilité d'obtenir des facteurs de qualité important. En tenant compte de cette contrainte technique, nous visons la réalisation de microcavités constituées de trois doublets Si/SiO_2 de part et d'autre de la couche active. Une étude théorique préliminaire, sans tenir compte de l'absorption par la couche de silicium, nous montre que le facteur de qualité attendu pour de telles microcavités est de l'ordre de 300.

Une étude préalable sur la faisabilité de telles microcavités est réalisée sur une microcavité contenant de part et d'autre de la couche active des miroirs de Bragg à deux doublets Si/SiO_2. Les analyses par microscopie électronique montrent, sur les échantillons recuits et non recuits, des interfaces Si/SiO_2 abruptes et peu rugueuses. Nous observons également clairement l'aspect polycristallin des couches de silicium sur l'échantillon recuit à 1100°C. Cette analyse montre le bon maintien de la structure des microcavités avec le recuit thermique. Il nous donne également accès aux épaisseurs réelles des matériaux.

Il faut noter cependant que les couches déposées constituant les miroirs de Bragg ne semblent pas homogènes en épaisseur. Ce point est à relier à la méthode d'élaboration et semble difficile à améliorer. De ce fait, une étude par simulation est alors exposée dont l'objectif est de montrer l'influence d'une fluctuation d'épaisseur d'une des couches constituant la cavité sur la résonance de cette dernière. Il ressort de cette étude qu'une variation de 10% sur l'épaisseur d'une des couches conduit à un décalage de la résonance de la microcavité de l'ordre de la dizaine de nanomètres. Dans notre cas, avec des largeurs à mi-hauteur des spectres de photoluminescence des nanocristaux de silicium de l'ordre de 130 nm (0,23 eV pour un spectre de photoluminescence centré à 869 nm (1,42 eV), un tel décalage ne constitue pas un problème majeur. Avec de telles largeurs, il sera toujours possible de trouver des centres luminescents centrés sur la résonance de la microcavité.

Par la suite, les microcavités sont analysées, comme l'ont été les miroirs de Bragg, en fonction de la température de recuit. Dans ces simulations, nous utilisons pour les couches minces et les miroirs de Bragg les paramètres (épaisseur, indice, absorption) déterminés précédemment. Les nouveaux paramètres sont ici l'épaisseur, l'indice optique et l'absorption de la couche active. Les spectres

simulés décrivent bien les spectres expérimentaux représentant l'évolution du pic de résonance de la microcavité en fonction de la température de recuit. Les réductions d'épaisseur des couches de silicium, de silice et de la couche active sont de l'ordre de 10, 15 et 6%. Le décalage vers le bleu du pic de résonance de la microcavité induit par le recuit est de l'ordre de 0,068 nm/°C. Contrairement à la variation d'épaisseur des couches constituant les miroirs de Bragg dont nous avons vu que l'influence était négligeable, l'effet du recuit thermique est important puisqu'il est, au final, de l'ordre de la centaine de nanomètres entre l'échantillon non recuit et l'échantillon recuit. Il est donc très important de quantifier ce décalage et d'en tenir compte dans le dessin des microcavités.

Finalement, l'étude de l'influence de l'épaisseur de la couche active à été réalisée. Des microcavités constituées de miroirs de Bragg à deux doublets Si/SiO_2 et de couches actives de différentes épaisseurs ont été réalisées. Ces couches actives étant elles-mêmes constituées de multicouches SiO/SiO_2, des échantillons contenant de 18 à 21 doublets SiO/SiO_2 ont été élaborés. Une évolution du pic de transmission de la microcavité de l'ordre de 4,5 nm par nm déposé est observée. Là encore, une telle influence de l'épaisseur de la cavité sera à prendre en compte afin de bien centrer la microcavité sur le pic d'émission des nanocristaux de silicium.

Ce chapitre se termine par la présentation de résultats d'analyse des microcavités par spectroscopie de photoluminescence. Dans le cas des nanocristaux de silicium en espace libre, la longueur d'onde d'excitation la plus efficace se situe dans l'ultraviolet. Nous utilisons généralement la longueur d'onde de 313 nm issue de la lampe à mercure. La situation est différente dans le cas des nanocristaux placés en microcavité puisque les couches de silicium absorbent fortement dans l'ultraviolet. Une analyse par spectroscopie de photoluminescence sélective a donc été réalisée en utilisant les différentes raies de la lampe à mercure. Elle montre que la longueur d'onde permettant de recueillir le maximum de signal issu de la cavité est de 546 nm. Nous utiliserons cette longueur d'onde par la suite.

La microcavité à miroirs de Bragg à deux doublets Si/SiO_2 a d'abord été étudiée. Un échantillon contenant des nanocristaux de silicium en espace libre est élaboré pour comparaison. Après recuit, la résonance le la microcavité, observée par spectroscopie de photoluminescence et par réflexion dans le domaine UV-visible, est bien située dans le large pic de photoluminescence des nanocristaux de silicium. Le signal de photoluminescence de la microcavité montre un pic étroit, de largeur à mi-hauteur 25 nm, situé à 780 nm. L'intensité de photoluminescence issue de la microcavité est plus faible que celle de l'échantillon de référence. Si nous supposons que les conditions de couplage entre nanocristal et cavité sont présentes, nous observons ici un simple effet de filtrage du signal des nanocristaux de silicium. Ceci peut également se traduire par un couplage faible de type Purcell avec un facteur de Purcell de valeur inférieure à l'unité. Cette interprétation est possible dans la mesure où le facteur de qualité de la microcavité reste faible (de l'ordre de 30) et le volume modal important (pas de confinement optique dans le plan de la microcavité). Par ailleurs, nous ne tenons pas compte, dans cette analyse, de l'absorption de la couche supérieure de silicium. Celle-ci réduit considérablement le signal de photoluminescence recueilli et issu de la microcavité. Le phénomène de filtrage et de modification de la densité spectrale optique à l'intérieur de la cavité est visible également lors d'analyses par photoluminescence résolue en angle. La position du maximum du pic de photoluminescence issu de la microcavité suit bien les lois d'évolution en angle de tels objets. Des lobes lumineux sont également mesurés sur cet échantillon témoignant de la redistribution spatiale de la lumière à l'intérieur de la microcavité.

Nous analysons ensuite la microcavité constituée de miroirs de Bragg à trois doublets Si/SiO_2. Deux échantillons de référence sont alors élaborés : le premier est un échantillon classique simplement constitué de nanocristaux de silicium. Le deuxième est identique mais possède sur sa partie supérieure une couche de silicium d'épaisseur équivalente à celle contenue dans le miroir de Bragg supérieur. L'objectif est de tenir compte de l'absorption de la couche de silicium. Le phénomène de couplage entre la cavité et les émetteurs de lumière est, cette fois-ci, nettement visible. La luminescence issue de la microcavité est plus fine et plus intense que celle issue des nanocristaux de silicium. Ceci est d'autant plus visible lorsque la comparaison se fait avec l'échantillon de nanocristaux de silicium pourvu d'une couche supérieure supplémentaire de silicium. Le pic de photoluminescence issu de la cavité nous permet d'évaluer le facteur de qualité de l'ordre de 90. La sélectivité en angle est, elle aussi, nettement visible, avec des lobes d'émission lumineuse bien séparés spatialement. Afin de confirmer la présence de couplage faible de type Purcell sur ce type de système, nous avons réalisé des analyses par photoluminescence résolue en temps. La théorie de couplage faible prédit en effet une diminution du temps de déclin de la photoluminescence dans le cas d'émetteurs couplé en régime de couplage faible à une microcavité. Ces expériences, bien que difficiles à réaliser sur nos systèmes étant donnés les faibles signaux obtenus, nous ont permis d'observer cette diminution du temps de déclin de photoluminescence. La modification obtenue est de l'ordre de grandeur de celle décrite dans la littérature.

General introduction

Silicon nanocrystals have attracted much attention for the beginning of the nineteenth. The discovery of the possibility to obtain an intense photoluminescence signal in the visible range with porous silicon by Canham *et al.* has opened new possibilities for the realization of optoelectronic components on silicon substrates. Such a discovery is really important as it gives the possibility to combine both electronic and optoelectronic components on the same silicon substrate.

It is well known that bulk silicon has an indirect band gap with energy of about 1.12 eV. Then, an electron must interact with a phonon in order to relax from the conduction band down to the valence band, and by satisfying the conservation of the impulsion vector. In this case, the probability of such a transition is low in comparison with the probability of occurrence of non-radiative transition. Thus, the bulk silicon is a bad photon emitter with a quantum yield of about 10^{-6}.

When the dimensions of silicon are reduced until few nanometers, we obtain structures called silicon nanocrystals, and new properties appear due to the carrier quantum confinement. First, we have an increase of the optical band gap. This band gap can be tuned over all the visible range by modifying the size of the silicon nanocrystal. Moreover, we observe an increase of the quantum yield, giving then the possibility to have an intense luminescence signal. The origins of those phenomena are still not well understood. One interpretation is the possibility, due to the Heisenberg uncertainty principle, to relax the selection rules on the momentum by reducing the size of the crystal. This fact yields then to an increase of the luminescence of the material. For example, it has been shown that the emission process can occur without phonon emission for nanocrystals with sizes below 2 nm.

Many applications are expected to be possible with such silicon nanocrystals materials. Many studies were dedicated to the realization and analysis of silicon-nanocrystal-based electroluminescent diodes. Few studies have been published showing the possibility to obtain optical gain in few silicon-nanocrystals-based systems. The obtained results are still debating in literature, and many efforts must be done to realize a silicon-nanocrystal laser. We can also mention the possibility to obtain silicon-nanocrystals-based devices emitting light at 1.55 µm. This is possible by doping matrices containing silicon nanocrystals with erbium ions. An important coupling between the nanocrystal and the erbium ion then appears, and energy transfers are possible between those two entities. Then, when the energy transfer process is efficient, nanostructured materials doped with erbium ions benefit of both an important photon capture cross section and of an intense emission at 1.55µm. Another application of the band gap engineering of the silicon nanocrystals is the possibility to realize efficient converter layers for solar cells. Many studies are currently devoted to the possibility of the use of silicon nanocrystals to enhance the efficiency of the solar cells. The aim of those studies is, for example, to include silicon nanocrystals with different sizes to enlarge the capture energy range of solar photons. In the field of optical devices realized with silicon nanocrystals, we see in literature that few groups have tried to control the spontaneous emission from those nanostructures. The main tool used for that is the optical microcavities realized with Bragg mirrors. In such systems, the coupling between optical confined modes and silicon-nanocrystals confined modes yield the enhancement (or the reduction) of the optical emission from the silicon nanocrystals and the change in the luminescence distribution. Such studies are useful for both realizing efficiency optical devices and analyzing coupling phenomenon between light and nanomaterials. Finally, we can also mention the possibility to use

silicon nanocrystals in non-volatile memories. In such systems, the nanocrystals are expected to give a better control of the number of careers localized in the device, to increase the retention time of such careers, and will give the possibility to use lower control voltages.

Many progresses have been realized in the growth of silicon nanocrystals. Different techniques are used, such as ionic implantation, sputtering, evaporation, laser deposition, chemical vapour deposition … For the analysis of optical and electrical properties of silicon nanocrystals, the key point is the control of the sizes.

In our group, many works have been devoted to the study of SiO_x layers. The deposition technique is reactive evaporation, for example of silicon under oxygen atmosphere. We also have studied the formation of SiN_x and GeO_x thin layers growth by using the same technique. Such samples are first studied for their own properties, to understand the growth processes. Recently, the study of SiO_x samples annealed under high temperature has shown the possibility to obtain silicon-rich clusters embedded in SiO_2 matrix. The optical properties and the formation of those clusters were analyzed in detail. Then, the idea of controlling the size of the silicon clusters arised. The realization of SiO/SiO_2 multilayers gives us the possibility to control the silicon nanocluster sizes. We show then that it is possible to obtain well crystallized silicon cluster after high temperature annealing of SiO/SiO_2 multilayers. The optical and structural properties of such nanocrystals have been studied in details. We also worked in the coupling between those silicon nanocrystals and the erbium ions. We demonstrate the possibility of an energy transfer between those two entities.

The aim of this work is to go further in the analysis of the silicon nanocrystals. More especially, we oriented the studies in two directions. The first one is to see if it is possible to analyze a reduce number of silicon nanocrystals. Such studies and such informations are scared in literature. Studying one or few nanocrystals will give the possibility to better understand the relaxation process in the silicon nanostructures and maybe to better control their emission process. Those points remain not understood. In the second direction, we look after the possibility to control the spontaneous emission from the silicon nanocrystals. As we mentioned above, this is possible by coupling the silicon nanocrystals with confined optical modes. Such confined optical modes can be obtained by realizing optical microcavities. The control of the emission process of silicon nanocrystals could have a technological interest, for example to improve the optical injection in optical fibres of light coming from a hypothetical silicon nanocrystal device. Moreover, the study of such systems could lead to the possibility of analyzing light/matter interactions. In particular, it could also give informations, from an indirect manner, about the optical properties of a single silicon nanocrystal.

In the first part of this manuscript, we describe the results we found in literature. We give details of the different existing possibilities to obtain silicon nanocrystals. We describe also the different approaches to obtain informations on single quantum dots and silicon nanocrystals. Then, we briefly describe the physics of optical microcavities and the origins of the light/matter coupling in such microcavities.

In the second part of the manuscript, we describe the setups we used in this study. First, we give details about the evaporation system and about the way to make silicon nanocrystals appear. Then, we systematically describe the setups we used for characterization of the samples, in particular the setups that have been developed during this work. We give also details about the different models and

programs we have written for analyzing of the transmission spectra. Finally, we mention in the chapter the different collaborations we started during the work.

The third chapter is dedicated to the description of the results concerning the analysis of few silicon nanocrystals. First, we discuss the results we obtained in the trial to isolate one or few nano-objects. To reach this aim, we tried to play with the growth procedure for controlling both the size and the surface density of the silicon nanocrystals. Then we described the results of nanostructuring the surface for isolating few silicon nanocrystals. Then, we discuss the results we had dealing with the optical characterizations of our samples.

In the fourth chapter, we describe the different steps we worked onto to realize the optical microcavities. The characterizations of the different materials we used in the realization of the microcavities are showed. The growth, the modelling and the characterization of both the Bragg mirrors and the optical microcavities are then described. Finally, we discuss the results we obtained by analyzing the luminescence from these optical microcavities. An estimation of the linewidth of silicon nanocrystals will be deduced, showing that microcavities may be another, less complicated, possibility to analyse the optical properties of single silicon nanocrystals.

Chapter 1. Bibliography and state-of-the-art

Introduction

In this chapter we give a short introduction into the theory of both light emitting silicon and optical microresonators.

First, by comparing bulk silicon to nanocrystalline silicon, the influence of the nano-structuring on the luminescence properties will be highlighted. It will be shown that the nano-structuring causes an enormous increase of the photoluminescence intensity and a shift of this photoluminescence to the visible spectral range. This increase can be explained by the increased recombination probability of an electron from the conduction band and a hole from the valence band (a so called electron-hole-pair or exciton), whereas the blueshift is due to Coulomb interaction of the electron and the hole.

The second part of this chapter aims at introducing the coupling between the silicon nanocrystals as emitter to an optical microresonator. By the optical microresonator, the optical density of states is drastically changed: there are only few defined allowed states instead of a continuum of states as in free space. The fundamental parameters that characterize the microresonator are introduced as the quality factor Q and the modal volume V, which both influence the Purcell factor F_P. F_P describes the change of the emission rate of the emitter when it is coupled to the microresonator.

1.1 Silicon nanocrystals

Bulk silicon: In semiconducting materials, the luminescence originates from the radiative recombination of the electrons and the holes over a forbidden band-gap. It is thus important to know the band-structure of those semiconductors in order to be able to influence their optical properties.

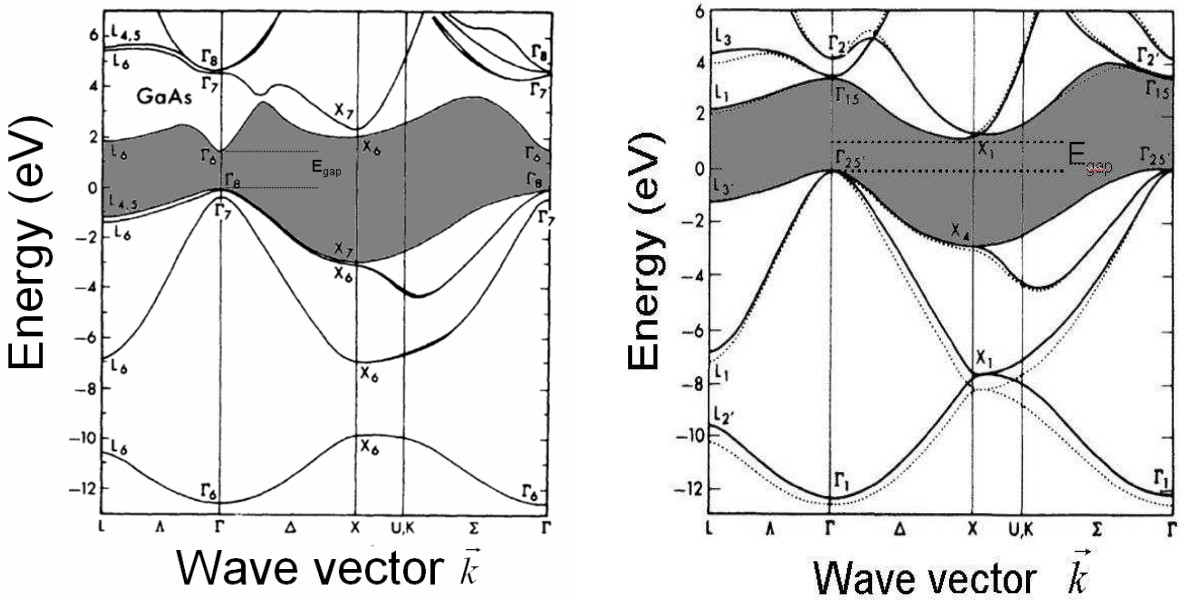

(a) *(b)*

Figure 1.1: Semiconductor band structures (a) GaAs; (b) silicon. The first is a direct band-gap semiconductor, the second an indirect one [22,OJ].

The band structures of GaAs and silicon are shown in Figure 1.1 (a) and (b) respectively. The difference between the two materials consists in the position on the k axis of the extremes of conduction and valence band, respectively. Materials as e.g. GaAs with the two extremes at the same k value are called direct semiconductors because an electron which has been excited to the conduction band can be desexcited directly falling down to the maximum of the valence band without changing the k vector. In contrary, in silicon, the extremes of the two bands are at different positions on the k-axis. It is called an indirect semiconductor because the direct transition between conduction and valence band is forbidden. To desexcite, the electron needs the interaction with a lattice vibration quantum, called phonon. The phonon finally induces a displacement of the electron on the k axis to a point at the same k value as the maximum of the valence band. Now, the electron can desexcite.

As we can see, the nature of the band-gap – whether direct or indirect – has an important influence on the interaction of a semiconducting material with an electromagnetic wave. In the case of GaAs, e. g. the recombination of an electron at the minimum of the conduction band with the hole at the maximum of the valence band at the same wave vector k has a high probability to occur as it is a two-particles-interaction. The momentum is thus conserved and the energy of the emitted photon corresponds to the energy of the band-gap. In this case, the radiative lifetime is very short, typically some nanoseconds. Its inverse, the radiative recombination rate $W_{rad.}=1/\tau_{rad.}$ is high which leads to a high radiative efficiency η, given by

$$\eta = \frac{W_{rad.}}{W_{rad.} + W_{nonrad.}} \tag{1-1}$$

where $W_{nonrad.}$ is the non-radiative recombination rate. Typically, η is of about 1% at room temperature and of about 10% at very low temperature.

In the case of silicon, the maximum of the valence band is at the centre of the first Brillouin zone and the minimum of the conduction band is at the point (0.86;0;0) π/a, a being the lattice parameter of silicon. In order to conserve the momentum, the interaction has to take place involving as a third particle a lattice vibration quantum, called phonon. Phonons are in general of low energy but possess a big momentum. The creation or annihilation of a phonon allows conserving the momentum of the three-particle-system. As the interaction between three particles is very improbable, the radiative lifetime is increased to the order of magnitude of the millisecond. In addition, the photoluminescence efficiency is very low as the nonradiative recombination centres are predominant. Thus, the efficiency of silicon varies between 10^{-4} – 10^{-5} % at room temperature. Furthermore, the bandgap of silicon is of 1.1 eV which corresponds to the near infrared spectral range. Thus, bulk silicon is a poor candidate for optoelectronic or photonic devices working in the visible spectrum.

Silicon nanocrystals: The discovery of an intense luminescence band in the visible at room temperature in porous silicon discovered by Canham [1] triggered the interest on the study of the optical properties of porous silicon on the level of application as well as the understanding of the recombination mechanisms. Canham proposes that the origin of the luminescence comes from the quantum confinement of the exciton provoked by the geometrical reduction of the dimensions of the silicon structure. The quantum confinement model in the silicon aggregates describes an increase of the emission energy and an increase of the radiative recombination rate. In porous silicon, the

photoluminescence band can be shifted throughout the whole visible spectrum by varying the porosity. In the case of silicon nanocrystals embedded in a matrix of silicon oxide, the photoluminescence band shifts down to 700 nm if the silicon concentration is reduced. The description by this model will be the topic of the following section. The origin of the band is subject of an intense debate in literature. Other models have followed the Canham's interpretation of the quantum confinement taking into account hydrogenated amorphous silicon, hybrid surfacial molecules or surface states [2]. Godefroo *et al.* [3] have investigated the origin of the photoluminescence in silicon nanocrystals in 2008 by means of photoluminescence under the influence of a strong magnetic field. They have shown that in the case of size-controlled silicon nanocrystals produced by evaporation, the origin of the luminescence is of non-confinement origin, if the silicon nanocrystals are annealed in controlled nitrogen atmosphere. A magnetic field dependent photoluminescence as a sign of quantum confinement was only found for samples that have been post-annealed in controlled hydrogen atmosphere. Otherwise, the photoluminescence has to originate from surface states, e.g..

Let us finally note that silicon as well as silicon oxide thin films can show multiple bands of different origins. One well-known defect in silica is the NBOH centre (**N**on**B**ridged **O**xygen **H**ole) which is due to a dangling oxygen bond [4,5]. This defect has been widely investigated and identified as the origin of the luminescence at 620 – 650 nm [6].

1.1.1 Quantum confinement of the exciton in silicon nanostructures

If a silicon crystal is reduced in its dimensions (~10 nm), the charge carriers are spatially confined. As a consequence, the energies of the carriers are quantified and increased. Figure 1.2 gives a schematic representation of the confinement effect in silicon. By reducing the diameter d of the silicon crystal, the energy gap increases.

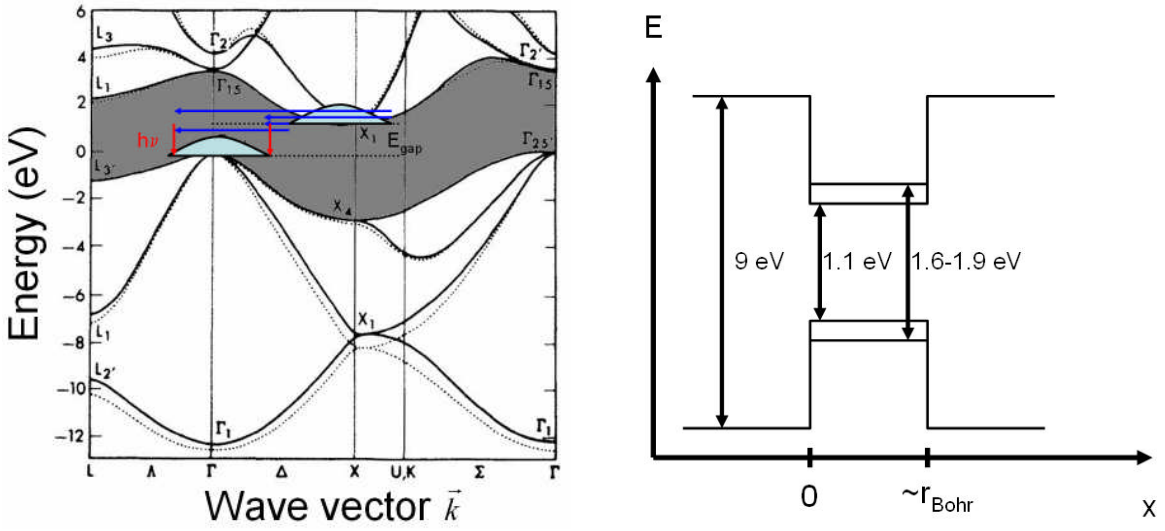

(a) *(b)*

Figure 1.2: Quantum confinement in nanocrystalline silicon (a) interpretation in terms of band-strucutre; (b) interpretation in terms of a quantum well.

In the framework of the effective mass approximation, the dependency of the forbidden energy gap from the diameter d of the structure can be written as quantum well of infinite depth. [7]:

$$E = E_g + \frac{2\hbar^2\pi^2}{d^2}\left(\frac{1}{m_e^*} + \frac{1}{m_h^*}\right) \qquad (1\text{-}2)$$

where E_g is the width of the forbidden bandgap of the solid material, d the characteristic size of the structure, m_e^* and m_h^* the effective masses of electron and hole.

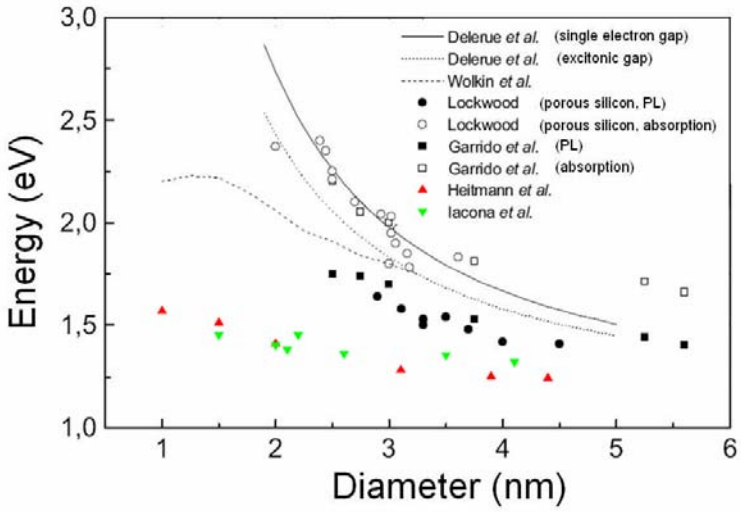

Figure 1.3: Confrontation of different experimental and theoretical work on the dependence of the emission energy on the diameter of the silicon nanocrystals (references are given in the legend).

The determination of the energy gap depends on the employed method and of several corrective factors as the spin-orbit coupling, the electrostatic interaction of the exciton (~1/d) or the exchange interaction (~$1/d^3$) [8]. However, the general evolution of the bandgap with the size of the silicon nanocrystal remains the same. Figure 1.3 shows the evolution of the energy as a function of the nanocrystal size for porous silicon as well as nanocrystalline silicon. Several experimental works are compared to theoretical calculations effectuated by Delerue *et al.* [7] and Wolkin *et al.* [9]. Empty symbols are for absorption measurements, full symbols are for photoluminescence measurements, respectively. Delerue *et al.* have shown by the method of linear combination of atomic orbitals (LCAO) that, in the case of spherical crystallites of silicon, the confinement energy evolutes as an inversely proportional function of the diameter $1/d^{1.39}$, whereas Heitmann *et al.* [10] obtain an inverse proportionality of the confinement energy only to $d^{0.6}$. This weaker variation of the confinement energy has been explained by a migration of the excitons from the smaller nanocrystals to the bigger ones. Iacona *et al.* [11] in constrast suggested that the exciton is trapped at a localized state in the gap and the radiative recombination takes place from this localized state of reduced energy.

1.1.2 Elaboration techniques for luminescent silicon nanostructures

Porous silicon

Porous silicon has been the first silicon-based system on which efficient room temperature photoluminescence has been observed. It is obtained by an electrochemical wet etching process on monocrystalline silicon employing fluoridic acid. To improve the etching process, an electric voltage is applied on the silicon substrate. The etching process leads to the formation of micropores of crystalline silicon. After the appropriate etching time, silicon filaments with a diameter of several nanometers are formed. Dangling bonds at the surface of the micropores are passivated by the hydrogen of the fluoridic acid [12]. During exposure to the air, the silicon filaments are progressively oxidized [13]. After this oxidation, the silicon filaments are sometimes considered as splitted into grains surrounded by silicon oxide [14].

Porous silicon has several very interesting properties for applications such as the high radiative recombination efficiency at room temperature and the fact that the emission wavelength can be shifted throughout the whole visible range. On the other hand, there are some important inconveniences: as a consequence of the large size distribution of the crystallites, the emission bandwidth is very large. In addition, the micropores are not very stable from mechanical and thermodynamical points of view. Finally, the wet etching technique is incompatible to common techniques in microelectronics. More convenient systems are essentially thin films of silicon oxide [15], silicon nitride [16] or multilayers of Si/SiO_2 [17], Si/CaF_2 [18] and SiO/SiO_2 [19]. In the following, we will discuss more in detail silicon nanostructures embedded in silicon oxide.

Silicon nanocrystals embedded in silicon oxide matrix

The fabrication of silicon nanostructures that are more stable than porous silicon can be achieved by embedding the silicon nanostructures into a thermodynamically stable matrix as silicon oxide, e.g. In the following we will detail different methods to fabricate stable silicon nanotructures.

Ion beam implantation: high energetic silicon ions with energies up to 200 keV are implanted into silicon oxide thin films [15, 20, 21]. After the implantation, the silicon ions are distributed in the matrix according to the beam energy and profile. To produce precipitation of the ions in nanoclusters, it is necessary to anneal them at high temperatures up to 1100°C. As a function of the irradiation dose, the concentration of silicon on the film can be precisely controlled and thus the size of the silicon nanoclusters. Even the vertical position of the silicon nanoparticles can be controlled by adjusting the acceleration voltage. Typically, this technique is used for very large scale integration (VLSI) microelectronics.

Segregation in a SiO_x thin film ($1<x<2$): the segregation of a sub-stoichiometric SiO_x layer can also be employed to generate silicon nanoparticles [11,22]. High temperature annealing at temperatures over 800°C leads to the decomposition of the SiO_x thin film into two thermodynamically stable components following the segregation equation

$$2SiO \rightarrow SiO_2 + Si \qquad (1\text{-}3)$$

By controlling the stoichiometry factor, one has the possibility to influence the size of the precipitations: the less excess silicon is in the film, the smaller are the crystallites. Such a kind of film can be produced by different techniques: evaporation [22], sputtering [23] or chemical vapour deposition [11].

Multilayers: in multilayered structures as Si/SiO_2 [17, 24, 25, 26] or SiO/SiO_2 [10], the size of the silicon nanoparticles can be controlled by the thickness of the Si or SiO layer, respectively. Both systems have to be annealed to obtain silicon nanocrystals. In the first system, the nanocrystals are created by the crystallization of the initially amorphous silicon layers on the system [17]. In the SiO/SiO_2 multilayers, segregation takes place as in the case of the SiO_x thin films. The aim of this deposition technique is that the intermediary SiO_2 layers avoid diffusion of silicon atoms between the silicon-rich layers. Thus, the growth is limited to the thickness of the silicon or SiO layers in the direction of the surface normal of the sample. As a consequence, the size distribution of the silicon nanocrystals is limited, too. Correspondingly, the bandwidth of the photoluminescence band is reduced with respect to the two above presented techniques [27]. At the same time the segregation temperature is increased with respect to SiO_x thin films.

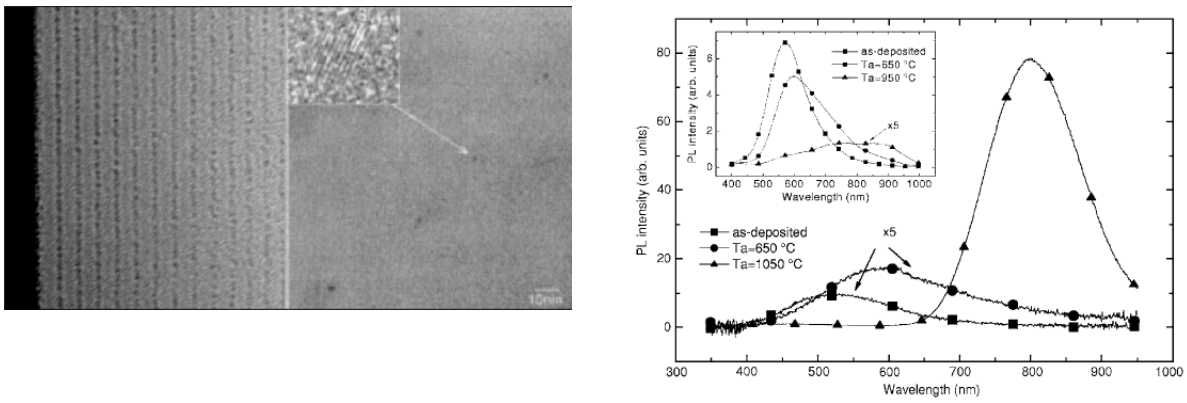

(a) *(b)*

Figure 1.4: silicon nanocrystals embedded in SiO_2 from SiO/SiO_2 multilayers (a) TEM images: nanocrystalline silicon of controlled size is observed; (b) photoluminescence spectra of size controlled silicon nanocrystals. Inset: photoluminescence spectra of an unstructured SiO thin film [27]

Single silicon nanocrystal: Marzin *et al.* have shown, in the case of III-V direct bandgap semiconductor, quantum dots that the ensemble photoluminescence is of Gaussian shape, whereas the photoluminescence of small mesas with a strongly reduced number of emitters shows discrete and very sharp emission lines compared to the ensemble photoluminescence bandwidth (see Figure 1.5) [28].

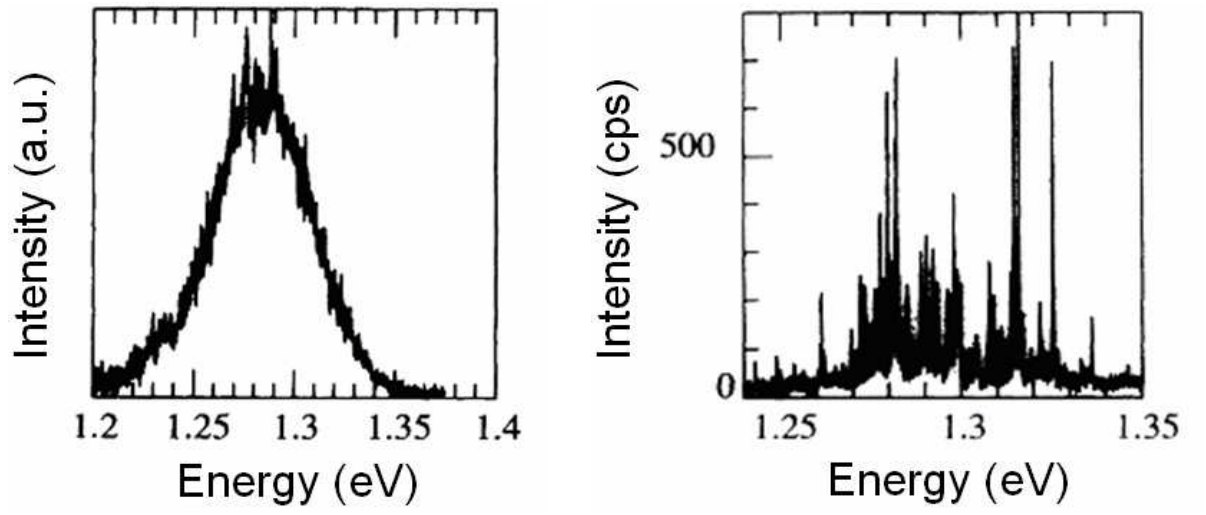

(a) *(b)*

Figure 1.5: photoluminescence of direct bandgap semiconductor quantum dots: (a) ensemble photoluminescence; (b) photoluminescence of few quantum dots [28]

In actual research, this mesa approach is commonly used to reduce the number of grains for single dot spectroscopy [29] or even more sophisticated applications in quantum optics.

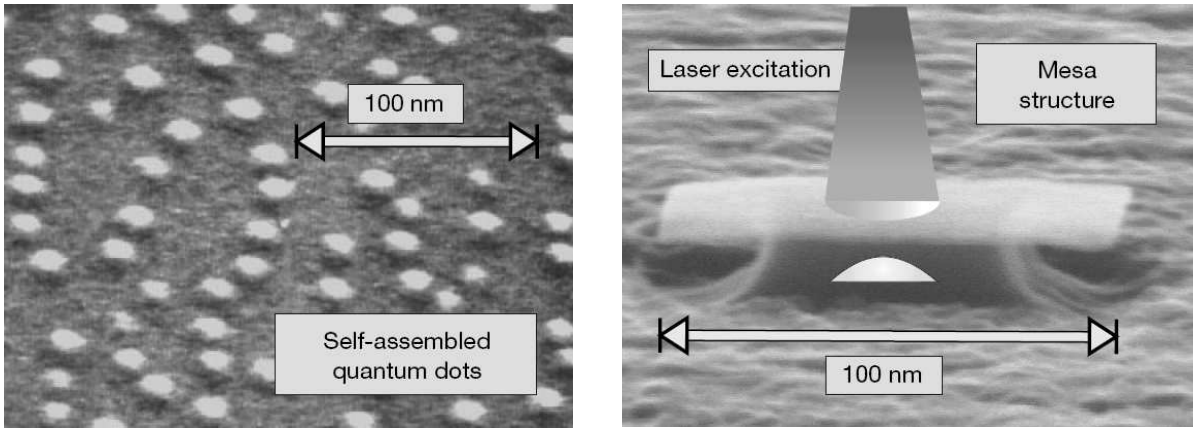

(a) *(b)*

Figure 1.6: example for a nanostructuring technique to reduce the number of excited quantum dots for single dot spectroscopy (a) ensemble of quantum dots of high density, unsuitable for single dots spectroscopy; (b) mesa structure, containing only a few quantum dots, suitable for single dot spectroscopy [29].

Despite the improvement of the bandwidth by introduction of the multilayer approach, the bandwidth of an ensemble of silicon nanocrystals does not allow any conclusion about the linewidth and thus about the recombination mechanism of a single silicon nanocrystal. A remaining size distribution [27] seems to blur this information.

In literature, there have been some attempts to do single dot spectroscopy on silicon nanocrystals. Valenta *et al.* [30] first developed a process to isolate single silicon nanostructures (see Figure 1.7 (a)). Silicon micropillars are produced employing electron beam lithography and reactive ion etching. To

further reduce the diameter of the pillars, they are thermally oxidized by high temperature annealing in oxygen atmosphere. Thereby, the diameter is reduced down to several tens of nanometers. When the diameter is reduced down to a size, at which confinement effects can take place, the oxide that has been formed around the remaining silicon core of the pillar is removed by wet etching with fluoridic acid. The uncovered silicon core is finally annealed in an oxygen atmosphere for a second time at even higher temperatures than before. This step leads to the formation of an almost spherical silicon nanostructure at the top of the nanopillar. The post is almost completely oxidized.

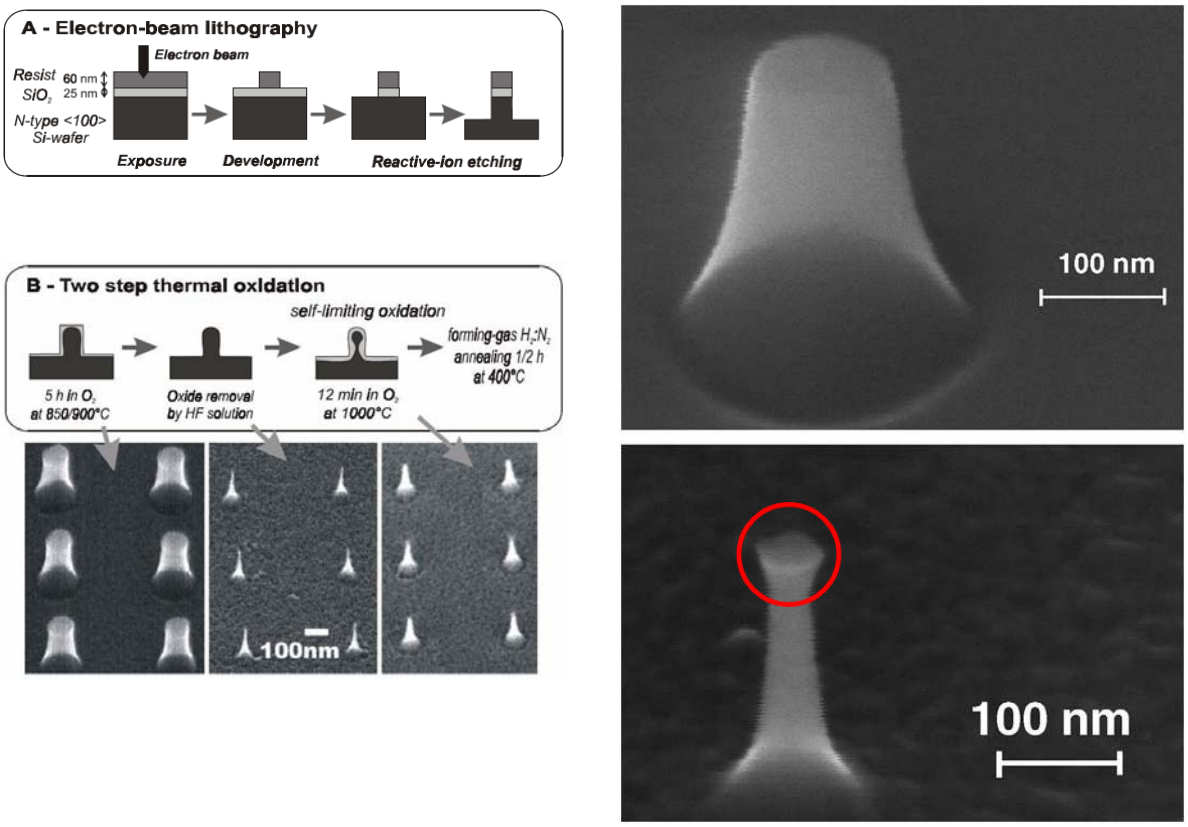

(a) *(b)*

Figure 1.7: the micropillar approach of Valenta et al.: (a) fabrication steps of the process with corresponding SEM images [30]*; (b) zoomed SEM images of single micropillars at the beginning (top) and the end (bottom) of the oxidation process* [31]*. Note the silicon nanostructure at the top of the pillar (red circle).*

They investigated the micropillars with a microphotoluminescence setup. The micropillars are excited with the 325 nm line of a He-Cd laser under glancing incidence. The photoluminescence as well as white light reflection from the sample is detected with a microscope along the surface normal. The signal is either coupled to an imaging spectrometer in the case of photoluminescence spectroscopy or to an optical camera in the case of the white light reflexion imaging.

The imaged photoluminescence at energies ranging from 1.5 to 2.0 eV is in good spatial agreement with the position of the pillars in white light imaging. The measured emission energies correspond to transitions in silicon nanocrystals with diameters ranging from 3 to 6 nm [7]. A further indication that the emission is due to single silicon nanocrystals is the detection of fluorescence intermittency

(blinking) where the intensity varies between two distinct levels. This phenomenon has been found for almost all systems containing individual quantum dots or single molecules. So, they conclude to have single silicon nanocrystals at the top of each nanopillar.

In general, as the photoluminescence efficiency is very low, the accumulation times for standard photoluminescence spectra with this photoluminescence setup are of 30 min.

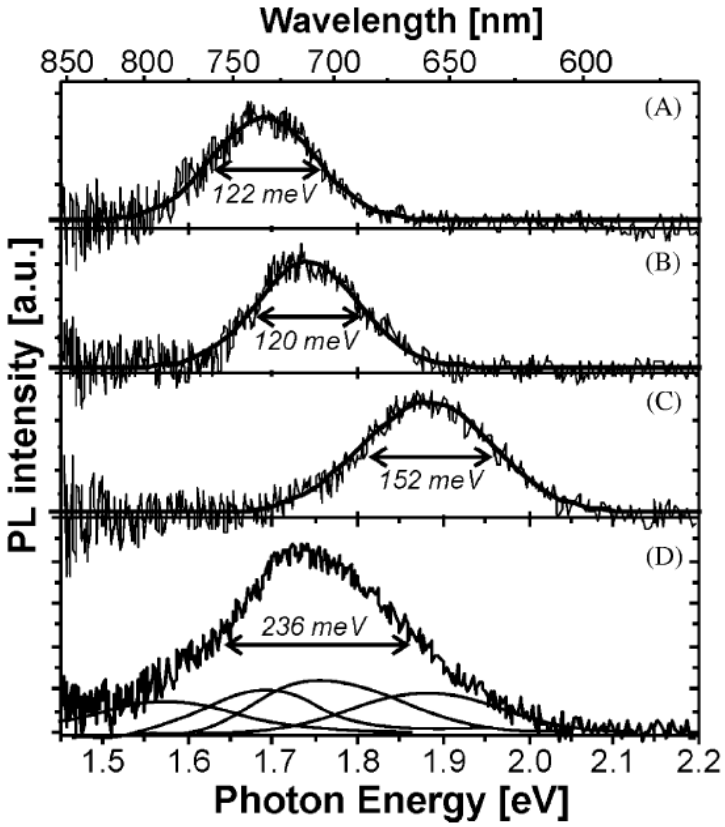

Figure 1.8: Room temperature photoluminescence spectra of three different single silicon nanocrystals (A-C) compared to the sum of nine spectra of single silicon nanocrystals (D) [32]

They observed room temperature photoluminescence of single silicon nanocrystals on the top of the micropillars with a linewidth of about 120 – 150 meV at emission energies corresponding to the transitions in silicon nanocrystals, i.e. between 650 and 900 nm [32]. If the sample is cooled down in a helium cryostat, the linewidth decreases drastically down over 14 meV at 80 K to 2.0 meV at 35 K [33].

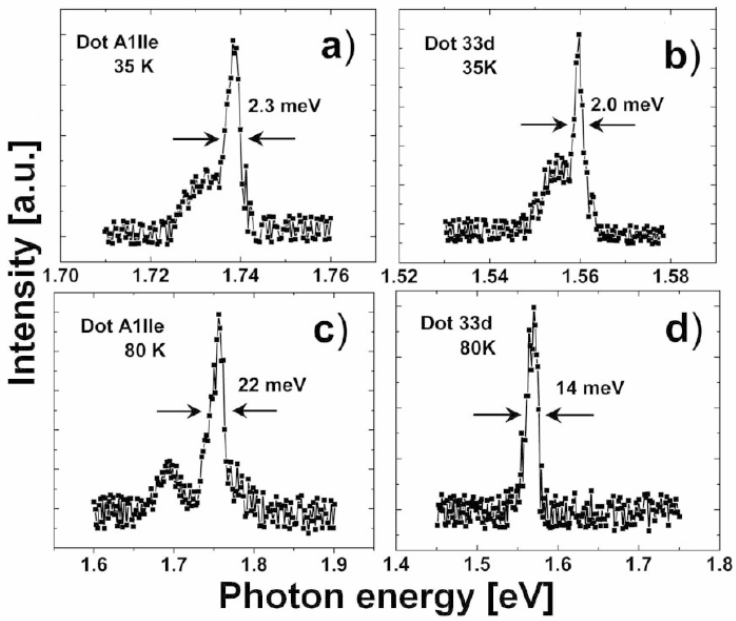

Figure 1.9: Low temperature photoluminescence spectra of individual silicon nanocrystals (a) and (b): 35 K; (c) and (d): 80K. The left column ((a) and (c)) shows the spectra of a silicon nanocrystal exhibiting phonon assisted photoluminescence. The right column ((b) and (d)) shows a silicon nanocrystal with zero-phonon photoluminescence [33].

Thus, they conclude that the emission linewidth of silicon nanocrystals can be as sharp as in the case of direct bandgap quantum dots. Nonetheless, they state that the emission properties of silicon nanocrystals are very different from nanocrystal to nanocrystal. Notably they discern three categories of silicon nanocrystals: one with a secondary peak which is clearly separated by 60 meV from the main peak at low temperature. The linewidth of those silicon nanocrystals is of about 150 meV at room temperature. Sychugov *et al.* [33] compare the shift of this secondary peak to a transverse optical (TO) phonon in bulk silicon, whose energy is of either 56 meV at the X point or 64 meV at the Γ point as the energy shift is independent of the emission energy and thus the dot size. They point out that only a third of their silicon nanocrystals show this TO feature at low temperature and that this fraction slowly increases with temperature. They suggest that strong localization of the carriers in the silicon nanocrystals can have a strong influence on the probability of no-phonon recombination.

A second class of silicon nanocrystals shows no remarkable phonon related peak. It seems that, in these silicon nanocrystals, the carriers are strongly localized. This can have a positive influence of the no-phonon recombination probability. Another possibility are local differences in geometry that change the probability of the TO phonon-assisted recombination either positively or negatively. The no or zero phonon transition has already been found by Kovalev *et al.* [6] and it has been interpreted as a breakdown of the k conservation rule due to Heisenberg's uncertainty relation for very small sizes (thus big spatial confinement). If this breakdown of the k conservation would be at the origin of the probability of the TO phonon assisted transition, the energy of the phonon should be a function of the size of the silicon nanocrystal. This has not been observed by Sychugov *et al.* [33]. They found that the shift of the phonon-related emission with respect to the main transition was a nearly individual parameter of each silicon nanocrystal. Thus, they concluded that the photoluminescence of each silicon nanocrystal is strongly influenced by its local environment.

A small secondary peak shifted by 6 meV to lower energies with respect to the main recombination feature is reported for both TO-assisted transition and zero-phonon transition. It is attributed to torsional or spherical acoustic phonon modes [34].

Valenta *et al.* [35] also report on electroluminescence measurements on single silicon nanocrystals. Thereby they state that the linewidth of the electroluminescence spectra of single silicon nanocrystals are comparable to the photoluminescence linewidth.

The inconvenient of the approach of etching nanopillars is that this process does not allow for complete control of the form of the nanocrystals. In addition, a combined study by transmission electron microscopy and photoluminescence on the same nanopillar revealed that in the middle of the nanopillar there is a crystalline rod remaining. Thus, it cannot be excluded that there is a coupling between the discrete states of the nanocrystal on the top of the pillar with the continuum of states in the substrate via this remaining silicon rod.

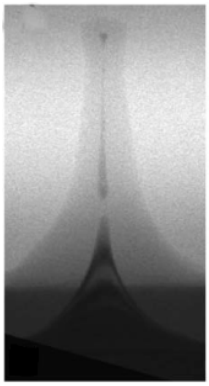

Figure 1.10: Nanopillar containing a single silicon nanocrystal on the top. Note the remaining rod in the middle part of the pillar.

To circumvent this general problem, there have been some attempts employing opaque metal masks in the case of embedded direct bandgap quantum dots. Yasin *et al.* [36] applied the technique to investigate GaInN quantum dots (see Figure 1.11). The photoluminescence is detected only through predefined nanometric apertures in the mask.

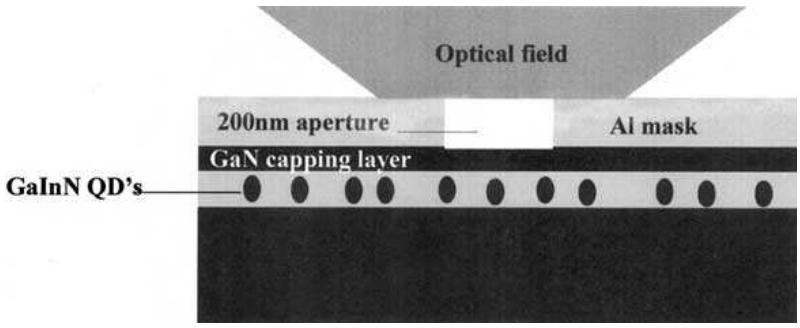

Figure 1.11: Opaque metal layer as mask. The photoluminescence of the quantum dots is detected only through nanometric apertures [36]

This masking technique has also been employed in the domain of silicon nanocrystals by Dumas *et al.* [37, 38]. They implanted silicon ions through the mask thus defining nanometric silicon-rich zones which have been analyzed by means of SEM (scanning electron microscopy) and imaging photoluminescence. The bright zones in the photoluminescence images correspond well to the apertures also detected by SEM (see Figure 1.12).

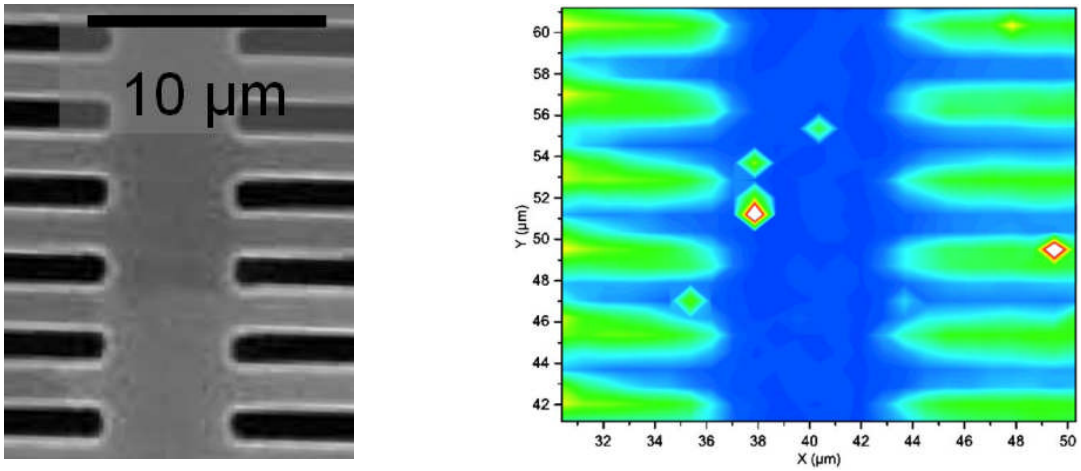

(a) *(b)*

Figure 1.12: SEM and photoluminescence images of silicon rich films under an opaque metal mask. Note the coincidence of dark apertures in SEM (absence of metal) on the left picture and the bright zones on the photoluminescence image on the right [37]*. The white spots may be due to reflected laser light scattered on impurities on the surface of the sample.*

In our case, we will use the same masking process on our deposited and annealed samples. The results of this analysis will be shown in chapter 3.

1.2 Microcavities

The aim of this work is partially to get information about the properties of single silicon nanocrystals. In the previous section, we resumed the results in literature about the spatial isolation of quantum dots. It is evident that most of the techniques that are employed are technically very demanding or have several inconveniences as the application of wet etching which is incompatible with very large scale integrated processes.

In the following, we will give a short summary of the optical properties of microcavities. We will consider the electric field distribution in a planar cavity which is the simplest geometry. The properties of the cavities that will be shown in a later section can in principle be deduced from the properties of the planar cavity by taking into account the different geometry (boundary conditions).

1.2.1 Principle

Light emission is the result of a coupling between an emitter (semiconductor, isolated atom in a Paul-trap or most generally an oscillating dipole) and the surrounding electromagnetic field [39]. In vacuum, i.e. in free space, the emitter can couple to an infinity of electromagnetic modes and its emission properties only depend on the intrinsic properties of the emitter. By modifying the spatial or spectral distribution of the electromagnetic field, we can also change the emission properties of the emitter. The following section will give an intuitive description of these modifications.

1.2.2 Free space spontaneous emission

Before considering the emission of a photon by an emitter into the cavity, we should rapidly remember the description of spontaneous emission in free space. The spontaneous transition rate results from Fermi's golden rule:

$$W_{free} = \frac{2\pi}{\hbar^2}\left|M_{12}\right|^2 g(\omega), \tag{1-4}$$

where M_{12} is the transition matrix element between the excited state and the ground state and $g(\omega)$ the density of photonic states. In free space, the photon density of states is written as

$$g(\omega) = \frac{\omega^2 V_0}{\pi^2 c^3}. \tag{1-5}$$

The transition matrix element corresponds to the scalar product of the vacuum electric field and the dipole moment, thus an electric dipole interaction:

$$M_{12} = \left\langle \vec{p} \cdot \vec{E} \right\rangle. \tag{1-6}$$

As the surrounding of the emitter is considered free of any source or sink, $\vec{E}$ denotes the vacuum electric field. By averaging over all possible directions, we finally obtain for the square of the transition matrix element

$$M_{12}^2 = \frac{1}{3}\mu_{12}^2 \vec{E}_{vac.}^2 = \frac{\mu_{12}^2 \hbar\omega}{6\varepsilon_0 V_0} \tag{1-7}$$

If we now insert (1-2) and (1-4) into (1-1), we obtain the expression for the radiative transition rate, which is the inverse of the radiative lifetime τ_R:

$$W_{free} \equiv \frac{1}{\tau_R} = \frac{\mu_{12}^2 \omega^3}{3\pi\varepsilon_0 \hbar c^3} \tag{1-8}$$

1.2.3 Modification of the electromagnetic field by a cavity

Such a planar microcavity – called Fabry-Perot interferometer type microcavities – is outlined in Figure 1.13. Two mirrors M_1 and M_2 with reflectivities R_1 and R_2, respectively, are confining a space in between of length $L_{cav.}$ eventually filled with a medium of refractive index n. The mirrors are aligned parallel to each other so that the light inside the cavity can only propagate along the surface normal of the mirrors.

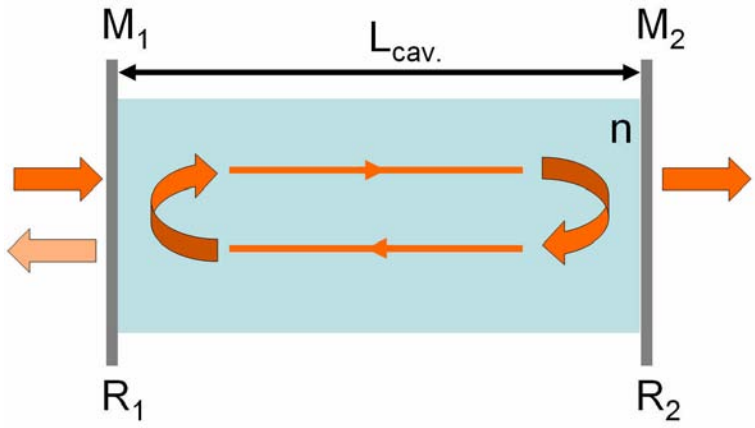

Figure 1.13: A planar cavity of length $L_{cav.}$ filled with a medium of refractive index n. The medium is laterally confined by two mirrors M_1 and M_2 of reflectivity R_1 and R_2, respectively.

Ideal loss-less planar cavity: In order to get a good idea of the physical process, let us consider the case of an ideal planar cavity. It is constituted of two planar non-absorbing mirrors of reflectance 1. These mirrors are oriented perpendicularly to the propagation of the light wave in a distance $L_{cav.}$ from each other. Compared to the emission wavelength, their extension in x and y direction is considered as infinite. The light is reflected on the surface of each mirror by interaction of the electromagnetic wave and surface plasmons of the mirror. Summing up incident and reflected waves, we obtain a stationary wave inside the cavity with oscillation nodes at the position of the mirrors. As the dimensions of the cavity are infinite in the x – y – plane, this resonance condition imposes a quantification of the wave-vector only in the z – direction: $k_z^m = m \cdot \pi/L$, m being an integer indicating the order of the resonance. Thus, we obtain an electric field E, which is proportional to sin $(k_z^m z)$.

If we place an emitter inside a cavity, where the electric field is modified with respect to free space, its coupling to the field and thus its emission depends on its position in the cavity (mainly z – direction). Consequently, the coupling between emitter and field depends on the intensity of the stationary wave $E^2 \sim \sin^2(k_z^m z)$ at the position of the emitter in the cavity. In a node, $E^2=0$, in an anti-node E^2 is maximal.

In the low loss regime, the transmission of the considered cavity can be described in the same way as the transmission of a Fabry-Perot interferometer:

$$T = \frac{1}{1 + (4F^2/\pi^2)\sin^2(\phi/2)}, \tag{1-9}$$

where $\phi = \frac{4\pi n L_{cav.}}{\lambda}$ is the phase shift of the electromagnetic wave in one round trip inside the cavity and

$$F = \frac{\pi \sqrt[4]{R_1 R_2}}{1 - \sqrt{R_1 R_2}} \tag{1-10}$$

is the so called finesse of the cavity. As we can easily see from equation (1-6), the transmission is maximum, if the phase shift $\phi = 2\pi$m, m being an integer. This is the case for wavelengths that fulfil the so called Bragg-condition

$$L_{cav.} = \frac{m\lambda}{2n}. \tag{1-11}$$

If we use the equation (1-6) for a transmittance of 50%, we get

$$\phi = 2\pi m \pm \frac{\pi}{F} \tag{1-12}$$

which allows for deducing almost directly the linewidth (or FWHM – full width at half maximum) of the transmittance peaks:

$$\Delta\phi_{FWHM} = \frac{2\pi}{F} \tag{1-13}$$

or written in terms of the finesse:

$$F = \frac{2\pi}{\Delta\phi_{FWHM}} \tag{1-14}$$

This implies that the finesse of a cavity gives an indication of the spectral resolution of the resonator.

The Maxwell equations allow us to determine distributions of electromagnetic fields in a given volume. Introducing a cavity into the considered volume will essentially modify the field distribution. The limits of the cavity impose boundary conditions that serve to solve the Maxwell equations. In an ideal loss-less cavity, the solutions of the Maxwell equations are stationary waves – mathematically eigensolutions of the equations – called modes characterized by a specific angular frequency or eigenvalue. In this ideal case, the barriers of the cavity completely separate the enclosed volume from

the exterior and especially from the continuum of electromagnetic modes of vacuum. An emitter placed inside the cavity can thus only couple to the modes permitted by the geometry of the cavity and its emission will be subject to their spatial and spectral structures.

In the case of the planar microcavity, the boundary conditions imposed by the two mirrors lead to the angular frequencies

$$\omega_m = m\frac{\pi c}{nL_{cav.}}. \tag{1-15}$$

Thus the mode frequencies can be influenced by changing the cavity length $L_{cav.}$ or the refractive index n of the medium filling the cavity. Given that the phase and the angular frequency are interdependent vie the wavelength, we can use equation (1-11) to express the linewidth of the resonant modes by the finesse, thus the structural properties of the cavity:

$$\frac{\Delta\omega}{\omega_m - \omega_{m-1}} = \frac{\Delta\phi_{FWHM}}{2\pi} = \frac{1}{F} \tag{1-16}$$

And finally, we obtain for the linewidth of the resonant modes as a function of the finesse:

$$\Delta\omega = \frac{\pi c}{nFL_{cav.}} \tag{1-17}$$

Planar cavity with losses: the aim of the ideal cavity is to have a simple solution to the Maxwell equations solving the problem. In reality, there are always loss phenomena that dissipate the electromagnetic energy contained in the cavity: losses by scattering at rugosities of the surface of the mirrors, losses by absorption in the case of metallic mirrors or losses by radiation in the case of mirrors with a reflectance inferior to unity. We will concentrate on the latter category as those losses are usually used to analyze the cavity.

As this system is not isolated from the exterior any more, the theoretical lifetime of a photon in the cavity is not infinite any more. We notice a spectral broadening of the modes which rigorously aren't any more stationary waves but "quasi-modes" of a spectral width $\Delta\omega_{cav.}$ depending on the radiative lifetime τ_R. In order to determine the lifetime of a photon in the cavity, we consider a number N of photons inside the cavity. After each round in the cavity, the number of present photons is reduced due to the fact that the reflectance is not unity any more. At each reflexion, the number of present photons has to be multiplied by the reflectance. Per half roundtrip, $\Delta N=(1-R)N$ photons are lost passing through one of the mirrors. Thus, we can write for the temporal evolution of the photon population in the cavity:

$$\frac{dN}{dt} = -\frac{\Delta N}{\frac{nL_{cav.}}{c}} = \frac{c(1-R)}{nL_{cav.}} N \tag{1-18}$$

with the ansatz $N = N_0 e^{-\frac{t}{\tau_{cav.}}}$, we obtain the average lifetime of a photon in the cavity, which is

$$\tau_{cav.} = \frac{nL_{cav.}}{c(1-R)} \tag{1-19}$$

In analogy to the free space decay rate of an emitter W_{free}, it can be useful to define the decay rate of the state "photon in cavity". It is defined as the inverse of the photon lifetime:

$$\kappa = \frac{1}{\tau_{cav.}} \tag{1-20}$$

As it was introduced above, the radiative lifetime can be correlated to the spectral linewidth of the cavity. Employing equations (1-7), (1-14) and (1-16), we obtain:

$$\Delta\omega = (\tau_{cav.})^{-1} \equiv \kappa \tag{1-21}$$

Thus, we have shown that the photon lifetime in the cavity or more correctly the photon loss rate influences the linewidth of the resonant modes in the same way as the linewidth of an atomic transition depends on its spontaneous emission rate.

The upper analysis revealed that a cavity is mainly characterized by two parameters: ω_m and F. The finesse at the same time has a strong influence on both the resonant mode, as $\Delta\omega$ depends on F and the cavity loss rate. To be able to compare different types of cavity geometries, it is thus convenient to introduce a quantity that allows for comparing different cavities: the quality factor Q:

$$Q = \frac{\omega_0}{\Delta\omega_0} = \frac{\lambda_0}{\Delta\lambda_0} \tag{1-22}$$

where ω_0 and λ_0 are the angular frequency and the wavelength of the resonance. The quality factor $Q_{cav.}$ of the cavity modes gives information about the spectral selectivity and the energetic capacity of a cavity. It is a figure of merit that allows us to quantify the potential of the cavities for the interaction with an emitter or for filtering a wavelength.

As only a proportion $Q_{cav.}$ of the energy is retained in the cavity, the electromagnetic modes of the cavity can couple to the continuum of modes of free space. An emitter that is supposed to be able to be placed inside the cavity can thus emit into the cavity modes and couple to the external field. The influence of the cavity remains visible as the distribution of the emitted field is changed spatially as well as spectrally.

Influence of the absorption: Up to now, we considered the case of an ideal, non-absorbing cavity. In real thin films, there is rarely no absorption. So it is important to consider the influence of the absorption. To be able to distinguish the pure contribution of the cavity and the contribution due to absorption, we can write:

$$\frac{1}{Q} = \frac{1}{Q_0} + \frac{1}{Q_{abs}} \tag{1-23}$$

Here, $Q_{abs.}$ describes a quality factor that is attributed to the absorption. It depends on the refractive index n as well as on the extinction coefficient k.

Influence of the emission spectrum: Up to now, we considered a monochromatic emitter which is coupled to a cavity. This was good to show the first principles. In thin films, an emitter is rarely monochromatic. So it is important to consider the influence of the spectral widths of both emitter ($\Delta\theta_{em.}$) and cavity ($\Delta\theta_{cav.}$). To be able to easily compare the properties of cavity and emitter, it is convenient to define a quality factor for the emitter, too:

$$Q_{em.} = \frac{\omega_{em.}}{\Delta\omega_{em.}} = \frac{\lambda_{em.}}{\Delta\lambda_{em.}} \tag{1-24}$$

It describes the spectral properties of the emitter. In practical, the emission band-width of the emitter is given. Thus, one has to adapt the cavity in a way that the quality factor of the cavity is superior to the quality factor of the emitter. Otherwise, the emission spectrum is almost unchanged with respect to the emitter in free space.

Redistribution of the emission: The coupling between the emitter and the cavity modes induces a modification of the geometric emission characteristics as well as the spectral ones. Those effects are widely used, from microphotonics – as in our case – to lasers.

Spatial redistribution: For a plane electromagnetic wave, we have the dispersion relation:

$$E(\vec{k}) = \frac{\hbar c}{n_{cav}}\left|\vec{k}\right| \qquad = \frac{\hbar c}{n_{cav}}\left[k_x^2 + k_y{}^2 + k_z{}^2\right]^{1/2} \tag{1-25}$$

$$= \frac{\hbar c}{n_{cav}}\left[\left(\frac{2\pi}{\lambda_x}\right)^2 + \left(\frac{2\pi}{\lambda_y}\right)^2 + \left(\frac{2\pi}{\lambda_z}\right)^2\right]^{1/2} \tag{1-26}$$

$$= \frac{\hbar c}{n_{cav}}\left[\left(\frac{2\pi}{\lambda_z}\right)^2 + k_{xy}{}^2\right]^{1/2} \tag{1-27}$$

Let us consider a punctual isotropic emitter placed at the anti-node of an electromagnetic mode inside the cavity. By coupling to the cavity modes, the emitter is allowed only to produce electromagnetic waves whose structure is identical to the one of the modes, i.e. in particular, the authorized wave vector is not arbitrary, but imposed by the length of the cavity $L_{cav.}$:

$$E(k) = \frac{\hbar c}{n_{cav}}\left[\left(\frac{2\pi}{L_{cav}}\right)^2 + k_{xy}^2\right]^{1/2}. \tag{1-28}$$

We chose the confined direction to be parallel to the z-axis. Thus, we can write the k-vectors as projections in the sample plane k_{xy} and along the surface normal k_z using the angle θ between the z-axis:

$$k_{xy} = k\sin\theta = \frac{E(k)}{\hbar c}\sin\theta \quad \text{and} \quad k_z = k\cos\theta \tag{1-29}$$

Thus, we can write for the dispersion relation:

$$E(k_{xy} = 0) = E(k_z) = E_0 = \frac{hc}{n_{cav}L_{cav}} = E(k)\cos\theta\,. \tag{1-30}$$

So

$$E(k) = E_0\left[1 + \frac{k_{xy}^2\hbar^2c^2}{n_{cav}^2E_0^2}\right]^{1/2} \tag{1-31}$$

Using the projections of the k-components, we deduce finally:

$$E(k) = \frac{E(k_{xy} = 0)}{\left[1 - \frac{\sin^2\theta}{n_{cav}^2}\right]^{1/2}} \tag{1-32}$$

The energy is inversely proportional to the wavelength λ, so that we can write:

$$\lambda(k) = \lambda(k_{xy} = 0)\left[1 - \frac{\sin^2\theta}{n_{cav}^2}\right]^{1/2} \tag{1-33}$$

If we consider small angles, we can employ Taylor expansion to simplify the expressions:

$$\lambda(k) = \lambda(k_{xy} = 0)\left[1 - \frac{\sin^2\theta}{n_{cav}^2}\right]^{1/2} \approx \lambda(k_{xy} = 0)\left[1 - \frac{1}{2}\frac{\sin^2\theta}{n_{cav}^2}\right] \tag{1-34}$$

$$\approx \lambda(k_{xy} = 0)\left[1 - \frac{1}{2}\frac{\theta^2}{n_{cav}^2}\right] \approx \lambda(k_{xy} = 0)\left[1 - \cos\left(\frac{\theta}{n_{cav}}\right)\right]. \tag{1-35}$$

A monochromatic, isotropic emitter placed at an antinode of the electric field induces an external emission as a concentric light cone instead of an isotropic emission as if it was in free space. Thus, the emission is spatially modified by the influence of the cavity modes.

This redirectioning effect is in particular used to improve the light extraction from electroluminescent diodes. Typically such diodes are fabricated of a material of high refractive index and thus, the extracted light intensity is very weak (typically of $1/4n_2$, what means 2 or 3 %) [40]. This modest extraction rate is due to the fact that modes emitted to an angle exceeding the critical emission angle of θ_c = arcsin (1/n) undergo total reflection. They remain inside the layer and are thus labelled guided modes.

In order to improve the extraction efficiency, it is necessary to modify the mode structure in a way that the extracted light is concentrated into a light cone. The easiest way to realize this is to adapt the thickness of the layer, thus creating a cavity formed by the interfaces between the film and the environment, in general air with refractive index n~1. In the case of a relatively thick layer with a thickness equal to a multiple of the wavelength l, it forms a multimode cavity, containing an elevated number of modes. If the number is too elevated, the spectral distribution of those modes is nearly isotropic and the directivity of the emission is not much varied compared to an isotropic emitter. In contrast, if we reduce the thickness of the film to the order of magnitude of the emission wavelength, only a single mode can persist in the film and the film works as a cavity, improving the out-coupling of the light to the exterior. The efficiency of those improved structures is increased by a factor ten compared to the films with unadjusted thickness.

1.2.4 Modification of the spontaneous emission rate

Up to now, we considered the system emitter – cavity only under a stationary point of view. In the following, we will describe the influence of the coupling on the spontaneous emission rate. This coupling has been investigated for the first time by Purcell in 1946 [41].

Weak coupling and Purcell effect: if the damping phenomena occur on a faster timescale than the radiative lifetime of the emitter, the coupling regime is denominated weak coupling. Let us consider again the case of a cavity that allows only one mode within the line-width $\Delta\omega_{em.}$of the emitter. In addition, the line-width of the emitter shall be small compared to the line-width of the cavity ($\Delta\omega_{em.} << \Delta\omega_{cav.}$). In this case, the interaction can be described within the framework of Fermi's golden rule,

as the emitter can interact with a continuum of modes of a spectral density ρ(ω) [42]. This modal density of a lossy cavity corresponds to the modal density of an ideal lossless cavity multiplied by a lorentzian influence of width $\Delta\omega_{cav.}$, which is due to the finite photon lifetime in the lossy cavity. Employing the normalization relation for a single resonant mode $\int_0^\infty g(\omega)d\omega = 1$, we set the modal density:

$$g(\omega) = \frac{2}{\pi\Delta\omega_{cav.}} \frac{\Delta\omega_{cav.}^2}{4(\omega - \omega_{cav.})2 + \Delta\omega_{cav.}^2}. \tag{1-36}$$

If we want to consider an emitter, emitting at the frequency ω_0, we obtain the upper equation at the frequency ω_0:

$$g(\omega_0) = \frac{2}{\pi\Delta\omega_{cav.}} \frac{\Delta\omega_{cav.}^2}{4(\omega_0 - \omega_{cav.})2 + \Delta\omega_{cav.}^2} \tag{1-37}$$

If cavity and emitter are in perfect resonance, i.e. $\omega_0 = \omega_{cav.}$, the equation simplifies to

$$g(\omega) = \frac{2}{\pi\Delta\omega_{cav.}} = \frac{2Q}{\pi\omega_0} \tag{1-38}$$

In analogy to the dipole interaction with the vacuum field of the free emitter, we can write for the transition matrix element

$$M_{12}^2 = \xi^2 \mu_{12}^2 \vec{E}_{vac.}^2 = \xi^2 \frac{\mu_{12}^2 \hbar\omega}{2\varepsilon_0 V_0} \tag{1-39}$$

where ξ is a factor describing the orientation of the dipole:

$$\xi = \frac{\left|\vec{p}\cdot\vec{E}\right|}{\left|\vec{p}\right|\left|\vec{E}\right|}. \tag{1-40}$$

With the expression for the photon density of states at the transition frequency of the emitter and the transition matrix element, we can deduce the transition rate from Fermi's golden rule:

$$W_{cav.} = \frac{2Q\mu_{12}^2}{\hbar\varepsilon_0 V_0}\xi^2 \frac{\Delta\omega_{cav.}^2}{4(\omega_0 - \omega_{cav.})2 + \Delta\omega_{cav.}^2}. \tag{1-41}$$

As we analyse two emitters, one in free space and the other coupled to a cavity, it is thus logical to introduce a quantity that allows us to compare the recombination properties of the two systems. This quantity is called the Purcell factor F_P and defined as:

$$F_P = \frac{W_{cav.}}{W_{free}} \equiv \frac{\tau_R^{free}}{\tau_R^{cav.}}. \tag{1-42}$$

With the upper equations for the recombination rates, we finally obtain

$$F_P = \frac{3Q\left(\frac{\lambda}{n}\right)^3}{4\pi^2 V_0}\xi^2 \frac{\Delta\omega_{cav.}^2}{4(\omega_0 - \omega_{cav.})2 + \Delta\omega_{cav.}^2} \tag{1-43}$$

If the resonance of emitter and cavity is exactly at the same frequency and if the dipoles of the field and the emitter are oriented in parallel, equation (1-29) is simplified to:

$$F_P = \frac{3Q\left(\frac{\lambda}{n}\right)^3}{4\pi^2 V_0} \tag{1-44}$$

This parameter will be very important in the chapter concerning microcavities because it allows us to quantify the quality of the interaction between our emitters and the microcavities. In general, if F_P is greater than unity, this indicates an enhancement of the recombination rate of the emitter by the cavity. If the Purcell factor is less than unity, this is an indication of an inhibition of the transition. As can be seen from the last equation, F_P depends mainly on two quantities that can be influenced during the fabrication of the cavity: the quality factor Q and the modal volume V_0. Thus, in order to have efficient enhancement of the transitions, high quality factors along with small modal volumes are needed. The following section will give an overview of the different approaches to maximize the Purcell factor.

1.2.5 Cavity geometries

Planar cavity: This is the simplest resonator geometry. As we discussed above, two planar mirrors impose the boundary conditions. In contrast to the introduction, the mirrors in general are not made of metal but of dielectric pairs (see Figure 1.14 (a), image taken from [43]). The sequence of dielectric

pairs imposes further boundary conditions and thus a selected wavelength range is completely reflected by the system. Only the resonance wavelength of this Fabry-Perot interferometer-like system can pass through the cavity.

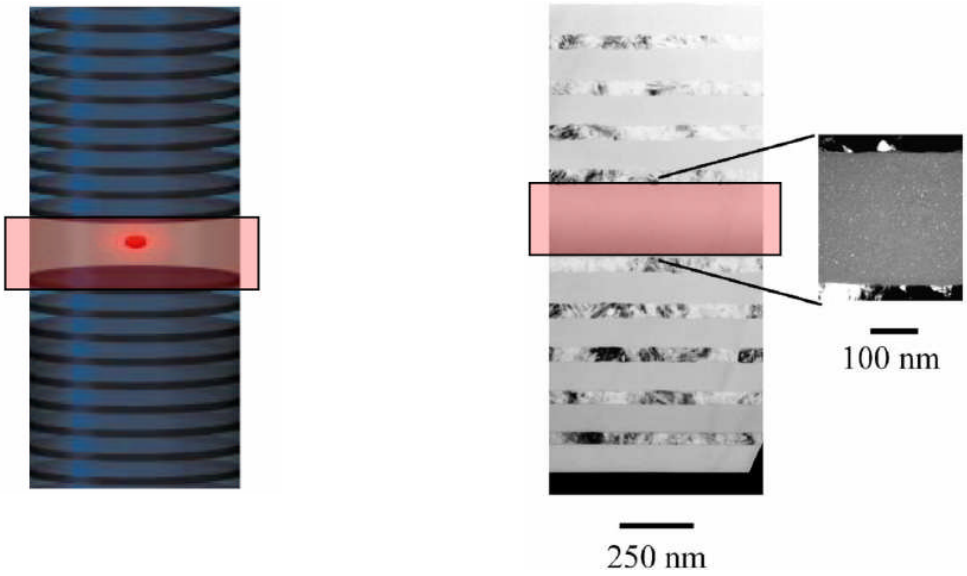

(a) *(b)*

Figure 1.14: (a) Sketch of a planar microcavity: there is only unidirectional light confinement. The optically active layer is marked by the red box. (b) Example for a planar microcavity coupled to silicon nanocrystals. The nanocrystals are situated in the layer marked by the red box [44].

The first results have been reported by Purcell, who investigated resonators in the wavelength range of microwaves [41]. As deposition techniques and optical characterization tools have advanced, the principle of the resonator has been transferred to the micro- and nanotechnology. Figure 1.14 (b) shows a transmission electron microscope image of a Si/SiO_2 dielectric-pairs-mirror-based microcavity containing silicon nanocrystals. Iacona *et al.* report a strong reduction of the photoluminescence linewidth from 140-220 nm for the reference sample without resonator to 14 nm for a cavity made of mirrors of three dielectric pairs. For a second set of samples containing five dielectric pairs per mirror, they even report a linewidth of 1.5 nm. The reported quality factors are of 80 and 500, respectively. Amans *et al.* [45] reported in 2004 on the spatial redistribution of the radial modes of silicon nanocrystals. The formerly isotropic emission of silicon nanocrystals in absence of a resonator is changed into a strong dependence of the emitted wavelength from the angle with the surface normal.

Micropillar cavity: the next logical step, if the thickness of the mirrors of planar microcavities is limited due to the fabrication process, would be to reduce the modal volume to further increase the Purcell factor. This can be technically realized by fabrication of micropillars, employing reactive ion etching, e.g. [46]. Thus, we pass from a planar geometry to a cylindrical one. Figure 1.15 (a) gives a schematical representation of a so called micropillar. One can clearly distinguish the several dielectric layers in the mirrors as well as the active layer. Figure 1.15 (b) shows a SEM image of a micropillar.

Figure 1.15 (c) shows a simulated field intensity distribution inside a micropillar cavity. Values for the quality factor reach up to 2000 [43]. In addition, the modal volume is reduced to $5(\lambda/n)^3$.

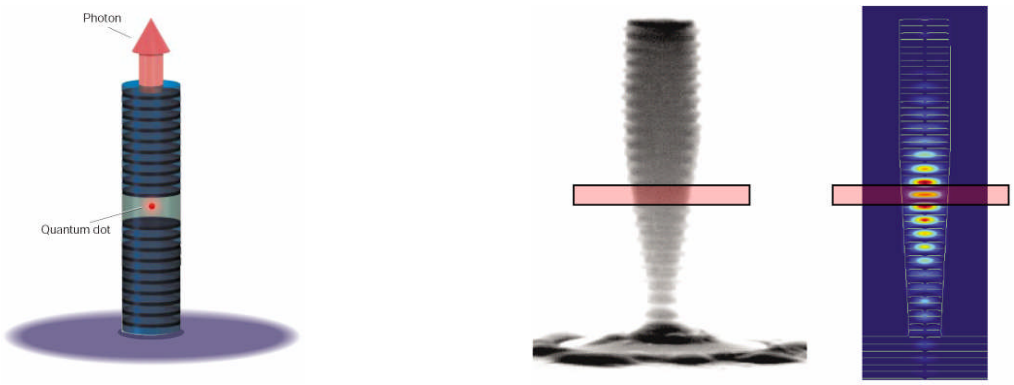

(a) *(b)* *(c)*

Figure 1.15: Micropillar microcavity: (a) sketch [43]*; (b) SEM image; (c) distribution of the amplitude of the electric field in the micropillar* [46].

Whispering gallery mode cavity: a completely different class of cavities are the so called whispering gallery mode (WGM) microcavities. Their geometry is either circular (microdisks), toroidal (microtoroids) or spherical (microspheres). They mainly use the mechanism of total internal reflection which leads to the light wave travelling all around the outer wall of the resonator without exiting the resonator.

Microdisks: they are usually consisting of a disk shaped part containing the active emitters on top of a pedestal of silicon. Typically these structures are created using selective etching which attacks the substrate but not the deposited film. The resonance effect is based on total internal reflection at the vertical disk wall. The quality factors are much more elevated with respect to the micropillar cavities: they can be of about 12000. The inconvenient of this geometry is the bigger modal volume of $6(\lambda/n)^3$ [43]. This resonator geometry has already been used to analyze the interaction with silicon nanocrystals. Zhang *et al.* reported in 2006 about the feasibility of large-scale production of such resonators [47]. Kekatpure and Brongersma reported in 2008 about optical loss processes in microdisk resonators containing silicon nanocrystals [48]. In addition, they report about quality factors $\geq$ 1000 and a Purcell factor of 6 outlining that, after further improvement, it could be raised to up to 50.

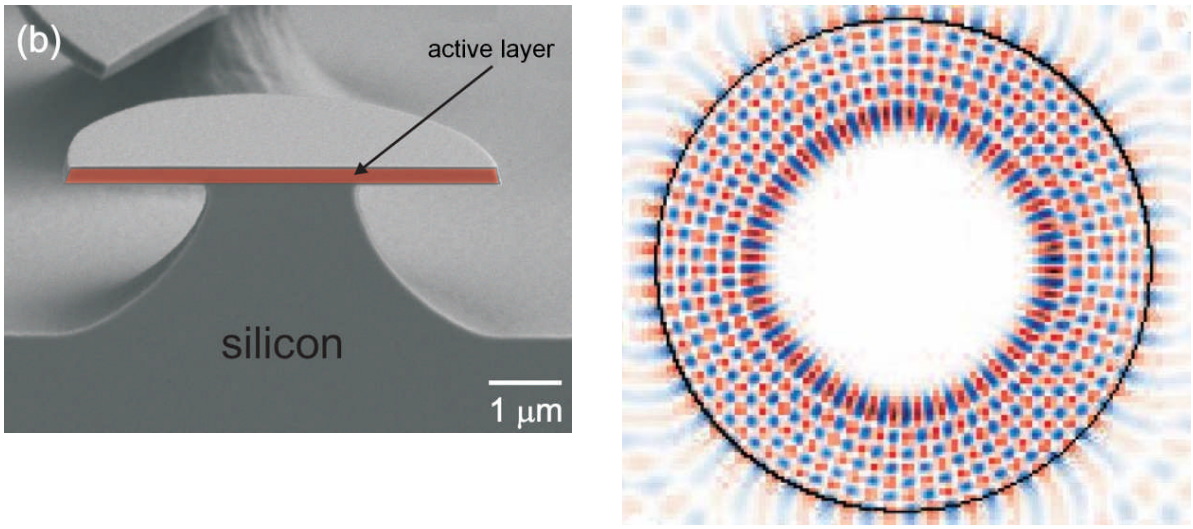

(a) *(b)*

Figure 1.16: Microdisk resonator: (a) vertical section – the active layer is marked in red. The mode form out from along the outer walls to the middle for increasing mode order. (b) Simulated electric field amplitude of a microdisk resonator [49].

Recently, Pitanti *et al.* presented a method to determine the line width of a single silicon nanocrystal from the spectrum of an ensemble of silicon nanocrystals coupled to a microdisk resonator [50]. Therefore, they use an empirical description of the Purcell factor given by Gérard and Gayral [51] for the case of the so called bad emitter regime, when the linewidth of the emitter is larger than the linewidth of the cavity mode:

$$\tilde{F}_P = g\frac{3}{4\pi^2}\frac{\tilde{\lambda}^3}{V_m}\left(\frac{1}{Q_{cav.}}+\frac{\Delta\omega_{em.}}{\omega_{em.}}\right)^{-1} f\left(\langle\omega\rangle\right), \qquad (1\text{-}31)$$

where $\omega_{em.}/\Delta\omega_{em.}$ represents a quality factor attributed to the emitter. By this very indirect method, they deduce a linewidth of single silicon nanocrystals at room temperature which is of 10 meV. Thus, the quality factor of the emitter is of about 200. They evoke that higher quality factors would not lead any more to higher Purcell factor as the linewidth of the emitter would be larger that the linewidth of the resonator modes in this case. This would lead to an increasing suppression of the photoluminescence signal as the intensity is simply filtered out. The more promising parameter to change would be the modal volume, which can still be reduced to improve the Purcell factor.

Microtoroids: They are a second class of total internal reflection based microresonators. They are fabricated in the same way as microdisk resonators, following by a pulsed laser annealing with a CO_2 laser. The laser annealing partially melts the sample and leads to the formation of a toroid at the outer bound of the microdisk with very smooth surfaces (see Figure 1.17 (a)). This is the big advantage of this type of cavity: due to the very smooth surface and the lack of defects, the quality factor is much more elevated with respect to microdisks ($Q \sim 10^8$ instead of 10^4). In addition, the resonant modes are

confined to the toroid, too (see intensity distribution in Figure 1.17 (b)). The photoluminescence in the inner part of the disk is due to uncoupled luminescence centers.

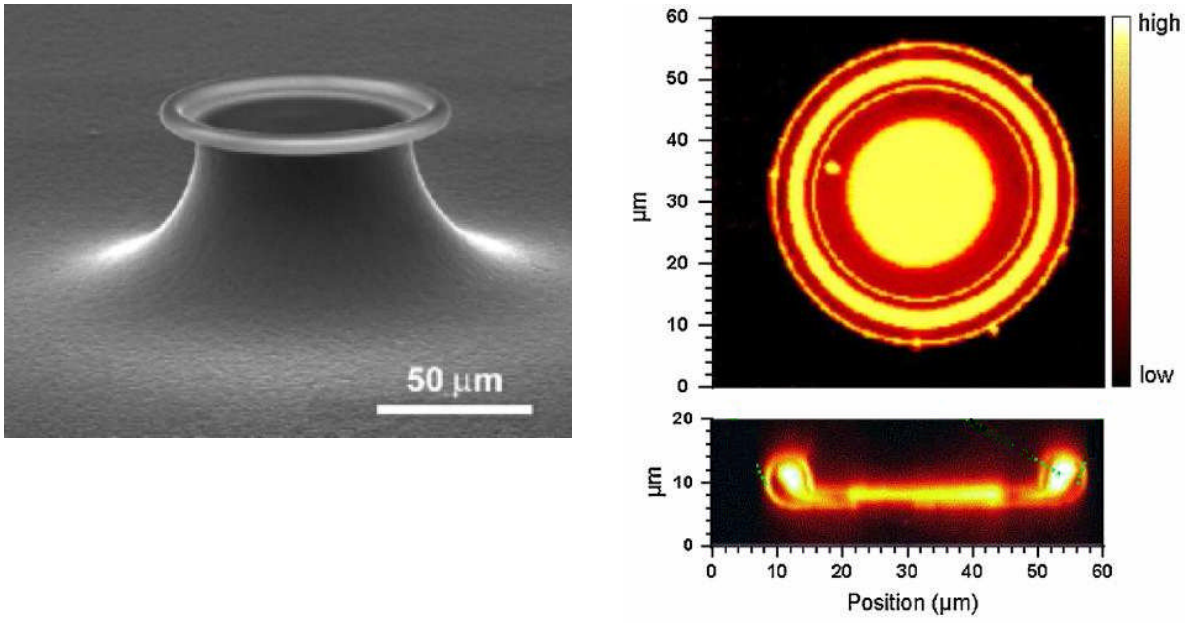

(a) *(b)*

Figure 1.17: Microtoroidal cavity geometry – (a) SEM image of a microtoroid (b) PL intensity distribution in a microtoroid. X-y- and y-z-sections are shown [52].

Microspheres: They are the three-dimensional extension of the microdisk. Light that is coupled to those structures travels along the inner side of the surface of the sphere due to total internal reflexions. Thus, the resonant modes are formed primarily close to the surface and only higher resonant modes extent to the middle of the sphere.

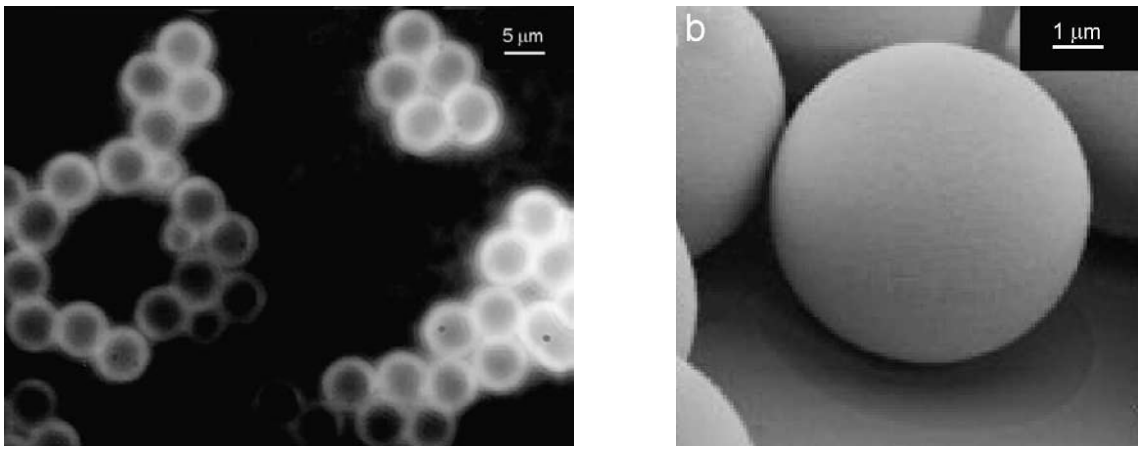

(a) *(b)*

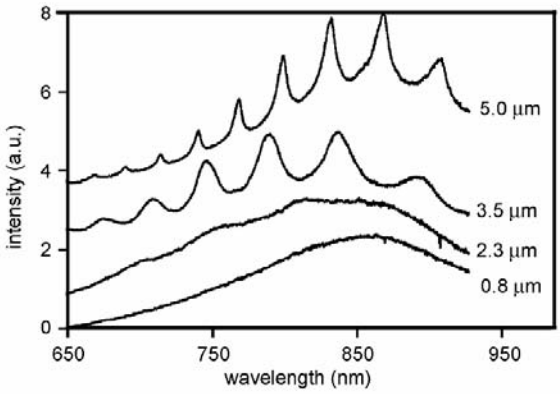

(c)

Figure 1.18 – Microspheres (a) optical image of luminescent microspheres ; (b) SEM image of a microsphere ; (c) photoluminescence spectra of silicon nanocrystals coupled to a silica microsphere for different sphere diameters [53].

Beltaos and Meldrum reported in 2007 about the coupling of silicon nanocrystals obtained from $SiO_{1.2}$ thin films to commercially available silica microspheres. A coupling to the cavity modes is clearly observed, as can be seen from Figure 1.18 (c). The observed quality factors range up to ~1500, but are strongly influenced by a lot of parameters as sphere diameter, thin film thickness and detection angle, e.g. More recently, Meldrum *et al.* [54] deduced a formalism to extract the not delta function like linewidth of an emitter from the photoluminescence spectra of a cavity. They generally confirm the results of Pitanti *et al.* [50] but show an improved approximation of the linewidth as they take into account the geometry of their resonator.

Choice of the cavity geometry: Because of the easiness of handling, we chose the approach of planar microcavities because it is fully compatible to the evaporation process which is actually used to produce the silicon nanocrystal samples. As the calculations of the emitter linewidth of Pitanti *et al.* and Meldrum *et al.* let suppose, we won't need extremely high quality factors. The needed order of magnitude should be reached with this approach. For future extension of the research, it is possible to reduce the planar cavities to micropillar cavities. Thus, the modal volume is extremely reduced and the Purcell factor should be increased over the limits that appear when we only increase the quality factor.

1.3 Summary & structure of this work

This chapter gave an overview of the physical properties of silicon nanocrystals. In addition, the work that has been realized on silicon nanocrystals was summarized. Next, the physical properties of optical microresonators were introduced. It is shown that the interaction of an emitter with the resonant modes of a cavity leads to a profound modification of the optical properties of the emitter.

The aim of this thesis is to develop the technical process to monolithically elaborate microresonators containing size-controlled silicon nanocrystals. A presentation of the techniques that have been employed to simulate, elaborate and characterize the model system will be given in the following chapter. In the third chapter, the influence of the stoichiometry factor on the nucleation and growth of the silicon nanocrystals will be presented. The aim is to inhibit interaction between the single silicon nanocrystals. Another aim is the isolation of a single silicon nanocrystal in order to investigate optical properties as e.g. the linewidth which are not accessible via ensemble measurements. In the fourth chapter we will detail the work that has been done on the implementation of a stable production process for monolithically grown microresonators. In the beginning, the optical constants of the single components of the microresonator as absorption coefficients and refractive index are determined as a function of the annealing temperature. After this, the behaviour of the wavelength selective mirrors is analyzed as a function of the annealing temperature. A densification of the components during the annealing is remarked and the thicknesses are adapted for having a microresonator with a resonance placed well at the maximum of the photoluminescence band of the silicon nanocrystals. At the end of this chapter, all the results are used for an estimation of the photoluminescence linewidth of single silicon nanocrystals, showing that microcavities are another, technically less demanding possibility to determine the photoluminescence linewidth of single silicon nanocrystals.

Chapter 2. Experimental & Theoretical Techniques

2.1 Introduction

In this chapter, we describe the techniques and methods which we applied during the fabrication and characterization of the SiO/SiO_2 multilayers embedded in Si/SiO_2 pairs based distributed Bragg reflectors. In the first section, the evaporator is presented. There, different types of thin layers of silicon and silicon oxides are deposited:

1. thin films of silicon and SiO_2 as components of the optical microresonators
2. thin films containing SiO/SiO_2 multilayers as the optically active layer of the microresonator
3. thin films of SiO_x ($x > 1$) to investigate the influence of the stoichiometry on the structural an optical properties of the thin films
4. thin films containing SiO_x/SiO_2 multilayers to investigate the influence of the silicon excess on the photoluminescence properties
5. thin films containing three layers of SiO_2, SiO_x and SiO_2 to investigate the influence of the silicon excess on the surface density or inter-crystal distance of silicon nanocrystals.

In order to create the silicon nanocrystals in the sample, it is necessary to anneal the sample reproducibly at temperatures up to 1150°C in a controlled atmosphere. The description of the annealing device is given in the second section. After the precipitation of the silicon nanocrystals, the samples are investigated by means of UV-VIS-NIR absorption spectrometry. Three different simulation methods have been employed to deduce the optical properties of the thin films as absorption parameters, refractive index and thickness. This technique is described in the third section of this chapter. The fourth section is dedicated to the glancing incidence X-ray reflection setup. With this technique, we confirmed the evolution of the thickness with the annealing temperature. The thickness of the layers has also been determined employing transmission electron microscopy to analyze cross-section prepared thin slices of the microresonator thin films. A supplementary energy filtered TEM study permitted the imaging of silicon nanoclusters that are not visible in common transmission electron microscopy. The description of the energy filtered transmission electron microscope as well as the sample preparation techniques are part of the fifth section. The SiO_x thin films prepared for the analysis of the influence of the stoichiometry factor have been analyzed by means of Fourier transform infrared (FTIR) absorption spectroscopy. Part of the samples has been analyzed using Raman spectroscopy. Finally, all samples have been analyzed by photoluminescence spectroscopy, which is presented in the last section of this chapter.

2.2 Evaporator

The technique used by our group is ultra-high vacuum (UHV, 10^{-8} Torr) evaporation. Figure 1.1 (a) shows the chamber and the controllers, figure 2.1 (b) shows the sources from which the material is evaporated. More detailed descriptions of the evaporation system are given in [16,22,55]. In this paragraph, only the elements which are necessary to understand the development of the thin layers will be explained.

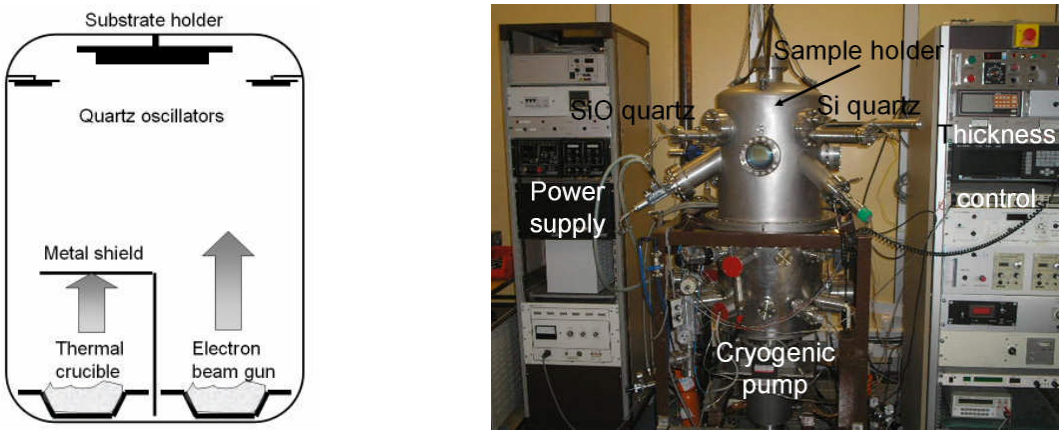

(a) *(b)*

Figure 2.1: (a) Sketch of the evaporation chamber. SiO and SiO_2 are evaporated at the bottom of the chamber. (b) Overview of the closed evaporator.

The substrates that we used are monocrystalline undoped [1,0,0] silicon wafers. Their crystalline orientation is chosen for the easiness of cleaving. The substrates are fixed face-down inside the upper part of the recipient. Their temperature is controlled by a heating coil working by Joule effect. Usually the temperature is maintained constant at about 100°C during the evaporation, the heating device correcting for the heating of the samples by the evaporation sources. SiO is evaporated from a Joule-effect-heated tantalum crucible. In contrast, the second crucible containing the SiO_2 is made of graphite and it is heated by electron beam bombardment (see Figure 2.2 (a)). Quartz oscillators are located vertically above the sources to measure the mass of the deposited material (see Figure 2.2 (b)). The quartz oscillators are mass sensitive because their resonance frequency depends on the mass of the oscillator. By measuring the detuning of the frequency, we are able to determine the deposition rate and to control the heating power in the evaporators in order to maintain the deposition rate constant. As the quartz oscillators are not perfectly at the same position as the sample holder, the measured deposition rate has to be corrected by a factor taking into account the geometry of the evaporator.

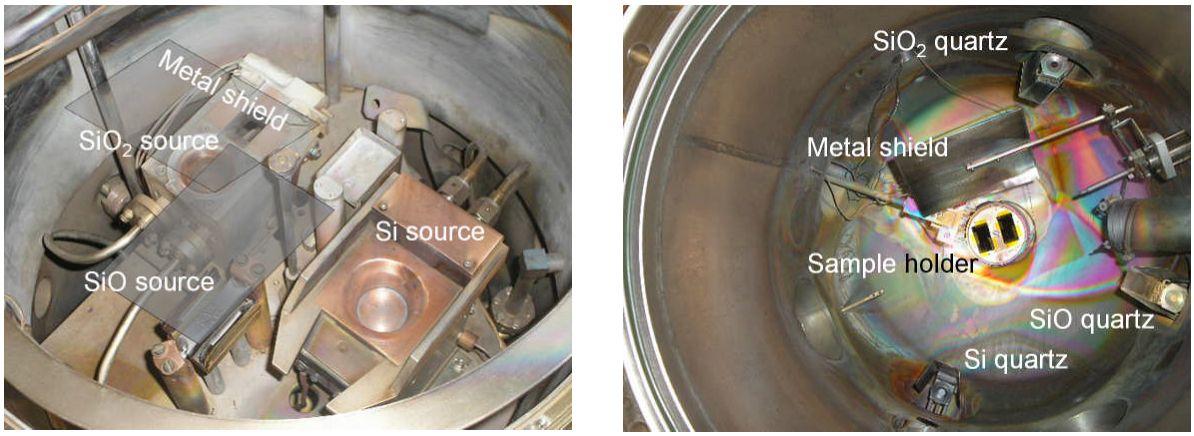

Figure 2.2: The SiO/ SiO_2 evaporation system: (a) The vapour sources are placed in the middle part of the recipient. (b) One can also see the shutter that controls the deposition of the material.

Thus, alternating layers of SiO and SiO_2 can be deposited onto the substrate with variable thickness of the layers by stopping the vapour flux of either SiO or SiO_2 by a metal shield. Repetition of the sequence creates SiO/ SiO_2 multilayer structures.

Layout of the samples

Multilayer samples: In order to avoid a large size variation of the silicon nanocrystals (as observed by Rinnert for 200 nm thick layers of SiO [22]), SiO/ SiO_2 multilayer structures are used. The chemically inert layers of SiO_2 hamper the diffusion of silicon particles from the SiO layers and allow for controlling the size of the crystals in the direction perpendicular to the deposition plane. Typically, the multilayer samples consist of 22 SiO/SiO_2 bilayers (thickness 3 nm SiO/5 nm SiO_2) [56].

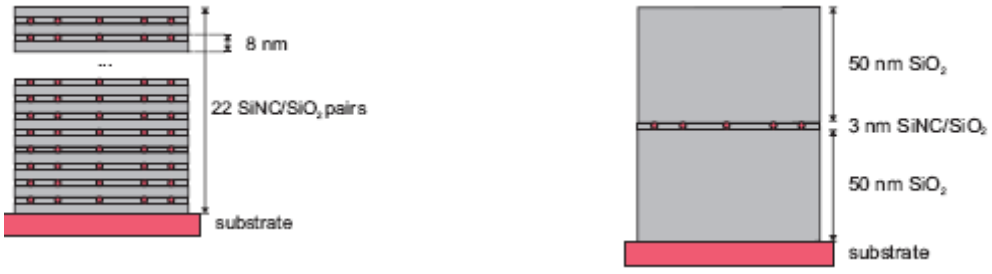

(a) *(b)*

Figure 2.3 : Different sample layouts – (a) multilayer sample; (b) single layer sample

Single layer samples: If the surface density of the nanocrystals has to be reduced, the first step is to create only one layer where the density of grains is about $10^{12}/cm^2$. The layout of the single layer sample is familiar to the one of the multilayer samples but we use only one 3 nm fine layer of SiO, where the nanocrystals shall be created by thermal annealing, between two 50 nm thick layers of SiO_2.

Stoichiometry: By co-evaporation of SiO and SiO_2 we are able to deposit SiO_x thin films with a stoichiometry factor x variable from 1 to 2. Employing the metal shield which is shown in figure 2.2 (a), it is possible to elaborate SiO_x/SiO_2 multilayers and SiO_2-SiO_x-SiO_2 single layer samples.

When the quartz monitor measures 1 unity of SiO_2, there is a deposition of 0.117 nm SiO_2 at the centre of the sample holder. With the density of 2.648 g/cm^2 we obtain a total surface density of

$$1.17 \text{ x } 2.648\ 10^{-8} = 3.0982\ 10^{-8} \text{ g/cm}^2.$$

The molar surface density is thus calculated by dividing by the molar weight of SiO_2, 60:

$$1.17 \text{ x } 2.648\ 10^{-8}/60 = 5.16\ 10^{-10} \text{ mol/cm}^2$$

Equivalently, we calculate for SiO (1 unit = 0.113 nm)

Surface density: 1.13 x 2.13 10^{-8} = 2.3856 10-8 g/cm^2

Molar density: 1.13 x 2.13 10^{-8}/44 = 5.42 10-10 mol/cm^2.

Now, the stoichiometry factor is defined as

$$x = \frac{[O]}{[Si]} = \frac{5.42v_{SiO} + 10.32v_{SiO_2}}{5.42v_{SiO} + 5.16v_{SiO_2}} \tag{2-1}$$

Thus, the ratio of the two deposition rates is

$$\frac{v_{SiO}}{v_{SiO_2}} = \frac{10.32 - 5.16x}{5.42x - 5.42} \tag{2-2}$$

Silicon excess: in addition to the stoichiometry factor one can also simply consider the percentage of silicon excess in the matrix. As SiO_x segregates into a pure silicon phase and SiO_2 matrix

$$SiO_x \rightarrow \frac{x}{2} SiO_2 + \frac{2-x}{2} Si \tag{2-3}$$

we can note that the silicon excess is the quantity of silicon which is not bound to oxygen:

$$excess\ Si = [Si] - \frac{[O]}{2} \tag{2-3}$$

The relative excess is finally:

$$relative\ silicon\ excess = \frac{[Si] - \frac{[O]}{2}}{[Si] + [O]} = \frac{1 - \frac{x}{2}}{1 + x} \tag{2-4}$$

with x being the stoichiometry factor of the as deposited film.

2.3 Thermal annealing

The annealing technique is the key factor of creating nanocrystals in a solid state matrix. During the annealing, silicon nanocrystals are created from atomic silicon appearing in the matrix by the following dissociation reaction at temperatures higher than 500°C.

$$2\ SiO \rightarrow SiO_2 + Si\ (nc) \qquad (2.5)$$

The annealing of SiO/SiO_2 multilayer and cavity samples has been performed in a rapid thermal annealing (RTA) device that consists of a water-cooled stainless-steel sample chamber in which the samples are placed onto a silicon carbide (SiC) sample holder (see Figure 2.4). The chamber is heated by the infrared radiation of 12 tungsten halogen lamps placed in the cover atop the chamber. The chamber is evacuated to HV by a rotary vane pump and a secondary turbomolecular pump. The minimum achievable pressure in this setup is 10^{-5} mbar. With this setup, we are able to anneal the samples at a maximum temperature of 1300°C which is controlled by a pyrometer, measuring the temperature of the SiC sample holder. At lower annealing temperatures, temperature control can be accomplished by thermocouples. A commercial control unit is controlling the heating power. Appropriate temperature ramps may be defined by a software furnished with the control unit and the heating of the sample is controlled with an accuracy of 1-2°C for of the final.

Additionally, the RTA allows us to to anneal in a controlled atmosphere. Two gas lines disposing of mass flow controllers permit annealing in fluxes of either nitrogen (N_2) or forming gas (10% H_2 + 90% N_2).

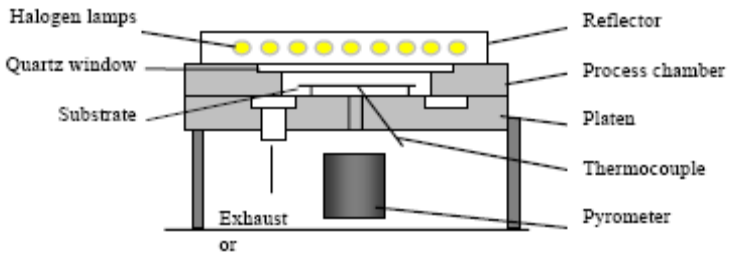

Figure 2.4: Principle of the RTA furnace

If not specially mentioned, the samples are usually annealed at 1100°C in N2 atmosphere. The temperature was raised from room temperature to the target temperature in five minutes. The target temperature was maintained for five minutes before the sample is cooled down within another five minutes.

2.4 UV-visible-NIR absorption spectrophotometry

2.4.1 Experimental

The optical measurements were performed on a dispersive dual beam Cary 5 spectrometer by Varian in the transmission configuration. The analysis of the transmission of films was performed in the ultraviolet, visible and near infrared spectral range (UV-Vis-NIR - 200-3000 nm). The spectrometer is equipped by two different radiation sources, a deuterium UV lamp and a tungsten filament lamp for the Vis-NIR spectral range. Two detectors are used, depending on the spectral range to analyze the intensity of the transmitted signal, a PbS photodetector for the NIR and a photomultiplier (PM) for the visible and UV ranges. The spectral resolution of 1nm is chosen which is quite sufficient for the type of measurement that we made (the device can work with a resolution of about 0.1 nm).

The substrates are fused silica plates with a thickness equal to 1 mm. This substrate has the advantage of having very low absorption across the spectral range studied, particularly in the near UV. Moreover, the dispersion relation of the refractive index is well known.

A reference spectrum from the air is recorded for each series of films with the substrate from the same slide to avoid possible effects due to the substrate. The transmission of the film deposited on the substrate is also seen from the air. The signal analyzed is the ratio of the two transmissions (Figure 2.5).

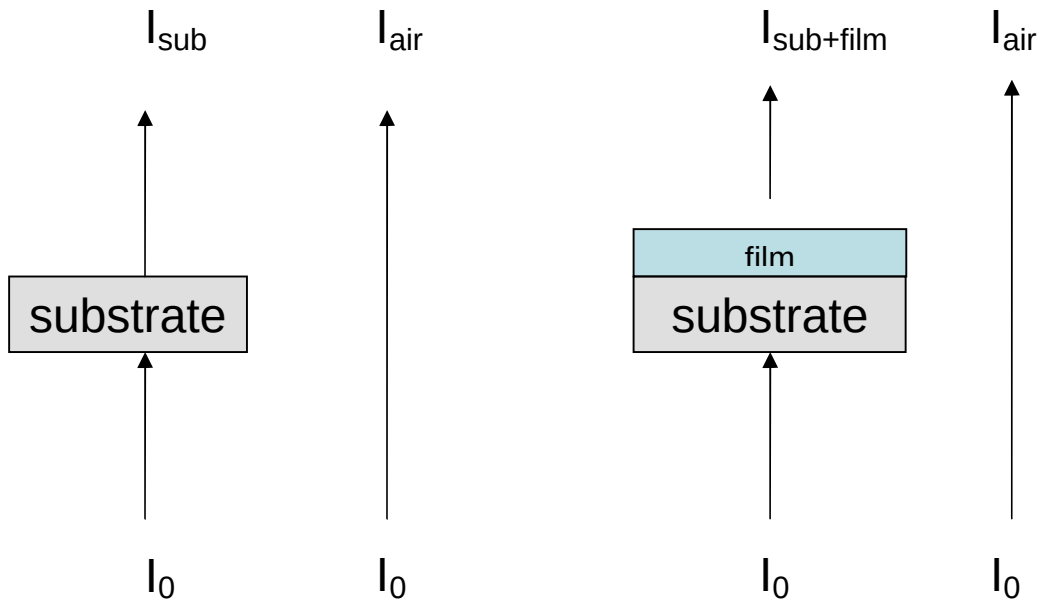

(a) *(b)*

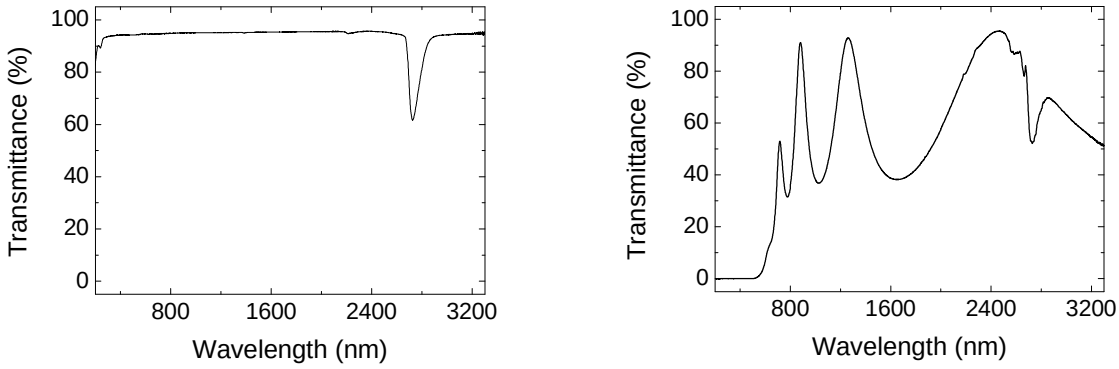

(c) *(d)*

Figure 2.5: The diagrams (a) and (b) represent the acquisition of the reference spectrum of the subsrate and the spectrum of film and substrate compared to air, respectively. The reference spectrum is shown in (c), a spectrum of substrate and film relative to the substrate is shown in (d).

The spectrum analysis is no longer influenced by the absorption due to OH bonds in the silica substrate around 2500 nm. However, the transmission given by the device is not representing the transmission of the film only because of the interference fringes from the difference in refractive index between the film and substrate.

The experimental spectra are then analyzed using a simulation program that we developed to obtain the values of optical gap, the refractive index, thickness and absorption. To get good accuracy on the values of these constants, the thickness of films deposited on the substrate is around 400 nm which gives a sufficient number of interference fringes.

Equivalence of transmission and reflexion spectra: Once the deposition process of the cavities is mastered, it is not necessary to analyse the whole UV-VIS-NIR spectral range, but only the spectral range around the resonance peak of the cavity. This is feasible also with a home-made setup that allows us to analyze both reflection and PL spectra of a sample with the same spectrometer. Figure 2.6 (a) compares the reflexion spectrum as obtained by the PL setup to the transmission spectrum obtained with a commercial UV-VIS-NIR transmission spectrometer. Both spectra show the resonance peak exactly at the same position. The simulation code also calculates the reflectivity and the simulated spectra are in good agreement with the measurements.

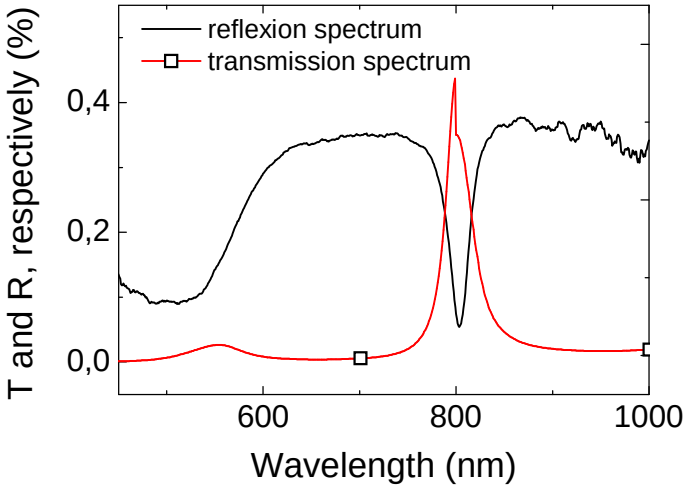

Figure 2.6: Experimental transmission and reflexion spectra of a microcavity, respectively. Even if the spectra are obtained by different setups, the resonance feature is at the same wavelength.

2.4.2 Principle of the direct simulation method

The difference of refractive indices of the substrate and the deposited film is causing interferences which significantly change the actual transmission of the film. Even if in a certain point of view, these interferences are a serious handicap in obtaining the coefficient of absorption, they are of interest to calculate accurately the thickness and refractive index of the film. For this purpose, it is necessary to simulate the transmission spectra. The simple expression of the transmission $T = T_0 \exp(-\alpha d)$, where α is the coefficient of absorption and film thickness is not correct in the case of measurements on thin films. We used the exact expression for the transmission of light interference effects [57, 58]. This expression is valid in the case of a thin film deposited onto a transparent substrate.

$$T = \frac{A \times \exp(-\alpha d)}{B - C \times \exp(-\alpha d) + D \times \exp(-2\alpha d)}$$

with

$$A = 16s(n^2+k^2)$$
$$B = [(n+1)^2+k^2][(n+1)(n+s^2)+k^2]$$
$$C = 2\cos(\phi)[(n^2-1+k^2)(n^2-s^2+k^2)-2k^2(s^2+1)]-2k\sin(\phi)[2(n^2-s^2+k^2)+(s^2+1)(n^2-1+k^2)]$$
$$D = [(n-1)^2+k^2][(n-1)(n-s^2)+k^2]$$
$$\phi = 4\pi nd/\lambda,\ \alpha = 4\pi k/\lambda$$

where n is the refractive index of the film, s the refractive index of the substrate, α the absorption coefficient of the film, λ the wavelength, k the extinction coefficient and d the thickness of the film.

The index of refraction of the substrate is known throughout the spectral range that we used, the simulation parameters are n, α and d. The upper, quite complicated equation is plotted by a homemade software code. Its great disadvantage is that it implies a manual fit of this complicated equation to the measured data. This procedure is more detailed in appendix A.

2.4.3 Swanepoel's method of envelopes

Whereas the direct calculus implicates a manual fit of the optical constants, the method being presented in the following represents a possibility to determine those constants almost automatically from a sole transmission spectrum. The method was published by Swanepoel in 1983 [58]. Its main difference from the upper treated direct calculus is the fact that this method uses the extremes of the interference fringes of the transmission spectrum to deduce the optical constants of a given thin film (see Figure 2.7). The calculus starts from an equation similar to the exact formula.

$$T=\frac{Ax}{B-Cx\cos(\phi)+Dx^2}$$

with

$$A=16n^2 s \qquad \phi=\frac{4\pi nd}{\lambda}$$

$$B=(n+1)^3(n+s^2) \qquad x=e^{-\alpha d}$$

$$C=(n^2-1)^3(n^2-s^2)$$

$$D=(n-1)^3(n-s^2),$$

First, the index of the substrate is determined by transmission measurements on the substrate. For the transmission of a bare transparent substrate, we have

$$T_s=\frac{2s}{s^2-1}\rightarrow s=\frac{1}{T_s}+\left(\frac{1}{T_s^2}-1\right)^{1/2} \tag{2.6}$$

After this, the transmission of a thin film deposited onto the same type of substrate is measured. Three zones corresponding to three different absorption regimes can be determined in the case of partly absorbing thin films: a zone of strong absorption at short wavelengths, called Tauc zone, where the absorption is due to transitions over the optical band gap, a zone of medium/weak absorption, called Urbach zone, in which the absorption is due to transitions in the band tails, which appear in amorphous materials. The third zone, in the infrared range, is the zone of transparency, corresponding to the optical band gap. In this zone, the refractive index is given by

$$n_{(1)} = (M+(M^2 - s^2)^{½})^{½}, \tag{2.7}$$

where

$$M = \frac{2s}{T_m} - \frac{s^2+1}{2} \tag{2.8}$$

whereas in the zone of medium/weak absorption, it is given by

$$n_{(2)} = (N+(N^2 - s^2)^{½})^{½} \tag{2.9}$$

where

$$N = 2s\frac{T_M - T_m}{T_M T_m} + \frac{s^2+1}{2} \tag{2.10}$$

Additionally, the absorption coefficient α can be determined:

$$e^{-\alpha d} = \frac{F - \sqrt{F^2(n_{(2)}^2 - 1)^3(n_{(2)}^2 - s^4)}}{(n-1)^3(n-s^2)} \tag{2.11}$$

where

$$F = \frac{8n_{(2)}^2 s}{T_i} \text{ and } T_i = \frac{2T_M T_m}{T_M + T_m}. \tag{2.12}$$

In the case of strong absorption, *x* and *n* are interdependent following Kramers-Kronig relations.

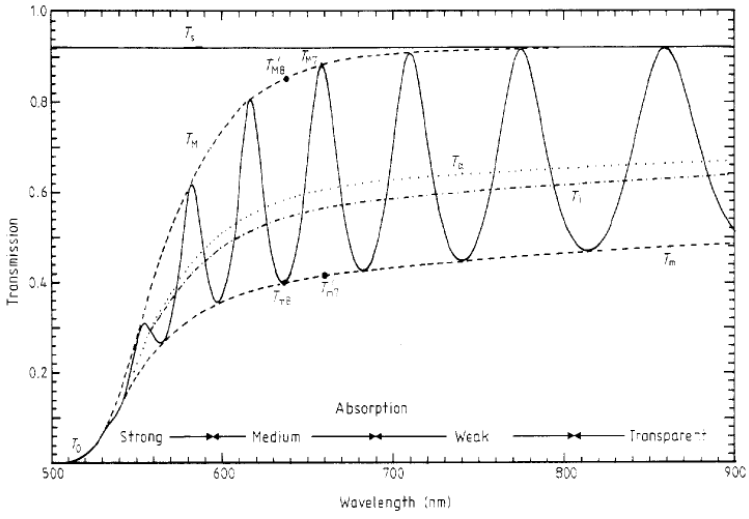

Figure 2.7: Transmission spectrum of amorphous silicon as measured by Swanepoel [58]. The index contrast between air, thin film and substrate causes interferences, which are at the origin of the wavy character of the transmission curve.

2.4.4 Principle of the transfer matrix simulation method

Similar to the direct calculus, the transfer matrix method (TMM) is developed from the Maxwell equations of electromagnetic waves passing through slightly absorbing matter. Whereas the direct calculus allows only for the calculation of the transmission of one thin layer, in the TMM, the equations, describing light passing through a more complicated sample, consisting of multiple layers, are decomposed into handy coefficient sets – matrices – that describe only the way of the light through one layer. At the end, the matrices are multiplied in order to obtain the transmission of the whole sample (see Figure 2.8).

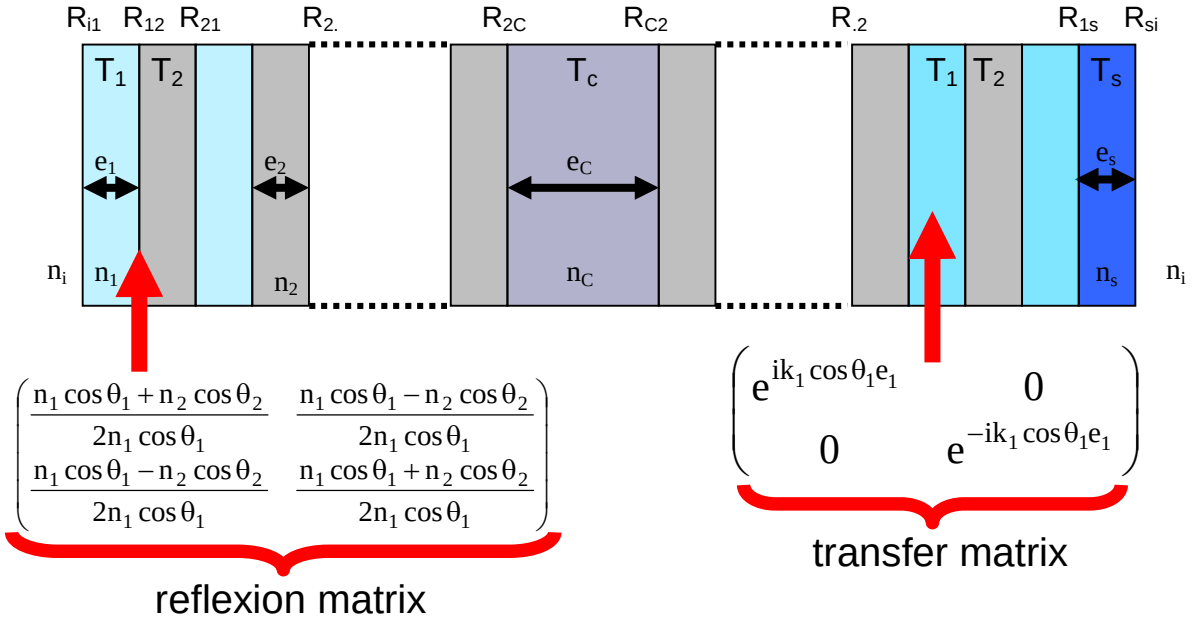

$$M = R_{i1}T_1R_{12}T_2R_{21}....R_2T_2\ R_{2C}T_C\ R_{C2}T_2\ R_2...T_1\ R_{1s}T_sR_{si}$$

Figure 2.8: Transfer matrix description of an optical microcavity. The propagation of the electromagnetic waves is treated layer by layer by the matrices R_{ij} and T_j and the propagation through the whole sample is described by the product of the propagation matrices of the individual layers.

A detailed description of the TMM can be found in appendix C.

2.5 Glancing incidence x-ray reflectivity

Glancing incidence x-ray reflectivity measurements allow us to determine the thickness, roughness, and density of a given film. This technique does not require crystalline films and works even with amorphous materials which is the case for a part of our samples in the as-deposited state. Due to interference effects of radiation reflected on the surface of the film and radiation reflected on the

interface between film and substrate, oscillations occur in the reflectance curve which can be fitted according to Fresnel's laws.

$$\sin^2\theta = \frac{p^2\lambda^2}{4d^2} + 2\delta \tag{2.13}$$

with d, λ and θ being film thickness, wavelength and detection angle, respectively. δ is a term which represents refraction. It depends mainly on the electronic density of states ρ in the material, the Bohr radius of the electrons r_e in the film and the atomic number Z.

$$\delta \cong \frac{\lambda^2}{2\pi}\rho r_e Z \tag{2.14}$$

The oscillation amplitude in the spectra for a given photon energy depends on the density of the material and its interface roughness, whereas the oscillation period is mainly determined by the layer thickness. In our laboratory, Cu Kα radiation with wavelength of λ = 1.54 Å is used.

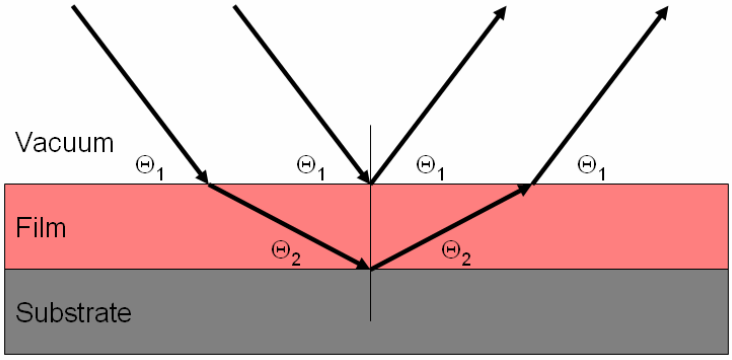

Figure 2.9: Layer thickness determination by X-ray reflectometry is based on interference effects of radiation reflected at two interfaces.

2.6 Transmission electron microscopy

2.6.1 Principe of the transmission electron microscopy

The principle of TEM is to place a sufficiently thin sample into a coherent electron beam, and observe the impact of the transmitted beam on a phosphorescent screen. The resolution R of a microscope is given in theory by the following formula:

$$R = (0.61\,\lambda)/(n \sin u) \tag{2.15}$$

with n being the refraction index of the medium between the objective and sample, u the aperture of the objective, 0.61 a coefficient associated with the Fraunhofer diffraction and λ the wavelength of radiation. For an optical microscope, $\lambda_{photon} \simeq 500$ nm and R ≃ 500 nm. For an electron microscope $\lambda_{e-} \simeq 0.001$ nm and R ≃ 0, 2 nm. We see that the practical resolution of an electron microscope is well

below its theoretical value. This is because the system of magnetic lenses is much less effective than optical lenses. Indeed, the magnetic lenses have a very small aperture u compared to classic optical lenses, which can cause high spherical aberration: the electrons arriving at the edges of the lens will focus before the electrons that pass through the centre of the lens. In addition to this, chromatic aberration of the incident beam occurs because the energy of electrons emitted by the filament fluctuates slightly.

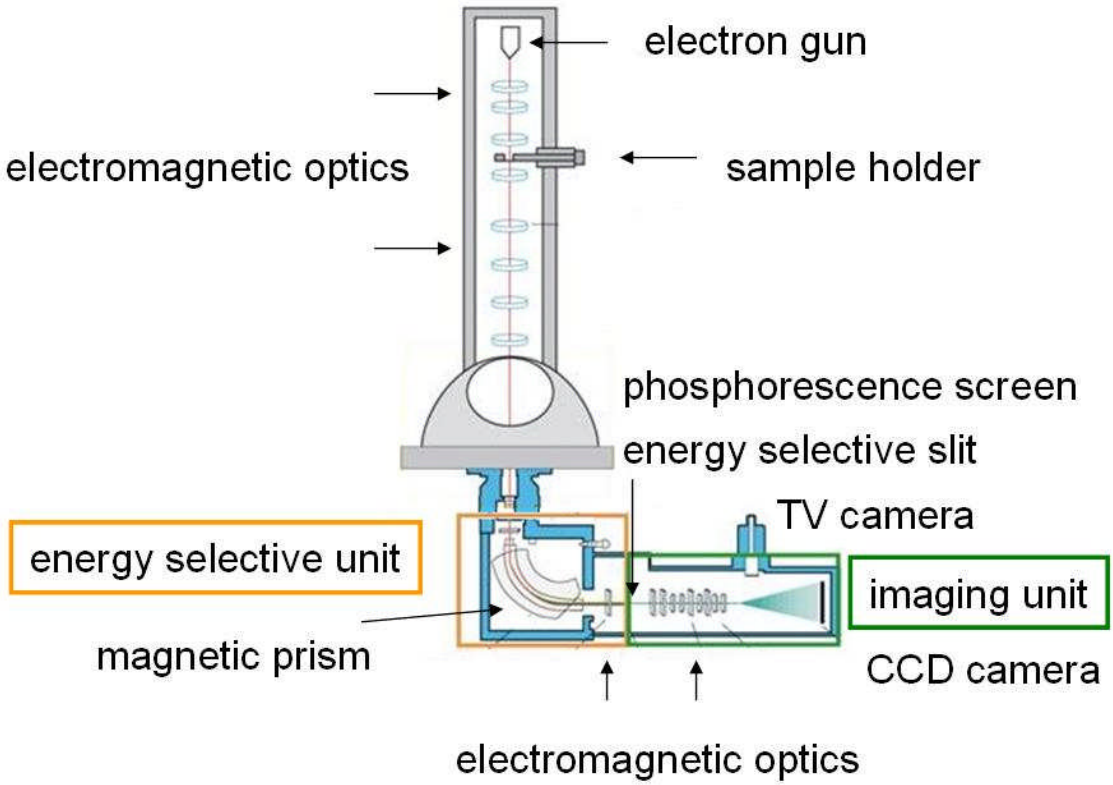

Figure 2.10: Schematic view of a transmission electron microscope (TEM) equipped with an electron energy filter between the beam column and the imaging unit. In a conventional TEM, the beam is directly projected into the imaging unit, whereas the intermediary energy filter allows for further spectroscopic analysis.

The diagram of a microscope is shown in Figure 2.10. It shows schematically the magnetic lenses, the diaphragms and the phosphorescence screen. The sample is represented by a black rectangle on top of the microscope; it is bombarded by an electron beam. The electron emission is produced by heating a filament of LaB_6 in the case of the Philips CM 200. A vacuum of approximately 10^{-7} Torr is established in the microscope. The electrons are accelerated by a voltage equal to 200 kV. With this microscope, it is possible to enlarge the image up to 750,000 times in high resolution mode. Images are recorded digitally by CCD camera with a low light level. The microscope works in either diffraction mode, or imaging mode. In diffraction mode, we look at the image formed in the focal plane the objective lens, showing a diffraction pattern of electrons. The focal plane in question is located at the objective diaphragm. The diffraction image is projected on the screen using the projector lenses and yields a diffraction pattern of the sample. In the image mode, the image plane, located at the diaphragm area, is selected and is projected on the screen.

Three types of contrasts are possible in the image: the absorption contrast, which depends on the electron density of atoms in the sample, the diffraction contrast which depends on the crystalline character of the sample and the phase contrast.

Absorption contrast: To see this type of contrast, we must collect all diffused or diffracted transmitted beams. The resulting image is not governed by the diffraction because all the beams are collected. Instead of this, the electrons that are absorbed by the sample are not collected and the areas that absorb the electrons appear dark in the image. In the case of silicon and silica, the electron densities are very similar implying that the contrast is very tenuous.

Diffraction contrast: Two imaging modes are possible, the bright field mode and dark-field mode. In the bright field mode, the objective aperture is placed to collect only the directly transmitted beam and not the diffracted beams. Thus, areas of the sample that diffract the incident electrons appear dark and areas that have transmitted the beam appear clear. The absorption contrast is also present. In the dark field mode, the objective aperture is positioned to select only one diffracted beam. Thus, areas that diffract in the direction chosen by the objective diaphragm will appear clear, while others appear black.

Phase contrast: By overlapping the transmitted beam with a diffracted beam, it is possible to obtain an interference pattern. This is a picture of the periodic potential created by the atoms. It is therefore not strictly an image of the atoms, but a projection of the potential created by these atoms. In this mode, said high-resolution mode, it is possible to see the plans and columns formed by atoms.

The transmission electron microscopy is used initially to observe multilayer samples in cross section. But it is an indispensable tool for the characterization of silicon nanocrystals. Studying the size distribution is possible employing any of the three imaging modes (bright field, dark field and high resolution), each with its advantages and disadvantages. In the literature, we can see that the three modes are used. The dark-field mode [59,60] allows for obtaining strong contrasts under the condition that the silicon aggregates are crystalline. The disadvantage is that one can’t image every grain, as one would have to describe the whole Ewald sphere. This is possible by rotating the sample, but the image would never be the same. In addition, a grain perfectly oriented to the chosen direction of diffraction will yield more diffraction intensity than a grain oriented imperfectly. Thus, the size of grains in the image depends on the dose of electrons received by the phosphor screen as a well-oriented grain appears very bright, and its contours are a little blurred. The effect of the error on the size is shown in Figure 2.11, where the (a) and (b) are bright field and dark field of same area. On the dark field, we see that some grains have a size much larger than that observed in bright field.

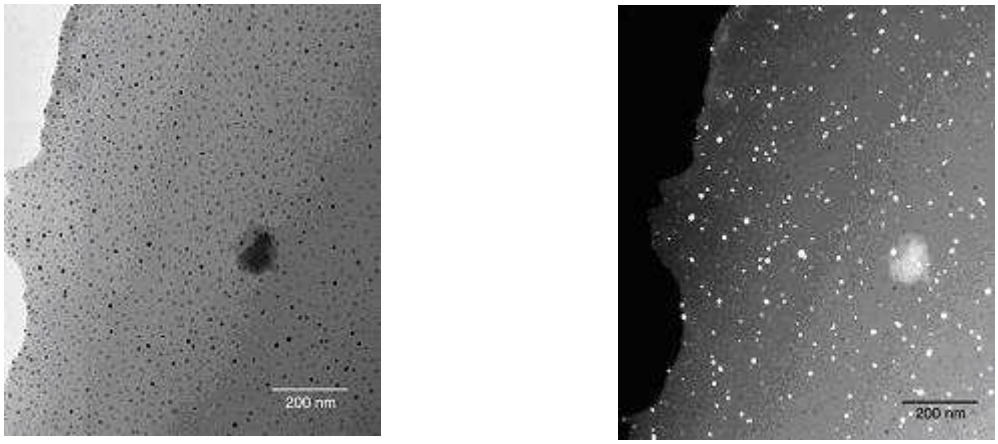

(a) *(b)*

Figure 2.11: Bright and dark field views of a thin SiO film annealed at high temperature

The high resolution mode lets one see the plans or atomic rows, so it may appear to be the most accurate method. However, the number of interference fringes that appear depends on the focus of the object. Additionally, in order to find the optimal conditions to analyze a grain, one has to observe one area for almost five minutes. During this time, the electron beam can already deteriorate this area.

Finally, the imaging mode we have chosen is the bright field mode. This mode is also the one chosen by Bonafos *et al.* [61, 62] which observed aggregates of group IV semiconductors in silica. This imaging mode facilitates the counting of grains as it lets take pictures for lower magnifications. To increase the contrast of grain, one has to defocalize slightly to reveal a white fringe around the grain that is called Fresnel fringe. This fringe introduces uncertainty in the extent that we can quantify by measuring the thickness of the same fringe that appears at the border of the sample, too.

2.6.2 Preparation techniques

As the films prepared by thermal evaporation have a thickness of about 1 μm, they are too thick to be transparent to an electron beam. The following three techniques are commonly employed to prepare slices that are fine enough to be transparent to electrons.

Microcleavage: This method consists of scrapping the specimen with a diamond point in order to get small fragments of the film. Those can be observed directly under the transmission electron microscope. In fact, for the observation of very small entities in an amorphous matrix, the specimen has to be very thin. A further inconvenient is the fact that one has to turn the specimen perfectly parallel to the electron beam in order to observe the alternances of SiO/SiO_2 bilayers in a multilayer sample or the alternances of Si/SiO_2 bilayers in the cavity samples. Another consequence is that this method does not allow for a precise control of the thickness of the pieces of the film that are investigated. Generally, those fragments are randomly oriented and rarely large enough to analyze the whole film. Still another disadvantage of this method is that the residuals are deposited onto a carbon film with a certain thickness which hampers the investigation of very small objects. The big advantage is now the very quick preparation of samples which in addition does not demand very much of the

whole sample. The method serves well for the observation of highly contrasting objects with sizes not smaller as 10 nm. So it does not serve very well neither for the analysis of silicon nanocrystals for the reason of weak contrast, nor for the analysis of cavities due to the reduced size of the analysed sample fragments.

Ion milling: This is a simple and effective preparation method. The already thinned sample (not thicker that 10 μm, preliminary polishing may be done by tripod method) is put into a vacuum compartment, where it is exposed to ions that are accelerated by a potential difference between their source and the sample. By adjusting the angle of incidence of the ions and the acceleration voltage, one can influence the thinning rate. The ion mill contains two ion sources, one under, one atop the sample, respectively. So, atoms that are detached from the sample during the exposure cannot deposit on the other side of the sample. In our case, we cannot use this method as the exposure to the ion beam causes a structural change of the film, as crystallization or demixtion. We would only be able to bombard the sample from the side of the substrate, but this would imply a deposit of polluting silicon (substrate) and copper (holding grid) onto the film. So, this method is incompatible to our samples.

Tripod method: This is a purely mechanic method to prepare thin slices for TEM. The slices are prepared by subsequent polishing of the sample by polishing disks containing more and more fine grains (30 μm down to 0.5 μm). After the finest grain, the thinning is accomplished by polishing with a felt disk, which contains a basic emulsion of silica spheres of 100 nm in size. The polishing is accomplished on a slightly tilted sample (tilt angle: 0.45°) what permits the preparation of an electron transparent zone, that is observable by TEM. The zone at the tip of the accomplished sample measures less than 10 nm in thickness, several microns in width and 1 to 2 mm in length. Even if this method allows for the preparation of slices thinner than 10 nm without structural modification of the sample, it is very delicate and long. Nonetheless, it allows for the observation of small entities such as single silicon nanocrystals in a several 100 nm large zone at the tip of the slice.

2.6.3 Electron energy loss spectroscopy

Electron Energy Loss Spectroscopy (EELS) is a spectroscopy that serves to analyze the energy spreading of the initially almost mono-energetic electrons of the electron beam of the transmission electron microscope, after their interaction with the sample. The interaction takes place inside the specimen and information about its structure can be obtained by passing the transmitted beam into a spectrometer.

Fast electrons passing through the matter undergo a great number of scattering events, which can be divided into two groups: elastic scattering, where the transmitted electrons do not suffer any energy loss and inelastic scattering of the electrons through interaction with the material.

Elastic scattering is due to Coulomb interaction with the atomic nucleus, which represents a highly repulsive centre. Electrons, approaching to its vicinity, can be deflected to large angles. Actually, most of the incoming electrons pass far from the centre of an atom, where the nuclear field is partially screened by the electronic cloud and electrons, therefore, are scattered only to smaller angles. Elastic scattering provides the most important contribution to the contrast in conventional TEM images.

With EELS, the energy spectrum mainly of the inelastically scattered electrons is analyzed. Amongst the various energy-loss processes, the most common ones and their energy range are the following:

Lattice vibration (phonon creation)	E < 0.1 eV
Collective plasmon excitation	5 eV < E < 30 eV
Interband transition	E < 10eV
Inner-shell electron excitation	13 eV < E
Excitation of free electrons (secondary electron emission)	E < 50 eV (causing background of the spectra)
"Bremsstrahlung"	X-ray background of the spectra caused by the strong deceleration of the electron passing through the material

Table 2.1: Most common energy-loss processes, analyzed by EELS

A typical low energy-loss spectrum is reported in Figure 2.12. The main peak, called "zero-loss", is caused by unscattered electrons, i.e. those electrons that are do not interact with the medium, and by those electrons that do not show measurable energy loss. Another contribution is formed by elastically scattered electrons and those that have excited phonon modes, for which the energy loss is less than experimental energy resolution.

The second prominent feature shown is the "plasmon peak". This is the feature, which the analysis of the surface density of the silicon nanocrystals is based on.

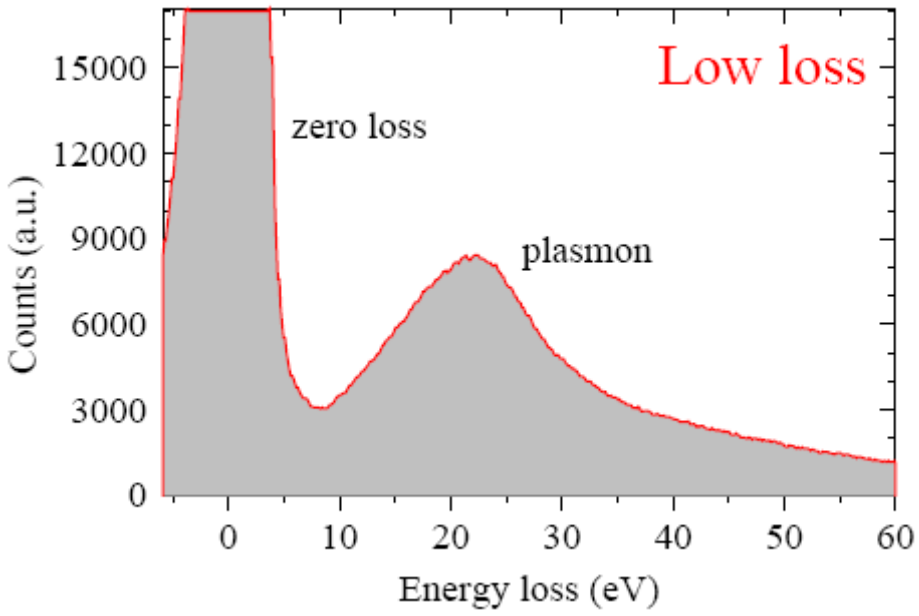

Figure 2.12: Energy loss spectrum of an electron beam interacting with electronic vibration states (plasmons) of the sample

2.6.4 Energy filtered transmission electron microscopy

As mentioned above, not all silicon nanocrystals appear on classical transmission electron micrographs, as they have to be in Bragg condition with the electron beam to be imaged. The surface density of 10^{10} grains/cm^2 determined by classical TEM is supposed to be widely underestimated. To circumvent this inconvenient, energy filtered transmission electron microscopy was employed. This technique is based on the upper mentioned electron energy loss spectroscopy. For every material that is supposed to be contained in the film, the energy filter is set at the corresponding plasmon energy (16 eV for silicon and 21 eV for silica, respectively) and a transmission electron micrograph is taken. A false colour image, superposing all micrographs that are taken, allows finally for the analysis of the surface density of all silicon nanocrystals, even those which are not in Bragg condition with the electron beam.

2.7 Infrared absorption spectroscopy

2.7.1 Principle

The infrared absorption spectroscopy is a characterization technique to distinguish the different modes of vibration of chemical bonds between the atoms of a material. The principle is based on a resonance phenomenon between incident electromagnetic radiation and the modes of vibration of atoms of the material. The incident radiation is absorbed when its frequency matches the eigenfrequency of a vibration mode of a bond of the studied material. The absorption spectrum shows a peak for the considered wavelength, which allows determining the nature of chemical bonds. A quantitative measure of the number of bonds can also be performed. Indeed, the Beer-Lambert law provides that intensity of the absorption peak is proportional to the thickness of the analyzed film and the density of the bonds. This coefficient of proportionality defines the absorption coefficient per unit of thickness and, in general, it differs little from one sample to another, thereby allowing quantitative comparisons.

For a molecule with a centre of symmetry, only the antisymmetric vibration (antisymmetric with respect to the centre of mass – heteropolar bonds) will active. The homopolar bonds as Si-Si are not active. Homopolar bonds show symmetric vibrations with respect to the centre of mass.

2.7.2 Vibrational spectrum in oxygen-rich amorphous silicon

Oxygen is a divalent atom located in a "bridged" site in which he has two silicon atoms as first neighbours. The local symmetry of the site occupied by the oxygen atom leads to three independent movements of the atom. The geometry of this connection is shown in Figure 2.13 and the three movements of the oxygen atom. These movements are characterized by reference to the axis of symmetry corresponding to the bisector of the angle Si-O-Si. There are two movements in the plane: one in the direction of the bisector which is a symmetric stretching and the other is a movement at

right angles to the axis of symmetry double in a direction parallel to a line joining the two silicon atoms. This is an asymmetric stretching movement. The third movement is in a direction perpendicular to the plane formed by the Si-O-Si group. This movement is a rocking motion. Movements of symmetric and asymmetric stretching of the oxygen atom are accompanied by a shift of the two silicon atoms in directions parallel but opposite phase. Given the site symmetry of oxygen, the three vibrations are active in infrared and Raman.

The frequencies of these vibrations have been determined from infrared absorption measurements performed on films of amorphous silicon prepared by sputtering silicon in an oxygen atmosphere [63] and on films made of amorphous silicon by implantation of oxygen ions [64]. The asymmetric stretching vibration is observed at 940 cm^{-1} and the symmetric stretching vibration at 650 cm^{-1}. A third vibration at 500 cm^{-1} is attributed to the rocking vibration.

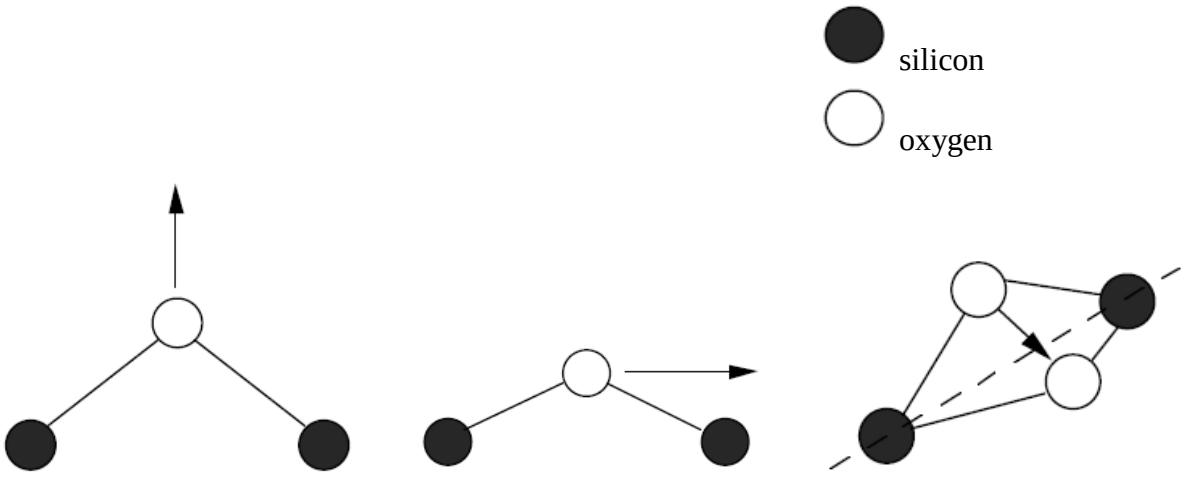

Figure 2.13 : Si-O-Si vibration modes: (a) symmetric stretching; (b) asymmetric stretching; (c) rocking

2.7.3 Vibrational characteristics in a- SiO_2

The vibrational spectrum of amorphous silica is very different from that presented by the amorphous silicon doped with oxygen. Although the vibration modes are always generated by the same movements of the oxygen atom, the second neighbours are oxygen atoms instead of silicon atoms.

The vibration frequencies identified in the literature have values that vary according to the authors. However there are still four modes.

	Pai [65]	Lin [66]	Jing [67]
Symmetric stretching	800	800 766-840	805

		(calculated)	
Assymmetric stretching (in phase)	1075	1080	1070
Assymmetric stretching (anti-phase)	1150	1175-1218 (calculated)	1100-1200
rocking	465	450	460

Table 1: Vibration frequencies of a- SiO_2 in cm^{-1}

Unlike the modes of vibration in amorphous silicon doped with oxygen, it appears a second asymmetric stretching mode. This arises from the interaction with second nearest neighbours. Indeed the oxygen atoms can be either in phase group or in opposite phase with the oxygen atom of the Si-O-Si group, leading to two different modes, respectively – the higher frequency corresponding to the antiphase vibration.

If a certain dispersion of results appears in the literature, this is due to the amorphous silica, which was reflected in angle dispersion in the bonds of the Si-O-Si group. This dispersion results in a higher width at half maximum of the vibrational bands and also the frequency shift of this absorption. In particular, Lin has shown – by calculating the vibrational spectrum of a-SiO_2 from the method of Bethe network taking into account the second nearest neighbours – that the frequencies of vibration modes were sensitive to the angle of the Si-O-Si group that is equal to 144° in quartz. For a change of angle from 134° to 154°, the frequency of antiphase asymmetric stretching mode ranges from 1175 to 1218 cm^{-1} and that of the symmetric stretching mode from 840 to 766 cm^{-1}. Given the perpendicular motion of the rocking mode, the associated frequency is less sensitive to vibration.

2.7.4 Analysis of the stoichiometry

The vibration frequency of the asymmetric stretching mode in the silicon oxide is 940 cm^{-1} for low oxygen concentrations in the material and 1080 cm^{-1} in a- SiO2. Pai et al. [65] propose a linear relationship between the ratio [O] / [Si] and the frequency of this stretching vibration mode. This purely empirical relationship, obtained experimentally from measurements made by electron microprobe, is accepted by many authors and is often used to determine the stoichiometry of oxide films on silicon. The relationship between the frequency ν of the vibration mode and the ratio x = [O] / [Si] is:

$$\nu = 965 + 50\ x\ (cm^{-1}) \tag{2.16}$$

The value of 965 cm^{-1} corresponds approximately to the value of the Si-O-Si vibration in a film of amorphous silicon with little oxygen. This value can vary from 940 to 980 cm^{-1} depending on whether or not there is hydrogen in the material. The slope, equal to 50 cm^{-1}, is obtained from the vibration frequency of Si-O-Si group in a- SiO_2 that can vary from 1060 to 1080 cm^{-1} according to the preparation method. This expression, which is an approximation of the actual stoichiometry, permits one to have a good idea of the value of x and especially to compare among materials prepared with the same technique. A similar trend of the lowest frequency modes at 465 and 800 cm^{-1} is also observed [68].

This change in frequency is interpreted in terms of chemical environment of the silicon atom of the Si-O-Si group. Oxygen is very electronegative, the Si-O bond is shorter than the Si-Si one and the force constant is increased. We can consider that the frequency changes continuously with the number of oxygen atoms in second neighbouring sites.

2.8 Raman spectroscopy

2.8.1 Working principle & fundamental notes

Many methods for studying the energy levels as absorption in the UV, visible and infrared ranges, nuclear magnetic resonance, X-ray fluorescence, for example, are primarily using resonance methods. Raman spectroscopy uses inelastic scattering phenomenon which generates a small difference between the excitation energy and detected energy; this difference is due to the energy of the analyzed levels. As it is not a resonant process, the probability that these transitions occur is low.

When a sample is excited by a monochromatic light, the incident radiation is scattered. This scattering may be due to the presence of inhomogeneities – if they are larger than the wavelength – or due to polarizability of the medium (Rayleigh scattering, more weakly than inhomogeneities). Both processes lead to diffusion at a frequency identical to that of the source. The Raman emission is a diffusion that occurs at a frequency that is different from the source, higher (anti-Stokes line) or lower (Stokes line) frequency. Both emission lines are symmetrical to the excitation and the energy gap between the source and the scattered intensity does not depend on the energy of the source. This is why it is called Raman shift. It is an intrinsic value of the investigated material. The observed frequencies are characteristic modes of vibration of molecules or crystalline lattices. The Raman effect, although very close to the infrared spectrometry, is a technique truly complementary because the Raman selection rules are different from those governing the absorption in the infrared range. Moreover, the relative intensities of corresponding bands are not the same. In a combined study of infrared and Raman spectroscopy, it is possible to use vibrational spectroscopy to analyze chemical bonds and structural configurations in a material.

The effect of an electromagnetic wave on the matter is to create an oscillating electric dipole. This dipole radiates at the frequency of the source and this oscillation is generally diffused. The scattering by a widely dispersed set of particles of sizes smaller than the wavelength of the source corresponds to a simple diffusion, the criterion being that the scattering of a particle does not disturb the diffusion of other particles. Let

$$\vec{E} = a\cos(\omega t)\vec{u} \tag{2.17}$$

be the incident wave of pulsation ω. We can distinguish the Rayleigh scattering and Raman scattering:

Rayleigh scattering: Let us assume that the particle has a polarizability α, the resulting dipole is

$$\vec{\mu} = \alpha \times \vec{E} = \alpha \times a\cos(\omega t)\vec{u}\ . \tag{2.18}$$

In general α depends on ω. If the particle is isotropic and $\vec{\mu}$ and $\vec{E}$ are collinear, the radiation resulting from the dipole corresponds to Rayleigh scattering.

Raman scattering: If we consider a molecular bond of which a frequency of vibration ω_v is activated by thermal effects for example, the polarizability becomes

$$\alpha = 1 + b\cos(\omega_\upsilon t) \tag{2.19}$$

in the approximation of the harmonic oscillator. The induced dipole is then:

$$\vec{E} = a\cos(\omega t)\vec{u} \tag{2.20}$$

$$\vec{\mu} = \alpha \times a\cos(\omega t)\vec{u} + ab\cos(\omega t)\cos(\omega_\upsilon t)\vec{u}\text{ , or} \tag{2.21}$$

$$\vec{\mu} = \alpha \times a\cos(\omega t)\vec{u} + \frac{1}{2}ab\left(\cos((\omega + \omega_\upsilon)t) + \cos(\omega - \omega_\upsilon t)\right)\vec{u} \tag{2.22}$$

In the last equation appear two frequencies which are different from that of the excitation $(\omega\text{-}\omega_v)$ and $(\omega+\omega_v)$. The low and high frequencies correspond to the Raman Stokes and anti-Stokes diffusion.

This traditional interpretation of the Raman effect can explain the origin of the two frequencies observed experimentally. However, the relative intensity of the two emitted waves can be explained by the quantum theory of Raman effect. We must indeed introduce two energy levels of the molecule whose respective populations are derived from the Boltzmann factor. The intensity ratio of Stokes lines and anti-Stokes lines is linked to this factor.

We are interested in the study of silicon oxide films only to the most intense line, the Stokes line.

2.8.2 Density of vibrational states in silicon

The interpretation of infrared and Raman spectra of amorphous silicon is related to the knowledge of the density of vibrational states, which is highly correlated with that of crystalline silicon. The nomenclature used to describe the various components of the spectra in amorphous silicon is described by comparison with those of the crystalline phase. On the other hand, theoretical models taking into account the structure of amorphous silicon were used to calculate the vibrational density of states of amorphous silicon by introducing the short and medium range. In this analysis, it is generally accepted that amorphous silicon can be described as a continuous random network consisting of groups of fourfold bound interlinked silicon atoms; the disorder is introduced by a distribution of bond angles and a topological disorder. The Raman diffusion and infrared absorption permit an indirect determination of the density of vibrational states. It is important to note that as neither long range order nor periodicity exist in amorphous silicon, all vibrational modes can contribute to Raman and infrared signals to the extent that the selection rules for allowed transitions have been relaxed. The vibrations which come into play through infrared or Raman spectroscopy depend on the type of vibration and how they involve the order in the material.

The calculated vibrational density of states of crystalline silicon [69] and the experimental Raman spectrum of a sample of crystalline silicon are represented in Figures 2.14 (a) and (b), respectively. The prominent bands of the vibrational density of states are centered at 480 cm^{-1}, 390 cm^{-1}, 325 cm^{-1} and 190 cm^{-1} and are called the transverse optical (TO), longitudinal optical (LO), longitudinal acoustic (LA) and transverse acoustic (TA) modes, respectively. It may be noted that, if the relative intensity of different peaks and their frequency are not fully consistent with the experience, all the bands are highlighted by the theory. An efficient theoretical method to study the vibrational modes

related to the structure is the use of the Bethe lattice [70], e.g. which models amorphous silicon by an aperiodic infinite lattice of silicon atoms with the same short-range order than crystalline silicon (inter-atomic distance and tetrahedral coordination).

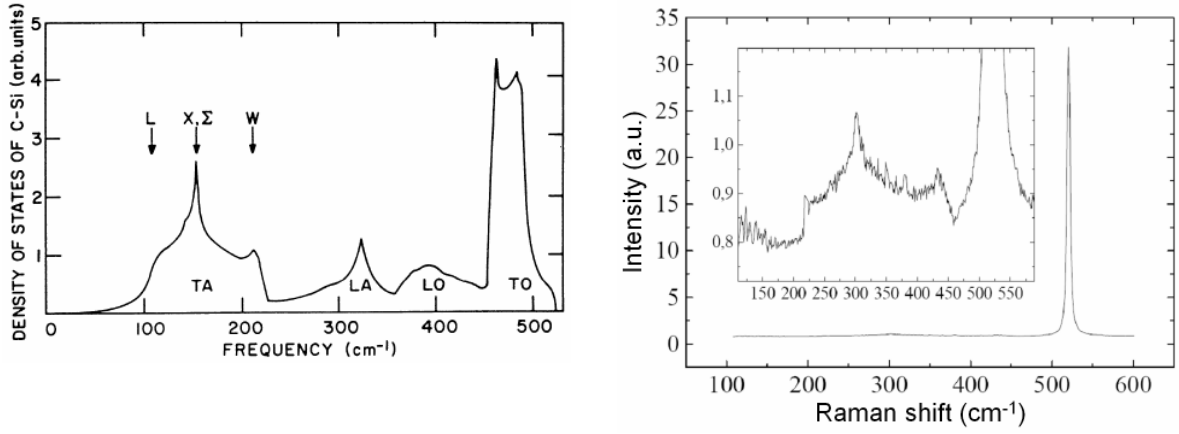

(a) *(b)*

Figure 2.14: Raman spectrum of silicon – (a) simulation employing the model of Wooten et al.[74]. *(b) measurement*

The density of states obtained by this model shows two of the four bands of crystalline silicon, the TA and TO bands. The lack of the LA and LO modes in the vibrational density of states of amorphous silicon obtained by the method of Bethe lattice is explained by the fact that these bands are related to a medium-range order. The TA and TO vibrations are instead the result of a short-range order (links to four neighbors and tetrahedral geometry). Meek [71] and Ishii *et al.* [72] have shown that the shape of the TO mode was also sensitive to the topological disorder and the fluctuation of interatomic distances.

Marinov *et al.* [73] have used the model of Wooten *et al.* [74], based on an algorithm generating a periodically repeated amorphous structure to 216 atoms with a box size of 16.28 Å. The average deviation of bond angles relative to the tetrahedron is 10.8 ° while the average deviation of the bond length compared to the distance Si-Si in crystalline silicon is 2.7%.

2.8.3 Raman effect in silicon nanocrystals

Iqbal *et al.* [64] have experimentally demonstrated a peak shift of the TO modes in films of nanocrystalline silicon for decreasing size of silicon crystals. The crystal size is calculated from the spectra of X-ray diffraction. They show that, for a crystal size less than 100 Å, the peak frequency decreases from 520.5 cm^{-1} frequency corresponding to macroscopic crystalline silicon, to 512 cm^{-1} for crystal sizes of about 35 Å. This decrease in frequency is correlated with the extension of the lattice parameter measured by X-ray diffraction. The physical origin of the lattice-parameter increase with decreasing size of the crystals seems to be related to the contribution of surface energy. The calculations of Alben *et al.* [75] have also shown an effect of phonon confinement could lead to a vibration frequency of 504 cm^{-1}.

To interpret the Raman spectra in nanocrystalline silicon, the model most often used is the phenomenological phonon confinement. This model is efficient to explain the shift of Raman peak,

widening and asymmetry. The important aspect of this model is the function of the phonon confinement in the crystallite. Thus the model of Richter [76] uses a Gaussian function whereas Fauchet *et al.* [77] are using different functions (hyperbolic sine). The wave function of the phonon can be written as

$$\Psi\left(\vec{k},\vec{r}\right)=W(\vec{r},L)\cdot f\left(\vec{k},\vec{r}\right) \tag{2.23}$$

where f (k, r) is a Bloch wave, L the characteristic dimension of the nanocrystal and W(r, L) the function of the phonon confinement. This wave function is then decomposed into Fourier series with values of wave vector centered on k = 0 corresponding to the first order Raman spectrum. Among the functions f used, it seems that the Gaussian function which represents a confinement box (near zero amplitude at the edge of the nanocrystal) best simulates the experimental spectra.

Few microscopic models describe the vibrational properties in silicon nanocrystals. Zi et al. [78,79] are involved in their model the polarizability of the bonds and force constants of vibration. The force constants in silicon nanocrystals are assumed to be identical to those of macroscopic silicon, assuming that the silicon atoms remain in the diamond structure with a low relaxation. The diagonalization of the matrix corresponding to the sphere of 357 atoms of silicon allows the calculation of vibrational frequencies and Raman spectra can be calculated. In particular the displacement of TO peak can be described by a power law

$$\Delta\pi = - A\ (a / L)^{b} \tag{2.24}$$

where $\Delta\pi$ is the difference in frequency compared to that of macroscopic crystalline silicon, A = 47.41 cm^{-1} and b = 1.44. This model differs significantly from the phenomenological model, especially for nanocrystals of sizes below 30 Å where the frequency shift is lower in the case of the microscopic model. However the general trend is similar and shows a decrease in the frequency of vibration of the TO peak for decreasing sizes of nanocrystals.

2.8.4 Discussion on the interpretation of the vibration at 480 cm^{-1}

The signal at 480 cm^{-1} is generally interpreted as the signal of an amorphous structure. Iqbal *et al.* have a different interpretation of this band, considering it comes from surface modes in Si-Si grain boundaries of a microcrystalline-type structure [64]. In addition to the TO component near 520 cm^{-1}, they have indeed observed a broad band located at 480 cm^{-1}. The intensity ratio of the amorphous band on the intensity of the crystalline band decreases with increasing size of the nanocrystals and therefore increases with the percentage of atoms on the surface of crystallites. The frequency of this vibration is changing from 498 cm^{-1} for crystals of large sizes at 480 cm^{-1} for the small sizes, highlighting a shift from one mode of vibration similar to that of bulk to a surface mode.

It is important to distinguish the different contributions to the vibration at 480 cm^{-1} which may be from one part of the amorphous structure and other modes of surface when the nanocrystals are present. A density spectrum of vibrational states is asymmetrical with a rapid decrease to higher frequencies. In pure amorphous silicon, the Raman spectrum of films studied by Iqbal *et al.* [64] have a symmetrical band at 480 cm^{-1}, which confirms the assumption of vibrational modes different from those appearing in amorphous silicon.

2.8.5 Raman scattering experiments

Raman scattering spectra were acquired on a spectrometer equipped with a liquid N_2 cooled CCD detector. The laser wavelength was the 488 nm emission line of an Ar^+ laser. A confocal microscope was used and the laser was focused on the sample by a ×50 objective (numerical aperture of 0.55). The laser irradiance was kept low (<1 kW cm^{-2}) to avoid any heating effect. This was verified by checking the phonon mode at 522.5 cm^{-1} of the bulk silicon substrate after a quite long period of laser irradiation (1 hour). Note that the absolute position of the bulk silicon phonon mode depends from the absolute calibration of the spectrometer and the temperature of the sample. It is common to use the emission line of mercury (from neon lamp) to perform a calibration of the spectrometer in absolute wavenumbers. However, using a blue laser at 488 nm, the spectral position of the mercury line and the spectral position of the phonon mode of bulk silicon are greater than the range of wavenumbers authorized by the high resolution grating at 1800 lines/mm. Therefore, it is necessary to move the grating after absolute calibration to retrieve the silicon spectrum, which always induces a wavenumber shift of 0.1-0.3 cm^{-1}. We thus have chosen to calibrate the relative wavenumber by imposing the bulk silicon mode at 522.5 cm^{-1} to avoid any spectral drift. The entrance slit of the spectrometer was fixed at 40 µm to obtain the best spectral resolution, i.e. 1.2 cm^{-1}. This enabled us to measure the spectral full width at half maximum (FWHM) of the bulk silicon phonon at 522.5 cm^{-1} at 300 K, which was 3 cm^{-1}. The samples were analyzed at several locations and the results were always consistent for a given sample. It is interesting to note that the laser line at 488 nm enabled us to record a resonant Raman spectrum for nanocrystalline silicon, whereas the 514 nm laser line available on the argon laser only revealed the phonon modes of the silicon substrate. This fact agrees with a higher band gap of nanocrystalline silicon compared to bulk Si (see below).

2.9 Photoluminescence

2.9.1 Continuous photoluminescence setup – general photoluminescence measurements

In the continuous PL setup (see Figure 2.15), an Hg-vapour lamp (Oriel, 200W) is used as light source. Measurements were performed by PL exciting with the emission lines from 311 nm (3.99 eV) to 546 nm (2.27 eV). Those lines were separated from the full spectrum of the lamp by a monochromator. The exciting light is focused onto the sample. To analyze the PL properties for a large range of temperatures, in this setup, temperatures ranging from 77 K (liquid nitrogen temperature) up to 600 K are accessible by a liquid nitrogen cryostat. Its windows are made of fused silica in order to avoid absorption of either excitation or fluorescence light. The fluorescence emitted from the sample can now be collected by two different ways:

1. a mirror reflects the fluorescence light emitted along the surface normal of the sample, which is afterwards focalized onto the entrance slit of the monochromator by a UV lens (f = 200 mm) and filtered by a low-pass filter that suppresses the reflected contributions of the excitation light.
2. an optical fiber, that is directly coupled to the entrance of the monochromator, collects the fluorescence. This configuration allows for angle resolved cw-PL measurements as the fiber is mounted on a homebuilt goniometric head which can be rotated around the excitation spot on the sample.

The monochromator contains three different reflection gratings (150, 300 and 1200 lines/mm). The detection system consists of a liquid nitrogen cooled, high sensitivity charge coupled device (CCD) camera with a chip size of 1024*256 pixels. Within the limitation by the gratings and the detector, we are able to measure PL within the range from 400 nm (3.1 eV) to 950 nm (1.3 eV). The advantage of the multichannel character of the CCD is the possibility to measure the whole spectral range from 400 nm to 950 nm without moving the grating. The setup has been carefully calibrated using a tungsten filament lamp. The spectra presented in the following have been corrected for the spectral response of the detector.

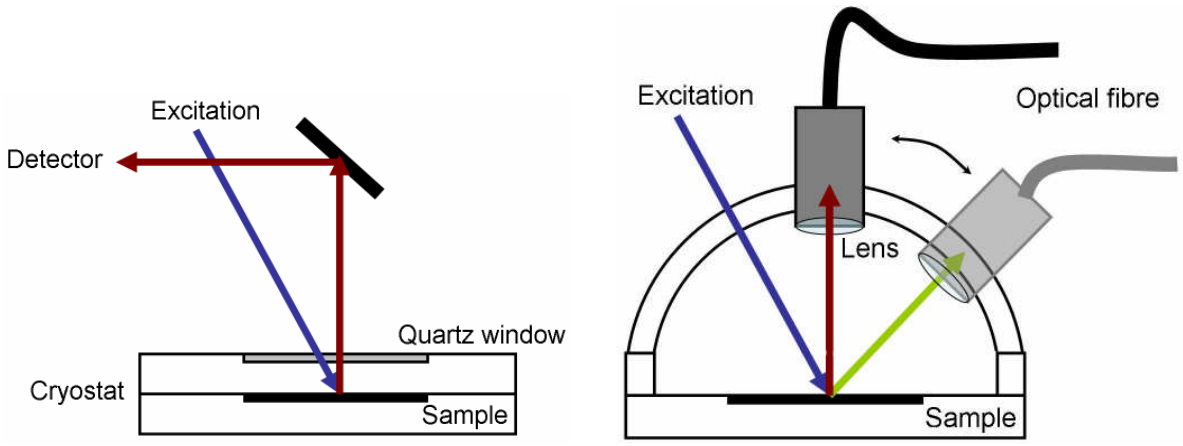

Figure 2.15: cw-PL setup (a) in the common configuration, detecting fluorescence along the surface normal; (b) with a fibre holder to detect angular resolved PL.

2.9.2 Time-resolved photoluminescence setup – lifetime measurements

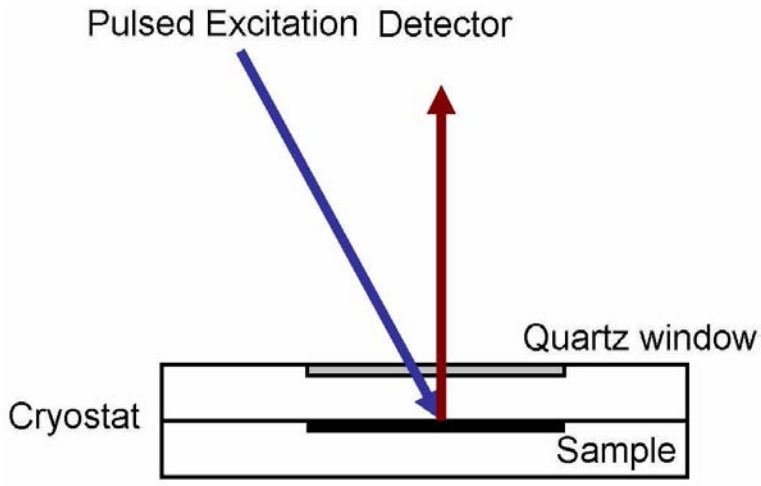

Figure 2.16: time-resolved PL setup

The second setup (see Figure 2.16) is equipped with a pulsed Nd:YAG laser as light source. Its third harmonic has a wavelength of 355 nm (3.49 eV), a mean intensity of 20mW/mm^2 at a repetition rate of 10 Hz and a mean pulse duration of 10 ns (manufacturer information). The laser illuminates the sample without focusing optics. The sample can be placed in a homebuilt liquid helium cryostat, to

record PL spectra at temperatures from 4K to room temperature. The fluorescence light is collected by a monochromator of the same type as the one at the first PL setup. The monochromator features two gratings with 600 lines/mm, one blazed at 500 nm (2.48 eV) the other at 1 μm (1.24 eV). The spectral range that can be covered by those gratings is 400 nm (3.1 eV) to 2 μm (0.62 eV). The detection system consists of a photomultiplier (PM). This setup is designed time-resolved measurements. The detection range is from 300 nm (4.13 eV) to 1.7 μm (0.73 eV). The bandwidth of the electronic components is about 1 GHz. This setup has also been carefully calibrated using a tungsten filament lamp. The measured spectra have been corrected for the response of the detector.

Chapter 3. Analysis of the silicon nanocrystals

3.1 Introduction

A lot of work has been realized to understand the optical properties of silicon nanocrystals. Already Canham [1] reported in the first paper about this luminescence, that the emission wavelength depends on the size of the silicon clusters in porous silicon. Kovalev *et al.* [80] reported in 1999 that the local confinement of electron-hole-pairs increases the probability of radiative recombination. Lifetime measurements as well as resonant excitation show nonetheless, that the emission occurs with involvement of phonons as the band-gap remains generally indirect even in nano-crystalline silicon. Pavesi and Ceschini [81] reported that the decay dynamics of silicon nanocrystals is very complex and leads to a stretched exponential decay of the intensity. They introduced the so called trap-controlled hopping of excitons to explain the interaction of adjacent nanocrystals. Belyakov *et al.* [82] attribute this stretched exponential decay and the lack of stable optical net gain to several different recombination possibilities that exist for the exciton. Amongst structural defects, that can create inter-band states and thus quench the photoluminescence, there is also a kind of dipole interaction that can take place directly between two adjacent nanocrystals.

Unfortunately, the analyzed samples contain nanocrystals of different sizes and it is difficult to link the characteristics of the photoluminescence spectrum and the size of the nanocrystals. The ideal would be to work with samples containing nanocrystals of a very fine size distribution or even to be able to analyze a single silicon nanocrystal. Different work has been done in this direction. For example, Zacharias *et al.* [83] developed the approach of subsequent deposition of alternating layers of SiO and SiO_2. This allowed for a remarkable reduction of the size distribution by the definition of an upper limit for the size of the nanocrystals compared to unstructured SiO layers. Nonetheless, they reported a surface density of silicon nanocrystals that is very high ($3 \cdot 10^{12}$ /cm^2) [84].

Most of the experiments realized with silicon nanocrystals have focused on investigations of large ensembles of silicon nanocrystals and very few experiments have been done on a single silicon nanocrystal. Such studies can give more precise information on spectral line-width of individual silicon nanocrystals. Isolating a single silicon quantum-dot could also give the possibility of realizing a source of single photons for quantum communication [85].

An original method for spatially localizing silicon nanocrystals is to implant silicon through stencil mask before annealing [38]. This technique has offered the possibility of observing a blueshift of the photoluminescence signal near the edge of the pattern where the smallest crystals are situated [37]. Another way was to apply sequential wet-etching/ oxidizing processes on silicon micropillars [31, 33]. Such processes led to the formation of one silicon nanostructure at the top of each pillar. The advantage of such a technique is the obtention of a regular arrangement of individual nanostructures easily locatable for spectroscopic analysis. The photoluminescence analysis of this kind of nanostructure has revealed sharp photoluminescence [86] and electroluminescence [35] peaks.

In order to determine precisely the optical properties of the nanocrystals, we tried in this work to investigate populations of silicon nanocrystals with the finest size distribution that is possible. This can be realized by working with the multilayer approach – finally even reduced to one single active layer – but in the same time working with a weak sub-stoichiometry and thus a low number of silicon nanocrystals. Afterwards, micro- and nanotechnologies were employed to select working zones of a reduced surface. This chapter will present the different possibilities.

Indeed, the group already owns a great competence in the fabrication of SiO/SiO_2 multilayers which – after annealing in a conventional furnace – lead to layers of silicon nanocrystals. In the beginning of the actual study, the annealing procedure of the samples was changed. The aim of the **first part** is to report on the improvements of the annealing procedure in order to be able to anneal samples in a reproducible way, amongst others by programming heating ramps, testing the properties of vacuum and controlled atmosphere.

In a **second part**, we analyze SiO_x thin film and SiO_x/SiO_2 multilayer samples (x>1) elaborated by co-deposition of SiO and SiO_2. The aim of this study is to reduce the surface density of silicon nanocrystals by reducing the silicon excess in the layer.

The SiO_x thin films have been analyzed by means of infrared absorption (FTIR) and photoluminescence as well as Raman spectroscopy. The results show a precipitation of the excess silicon for low annealing temperatures and crystallization for very high annealing temperatures. The results, that we obtained, are in good agreement with literature.

In a **third part** the common technique of multilayer structure by subsequent evaporation of different materials is applied. The aim is to reduce the large size distribution which has been determined by Raman spectroscopy. Photoluminescence and Raman spectroscopy were employed to analyze those SiO_x/SiO_2 multilayers (x = 1; 1.25; 1.5; 1.75). The surface density was directly determined by means of energy filtered transmission electron microscopy (EFTEM) on a single thin layer of SiO_x embedded between two SiO_2 layers. Photoluminescence and EFTEM results have been compared. Finally, in order to further reduce the number of analyzed grains, we employed electron beam lithography to realize apertures of very small surface through which we analyzed the photoluminescence properties of the multilayers and trilayers.

Overview of the samples that are analyzed in this chapter

Classical thin films of SiO_x

Samples Code	**SiO_x**
423	x = 1
---	x = 1.25
421	x = 1.5
---	x = 1.75

Multilayered samples of SiO_x/SiO_2

Samples Code	**SiO_x**
426	x = 1
432	x = 1.28
422	x = 1.5
433	x = 1.75

Tri-layers for EFTEM

Samples Code	**SiO_x**

401A2	$x = 1$
448A1	$x = 1.28$
447A1	$x = 1.5$
449A1	$x = 1.75$

3.2 Preliminary investigations on SiO_x thin films

It is possible to obtain SiO_x ($1 \leq x < 2$) thin films with different compositions of silicon and oxygen. Such films have been elaborated by reactive evaporation of silicon under oxygen atmosphere by Rinnert *et al.* [87]. Kahler and Hofmeister [88] have fabricated silicon nanocrystals in SiO_x thin films by reactive evaporation of SiO powder under different oxygen pressures. Wora-Adeola [89] proposed an elaboration by co-evaporation of silicon and SiO_2. As we are interested in low silicon excess in this study, we chose the co-evaporation of SiO and SiO_2.

The different oxygen concentrations are realized by adjusting the ratio between the deposition rates of the two sources, respectively. The nominal stoichiometry factors for the two series presented here are equal to 1 and 1.5, respectively.

3.2.1 Infrared absorption spectroscopy

The SiO_x films that have been prepared by co-evaporation of SiO and SiO_2 could have an inhomogeneous internal structure. For a given x, the SiO_x film could show very different microscopic compositions. It could be homogeneous or it could be a mixture of zones consisting of SiO included in SiO_2 or vice versa, depending on the overall stoichiometry factor x. This overall factor x, which represents the ratio of the number of oxygen atoms and the number of silicon atoms, can be measured by energy dispersive X-ray spectroscopy (EDXS). In the case of co-evaporation of Si and SiO, it has been shown that the overall composition of a SiO_x film remains constant, i.e. that there is no oxidation of the sample during the annealing process, whereas the composition of the matrix may change because of the decomposition reaction

$$2\ SiO \rightarrow Si + SiO_2, \tag{3-1}$$

that occurs in the film during the high temperature annealing [90]. In fact, we have during annealing the reaction

$$SiO_x \rightarrow \frac{x}{x+y} SiO_{x+y} + \left(1 - \frac{x}{x+y}\right) Si \tag{3-2}$$

with y less than x. When the reaction is completed, x+y will be equal to 2.

As the infrared absorption spectroscopy is a technique which is sensitive to the vibration modes of the atomic bounding, it allows us to analyze the evolution of the decomposition of the matrix. The analysis is based on the determination of the vibration modes of the Si-O-Si bonds. For orientation, we

give the literature values for the different vibration wave-numbers of amorphous SiO_2 in the following table:

	Pai [91]	Lin [92]	Song [93]
Rocking	465	450	460
Symmetric stretching	800	800 766-840 (calculated)	805
Assymmetric stretching (in phase)	1075	1080	1070
Assymmetric stretching (anti-phase)	1150	1175-1218 (calculated)	1100-1200

Table 3.1: Vibration frequencies of a- SiO_2 in cm^{-1}

Typically, the absorption band around 1080 cm^{-1} is used to analyse a changing of the composition of the matrix SiO_y because the frequency ν of this mode is shifted to the higher frequencies as a linear function of *y*, according to the work of Pai *et al.* [91]. In our group, such a relation was determined using SiO and SiO_2 reference samples:

$$y = (\nu - 918)/81. \qquad (3\text{-}3)$$

The difference between the values obtained by this formula and those obtained by the formula proposed by Pai *et al.* is lower than 3%.

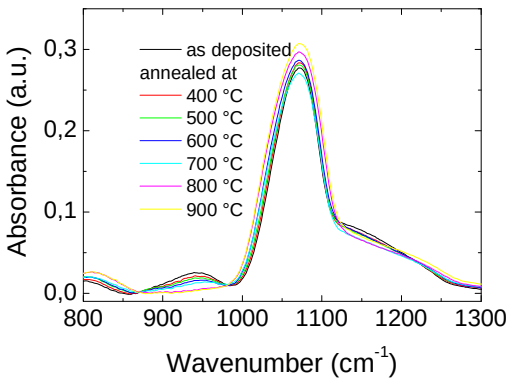

(a)

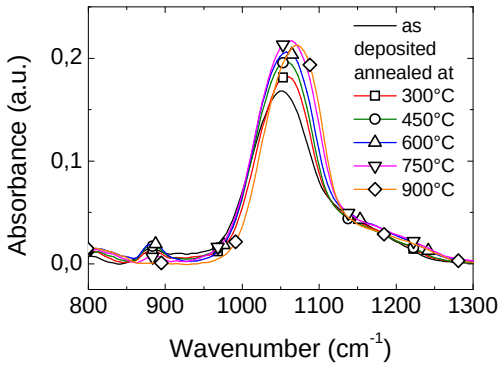

(b)

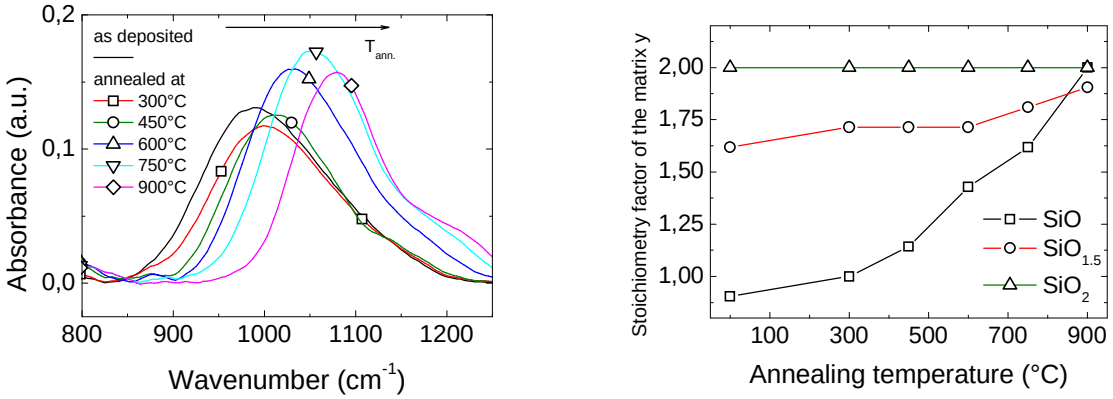

(c) *(d)*

Figure 3.1: Infrared absorption properties of thin SiO_x films; absorption spectra of (a) SiO_2; (b) $SiO_{1.5}$; (c) SiO; (d) evolution of the stoichiometry factor of the matrix as a function of the annealing temperature for the three thin films

Figure 3.1 (a, b and c) show the evolution of the asymmetric stretching of the Si-O-Si group in SiO_2, $SiO_{1.5}$ and SiO films as a function of the annealing temperature, respectively. The results concerning the FTIR results of SiO_2 are taken from ref. [89]. For the SiO_2 film, the peak presents a maximum at 1080 cm^{-1}, which corresponds to y equal to 2. As expected, this peak does not shift for the SiO_2 film because the SiO_2 film is stable with temperature. On the contrary, a clear displacement of the asymmetric stretching peak is observed for the sub-stoichiometric SiO and $SiO_{1.5}$ alloys.

Figure 3.1 (d) summarizes the shift of the stoichiometry factor y of the matrix as a function of the annealing temperature for the SiO and $SiO_{1.5}$ alloys. For the SiO film, y shifts clearly to higher values with the annealing temperature. It shifts from 0.9 in the as-deposited state to 2 when the film is annealed at 900°C. This is an indication that the film tends to dissociation into the two thermodynamically stable components Si and SiO_2. Remember that the Si-Si bonds are homopolar and thus not detectable by FTIR. The dissociation process is practically not visible at 300°C, but it is clearly observed with the 450°C anneal. On the contrary, the matrix of the as-deposited $SiO_{1,5}$ film is already closer to the stoichiometry of a pure SiO_2 film. It shifts only from 1.62 to 1.9 with the annealing temperature and the displacement is well visible only after the 750°C anneal.

In addition to the absorption bands related to the Si-O-Si bonds, there exists an additional absorption band, which is due to structural defects in the as-deposited sample. This band is situated at 945 cm^{-1}. It is supposed to disappear with the annealing. In fact, all samples show this band as can be seen on figure 3.1 (a) - (c). In general, it is much less intense than the asymmetric stretching band. For all the three compositions, the defect-related band disappears for an annealing temperature of 900°C.

In summary, the infrared absorption properties of the SiO_x thin films made by co-evaporation of SiO and SiO_2 have been analyzed. The asymmetric stretching absorption band of Si-O-Si bonds in the films was used to determine the stoichiometry of the matrix. It was found that the stoichiometry factor y evolutes as a function of annealing temperature for both analyzed compositions. For the silicon-rich composition (SiO), it evolutes steadily from 0.9 to 2 with increasing annealing temperature. This is a

sign of the low thermal stability of SiO. At high temperatures, the SiO tends to separate into the two thermodynamically stable components Si and SiO_2. For the oxygen rich composition ($SiO_{1.5}$), y shifts from 1.62 to 1.9. The shift is remarkable only for relatively high annealing temperatures. This is an indication that evidently, the matrix of the as deposited thin film is already closer to the thermodynamically stable SiO_2. Nonetheless, the incomplete shift to y = 2 with the annealing temperature up to 900°C indicates that the remaining silicon access is still disturbing the structure. Thus, we can conclude that the demixion reaction is not yet completed.

3.2.2 Photoluminescence spectroscopy of SiO and $SiO_{1.5}$ thin films

Whilst the reorganization of SiO and $SiO_{1.5}$ to SiO_2 is well observable employing FTIR absorption spectroscopy, it is rather difficult to clearly analyze single structures which are created during the dissociation. Photoluminescence spectroscopy is a very sensitive characterization tool, which allows us to analyze the creation of defect structures and amorphous or crystalline nanoparticles inside the matrix. The following analysis is thus a complement of the upper FTIR spectroscopy, in order to conclude more precisely on the reorganization process of the SiO_x thin films.

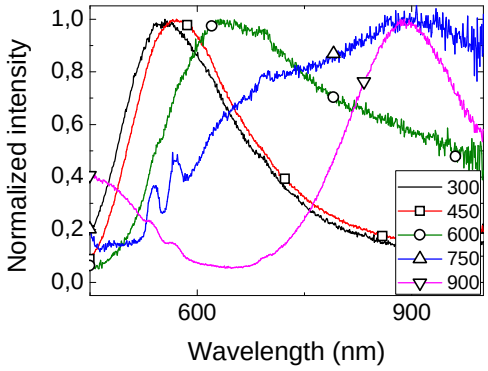

(a)

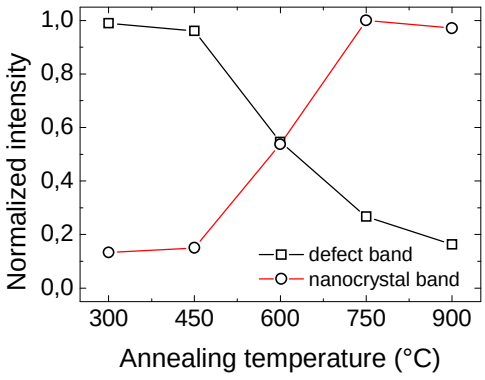

(b)

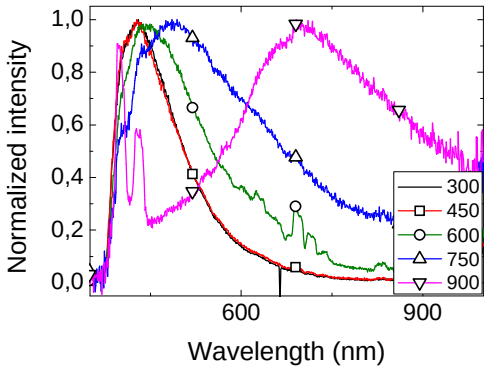

(c)

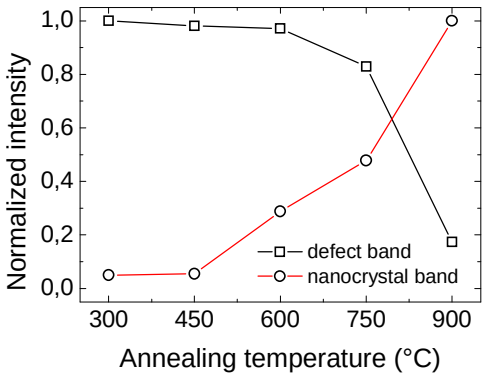

(d)

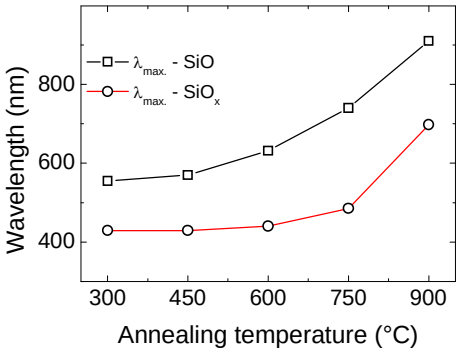

(e)

Figure 3.2: photoluminescence properties of SiO and $SiO_{1.5}$ thin film excited with the 313 nm line of a Hg vapour lamp. (a) normalized photoluminescence spectra of SiO films; (b) normalized intensity of defect-related (550 nm) vs. nanocrystal-related (900 nm) photoluminescence as a function of annealing temperature for the SiO film;(c) normalized photoluminescence spectra of $SiO_{1.5}$ thin films; (d) normalized intensity of defect- related (430 nm) vs. nanocrystal-related (700 nm) photoluminescence as a function of annealing temperature for the $SiO_{1.5}$ film; (e) emission wavelength of maximum photoluminescence intensity for the two films as a function of annealing temperature.

Figure 3.2 reports the photoluminescence properties of thin SiO and $SiO_{1.5}$ films. Figure 3.2 (a) shows the normalized photoluminescence spectra of SiO thin films for the different annealing temperatures. The SiO thin film shows an intense and broad emission band at around 550 nm for low annealing temperatures. In literature, this emission band is attributed to a dangling bond due to a silicon vacancy in the Si-O-Si group [94, 95, 96, 97]. This defect is also known as non-bridging oxygen hole centre (NBOHC). From the spectra of the samples annealed at 600°C and 750°C, respectively, one can see that there is a second photoluminescence band appearing only for annealing temperatures exceeding 600°C. The defect-related band finally disappears completely for an annealing temperature of 900°C. Figure 3.2 (b) resumes the evolution of the intensity of the two photoluminescence bands as a function of the annealing temperature. It is clearly visible that, for low annealing temperatures, there is an intense defect-related photoluminescence, which is reduced with increasing annealing temperature. This is an indication for the structural reorganization, which leads to a reduced number of dangling bonds in the matrix and thus a reduced photoluminescence intensity of this band. This observation is well in correspondence to the evolution of the stoichiometry factor of the matrix, which is shown in figure 3.1 (d). On the other hand, a new photoluminescence band appears at longer wavelengths for high annealing temperatures. In literature, it is attributed to either amorphous silicon nanoparticles [98, 99, 100, 101, 102] or silicon nanocrystals [1, 80, 103, 104]. This band has no correspondence in FTIR measurements, as the homopolar Si-Si bonds in the silicon nanocrystals do not interact with infrared radiation.

Figure 3.2 (c) reports the normalized photoluminescence spectra of $SiO_{1.5}$ thin films annealed at temperatures ranging from 300°C to 900°C. The films show an intense and large photoluminescence band at around 430 nm for low annealing temperatures. As in the case of the SiO films, this emission could be related to defects in the matrix. In literature, there are some works that report a photoluminescence emission from self trapped excitons in the SiO_2 lattice in this spectral range [95, 105, 106]. Like in the case of SiO, a second photoluminescence band appears at longer wavelengths

for higher annealing temperatures. However, the intensity of the defect- or self-trapped-exciton-related photoluminescence band is reduced for higher annealing temperatures with respect to the SiO film. Equally, the intensity of the silicon nanoparticles related band is increased for higher annealing temperatures than in the SiO film (see figure 3.2 (d)).

Finally, if we consider only the wavelength of the maximum of the photoluminescence, it seems that the emission wavelength as a function of the annealing temperature is always shorter for the $SiO_{1.5}$ thin film than for the SiO film (see figure 3.2 (e)). For the emission band at lower wavelengths, this could be due to different nature of this band in the two considered films. Otherwise, it could be possible that the different oxygen concentrations in the two films lead to changed energy levels of the defects. Thus, the emission could originate from the same process, but could be of different wavelength as a consequence of the different oxygen concentrations. For the emission band at longer wavelengths, this could be interpreted as an indication that the diffusion of silicon atoms which is primordial to the formation of silicon nanocrystals is less efficient for $SiO_{1.5}$ than for SiO at the same annealing temperature.

All those observations are consistent with the FTIR analysis, reported in the section above. The reduction of the photoluminescence band of the dangling bonds with increasing annealing temperature coincides with the shift of the infrared absorption maximum towards the absorption maximum of the asymmetric stretching vibration mode of a SiO_2 thin film.

In summary, we analyzed SiO and $SiO_{1.5}$ thin films by means of photoluminescence spectroscopy. We found that the photoluminescence of these thin films is originating from different luminescence centres in the films depending on the annealing temperatures. For low annealing temperatures, generally, the photoluminescence is induced by structural defects or self-trapped excitons in the SiO_2 matrix. For the highest annealing temperatures, the photoluminescence is due to quantum confinement in silicon nanoparticles in the SiO_2 matrix. The results of photoluminescence are coherent with the results of FTIR experiments performed on the same samples. The disappearing of the defect-related photoluminescence band coincides with the trend of the stoichiometry factor of the matrix $y \rightarrow 2$.

3.2.3 Photoluminescence and Raman modelization of the experimental spectra

A detailed characterization of the optical properties and a study of the particle size and of the crystalline or amorphous state of the silicon aggregates have been performed. Both photoluminescence spectroscopy and Raman spectroscopy were employed. The results are reported in Miska *et al.* [107]. The following section will present the model that we used. After this, our results are resumed.

Raman scattering experiments: Raman scattering spectra were acquired on a spectrometer equipped with a liquid N_2 cooled CCD detector. The laser wavelength was the 488 nm emission line of an Ar^+ laser. A confocal microscope was used and the laser was focused on the sample by a ×50 objective (numerical aperture of 0.55). The laser irradiance was kept low (<1 kW cm^{-2}) to avoid any heating effect. This was verified by checking the phonon mode at 522.5 cm^{-1} of the bulk silicon substrate after a quite long period of laser irradiation (1 hour). Note that the absolute position of the

bulk silicon phonon mode depends from the absolute calibration of the spectrometer and the temperature of the sample. It is common to use the emission line of mercury (from neon lamp) to perform a calibration of the spectrometer in absolute wavenumbers. However, using a blue laser at 488 nm, the spectral position of the mercury line and the spectral position of the phonon mode of bulk silicon are greater than the range of wavenumbers authorized by the high resolution grating at 1800 lines/mm. Therefore, it is necessary to move the grating after absolute calibration to retrive the silicon spectrum, which always induces a wavenumber shift of 0.1-0.3 cm^{-1}. We thus have chosen to calibrate the relative wavenumber by imposing the bulk silicon mode at 522.5 cm^{-1} to avoid any spectral drift. The entrance slit of the spectrometer was fixed at 40 µm to obtain the best spectral resolution, i.e. 1.2 cm^{-1}. This enabled us to measure the spectral full width at half maximum (FWHM) of the bulk silicon phonon at 522.5 cm^{-1} at 300 K, which was 3 cm^{-1}.The samples were analyzed at several locations and the results were always consistent for a given sample. It is interesting to note that the laser line at 488 nm enabled us to record a resonant Raman spectrum for nanocrystalline silicon, whereas the 514 nm laser line available on the argon laser only revealed the phonon modes of the silicon substrate. This fact agrees with a higher band gap of nanocrystalline silicon compared to bulk Si (see below).

Confinement model for luminescence and Raman spectra: Following the approach developed by Meiers *et al.* [108], the photoluminescence emission properties of the silicon nanocrystals sample was modeled as the sum of individual contributions of particles of diameter ϕ, which was assumed to follow a log-normal distribution law. The photoluminescence emission intensity $I_{PL}^{np}(h\nu,\phi)$ of one particle of diameter ϕ ,is given by a Gaussian function according to:

$$I_{PL}^{np}(h\nu,\phi)=\frac{1}{\Delta E\sqrt{2\pi}}\exp\left(-\frac{\left[h\nu-E_g(\phi)\right]^2}{4\Delta E^2}\right) \tag{3-4}$$

In this equation, ΔE is the spectral bandwidth of the emission band, ν the frequency, $E_g(\phi)$ the energy band gap for the silicon nanocrystal. The later is supposed to follow the experimental relationship reported by Delerue *et al.* [109]:

$$E_g(\phi)=E_0(Si\ \text{bulk})+\frac{3.73}{\phi^{1.39}} \tag{3-5}$$

where E_0 is the indirect band-gap of bulk Si (1.17 eV) and ϕ the silicon nanocrystal diameter in nm. The probability to have a silicon nanocrystal of diameter ϕ is modeled using a log-normal distribution law [109]:

$$\mathrm{p}(\phi,\phi_0,\sigma)=\frac{1}{\sqrt{2\pi}}\frac{1}{\phi\times\mathrm{Ln}(\sigma)}\exp\left(-\frac{1}{2}\left(\frac{\mathrm{Ln}\left(\frac{\phi}{\phi_0}\right)}{\mathrm{Ln}(\sigma)}\right)^2\right) \tag{3-6}$$

where ϕ_0 is the average diameter and σ is the width of the diameter distribution ($\ln(\sigma)$ being the width of the log-normal distribution). Then, the total photoluminescence spectrum can be given by:

$$I_{PL}^{tot} = \int_{\phi=0}^{\infty} f_{osc}(\phi).p(\phi,\phi_0,\sigma).I_{PL}^{np}(h\nu,\phi).d\phi \tag{3-7}$$

with the oscillator strength given by [109]:

$$f_{osc}(\phi) = 1.4\times10^{-6} + 1.7\times10^{-6}\exp\left(\frac{11.24}{\phi^{1.39}}\right) \tag{3-8}$$

This model can be adjusted to experimental data by fitting the three parameters ΔE, ϕ_0 and σ.

The Raman scattering spectra were also adjusted by a phenomenological model based on the quantum confinement effect and recently published by Faraci *et al.* [110]. These authors have proposed a new confinement function for modeling the Raman spectrum of a particle with a given diameter ϕ. We have extended this model by including the distribution in diameter of the silicon nanocrystals, and using the same log-normal statistical law given in equation (3-6). In the confinement model, the Raman spectrum is calculated by equation (3-12) that uses the confinement coefficient $C(\mathbf{q},\phi)$, $\boldsymbol{q}$ being the reciprocal phonon wave vector that can explore the entire first Brillouin zone of the crystal due to the confinement effect.

$$I_{Raman}(\omega) \propto \left[n(\omega)+1\right]\int_{BZ} C(\mathbf{q},\phi)^2 L(\omega,\mathbf{q}) d^3\mathbf{q} \tag{3-9}$$

Here, ω is the Raman wavenumber, $n(\omega) + 1$ is the statistical Bose-Einstein factor for phonons, $C(\mathbf{q},\phi)$ is the confinement coefficient, calculated by the Fourier transform of the spatial function used to confine the phonon wave function inside the particle of diameter ϕ. $L(\omega,\mathbf{q})$ is the Lorentzian function coming from the oscillating dipole model. For a particle with a diameter ϕ, the possible wave vectors are quantified and given by:

$$k_n = n\pi/\phi \tag{3-10}$$

with n being even for the TO phonon mode of Si : $n = 2, 4, ..., n_{max}$, n_{max} being equal to the nearest integer lower or equal to $2\phi/a$, and $a = 0.543$ nm being the Si lattice parameter.

In their model, Faraci *et al.* choose a sum of sinus cardinal functions to model the confinement effect. This leads to the following expression of $C(\mathbf{q},\phi)$:

$$C_n(\mathbf{q},\phi) = 3\frac{\sin(q\phi/2)}{\pi^3\phi^3 q(k_n^2 - q^2)} \tag{3-11}$$

The Raman spectrum for a particle of diameter ϕ is then given by :

$$I_{Raman}(\omega,\phi) \propto \sum_n \int_{(n\pi-1)/\phi}^{(n\pi+1)/\phi} \frac{C_n^2(\mathbf{q},\phi)}{\left[\omega-\omega'(\mathbf{q})\right]^2 + (\Gamma/2)^2} d\mathbf{q} \tag{3-12}$$

with Γ the natural bandwidth, typically fixed to 3 cm^{-1}, and the dispersion curve for the TO phonon modes of silicon is that of bulk Si [117]:

$$\left[\omega'(\mathbf{q})\right]^2 = A + B\cos(a\mathbf{q}/4) \tag{3-13}$$

With $A = 1.714 \times 10^5 cm^{-2}$ and $B = 1.00 \times 10^5 cm^{-2}$.

The Raman spectrum for a distribution of silicon nanocrystals having a diameter ϕ and following the distribution law of equation (3-6) is then simply given by the relation:

$$I_{Raman}(\omega) = \int_{d=0}^{\infty} p(\phi, \phi_0, \sigma).I(\omega, \phi)d\phi \qquad (3\text{-}14)$$

In summary, the optical and vibrational properties of silicon nanocrystals were studied in a SiO thin film elaborated by evaporation. The thin film has been deposited on intrinsic silicon wafers. The photoluminescence and Raman spectra were fitted by phenomenological exciton and phonon confinement models. The coherence between the two models and experimental data is demonstrated and gives support to the notion of exciton and phonon confinement effect in silicon nanocrystals embedded in silica matrix.

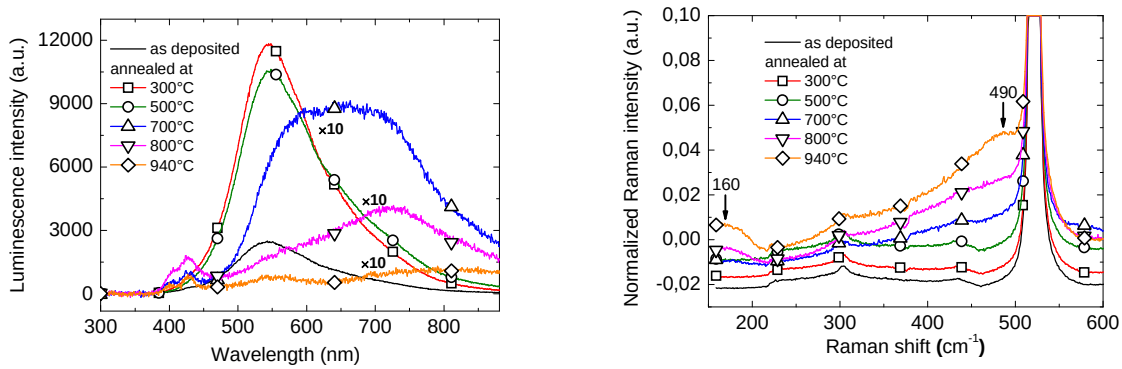

(a) *(b)*

Figure 3.3: (a) luminescence spectra of 200 nm thick SiO samples (monolayer) annealed at different temperatures and (b) Raman scattering spectra of the samples annealed at different temperatures.

Photoluminescence spectra of the monolayer samples annealed at different annealing temperatures T_a are reported in Fig. 3.3 (a). For T_a below 600°C, the photoluminescence band, visible at around 540 nm (2.3 eV), has been attributed to pure SiO [111] and may correspond to the luminescence of the defects in this material. For higher temperatures, this band disappears and a new band appears at higher wavelengths. With annealing, this band shifts towards higher wavelength and considerably broadens. In this system, the demixion process yields the formation of amorphous silicon nanoclusters *via* silicon atoms diffusion. Then, in the absence of any thermal diffusion barrier, large silicon structures are formed by diffusion and coalescence of silicon atoms. Then, the higher T_a is, the bigger the aggregates are, and the wider is the size distribution of these particles within the 200 nm thickness of the SiO layer. Consequently, due to coalescence phenomenon, the quantum confinement is less efficient, which explains the decrease and the red shift of the maximum of the luminescence intensity with high-temperature annealing. The photoluminescence disappears before the crystallization of silicon.

The corresponding Raman spectra for all these samples are reported in Fig. 3.3 (b). With increasing T_a, two Raman bands at around 490 and 160 cm^{-1} are growing up, indicating the formation of amorphous silicon within the SiO layer. Figure 3.4 shows the difference spectrum between the monolayer sample annealed at 940°C and the as-deposited sample. The structure of the resulting band has been spectrally decomposed using four Gaussian functions. The band at 479 cm^{-1} is characteristic of the TO phonon modes of amorphous Si clusters, whereas those at 415 and 333 cm^{-1} are respectively the LO and LA phonon modes of these amorphous structures. The band at 495.8 cm^{-1} could be attributed to either the D1 defect band of the SiO_2 phase formed by the demixion process or a TO-LO splitting at the L point of the first Brillouin zone of amorphous silicon clusters. No clear signal for Si nanocrystals is obtained by this spectral subtraction procedure since the annealing temperatures are too low to obtain crystallization or, if the crystallization occurs, the silicon crystals have dimensions much larger than few nanometers. These experiments show that it is necessary to better control the size of the silicon aggregates till the crystallization, which can be obtained with multilayered structures.

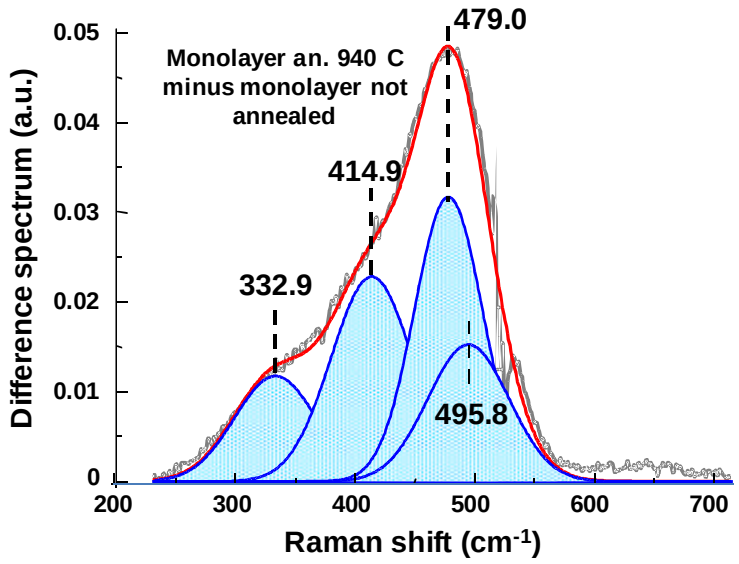

Figure 3.4: Spectral decomposition by Gaussian functions of the difference spectrum obtained by subtracting the spectrum of the as deposited monolayer to the spectrum of the monolayer annealed at 940°C.

3.3 Formation of the silicon nanocrystals in the SiO_x/SiO_2 multi-layers by RTA annealing

First annealing tests showed that it is impossible to work under vacuum conditions at high temperatures because the silicon substrates degas and pollute the furnace chamber as well as the observation window of the pyrometer that controls the temperature of the rapid thermal annealing (RTA) furnace. Thus, the temperature of the substrate holder would not be correctly detected.

In order to understand the differences between the annealing regimes, figure 3.5 reports the photoluminescence properties of a SiO/SiO_2 multilayer sample that has been annealed under different conditions (primary vacuum, secondary vacuum and N_2 gas flux at atmospheric pressure). The

thicknesses of the SiO and SiO_2 layers are equal to 3 and 5 nm, respectively. The number of SiO/SiO_2 bilayers is equal to 22.

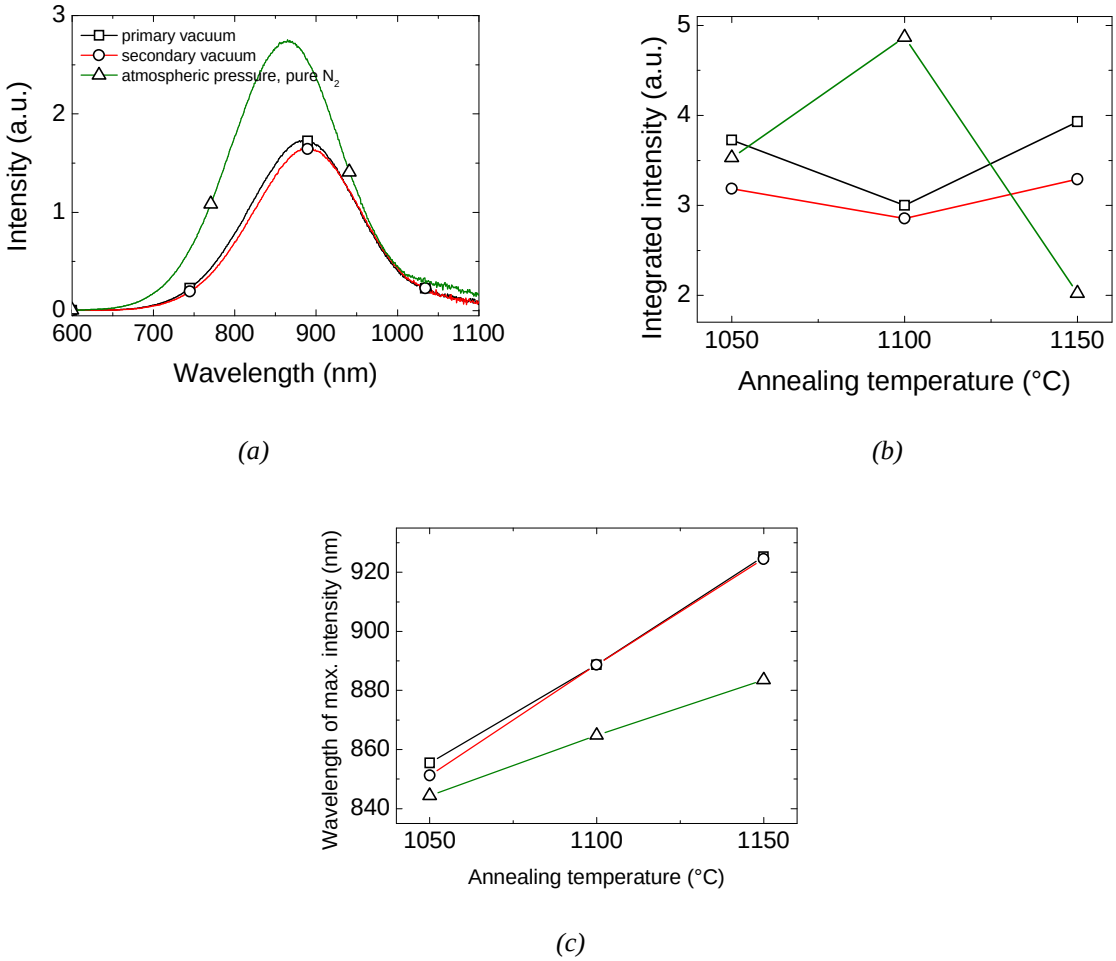

Figure 3.5: Influence of the different annealing parameters on the photoluminescence properties of multilayered SiO/SiO_2 samples.

Figure 3.5 (a) shows the photoluminescence spectra after an annealing at 1100°C for the three different pressure regimes: primary and secondary vacuum as well as a controlled nitrogen atmosphere at full atmospheric pressure, respectively. Figure 3.5 (b) reports the integrated intensity as a function of the annealing temperature. The most intense luminescence is produced from a sample annealed in nitrogen atmosphere at 1100°C. Figure 3.5 (c) shows the wavelength of the maximum photoluminescence intensity as a function of the annealing temperature. The rise of the emission wavelength can be interpreted as a growth of the silicon nanocrystals. In general, the growth of the crystals seems to be nearly the same for both primary and secondary vacuum. The nanocrystals that are created under the same temperatures and in a nitrogen flux at ambient pressure seem to be smaller compared to the nanocrystals created in vacuum, respectively. This is maybe due to the fact that the annealing is less efficient because of thermal loss by conduction or convection through the gaseous atmosphere.

3.3.1 Photoluminescence and Raman models for multilayered samples

Figure 3.6 reports the photoluminescence spectra of the multilayered samples annealed at different temperatures T_a. For T_a below 850°C, no significant phenomenon occurs. A large photoluminescence peak, centered at around 570 nm, corresponds to the defects in silica previously observed for the monolayer sample. For T_a = 950 and 1050 °C, the luminescence peak at 570 nm is strongly reduced and large peaks centered at 844 and 848 nm, respectively, can be observed.

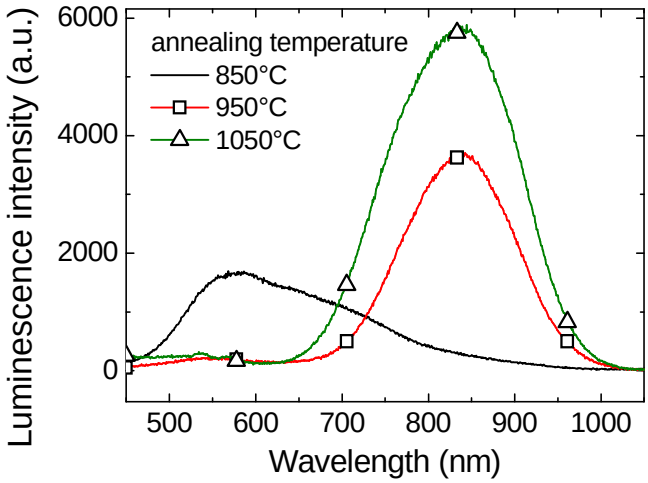

Figure 3.6: Photoluminescence spectra of the multilayer sample annealed at three different temperatures.

These signals may correspond to the luminescence of silicon nanocrystals [112] and may be the sign of a quantum confinement of excitons in the silicon nanostructures. The FWHM of the multilayer photoluminescence peak, ~ 150 nm for the sample annealed at 950°C, is smaller than the one of the monolayer sample, ~ 280 nm for the sample annealed at 800°C. This observation validates the multilayers approach to obtain both a narrower size distribution of the silicon nanocrystals and a final structure (matrix + nanocrystals) with fewer defects. The photoluminescence peak of the sample annealed at 950°C is symmetric, but the one of the sample annealed at 1050°C lets appear a shoulder at around 750 nm. This band has been attributed in the literature to Si=O bonds. Pavesi *et al.* [113] reported a photoluminescence signal at 850 nm that they attributed to Si=O bonds located at the surface of the silicon nanocrystals prepared by ion implantation and successive thermal annealing. Han *et al.* [114] reported photoluminescence spectra of intermediate phase silicon structure realized by annealing a-Si/SiO_2 multilayers and showing the same shape of photoluminescence spectra as ours. In this system, they attributed the two peaks to Si=O bonds and to non-bridging oxygen holes centers. In our case, in order to clarify the origin of the photoluminescence peaks, we analyzed the multilayer samples annealed at 950 and 1050°C as a function of temperature. Spectra obtained at 300 and 77 K for both samples are reported in figure 3.7.

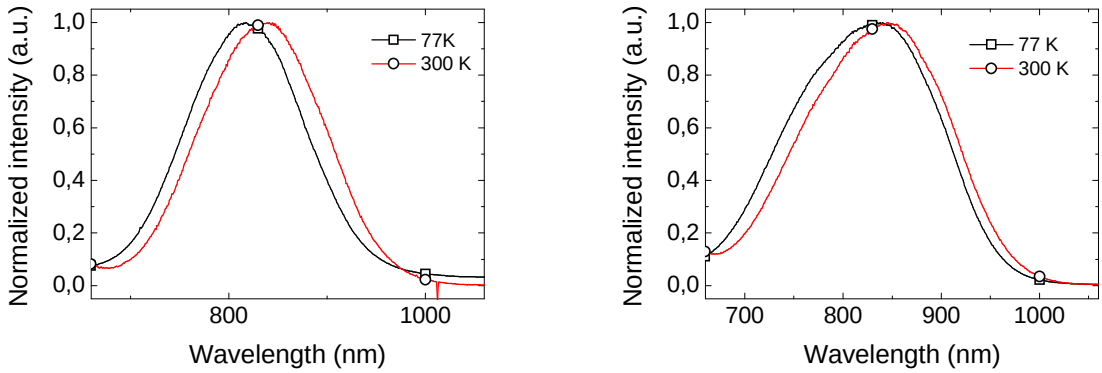

(a) *(b)*

Figure 3.7: photoluminescence spectra of silicon nanocrystals obtained after annealing at (a) 950 and (b) 1050 °C for two analysis temperatures equal to 77 (liquid nitrogen) and 300 K (ambient temperature), respectively.

The shape of the photoluminescence peak of the sample annealed at 950°C does not change with the analysis temperature. The spectrum is simply blue-shifted with decreasing temperature. For the sample annealed at 1050°C, the spectrum is also blue-shifted with decreasing temperature, but the shoulder located at 750 nm is still visible and seems to be more prominent. As a consequence, this peak, which doen't shift with temperature, can be attributed to defects in the structure.

The verification of the origin of the main photoluminescence peaks centred at 844 and 848 nm has been done by analyzing the position of the luminescence maximum of the samples with temperature.

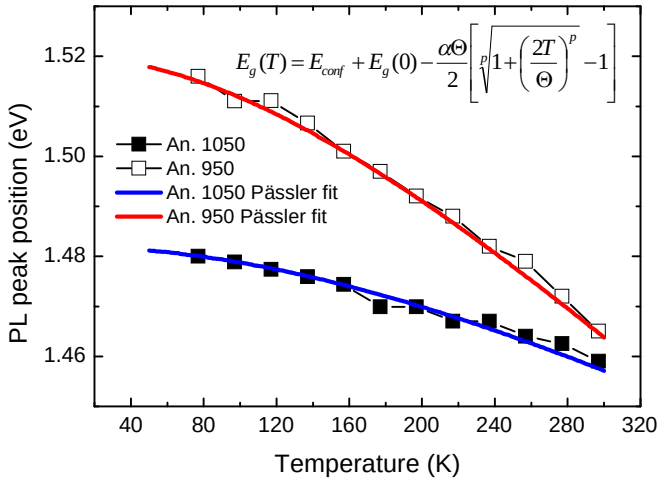

Figure 3.8: Evolution of the energy of the maximum photoluminescence emission as a function of the analysis temperature for multilayer samples annealed at 950 and 1050 °C. The experimental points are fitted using the Pässler's law in equation (3-15).

Figure 3.8 reports the energy of this maximum for two multilayered samples versus the analysis temperature. Both samples show the same trend, i.e. a decrease of the maximum emission energy with an increase of the sample temperature. The sample annealed at 950°C gives the strongest variation with temperature. Pässler *et al.* [115] have modelled the effect of temperature on the band gap energy of bulk semiconductors, and this equation can be applied to luminescent nanocrystals using the following equation:

$$E_{PL}(T) = E_{conf} + E_g(0) - \frac{\alpha\Theta}{2}\left[\sqrt[p]{1+\left(\frac{2T}{\Theta}\right)^p} - 1\right] \qquad (3\text{-}15)$$

In this equation, $E_g(0)$ is the gap energy of bulk silicon at 0 K (1.17 eV), E_{conf} is the confinement energy in eV, α is a parameter that represents the slope of the curve at $T \to \infty$, $\Theta(\equiv \hbar\omega/k)$ is related to the average phonon temperature in the material and p is an exponent parameter (between 2 and 3). The two experimental sets of data of figure 3.8 have been successfully fitted by this equation. Table 3.2 reports the corresponding values of $E_{conf.}$, α, $\frac{\Theta}{2}$ and *p*. The values found for α, $\frac{\Theta}{2}$ and *p* are close to the ones reported in the literature for bulk silicon [116].

Annealing temperature (°C)	E_{conf} (eV)	$E_g(0)$ (eV)	α (meV.K^{-1})	$\Theta/2$ (K)	p
950	0.35	1.17	0.35	200	2
1050	0.312	1.17	0.2	300	2

Table 3.2: Values of the fitting parameters by equation (3-15) of the PL data of Figure 3.8 for the samples annealed at 950 and 1050°.

The fact that the energy of the maximum photoluminescence peak of the multilayer samples can be modelled by equation (3-15) confirms the presence of silicon nanocrystals in the samples. We can say that the main photoluminescence peak at around 844-848 nm originates from exciton recombination in silicon nanocrystals. We also observe that the confinement energy is a little bit higher for the sample annealed at 950°C. This can be explained by the fact that silicon nanocrystals have an average diameter slightly smaller for T_a = 950°C, while for T_a = 1050°C, the segregation process could be more complete and yield bigger nanostructures.

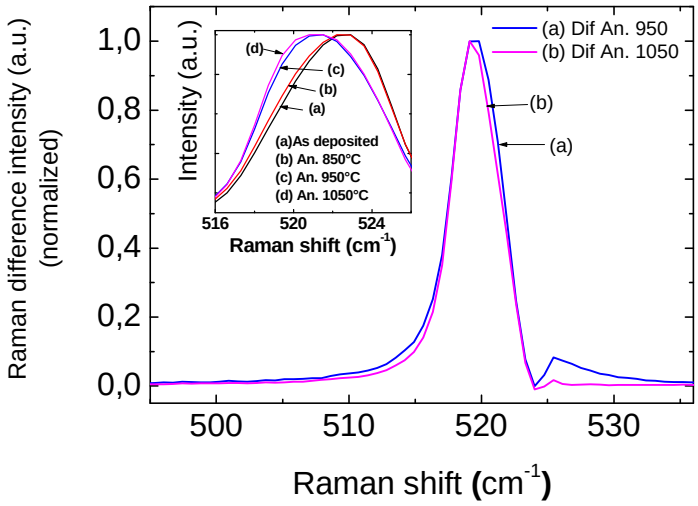

Figure 3.9: Raman scattering difference spectra of the multilayer samples corresponding to the difference between annealed and unannealed samples. The original Raman peaks are plotted in the insert as a function of the annealing temperature.

The corresponding Raman scattering spectra of the multilayer samples are reported as an inset in figure 3.9. An intense phonon peak around 520 cm^{-1} assigned to crystalline silicon Raman mode is clearly observed. It corresponds to the superposition of the phonon mode of bulk silicon of the substrates (near 522.5 cm^{-1}) and the phonon modes of silicon nanocrystals. A small but significant downshift of the Raman peak can be seen for the samples annealed at 950 and 1050°C in comparison with the Raman peak of the as-deposited sample and the sample annealed at 850°C. Such downshift has been attributed in literature as a sign of the quantum confinement of phonons inside the silicon nanocrystals [116]. The normalized difference spectra between the annealed and the as-deposited samples are also plotted in figure 3.9 for T_a = 950°C and 1050°C. They are slightly downshifted if compared to the bulk silicon since the maxima of these difference spectra are located around 519 cm^{-1}. The spectra are asymmetric and broadened in the low-wavenumber side. This feature is a characteristic of phonon confinement in nanostructures that leads to a relaxation of the q-vector selection rule [116].

In the following, the sample corresponding to the best exciton confinement energy will be chosen as a good material to test both exciton and phonon confinement models. Thus we have selected the multilayer sample annealed at T_a = 950°C.

Comparison with experimental data on multi-layered samples: In figure 3.10 (a) are reported both experimental and theoretical photoluminescence spectra of the multilayer sample annealed at 1050°C. The parameters ΔE, ϕ_0 and σ were fitted to adjust the luminescence model to the experimental emission spectra. Then the values obtained for ϕ_0 and σ were then directly used in the phonon confinement model presented above. Therefore it is important to note that no new fitting procedure was applied for the phonon confinement model. Theoretical and experimental Raman spectra are plotted in figure 3.10 (b).

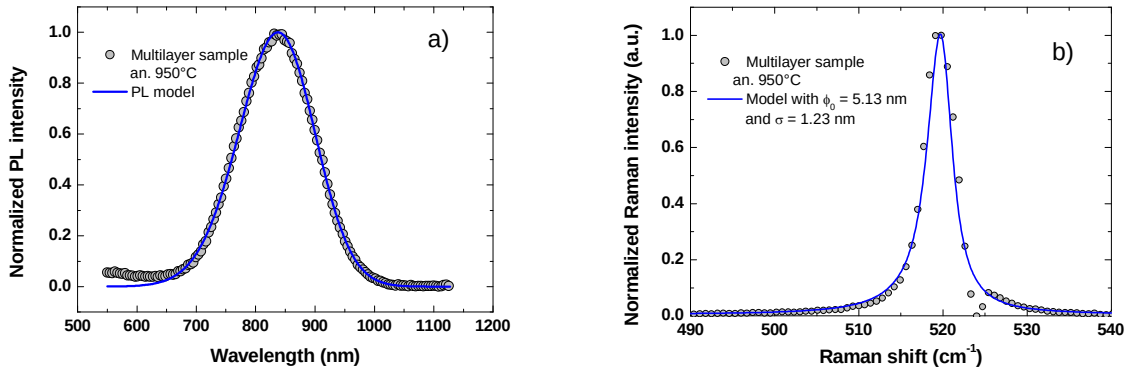

Figure 3.10: (a) Modeling of the luminescence emission band of the silicon nanocrystals of the multilayer sample annealed at 950°C using a log-normal statistical law for taking into account the diameter distribution of the silicon nanocrystals. ϕ_0 and σ are parameters for the central diameter and the distribution width, respectively. (b) Modeling of the Raman band of the same sample. The experimental spectrum was obtained by subtracting the spectrum of the as deposited multilayer sample to the one annealed at 950°C. The log-normal law for diameter distribution obtained by fitting the luminescence band was applied to the phonon confinement model using the same values for ϕ_0 and σ.

It is clear that the luminescence model enables to properly fit the photoluminescence spectra. But the most interesting result is that the phonon confinement model also gives a good fit of the phonon spectra at around 519 cm^{-1} by using the values of ϕ_0 and σ deduced from luminescence analysis. The two models are thus in close agreement and reveal the useful combination of photoluminescence and Raman spectroscopies to obtain the size distribution of the silicon nanocrystals in the sample. It also firmly evidences the better control of electronic and phononic properties of such silicon nanocrystals using multilayered structures. The average size obtained by the spectral fitting procedure is around 5 nm, which is slightly bigger than the thickness of the SiO layer. It could signify that, during the annealing process, the growth of silicon nanocrystals is not strictly confined in the SiO layers. The crystals may also be oblate, with a slightly bigger size in the plane of the SiO layers. The confinement models (that consider spherical crystals) can account for this geometry by increasing the mean diameter and slightly relaxing the confinement of excitons or phonons.

If we refer to the size distribution of the silicon nanocrystals obtained by TEM with a 4-nm SiO layer, the silicon nanocrystal diameter is approximately 4.1±1.7 nm [112]. This result is in rather good agreement with the values of ϕ_0 and σ obtained with the theoretical analysis of experimental photoluminescence and Raman spectra (5.13±1.23 nm). The size obtained by spectral fitting is slightly higher than that obtained by TEM. This may be due to the fact that statistics realized with TEM measurement are made using a rather small number of silicon nanocrystals and is very sensitive to the subjective definition of crystalline area by the operator. Moreover, the difference between our model and TEM measurements can also be attributed to residual stress and surface defects of nanocrystals that may exist in such nanometric multilayered structures [117]. Indeed, a compressive residual stress would slightly upshift the Raman phonon peak [118]. While the internal residual stress is not taken into account in our study, the theoretical analysis of spectroscopic results using quantum confinement

models and TEM results are in good agreement. This self-consistency constitutes a strong argument in favor of the existence of such confinement effect in nanocrystalline structures.

3.3.2 EFTEM analysis

In order to verify that the SiO_x alloys with x exceeding unity contain fewer nanocrystals than the SiO alloy, we employed transmission electron microscopy. In order not to be disturbed by the eventual superposition of the nanocrystals when the electron beam passes through the film, the appropriate samples have been deposited as $SiO_2/SiO_x/SiO_2$ tri-layers with thicknesses of 9/3/9 nm, respectively. In this way, after the annealing at 1100°C, the nanocrystals are inserted in a single layer that is analyzed perpendicular to the plane. The additional advantage of this configuration is, identically to the multilayers, to know that the growth of the nanocrystals in the SiO_x layer is blocked by the stable SiO_2 layers and that the grains have thus an identical size, equal to the thickness of the SiO_x layer [56].

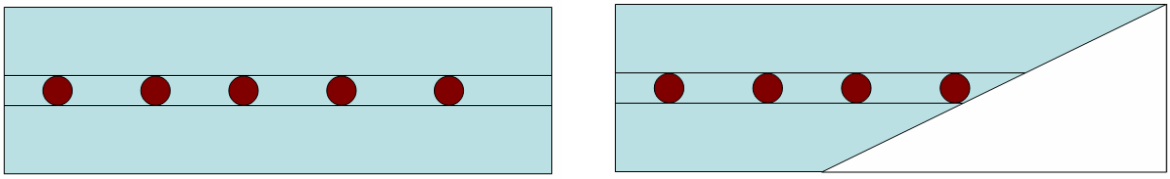

(a) *(b)*

Figure 3.11: Sample before (a) and after (b) thinning with the tripod method. The tip of the thinned sample is transparent to electrons.

The slices for energy filtered transmission electron microscopy (EFTEM) have been fabricated at Nancy by the purely mechanical tripod method (see sketches in figure 3.11) as the films are very sensitive to high temperatures. Afterwards, they have been analyzed by the electronics department of the University of Barcelona.

In order to obtain information about homogeneity over the sample surface, measurements in different regions of the samples were performed. We observed that the samples are quite homogeneous, finding a large density of silicon nanocrystals over the whole explored regions. In figure 3.12 we present EFTEM images of the four analyzed samples: SiO, $SiO_{1,25}$, $SiO_{1,5}$ and $SiO_{1,75}$.

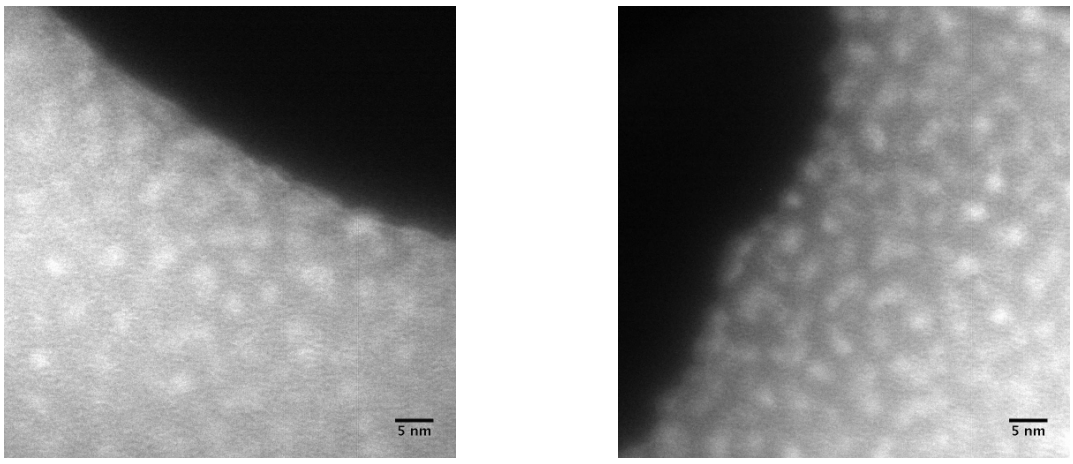

(a) *(b)*

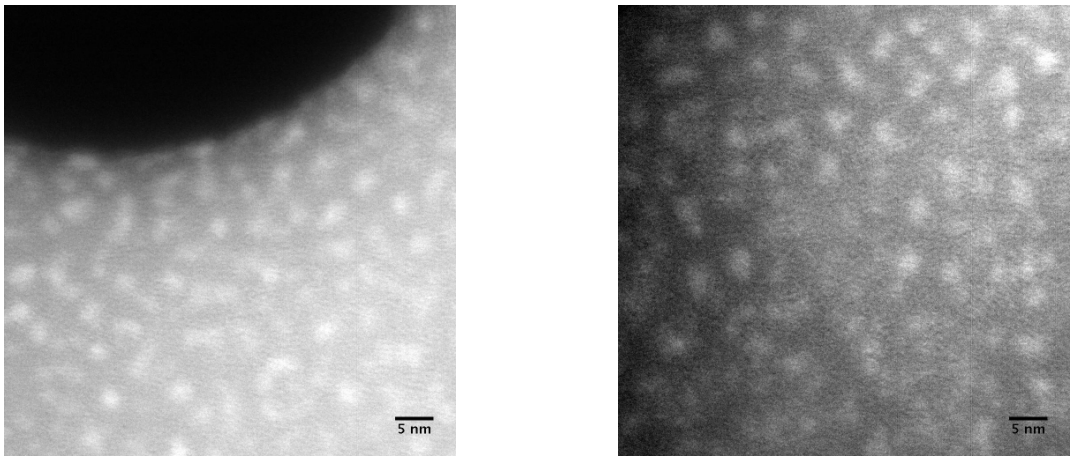

(c) *(d)*

Figure 3.12: EFTEM images of samples (a) SiO, (b) $SiO_{1,25}$, (c) $SiO_{1,5}$ and (d) $SiO_{1,75}$. The brightest zones are referred to silicon nanocrystals.

From the whole set of images, we have estimated the superficial density of silicon nanocrystals. In figure 3.13 (a), the evolution of the superficial density of silicon nanocrystals is reported as a function of the Si excess in the SiO_x films. The density of silicon nanocrystals increases from 2.6×10^{12} to 4.6×10^{12} cm^2, laying in the same order of magnitude. On the other hand, we found silicon nanocrystal sizes very similar as the Si excess varies in the samples (all the values lay within the range 2.3 and 2.5 nm). In figure 3.13 (b), we have plotted the obtained values.

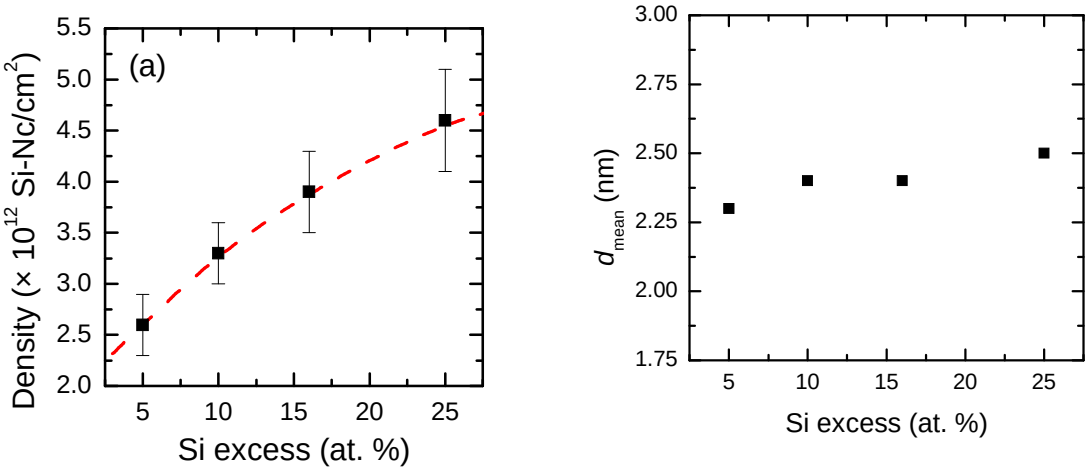

Figure 3.13: (a) Surface density of Silicon nanocrystal in the SiO_x/SiO_2 films for different silicon excesses. (b) Silicon nanoparticle diameter (d_{mean}) of the SiO_x/SiO_2 films for different silicon excesses. The dashed lines are guides to the eye.

Considering now the obtained values of silicon nanocrystal size, surface density and thickness of the layer (around 2.5 nm, as it has been the maximum silicon nanocrystal size measured), we can calculate the amount of silicon in the layer and thus the silicon excess or the composition of the SiO_x layers. Finally, the determined values of the silicon excess slightly differ from the values which have been calculated from the deposition rates.

Samples Code	SiO_x	Si excess (at. %) nominal	Si excess (at. %) Calculated by EFTEM
401A2	$x = 1$	25	16.5
448A1	$x = 1.25$	16	14.0
447A1	$x = 1.5$	10	9.1
449A1	$x = 1.75$	5	5.3

Table 3.3. : A short summary of the composition of the samples that have been analyzed at Barcelona

The difference between the nominal silicon excess and the silicon excess determined from EFTEM images could be explained by a kind of over-saturation of silicon of the thin films with the highest silicon excess. This could lead to a remaining lower silicon excess in the whole matrix after annealing.

3.3.3 Photoluminescence

The aim of employing SiO_x/SiO_2 multilayers instead of SiO/SiO_2 multilayers was to reduce the surface density. In this section we will investigate the influence of the different compositions on the photoluminescence properties.

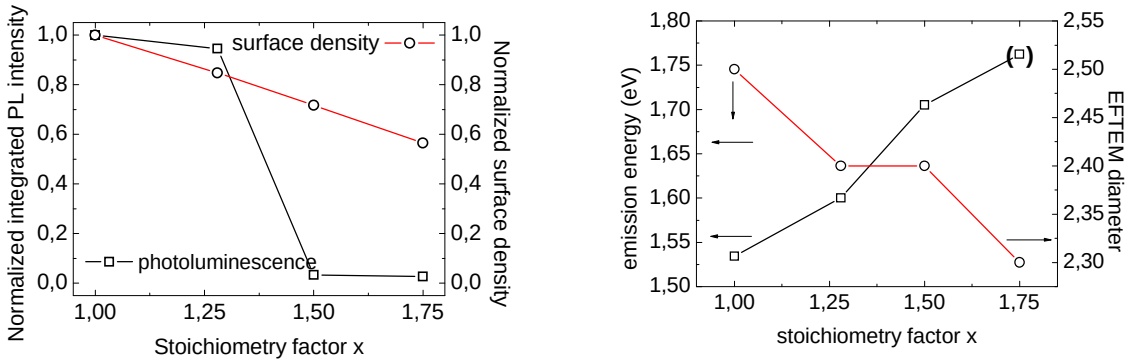

(a) *(b)*

Figure 3.14: (a) Surface density correlated to photoluminescence signal as a function of the stoichiometry factor x; (b) emission energies correlated to the grain sizes of the silicon nanocrystals as determined by EFTEM measurements.

The measured surface density can be correlated to the photoluminescence of the samples for high silicon excess as shown in figure 3.14 (a). A brutal reduction of the photoluminescence intensity between x = 1.25 and x = 1.5 is observed and could be explained by the introduction of additional dangling bond defects in the matrix as the relative oxygen content is increased.

Figure 3.14 (b) shows the energy of the maximum photoluminescence intensity and the EFTEM diameter as a function of the stoichiometry factor x. As expected, the emission energy decreases when the nanocrystal diameter increases.

In summary, it is possible to vary the surface density of silicon nanocrystals by evaporation of SiO_x alloys of different oxygen contents. Those nanocrystals have almost all the same size, defined by the thickness of the SiO_x layer.

3.4 Application of lithographic techniques to further reduce the surface density

In the upper sections, we have shown that it is possible to reduce the surface density of silicon nanocrystals. In addition, the photoluminescence intensity is directly proportional to the surface density. In order to analyse a strongly reduced number of silicon nanocrystals, it is nonetheless necessary to employ further micro- and nanotechnologies. We have employed electron beam lithography in order to define small excitation areas. In this chapter, we describe a process of etching micrometric apertures into an opaque metallic mask.

Material	Surface density	Nanocrystals per circle of 100 nm
SiO_1	$4{,}6 \cdot 10^{12}$ cm^{-2}	363.4
$SiO_{1.28}$	$3{,}9 \cdot 10^{12}$ cm^{-2}	308.1
$SiO_{1.5}$	$3{,}3 \cdot 10^{12}$ cm^{-2}	260.7
$SiO_{1.75}$	$2{,}6 \cdot 10^{12}$ cm^{-2}	205.4

Material	Surface density	Nanocrystals per circle of 50 nm
SiO_1	$4{,}6 \cdot 10^{12}$ cm^{-2}	90.2
$SiO_{1.28}$	$3{,}9 \cdot 10^{12}$ cm^{-2}	76.4
$SiO_{1.5}$	$3{,}3 \cdot 10^{12}$ cm^{-2}	64.7
$SiO_{1.75}$	$2{,}6 \cdot 10^{12}$ cm^{-2}	51.0

Material	Surface density	Nanocrystals per circle of 10 nm
SiO_1	$4{,}6 \cdot 10^{12}$ cm^{-2}	3.634
$SiO_{1.28}$	$3{,}9 \cdot 10^{12}$ cm^{-2}	3.081
$SiO_{1.5}$	$3{,}3 \cdot 10^{12}$ cm^{-2}	2.607
$SiO_{1.75}$	$2{,}6 \cdot 10^{12}$ cm^{-2}	2.054

Table 3.4: estimation of the number of nanocrystals per aperture

Table 3.4 summarizes the number of silicon nanocrystals per aperture for three aperture sizes, respectively. The largest value of 100 nm corresponds to the lower aperture size limit for a process employing an opaque aluminum mask. The value of 50 nm corresponds to the lower aperture size limit of the so-called lift-off process which is available at the electron beam lithography facility at Nancy. The third value of 10 nm corresponds to a structuring technique that has been proposed by Pallandre [119].

For a first proof of principle, we decided to employ the aluminum mask approach which still allows detecting a relatively strong photoluminescence signal. This is used to verify the complete etching of the apertures.

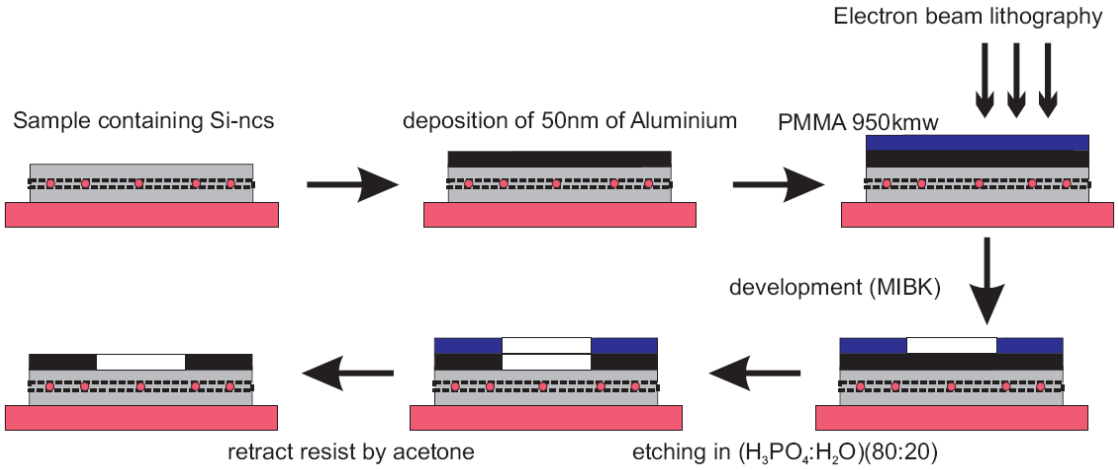

Figure 3.15: lithographic process to generate apertures of 100 nm diameter.

The fabrication process is explained in figure 3.15. After the classical production of the silicon nanocrystals by evaporation and high temperature annealing, the aluminum mask is deposited onto the sample. An electro-sensitive resist of poly-methyl-methacrylate (PMMA) of a molecular weight of 950.000 is deposited after this. This resist is exposed to an electron beam during the following electron beam lithography step. The PMMA that has been exposed to the electron beam becomes soluble in a so-called developer solution, methyl-iso-butyl-ketone (MIBK). After development of the resist in the MIBK for 1 minute and rinsing in isopropylic alcohol for 30 seconds, the sample is exposed to diluted phosphoric acid for 5.25 minutes, which is the time to etch 50 nm of aluminum. This etching rate was determined during a preliminary study [120]. After the etching of the aluminum mask, the remaining resist is removed by dissolution in acetone in an ultrasonic bath.

The metal mask consists of an aluminum layer in which apertures are created of different sizes and shapes from squares of 2µm edge length down to circle shaped 100 nm apertures with a distance of 10 µm to each other. The structures are arranged in 100 µm · 100 µm fields.

Evaluation of the mask thickness: The thickness of the masking layer is an important parameter for the creation of apertures. On the one side, the layer has to be opaque in order to mask all the nanocrystals except the few nanocrystals under the apertures. On the other side, a preferably thin layer is necessary to optimize the size of the apertures in the mask as it was observed for a sample with an aluminum layer thickness of 100 nm. Even if the mask was opaque, it could not be used as the minimum aperture size was 200 nm and thus too big for the isolation of a sufficiently low number of silicon nanocrystals.

Thus, the opacity of the aluminum mask was tested for different layer thicknesses using a multilayer sample as substrate for the mask as the multilayer sample contains 22 layers of silicon nanocrystals providing a much more intense photoluminescence signal than a single layer that shall be used in the final sample layout**.** Figure 3.16 (a) shows photoluminescence spectra of multilayer samples with

different thicknesses of the deposited aluminium layer. For the 30 nm thick layer, there is a residual signal from the nanocrystals around 800 nm of about 20 counts per second. For the 50 nm thick layer, however, no remarkable signal of the silicon nanocrystals was observed. The remaining peaks at about 405 nm and 436 nm originate from diffused emission lines of the mercury light source.

Figure 3.16 (b) shows the vector graphics that has been used to command the electron beam lithography. The structure consists of 8 by 8 apertures of different sizes with a pitch of 10 µm in each direction. In the upper half of the 100 µm by 100 µm wide field, each horizontal line contains apertures of the same size which have been written with a varying exposure dose, i.e. a varying electron current. The apertures in the first line are 2 µm by 2 µm wide squares. The second line contains 1 µm by 1 µm wide squares. The third line contains 500 nm by 500 nm wide squared apertures, whereas the fourth line contains 200 nm by 200 nm wide squares. The lower half of the whole field is composed of 100 nm wide circle shaped apertures. They differ from each other equally by their exposure dose. In order to be able to locate them under the microscope, the apertures of the lower half of the field are separated from each other by a sort of alignment mark. Nonetheless, the alignment mark is in a distance of about 5 µm from the small aperture, in order not to influence photoluminescence measurements on the small aperture.

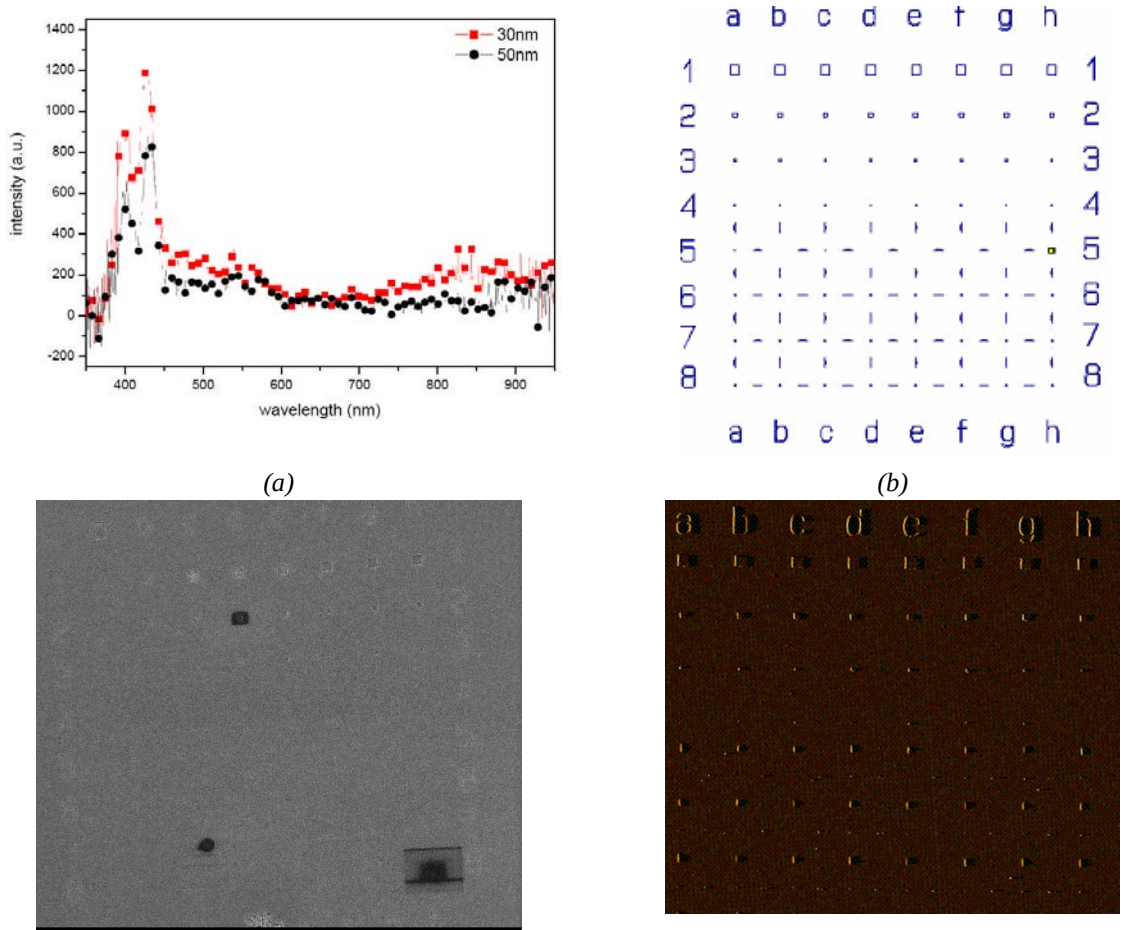

(a) *(b)*

(c) *(d)*

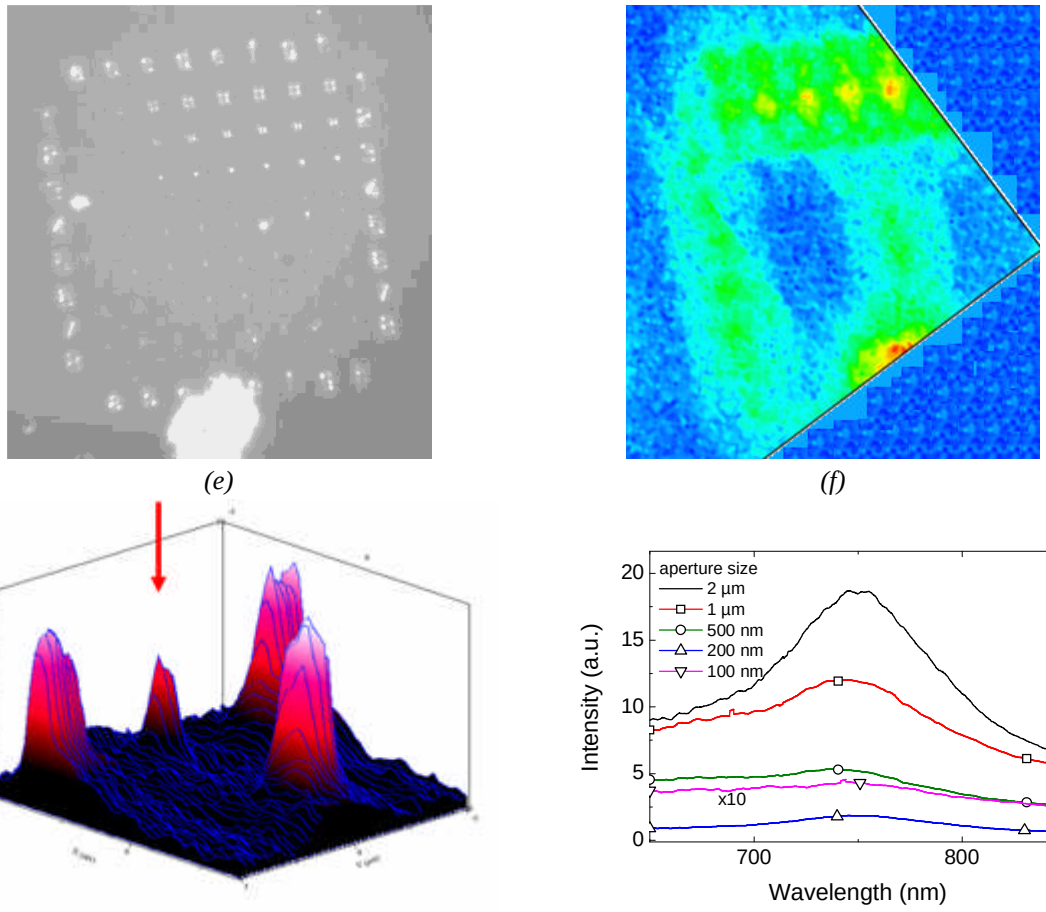

Figure 3.16: Lithographed aperture field – (a) opacity of the mask; (b) vector graphics for electron beam lithography; (c) SEM image of the realized structure; (d) AFM image; (e) contrast enhanced optical image; (f) APD voltage cartography; (g) fluorescence cartography of one of the smallest apertures. The arrow marks the aperture; (h) photoluminescence spectra of a multilayer sample for different aperture sizes, respectively.

Figures 3.16 (c) and (d) show scanning electron (SEM) and atomic force microscope (AFM) images of a realized structure field, respectively. The dark zones in figure 3.16 (c) are due to charge effects on the sample, caused by more localized analysis with the SEM of several apertures.

Figures 3.16 (e) and (f) show an optical image of the structure field and intensity cartography of the photoluminescence of silicon nanocrystals, respectively. The images have been produced employing twice the same micro-photoluminescence setup, but two different methods to analyze the signal. For figure 3.16 (e), the reflected intensity of a white light source was projected on a CMOS-camera. For orientation, note the big impurity at the lower side of the structure field. In figure 3.16 (f), the photoluminescence signal of the sample is reported, with colours corresponding to the count rate of an avalanche photodiode (APD). The analyzed wavelength has been fixed by a narrow band-pass filter to 720 nm +/- 5nm so that the detected signal originates essentially from silicon nanocrystals. The intensity profile corresponds well to the optical image of figure 3.16 (e).

Figure 3.16 (g) shows a 3D cartography of the photoluminescence intensity around a 100 nm wide aperture. The arrow marks the aperture. The bigger features around the aperture result from the upper mentioned alignment marks.

Figure 3.16 (h) reports the photoluminescence spectra of a multilayer sample for different aperture sizes in the aluminum mask, respectively. A clear decrease with aperture size is observed. Even for the smallest apertures, a weak photoluminescence signal was observed. This proves the feasibility of the optical isolation of few silicon nanocrystals by this method.

Nonetheless, the linewidth of the photoluminescence detected on the smallest apertures is not remarkably changed. The calculus in the beginning of the chapter gives an indication of the number of silicon nanocrystals under this aperture. So we still have to improve the photoluminescence of our samples and, in the same time, we still have to increase either the inter-nanocrystal distance or to reduce the aperture size.

In summary, in this section, we developed a process to optically isolate a reduced number of nanocrystals. By means of electron beam lithography followed by wet etching, micrometric structures have been created. The apertures have been analyzed by optical microscopy, scanning electron microscopy, atomic force microscopy as well as scanning fluorescence microscopy. The four analysis methods confirmed the correct etching of the sample. Subsequent photoluminescence spectroscopy revealed that even from the smallest apertures, photoluminescence was detected. Nonetheless, the photoluminescence spectrum of the smallest apertures does not substantially differ from the photoluminescence spectrum observed on the unmasked sample.

3.5 Conclusion

In the first part of this chapter, we studied silicon nanostructures by photoluminescence and Raman spectroscopy. Samples have been made by evaporation and subsequent annealing under vacuum. Two kinds of samples have been elaborated and analyzed. The first kind of sample is constituted , before annealing, by a thick SiO layer. The second one is a SiO/SiO_2 multilayer. The thicknesses of the SiO and SiO_2 layers in the multilayers are of 4 and 5 nm respectively. In SiO monolayer sample annealed between 600 and 940°C, the demixion process induces the appearance of amorphous silicon areas which show a photoluminescence band in the visible range and a Raman spectrum with typical large bands at 160 and 490 cm^{-1}. In SiO/SiO_2 multilayer samples annealed at 950 and 1050 °C, the diameter of the Si nanocrystals is controlled by the thickness of the SiO layer. The photoluminescence band is intense and narrow peak and the Raman spectrum shows an asymmetric band at 519 cm^{-1}. For this sample, Raman spectra have been modeled as well as photoluminescence spectra. We modify the model of Faraci *et al.* [110] for Raman spectra and of Meiers *et al.* [108] for photoluminescence spectra by including a size distribution of silicon nanocrystals diameters and the corresponding central diameter and distribution width are in good agreement with those measured by TEM. This constitutes a good experimental evidence of the confinement effect for both excitons and phonons in silicon nanostructures embedded in silica matrix. Finally, the phenomenological models used in this study enable to easily and quite confidently retrieve a good estimation of the size distribution of nanocrystals in a sample, which is quite interesting from a methodological point of view.

In the second part of this chapter, we employed co-evaporation of SiO and SiO_2 in order to elaborate SiO_x thin films with $1 \leq x \leq 2$. FTIR measurements revealed the demixion reaction of the silicon oxides during high temperature annealing into the two thermodynamically stable components Si and

SiO_2. SiO has shown to demix more completely as after the annealing at the highest annealing temperature, the stoichiometry of the matrix was of y = 2, as determined by FTIR. $SiO_{1.5}$ is inert up to an annealing temperature of 750°C. Only for an annealing temperature of 900°C, a shift of the stoichiometry is observed. The demixion seems incomplete, as the stoichiometry of the matrix does not reach y = 2.

Photoluminescence measurements revealed that the luminescence of these thin films is originating from different luminescence centres in the films depending on the annealing temperatures. For low annealing temperatures, generally, the photoluminescence is induced by structural defects in the SiO_2 matrix. For the highest annealing temperatures the photoluminescence is due to silicon nanoparticles in the SiO_2 matrix.

In a third part of this chapter, we describe the analysis of SiO_x/SiO_2 multilayers equally elaborated by co-deposition of SiO and SiO_2. The annealing parameters of a new rapid thermal annealing device have been determined employing SiO/SiO_2 multilayers. After this optimization, the influence of the stoichiometry factor on the photoluminescence of the multilayer samples has been investigated. In general, we observed a reduction of the emission wavelength with increasing stoichiometry. This has been explained as a reduction of the grain size. At the same time, the emission intensity was strongly reduced. This could be partly attributed to a reduced number of grains that are formed due to the reduction of the silicon excess in the film. To confirm this observation, $SiO_2/SiO_x/SiO_2$ trilayers have been fabricated yielding detectable photoluminescence of only one layer of size controlled silicon nanocrystals. The photoluminescence of the trilayer samples evolutes identically to the photoluminescence of the multilayers. After the photoluminescence experiments, the samples have been analyzed by EFTEM. The above-mentioned slight reduction of the size has been found as well as a reduction of the surface density of the silicon nanocrystals as a function of the stoichiometry factor x. The surface density was shown to be very high ($\sim 10^{12}$ grains/cm^2). This complicates single dot spectroscopy.

Therefore, in a fourth part of this chapter, we employed lithographic processes in order to further reduce the surface density of silicon nanocrystals. We developed an opaque metal mask with small apertures down to diameters of about 100 nm. The feasibility of the process has been shown as photoluminescence measurements are possible even on the smallest apertures. Nonetheless, for instance, the detected spectra are not exploitable for single dot analysis. This led to the decision to couple the silicon nanocrystals to an optical microresonator in order to deduce the single dot linewidth from spectroscopy on microresonators.

Chapter 4. Study of silicon nanocrystals inserted in microcavities

4.1 Introduction

Silicon nanocrystals can emit visible light and they attracted much attention as possible elements of integrated all-silicon nanophotonic devices, replacing actual silicon-based integrated microelectronic devices. But as light source or single photon source, they suffer from their long radiative lifetime compared to direct – bandgap – semiconductor nanocrystals. One possibility to increase the radiative recombination rate is to couple the silicon nanocristal to microcavities and make the electronic modes of the nanocrystals interact with the optical ones of the microcavity.

The simplest approach for this purpose is the monolithic elaboration of two one-dimensional distributed Bragg reflector (DBR) stacks, made of dielectric, transparent material, surrounding the optically active layer of silicon nanocrystals. Such a system was produced, for example, by Belarouci and Gourbilleau [121] as well as Amans *et al.* [45] who report on a spectral and spatial redistribution of the emission intensity of silicon nanocrystals coupled to optical microcavities compared to their uncoupled counterparts. Additionally a weak reduction of the radiative lifetime is observed by them.

In this chapter, we tried to reduce the photoluminescence linewidth of an ensemble of silicon nanocrystals and to improve the photoluminescence intensity. Therefore, we sandwiched the multilayer containing the silicon nanocrystals between two distributed Bragg reflectors consisting of a sequence of pairs of dielectric layers. Our aim was to realize optical cavities.

In a **first** part of this chapter, we explain our choice to realize the Bragg mirrors by consecutive evaporations of Si and SiO_2 layers.

In a **second** part, we will describe the determination of the optical properties as refractive index and optical absorption of Si and SiO_2 layers in order to obtain the optimal thicknesses of these layers, respectively. In order to get the resonance phenomenon, the thickness of the layers has to match the quarter of the wavelength of the maximum intensity of the silicon nanocrystals photoluminescence divided by the refractive index of the appropriate layer. This study, described in chapter 2, is necessary because the properties of thin films generally depend on the fabrication technique. Additionally, it is necessary to anneal the multilayer at high temperature to generate the silicon nanocrystals and it will be shown that the optical properties and the thickness of thin films are strongly influenced by thermal annealing.

In a **third** part, we will describe the optical transmission properties of Si and SiO_2 based distributed Bragg reflectors. It will be shown that the transmittance spectra of those samples present a band of almost complete reflexion except a fine transmission band which will be used to couple to the light of the microcavity.

A **fourth** part will describe the structure and the photoluminescence properties of the microcavity. It will be shown that this microcavity allows for a remarkable reduction of the photoluminescence linewidth as well as a modification of the intensity and the radiative lifetime.

Finally, in a **fifth** part, we will employ the results which we obtain during this thesis to give a first raw estimation of the photoluminescence linewidth of a single silicon nanocrystals showing that is it possible to extract single dot properties out of the luminescence of an ensemble measurement.

4.2 Choice of the materials for the distributed Bragg reflector

The Bragg mirrors are constituted by a succession of transparent dielectric layers. The properties of the Bragg mirrors depend on the refractive indices of the layers, on their absolute values but also on their difference. Different materials have been used as e. g. SiO_2, TiO_2 [122], or SnO_2, which are available at Nancy. The choice of one material has been guided by a theoretical study of the efficiency of distributed Bragg reflectors constituted by different materials. It is also possible to work with Si [121].

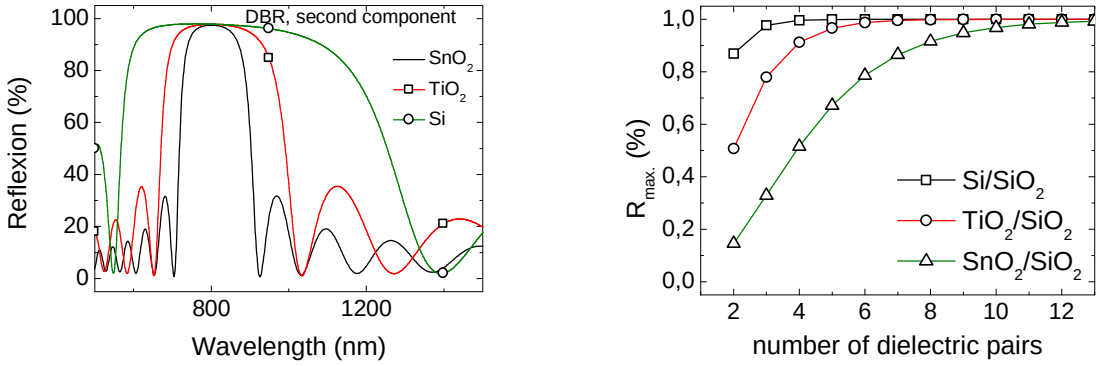

(a) *(b)*

Figure 4.1: Choice of the material (a) simulation of the reflexion of DBR of different components; (b) maximum reflectivity as a function of the number of dielectric pairs

SiO_2 is a transparent dielectric material with a refractive index equal to 1.45 at 600-800 nm, which is already used to elaborate the multilayer. It is thus natural to use it for the distributed Bragg reflectors, too. At 800 nm, SnO_2, TiO_2 and Si possess refractive indices equal to about 1.9, 2.3 and 3.4, respectively. The difference of these indices with that of SiO_2 is large enough to create a sufficiently large stop-band, but we don't have experience with the evaporation of TiO_2 and SnO_2. Their use as constituents of a distributed Bragg reflector based microcavity would demand an additional complete study of the evolution of their structure and their optical properties as a function of the annealing temperature. First attempts to deposit those materials have been accomplished.

Evaporation tests with Ti under oxygen atmosphere have shown to be difficult to control as Ti has a high oxygen affinity and therefore the oxygen pressure is not stable during the evaporation process. Obtaining a TiO_2 layer is then possible, but a homogeneous stoichiometry is not ensured.

Evaporation tests with SnO_2 powder in ultra high vacuum showed a more regular evaporation of the material. Nonetheless, high temperature annealing tests revealed that SnO_2 films do not withstand the high annealing temperatures that are necessary for the creation of the silicon nanocrystals.

Another discussion about the choice of the material concerns the reflectivity of the mirror which depends of the difference between the refractive indices of the two materials and also of the number of layers. The refractive index has also an influence on the thickness of the layer since the thickness is inversely proportional to the index. The total thickness of the mirror is an important parameter since;

with too thick layers, mechanical stress provokes the detachment of the films from the substrate. Thus, reflexion curves of Bragg mirrors with the different possible materials and with different numbers of bilayers were simulated (figure 4.1 (a)). The highest reflectivity is given in the figure 4.1 (b). This figure shows that the reflectivity is almost equal to one with only 3 bilayers for Si while it is neccessary to have 6 and 10 bilayers for TiO_2 and SnO_2, respectively, to have a reflectivity greater than 97%. In addition, as a consequence of the high refractive index of silicon, the thickness of Si to be evaporated is the lowest.

In summary, we compared three different possible components of the distributed Bragg reflectors by simulating the maximum reflectance. Because of the reduced thickness due to an elevated refractive index, we decided to work with Si and SiO_2 based distributed Bragg reflectors. Nonetheless, the disadvantage of silicon is a relatively high absorption throughout the visible range, which can have an important influence on the intensity of the excitation light and on the PL intensity emitted by the nanocrystals in the microcavity.

4.3 Optical properties of the Si and SiO_2 thin films

4.3.1 Experimental procedure

The optimal thicknesses of the Si and SiO_2 layers of which the distributed Bragg reflector is composed have to be equal to $\lambda/4n$ after an annealing at 1100°C that is necessary to precipitate the silicon nanocrystals in the active layer. We have thus to determine the refractive indices of all constituents which vary as a function of the annealing temperature. Indeed, materials deposited by evaporation are more or less porous and this porosity is reduced during the annealing. Additionally, silicon changes the structure as it crystallizes at around 600°C. It is thus necessary to know the evolution of the optical index and the thickness of the layers as a function of the annealing temperature. This evolution allows for the determination of the initial thickness of the layers before annealing to obtain the necessary $\lambda/4n$ thickness after densification during the annealing at 1100°C. The absorption coefficient is also an important parameter as the incident light as well as the photoluminescence signal has to travel through several silicon layers of an important total thickness.

To determine the optical properties of Si and SiO_2 we deposited layers of 400 nm on fused silica substrates. Fused silica is transparent down to a wavelength of 150 nm, thus permitting transmission measurements from the ultraviolet (UV) up to the near-infrared (NIR) spectral range. We chose the highest thicknesses that were possible to have a lot of interferences in the spectrum. This allows an easier data processing.

The silicon films deposited onto fused silica substrates and annealed at different temperatures have been analyzed by transmission measurements from 200 nm to 3300 nm. The experimental spectra have been treated in two different manners: use of Swanepoel's method of envelopes [58] and simulation of the rigorous expression of the transmission which is named "formal method" in the following. These methods, which are detailed in the appendices 1 and 2, permitted to determine the thickness and the complex index of the layers and other parameters related to the structure of the film such as the Tauc gap or the Urbach energy. Ellipsometry measurements have also been employed to

confirm the values of the thickness and the complex index. In addition, the thickness of layers of a nominal thickness of 20 nm has been analyzed by X-ray diffraction measurements for the different annealing temperatures.

Transmittance spectra of thin SiO_2 films deposited onto fused silica substrate do not present any interference as the index difference between film and substrate is obviously too small. We used thus SiO_2 films on monocrystalline silicon substrates and performed only ellipsometry measurements as the silicon substrate is not transparent in the visible range. X-ray diffraction measurements have been also realized to follow the evolution of the thickness as a function of the annealing.

Material	Thickness (nm)	Analysis
SiO_2	23.4	X-ray reflectivity , ellipsometry
	400	UVVIS
Silicon	23.4	X-ray reflectivity , ellipsometry
	400	UVVIS

Table 4.1 Sample configurations and analysis techniques

4.3.2 Properties of the silicon layer

The modelization is done as follows:

1. Swanepoel's method is employed to approximate index, thickness and absorption of the thin film.

2. After the approximation, a formal method is used which simulates the rigorous formulae, that describe the transmittance spectrum. This method uses eight parameters that have to be adjusted. Thus, we need to follow a rigorous protocol which will be described in the following.

First, the Tauc energy gap is determined simply from the transmittance spectrum. If we suppose the reflectivity to be equal to zero, we can easily deduce the absorption from the transmittance. In the energetic range of the band-gap, we observe a steep increase of the absorption. For direct band-gap semiconductors, it can be written as a function of the photon energy:

$$(\alpha E)^{1/2} = B\left(E - E_g\right), \tag{4-1}$$

We trace this relation and obtain a curve, that is partially linear and the gradient of this linear part allows an estimation of the Tauc energy gap E_g.

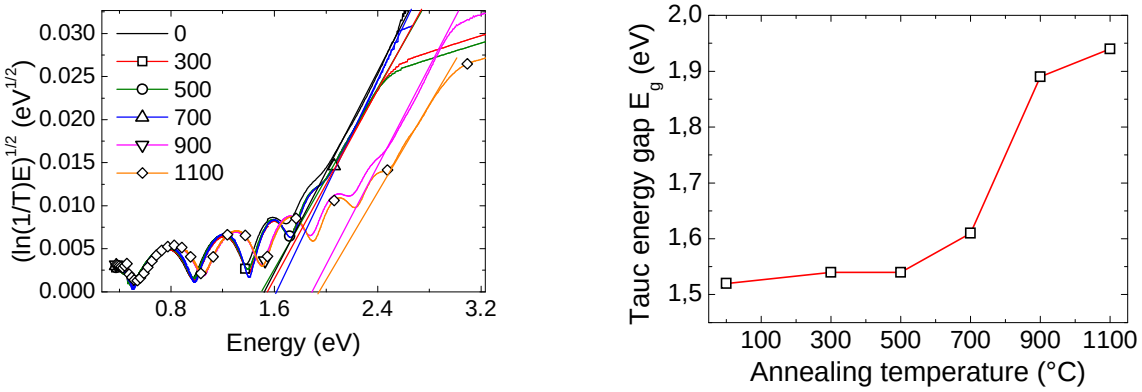

(a) *(b)*

Figure 4.2: Tauc energy gap E_g – (a) Determination of the Tauc energy gap by linear fit; (b) The Tauc energy gap increases with the annealing temperature

Figure 4.2 (a) shows the plots of $(\alpha E)^{1/2} = B(E - E_g)$ for different annealing temperatures and 4.2 (b) summarizes the Tauc energies as a function of annealing temperature. The increase of the gap with the temperature can be interpreted as a disappearance of the defects creating intra-band states. Similar values of the Tauc energy gap of polycrystalline silicon prepared by remote plasma CVD have been analyzed in the same way and reported by Lim *et al*. [123]

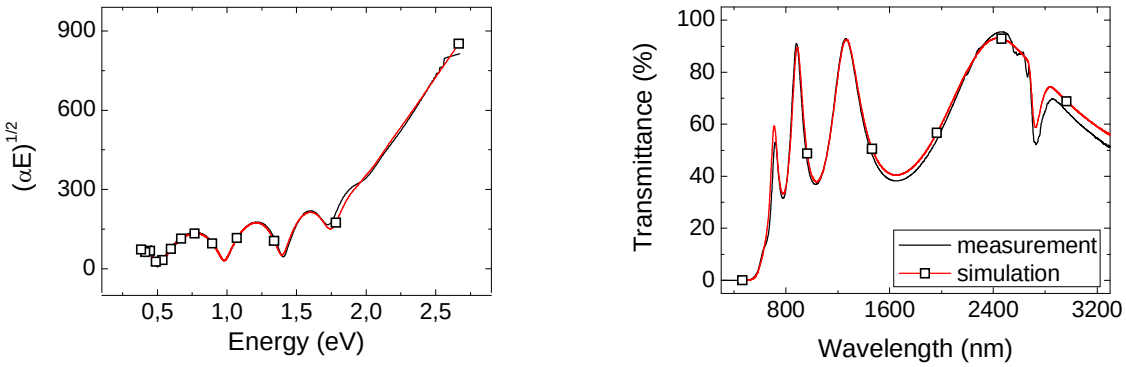

(a) *(b)*

Figure 4.3: Comparison of simulation and measurement after all adjustments for a sample annealed at 700°C (a) Spectrum in the representation to determine Tauc energy E_g. (b) Experimental and simulated transmittance spectrum of a thin silicon film.

Once this parameter is fixed, we can proceed with the following steps:

- adjust the first contribution to the refractive index, n_0 and the thickness.
- adjust the other contributions to the refractive index, n_1 and n_2

- adjust the absorption parameters of the Urbach absorption regime α_0 and E_u
- (re)adjust the absorption of the Tauc absorption regime B and E_g.

Figure 4.3 (a) shows the plot of $(\alpha E)^{1/2} = B(E - E_g)$ as well as its fit. We observe a good agreement over the whole analyzed spectral range. Only a small zone between the two absorption regimes at around 1.8 eV seems to be not well described by the simulation. It has been suggested to treat this region as a third absorption regime with the same equation as in the Urbach regime with its own appropriate parameters. As in our case, such a precision was not necessary and as the number of parameters was already high enough, we did not take into account this range. Figure (b) compares the measured transmittance spectrum to a simulation of the rigorous theoretical expression of the transmission of a thin silicon film, taking into all the parameters, which have been determined during the procedure.

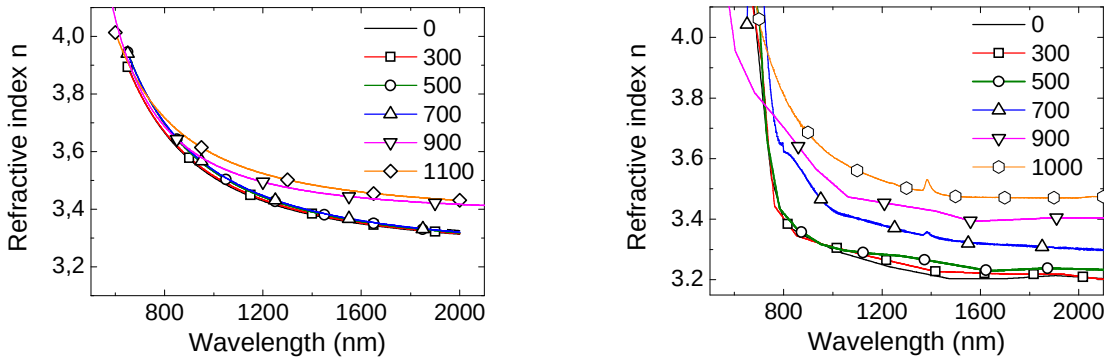

(a) *(b)*

Figure 4.4: (a) Refractive indices as determined by simulation of the rigorous formula. (b) Refractive indices as determined by Swanepoel's method.

The results of the simulation are reported in figure 4.4 for the formal method (a), and for Swanepoel's method of envelopes (b), respectively. With the formal method, the curves are identical for the as-deposited film and for the films annealed at temperatures less than or equal to 700°C. The values for the curve corresponding to the 900°C anneal are greater, mostly in the high-wavelengths range, certainly because of the crystallization of the silicon film which corresponds to a densification of the film. These values are coherent with the results in literature [124].

The evolution is the same for the results obtained by the Swanepoel's method, but the curve begins to evolve with the 700°C anneal. The results are equivalent for the annealing at 900°C, especially at longer wavelengths. For shorter wavelengths, Swanepoel's method produces less accurate index values. This is certainly due to the disappearance of the interferences in the strong absorption regime of the experimental spectrum which corresponds approximately to energies greater than the Tauc energy (1.5 eV), namely to wavelengths shorter than 820 nm. It seems also that the Swanepoel's method underestimates the value of the refractive index with respect to formal method.

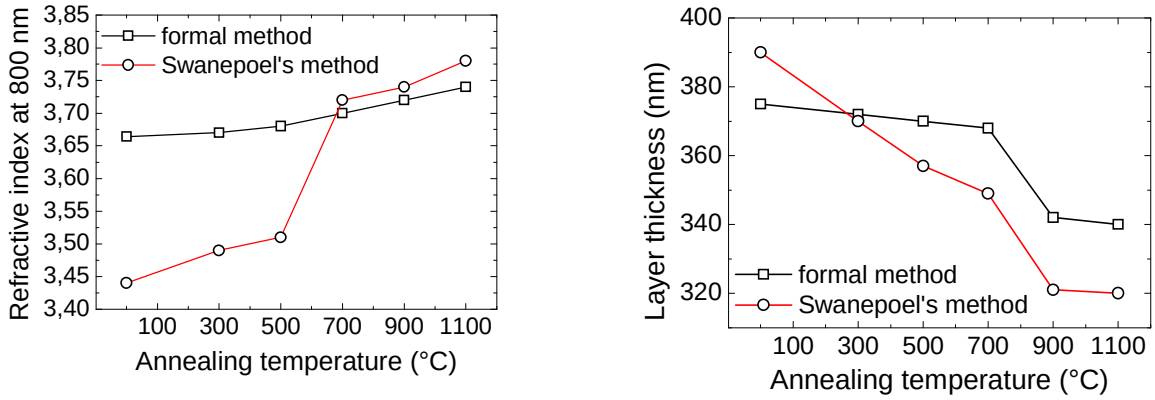

(a) *(b)*

Figure 4.5: (a) The refractive index at 800 nm as a function of the annealing temperature. (b) The layer thickness as a function of annealing temperature.

As later, we are going to analyse the photoluminescence at 800 nm of the silicon nanocrystals placed into optical microcavities, the value of the refractive index which occurs in the calculations of the thicknesses of the layers of the Bragg mirrors is the value at 800 nm. This value varies with the annealing temperature. Therefore, we have summarized in figure 4.5 (a) the refractive indices of silicon at 800 nm as a function of the annealing temperature. As it has been stated above, measurements at 800 nm obtained by Swanepoel's method are very defective for low annealing temperatures due to the presence of strong absorption. So, the measurements presented in the figure coincide with the values obtained by the formal method only for high annealing temperatures. At this wavelength, the refractive index increases slowly with the annealing temperature, from 3.66 for the as-deposited film to 3.75 for the film annealed at 1100°C.

The simulation methods allow us to deduce the thickness of the film which is reported in figure 4.5 (b). Both methods produce equivalent results. We can notice a reduction of the thickness of the film with increasing annealing temperature. This is very important, because it will have an important influence on the design of the optical microcavities. In both cases, the evolution of the thickness shows no brutal variation up to a temperature between 700°C and 900 °C. For higher temperatures than this, a stronger reduction is observed. The thickness reduction for the annealing at 900°C is of 10.7% for the formal method and of 17.7% for Swanepoel's method, respectively. As it has been discussed above, concerning the evolution of the refractive index as a function of the annealing temperature, the evolution of the thickness could also be related to the crystallization of the initially amorphous silicon.

In addition to the analysis of the film thickness by optic measurements, the thickness evolution has been examined by X-ray diffraction (XRD) measurements. Analogously to the optical interferences that served in the upper-mentioned simulations, X-ray interferences are used to determine the thickness of this sample series (see figure 4.7 (a)). Figure 4.7 (b) reports the evolution of the thickness as a function of the annealing temperature, as determined by XRD. The same trend of a slow reduction of the thickness was observed for lower temperatures whereas, at higher temperatures, a brute reduction of the thickness occurs. The reduction of the thickness as determined by XRD is of 11% for the annealing at 1100°C. The general evolution and also the overall thickness reduction are in a good

agreement with the formal simulation method for the visible transmission. Nonetheless, it should be noted that the densification process started already at lower temperatures as reported for the visible transmission measurements.

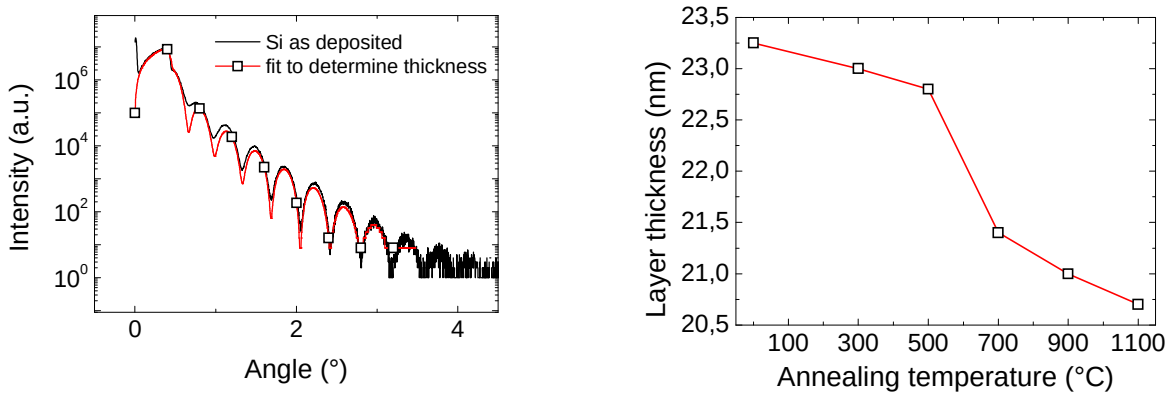

(a) *(b)*

Figure 4.6: XRD measurements of the thickness of a silicon layer. (a) XRD spectrum and the theoretical fit from which is deduced the thickness. (b) Thickness of the films as a function of annealing temperature.

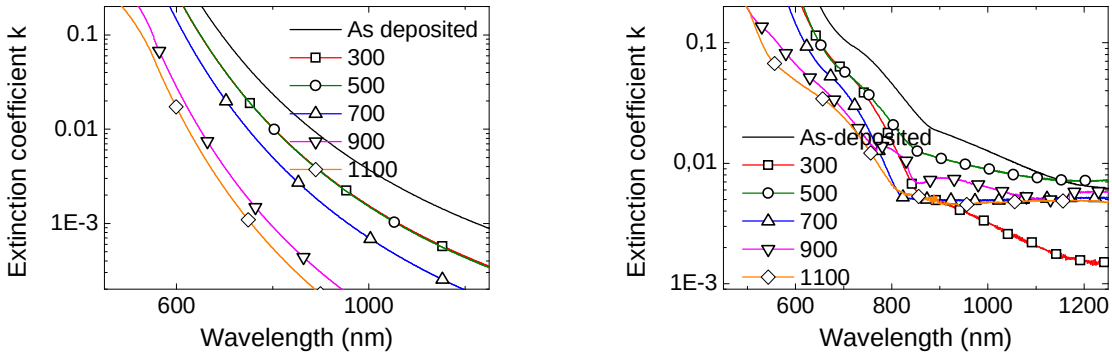

(a) *(b)*

Figure 4.7: (a) Extinction coefficient k as determined by simulation of the rigorous formula. (b) Extinction coefficient k as determined by Swanepoel's method.

The extinction coefficient k can also be obtained by the simulation methods. Figure 4.7 shows the wavelength dependent extinction coefficient k for the formal method (a) and Swanepoel's method (b) respectively.

The two methods give nearly identical results. The absorption is nearly zero in the infrared range over about 1100 nm. In the visible range, the absorption is strongly increased due to transitions between valence band and conduction band. We observe a decrease of k at a given wavelength as a

function of the annealing temperature. This corresponds to a shift of the entire spectrum towards shorter wavelengths. The shift indicates a reduction of the localized band-tail states for the lower annealing temperatures and their disappearance as the film crystallizes at higher annealing temperatures.

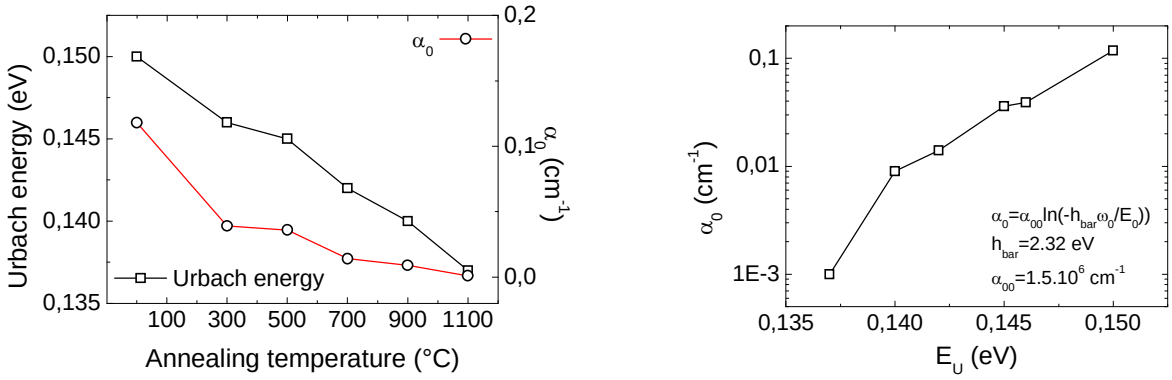

(a) *(b)*

Figure 4.8: a) Urbach energy E_u as determined by the formal method as a function of annealing temperature b) α_0 as a function of E_U

The absorption of the materials can also be characterised by other parameters. So the absorption parameter in the range of medium absorption can be written as

$$\alpha = \alpha_0 \exp\left(\frac{E}{E_u}\right), \tag{4-2}$$

and the absorption parameter in the range of strong absorption as

$$\alpha = \frac{B}{E}\left(E - E_g\right)^2, \tag{4-3}$$

The evolution of the Urbach parameters E_U and α_0 as a function of the annealing temperature are reported in figure 4.8 (a). The value of E_u, between 140 and 150 meV, corresponds well to the expected values as these can vary between 85 meV and 247 meV [125]. Both E_U and α_0 are reduced with increasing temperature. This behaviour can be interpreted in terms of a disappearance of defects that were initially present in the amorphous and porous silicon before annealing and/or the crystallization of the layer.

The values of α_0 are reported as a function of E_U in figure 4.8 (b). Equivalent values reported in literature are as circles [126]. We observe that for the same values of E_U, α_0 values are lower than for doped Si:H. This may be due to the fact that our system is different: polycrystalline and non-hydrogenated silicon.

The Urbach parameters are well known for hydrogenated silicon. For this kind of sample, Orapunt and O'Leary [126] report α_0 as a function of E_U. As they report, in the case of hydrogenated silicon, α_0 evolutes as follows:

$$\alpha_0 = \alpha_{00} e^{\frac{\hbar\omega}{E_u}}, \tag{4-4}$$

where α_{00} is a so called focus parameter, which is common to all their samples. We plotted α_0 as a function of E_U, as can be seen in figure 4.7 (b). With respect to their values, our values of E_U are higher for the same value of α_0. Indeed, our non-hydrogenated samples contain more intra-band defect states, even if they are once crystallized.

Moreover, our values seem to be in agreement with those obtained in literature on polycrystalline silicon, investigated by Lim *et al.* [127], e.g. This argument, combined with the elevated value of the Tauc energy gap (1.9 eV for silicon annealed at 900°C, see figure 4.8 (a)) lets us conclude that we have crystalline silicon after high temperature annealing.

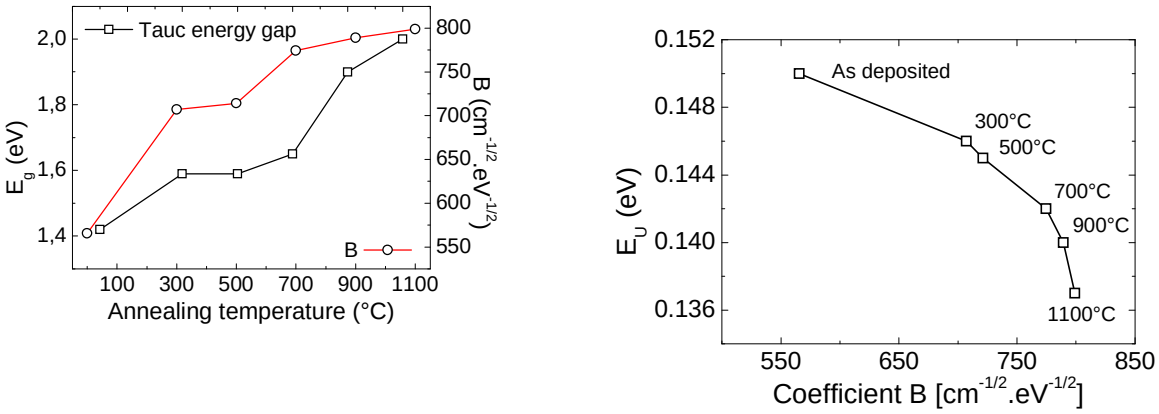

(a) *(b)*

Figure 4.9: a) coefficient B and Tauc gap as determined by Swanepoel's method. b) E_U as a function of B

Figure 4.9 (a) shows the evolution of B and the Tauc energy gap E_g as a function of the annealing temperature. The values of E_g and B are coherent with the values obtained in the literature, which varies between 1.14 and 1.78 and between 540 and 845 $cm^{-1/2}eV^{-1/2}$ in the work of Fogal *et al.* [125]. The values of E_g are slightly modified with respect to the initial ones. The increase of E_g corresponds to the partial disappearing of intra-band defects. The values of E_g seem to be coherent with the values in literature for polycrystalline silicon [124]. Additionally, the coefficient B is sensitive to the electronic structure. Its evolution gives an insight into an important change of this electronic structure with the annealing.

Several authors plot E_U as a function of B in order to quantify the order of the system. As shown in figure 4.8 (b), we observe a decrease of E_U with B. Zanatta *et al.* [128] also observed such a behaviour and they correlate the decrease of E_U for high values of B to an increase of the order in the material due to crystallization of the film. The evolution of E_U, as shown in 4.8 (b) is thus a further indication of a crystallization of the sample at high annealing temperatures.

In summary, we analyzed silicon thin films by means of transmittance spectroscopy and subsequent numerical simulation. We determined the refractive index, which is of 3.74 at the design wavelength

of the cavity (900 nm) for a thin film annealed at 1100°C. A strong changing of the absorption properties has been found and has been interpreted as a crystallization of the thin film by comparing the behaviour of the thin film to literature.

4.3.3 SiO_2 layer

The transmittance spectrum of a SiO_2 film, deposited on a fused silica substrate does not show reasonable interferences to apply the upper simulation methods, as the refractive indices of film and substrate are nearly identical. Thus, the SiO_2 film has been deposited onto monocrystalline silicon substrates. The nominal deposited film thickness was of 23.4 nm. It was analyzed by means of ellipsometry technique by A. EnNaciri from LPMD at Metz to get access to the refractive index and the thickness of the film. In addition, the thickness was determined by X-ray reflectivity measurements.

The refractive index is presented in the figure 4.9 (a). As in the case of silicon, the curves are very flat in the range of big wavelengths and the refractive index increases for small wavelengths. The increase is much less pronounced than in the case of silicon. The values of the refractive index vary from 1.44 to 1.48. This index does not vary clearly as a function of the annealing temperature (Fig 4.9.b) as we observed a relatively elevated dispersion of the values, but this dispersion can be due to the simple fact that the values are very close to each other and the variations are in the order of magnitude of the experimental errors. The absorption is not represented because it is evidently equal to zero in the analyzed spectral range.

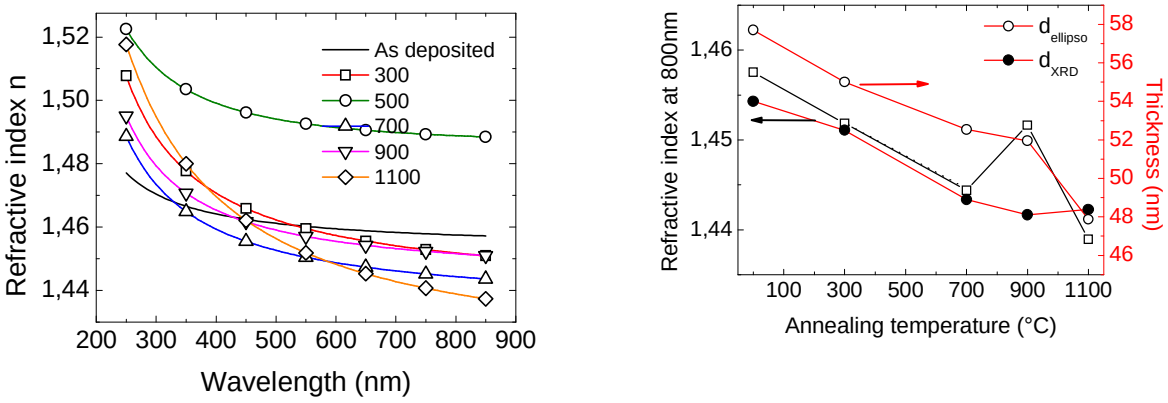

(a) *(b)*

Figure 4.10: (a) Refractive index of a SiO_2 layer determined by ellipsometry as a function of the annealing temperature. (b) Refractive index at 800 nm as a function of the annealing temperature

Ellipsometry also allows us to determine the thickness of the films. In addition, the thickness was measured by glancing angle X-ray reflectivity. As in the case of silicon, X-ray reflectivity measurements also show a densification of the films as a function of annealing temperature, (see figure 4.9 (b)). Effectively, this effect is much less pronounced than in the case of silicon as now, the relative variation of the thickness is only of about 11% after the annealing at 1100°C.

In summary, we analyzed SiO_2 thin films by means of ellipsometry and subsequent numerical simulation. We determined the refractive index, which is of 1.44 at the design wavelength of the cavity (900 nm) for a thin film annealed at 1100°C. The tendency of the thin film to densification during high temperature annealing has been found on the SiO_2 thin film, too.

4.3.4 Active SiO/SiO_2 layer

As in the final sample design, the main parameters to influence the resonance wavelength of the microcavity are thickness and refractive index of the optically active layer, it is necessary to study the optical properties of a SiO/SiO_2 multilayer.

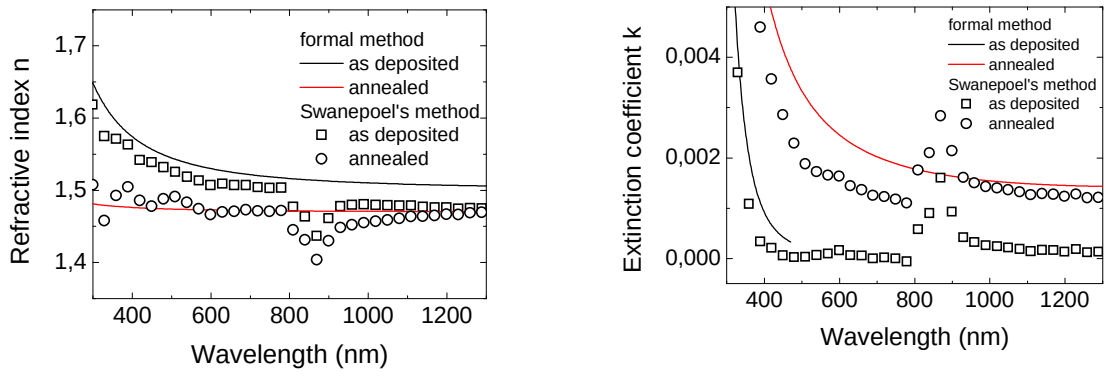

(a) *(b)*

Figure 4.11: optical properties of the active layer: (a) refractive index; (b) extinction coefficient as a function of the wavelength.

Figure 4.10 (a) and (b) report the refractive index as a function of the wavelength for the as-deposited sample as well as for the one annealed at 1100°C. For the as deposited sample, the refractive index is higher, equal to 1.51 at high wavelengths and it increases for wavelengths below 600 nm. After the annealing, the refractive index is equal to 1.48. Generally, the refractive indices do not vary much as a function of the wavelength. The extinction coefficient is relatively weak for the as-deposited sample whereas it is slightly increased after the annealing.

4.4 Distributed Bragg reflectors

4.4.1 Influence of the number of dielectric pairs

The quality factor of a cavity depends on the reflectivities R_1 and R_2 of the distributed Bragg reflectors surrounding the cavity:

$$Q = \frac{2nd\pi(R_1R_2)^{1/4}}{\lambda(1-(R_1R_2)^{1/2})}, \tag{4-5}$$

where

$$R = \left(\frac{1-\frac{n_S}{n_0}\left(\frac{n_L}{n_H}\right)^{2N}}{1+\frac{n_S}{n_0}\left(\frac{n_L}{n_H}\right)^{2N}} \right)^2 \text{ in the case of an even number N of dielectric pairs} \tag{4-6}$$

$$R = \left(\frac{1-\frac{n_L}{n_0}\frac{n_L}{n_S}\left(\frac{n_L}{n_H}\right)^{2N}}{1+\frac{n_L}{n_0}\frac{n_L}{n_S}\left(\frac{n_L}{n_H}\right)^{2N}} \right)^2 \text{ if the number of dielectric pairs N is odd} \tag{4-7}$$

Thus, the quality factor depends on the number N of dielectric pairs in each distributed Bragg reflector [129]. In fact, Q increases with N and we have interest to choose a high value for N. Contrary to this requirement, evaporated films which have a too elevated thickness undergo mechanical stress that induces a detachment of the films and thus their destruction. This constraint obliges us to reduce the number of dielectric pairs. For the first time, we studied the influence of the number of dielectric pairs on the transmittance spectrum of the distributed Bragg reflector, in order to determine the minimum number of dielectric pairs that are necessary to observe a notable cavity effect.

The study of the Si and SiO_2 thin films allowed us to determine the refractive indices of those materials at 800 nm which are of 3.9 and 1.6, respectively. Thus, we fabricated a series of distributed Bragg reflectors in the way that the optical thickness of each dielectric layer was of $4n \cdot e=800$ nm. Since 800 nm is the wavelength of the maximum intensity of the photoluminescence of the silicon nanocrystals, it is chosen to be the design wavelength of the stop-band of the distributed Bragg reflectors and the distributed Bragg reflector based cavities. With the above-mentioned refractive indices, we obtained thicknesses to be deposited of 51.3 and 125 nm, respectively.

For check of feasibility and long term reliability of the evaporation process, we deposited Si/SiO_2 based distributed Bragg reflectors stacks of increasing number of Si/SiO_2 sequences, increasing from 2 to 5.

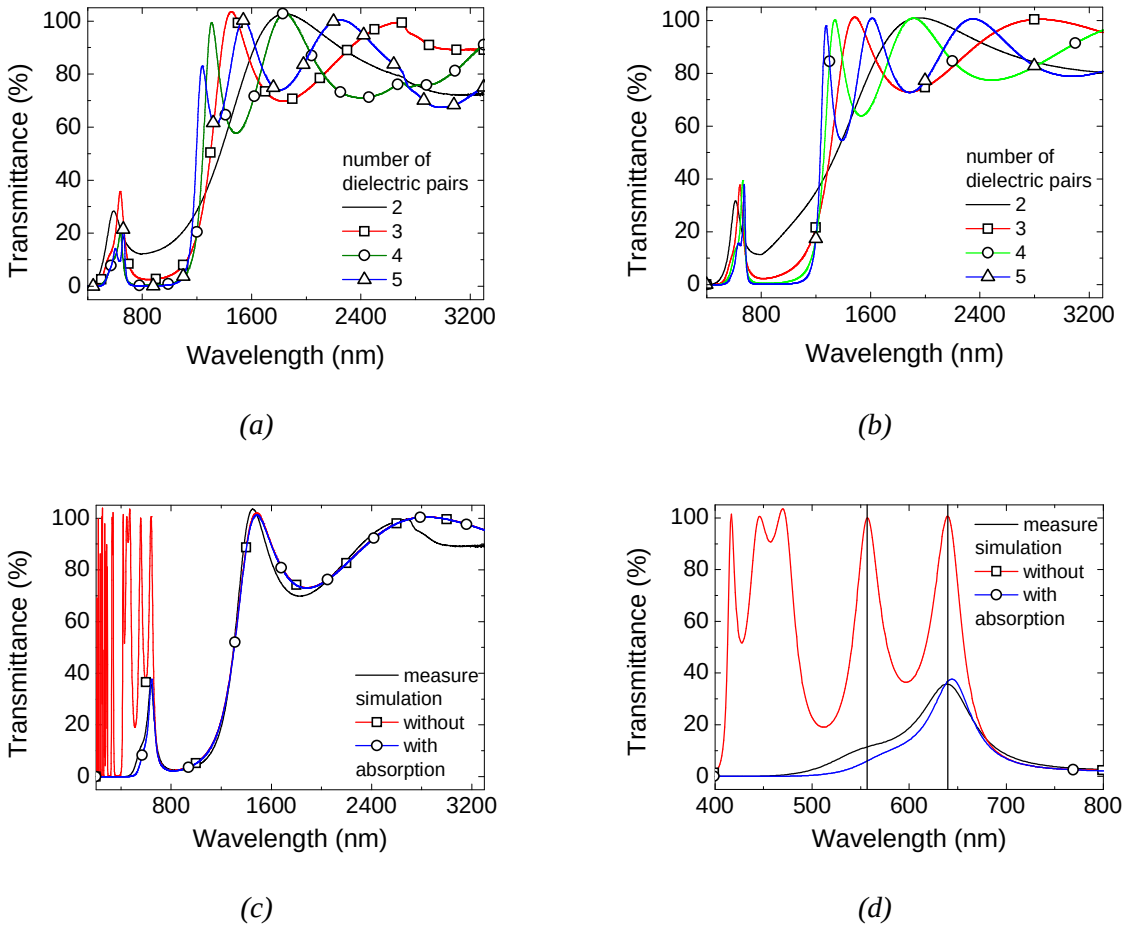

Figure 4.12: comparison of measured and simulated transmittance spectra of the DBR. (a) Experimental UV-VIS-NIR-transmittance spectra of Si/SiO_2-DBRs; (b) Simulated UV-VIS-NIR-transmittance spectra of Si/SiO_2-DBRs; (c) Simulated UV-VIS-NIR-transmittance spectra of Si/SiO_2-DBR consisting of 3 dielectric pairs; (d) Comparison of simulation and measurement in a short wavelength range.

The experimental UV-VIS-NIR transmittance spectra are presented in figure 4.11 (a). Destructive interference creates a more and more marked stop band as the number of Si/SiO_2 sequences was increased. For more than three sequences, the transmittance of the distributed Bragg reflectors was of less than 1% in the spectral range of the stop band. The wavy structure of the spectra at wavelengths exceeding 1100 nm is due to interferences of waves that are not in the Bragg condition.

Figure 4.11 (b) shows a simulation of the transmittance spectra of as deposited distributed Bragg reflector stacks with increasing number of dielectric pairs with the appropriate values of refractive index and thickness, respectively.

The simulation confirmed our measurements that have shown a steeper stop-band and a decreasing transmission as a function of the number of dielectric pairs. The general evolution of the interferences was remarkably close to the experimental data for wavelengths exceeding 1100 nm. This is shown in figures 4.11 (c) and (d), using the example of the Bragg reflector consisting of three Si/SiO_2 dielectric pairs.

However, for shorter wavelengths, especially lower than about 700 nm, simulated and measured data strongly differed. Indeed, the simulations showed the stop-band as expected from the theory, whereas

for shorter wavelengths, the transmission wasn't of 100% any more, but only of about 20-30%. This disagreement is certainly due to the fact that, in the beginning, the absorption of the silicon layers, as determined in section 4.2.2.1 was not yet taken into account in the simulation. The simulated spectra taking into account the absorption are shown as the blue line (circles) in figures 4.11 (c) and (d).

The comparison of simulation and measurement showed the quality of the simulation codes. Using the determined values of the indices and the corresponding thicknesses, the simulated spectra fitted well the measured spectra. Nonetheless, there were remaining differences in the spectra, as can be seen e.g. in the higher wavelength part (from about 1000 nm – 2400 nm) of the spectrum shown in figure. This may be due to inhomogeneities of the thickness of the different layers during the evaporation. Indeed, TEM cross section analysis revealed an inhomogeneity especially of the thickness of the SiO_2 layers.

A final confrontation of the simulated and the measured reflectivity as a function of the number of dielectric pairs proved a good agreement of simulation and measurement. The remaining, very small differences may be due to the influence of the inhomogeneities of the thickness of the single dielectric layers.

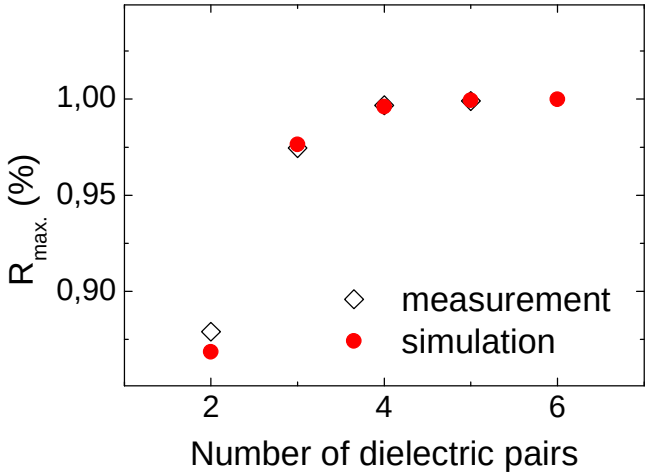

Figure 4.13: The maximum reflectance of DBR is in good agreement with the theoretical prediction.

In summary, in this preliminary section, we analyzed the influence of the number of dielectric pairs on the maximum reflectance of a distributed Bragg reflector. For experimental reasons, we considered the transmittance of distributed Bragg reflector samples by means of UV-VIS-NIR transmittance spectroscopy and subsequent simulation. Measurements and simulations have been found to be in good agreement. We found that, for our materials, the number of dielectric pairs should be at least three for having a maximum reflectance in excess of 99 % (Figure 4.13). Nonetheless, there have been some small deviations between measurement and simulation. Those will be investigated in the following section and in the section concerning the microcavities.

4.4.2 Influence of the annealing temperature

By examining the single layers in section 4.2.2.2 we noticed that the thermal treatments provoked a strong reduction of the thickness of the layer and a slight increase of the refractive index. As the optical thickness of a layer is defined as

$$d_{opt.} = d_{real} \cdot n, \tag{4-8}$$

the change of thickness and refractive index could influence the optical properties of a sequence of dielectric layers.

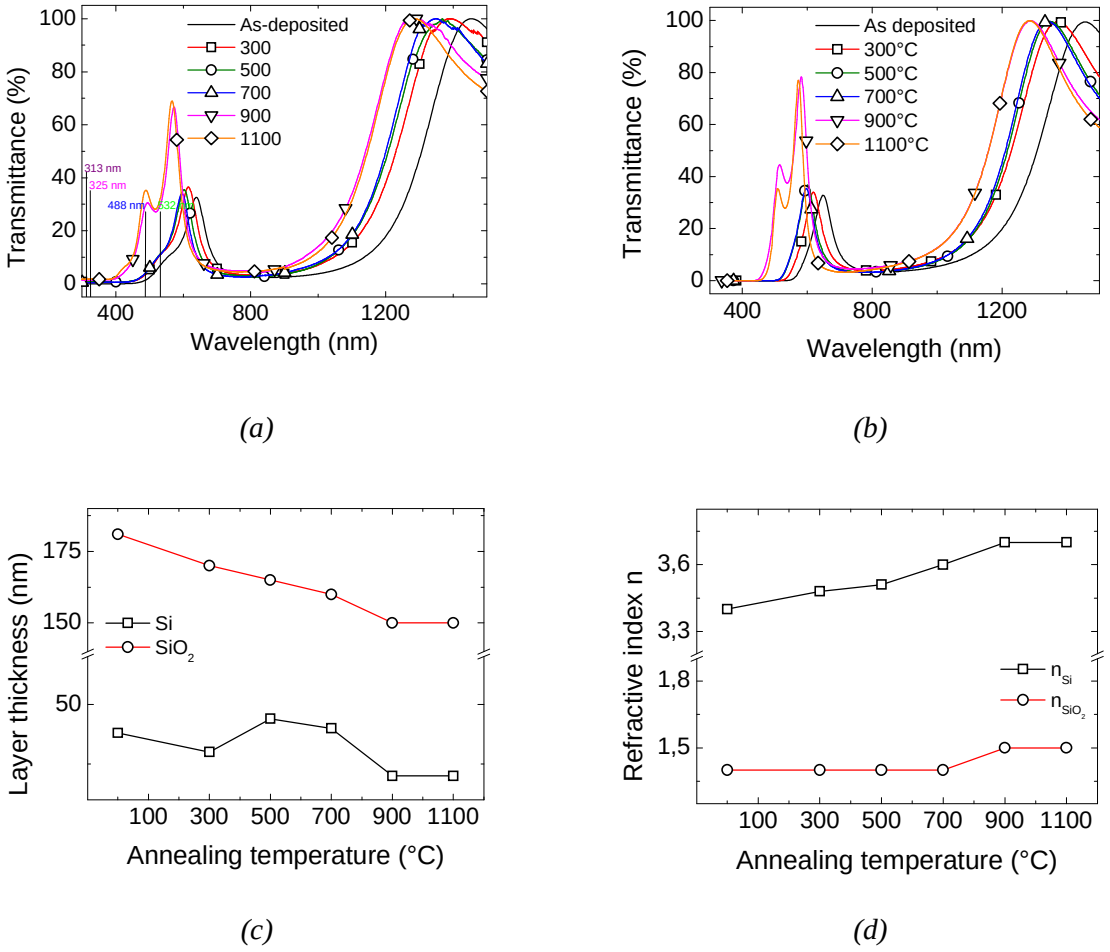

Figure 4.14: experimental (a) and simulated (b) UV-VIS-NIR spectra of a DBR containing three Si/SiO_2 layer pairs for different annealing temperatures; the laser wavelengths that are available in the laboratory are marked in (a); (c) layer thickness of silicon and SiO_2, respectively, as a function of annealing temperature; (d) the refractive index at 800 nm as a function of annealing temperature, as employed during the fit.

Figure 4.14 (a) shows the ensemble of experimental transmittance spectra obtained from a distributed Bragg reflector containing three Si/SiO_2 dielectric pairs, as deposited and annealed at temperatures ranging from 300°C to 1100°C. Figure 4.13 (b) shows the ensemble of simulated transmittance spectra. These have been obtained by taking into account the corresponding refractive indices and the densification behaviour of the thickness of the appropriate single thin films of Si and SiO_2.

With increasing annealing temperature, all transmittance spectra are blueshifted. The observed blueshift is of about 100 nm for an annealing temperature of 1100°C.

The thicknesses are summarized in 4.13 (c). The thickness of the SiO_2 layer is reduced by 17%, the thickness of Si by 20%. In contrary, the refractive indices which are resumed in 4.13 (d) are increased by only 7% and 9%, respectively.

Thus, this blueshift indicates that the influence of the decrease of the thickness rules out the influence of the increase of the refractive index. In other words, the optical thickness of the films is reduced.

4.4.3 Importance of the layer thickness

As we have seen in figure 4.13 (c), the thickness of the single components of the distributed Bragg reflectors is susceptibly reduced. In the following, we will investigate by simulation, what is the necessary thickness accuracy to design proper distributed Bragg reflectors.

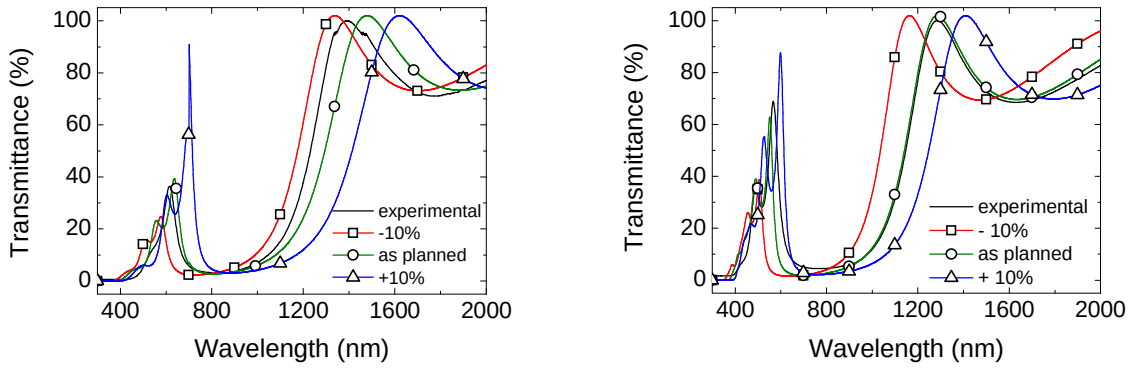

(a) *(b)*

Figure 4.15: influence of the layer thickness on the optical transmission properties of a DBR based on three Si/SiO_2 dielectric layer pairs; (a) transmittance of the as deposited sample as a function of the wavelength; (b) transmittance of the sample annealed at 1100°C as a function of the wavelength.

Figure 4.15 shows transmittance spectra of a distributed Bragg reflector containing three Si/SiO_2 dielectric pairs. In both figures, the experimental spectrum is compared to theoretical spectra. During the simulation, the layer thickness of both layers was stepwise changed by +/- 10%. For figure (a), we employed the refractive indices and the thicknesses of the as-deposited material. For figure (b), we employed the refractive indices and the thicknesses of the thin films annealed at 1100°C.

An important blue-shift of the entire spectrum is observed for decreasing layer thickness. This can be explained by the fact that the design wavelength of the distributed Bragg reflector depends on the thickness of the layers

$$\lambda_{DBR} = 4 \cdot n \cdot e. \qquad (4\text{-}9)$$

If the films in the sample are densified, this induces a blue-shift, which is proportional to the reduction of the thickness.

In summary, we have seen that the high temperature annealing induces a blue – shift of the photonic stopband. Simulations have proved that this shift is due to a reduction of the layer thickness during the annealing which rules out the increase of the refractive index at the same time. Thus, for the fabrication of the microcavities which will have to be annealed at 1100°C, we will design the distributed Bragg reflector in a way that the layer thickness is of

$$d_{dep.} = \frac{d_{ann.}}{1-x}^{Bragg} = \frac{800}{4n_{ann.}(1-x)} = \frac{800}{4n_{dep.}(1-y)(1-x)} \qquad (4\text{-}10)$$

where $d_{dep.}/n_{dep.}$ and $d_{ann.}/n_{ann.}$ are the thickness and refractive index of the as deposited and annealed film, respectively. x and y are the observed percentages of reduction of thickness and refractive index. By this formula, we can calculate the thickness to be deposited for the two films in order to obtain a stop-band at 800 nm, the wavelength of maximum photoluminescence intensity of silicon nanocrystals. The thickness is of 160.6 nm in the case of SiO_2 and of 67 nm in the case of silicon.

4.5 Microcavities

After the determination of the optical constants on the single layers and the analysis of the influence of the thermal treatment on the distributed Bragg reflectors, we finally consider complete microcavity samples.

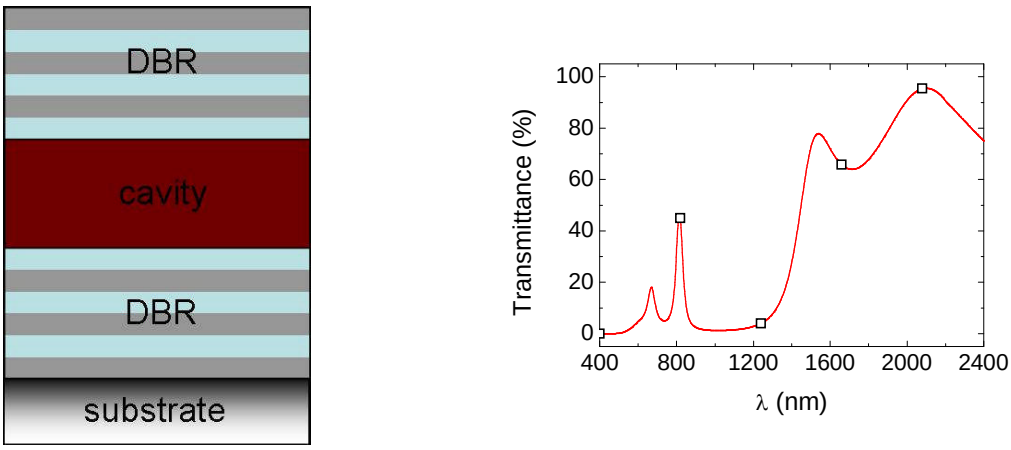

(a) (b)

Figure 4.16: (a) sketch of an optical microcavity; (b) typical transmittance spectrum of an optical microcavity with a resonance feature at a wavelength of 800 nm.

Figure 4.16 (a) shows a sketch of the structure of an optical microcavity. The optically active layer is called cavity. It is surrounded by the wavelength selective distributed Bragg reflectors, which have been investigated in the precedent section. Figure 4.14 (b) shows a typical transmittance spectrum of an optical microcavity. The low transmittance part between 600 nm and 1600 nm corresponds to the stop-band of the Bragg mirrors, whereas the fine high transmittance feature at 800 nm is due to the

equality of half an integer multiple of this wavelength with the optical thickness n·e of the optical cavity, the so called Bragg condition

$$\lambda_{res.} = 2\, n \cdot e. \tag{4-11}$$

In the following, we shall first examine the influence of the quality of the Bragg mirrors on the quality of the microcavities by simulation of the transmittance spectra. Here, it is important to analyze the influence of the number of the dielectric pairs per Bragg mirror on the quality of the microcavity. In addition, it has been shown that the regularity of the thickness of the dielectric layers is important for the design of the resonance wavelength of the cavity, too.

After these preliminary considerations, the samples were fabricated. Two sets of samples have been fabricated: one consisting of two Si/SiO_2 pairs per Bragg mirror, and one consisting of three Si/SiO_2 pairs per Bragg mirror. The samples have been analyzed by means of transmission measurements and photoluminescence spectroscopy, as well as transmission electron microscopy.

4.5.1 Influence of the number of dielectric pairs in the Bragg mirrors

As we want to observe silicon nanocrystals in the weak coupling regime with the cavities, the crucial parameter to discuss is the Purcell factor

$$F_p = \frac{3Q(\lambda/n)^3}{4\pi^2 V} \tag{4-12}$$

It depends on two significant entities: the mode volume V, i.e. the volume that is filled by the stationary light wave, and the quality factor Q that depends on the reflectivity of the Bragg reflectors, which – amongst others – depends on the number of dielectric pairs N. As the quality factor depends exponentially on the number of dielectric pairs (see figure 4.17 (b)), we finally have to do a trade off between the number of dielectric pairs and the technical limits of the evaporation process.

Typically, the total thickness of a film deposited by thermal evaporation cannot exceed one micron. Thus, we deposited two and three dielectric pairs per Bragg reflector, respectively.

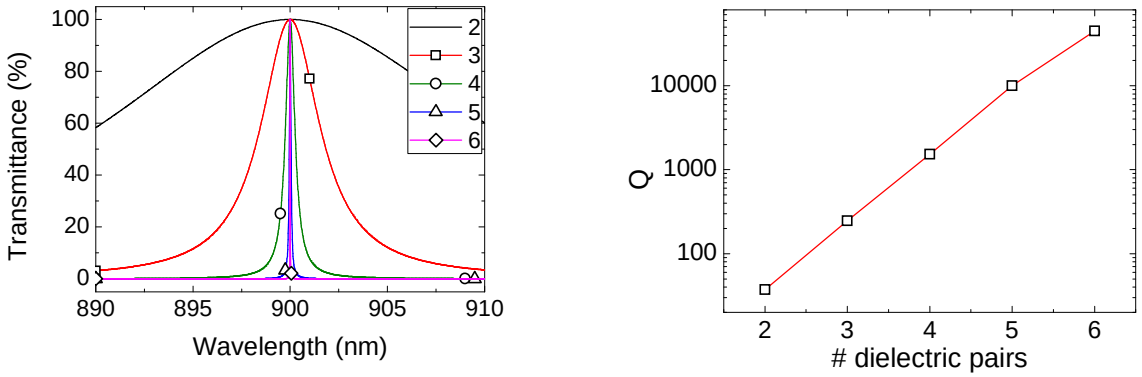

(a) (b)

Figure 4.17: (a) Simulated resonance peak for an increasing number of dielectric layer pairs; (b) Logarithmic plot of the quality factor of the cavity parallel to the direction of sample growth.

In summary, we have shown that the quality factor of the cavity depends exponentially on the number of dielectric pairs. For technical limitations of the evaporation technique, we are limited to a total thickness of about 1.5 µm, which corresponds to the thickness of a microcavity consisted of three Si/SiO_2 dielectric pairs at each side of the silicon nanocrystal layer.

4.5.2 Fabrication of the cavities and study of their thermal stability

For the single layers, we observed a crystallization process at high annealing temperatures. This process could, together with structural stress during the high temperature annealing, lead to a detachment of the film and thus to its destruction. We effectuated high temperature treatments of the cavities and analyzed them by means of transmission electron microscopy. The results and implications of this analysis will be detailed in the following section.

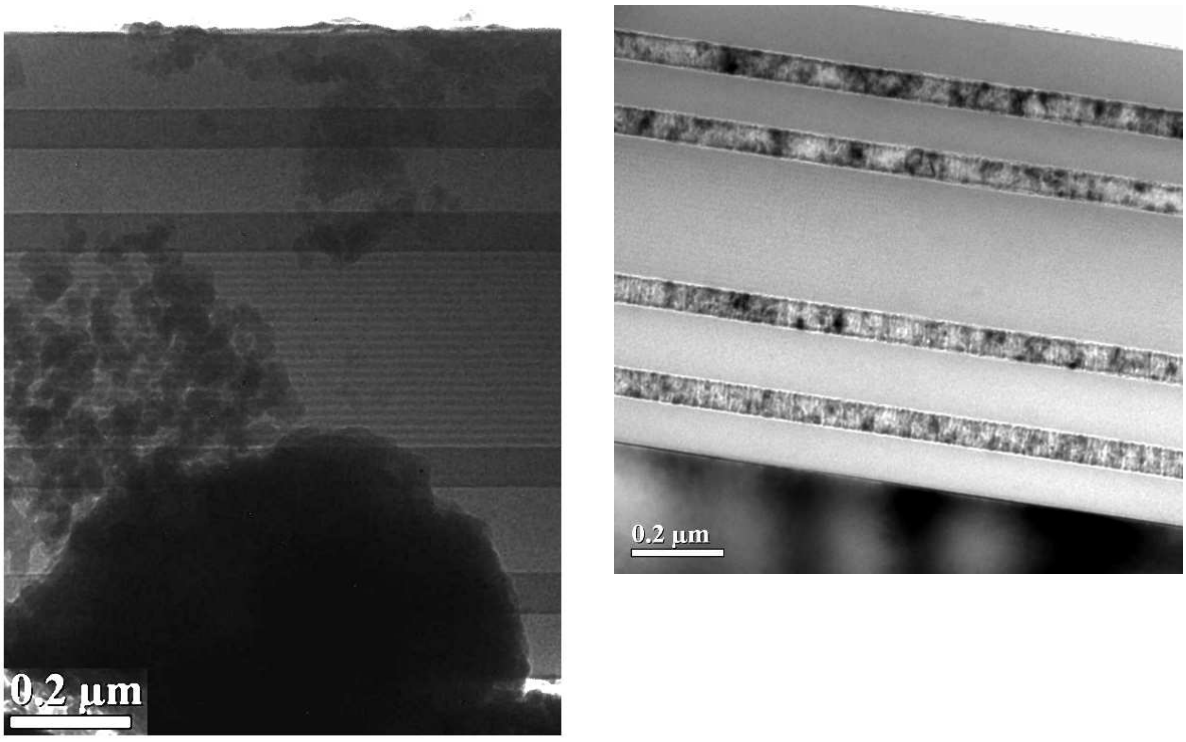

(a) *(b)*

Figure 4.18: cross-sectional transmission electron micrographs of a microcavity based on two pairs of Si/SiO_2 layers and the active layer of SiO/SiO_2 multilayers. (a) as deposited; (b) annealed at 1100°C

Even if the single layers of Si and SiO_2 withstand the high temperature annealing up to 1100°C, it is not evident that the entire microcavity will do so, too. Therefore, we prepared and observed by transmission electron microscope as-deposited (a) and annealed samples (b) which are shown in figure 4.18. The images (a) and (b) show well visible layers for the distributed Bragg reflectors. The periodicity is well preserved, even if we have sometimes difficulties to maintain the different thicknesses constant. For this reason, we will study in paragraph 4.5.5 the influence of a disturbance of the periodicity of the layers on the transmittance spectrum. The interfaces are flat, which indicates that there is no appreciable interdiffusion between Si and SiO_2, even after high temperature annealing. The silicon layer is amorphous in the annealed sample, whereas it is polycrystalline if annealed at high

temperature. This is a direct confirmation for the indications of crystallization that we found in the section on the single components. The multilayered structure of the active layer is also observed for the annealed sample. These figures show the high stability of the microcavities even after high temperature annealing. We also found that the annealing improves the adhesion to the substrate.

In summary, the high temperature annealing does not lead to a destruction of the microcavity samples. Transmission electron microscope images revealed that the thicknesses of all layers are almost correct. The surfaces are flat and the crystallization of the silicon layer that was supposed on the silicon thin films is directly confirmed.

4.5.3 Importance of a constant layer thickness

While investigating the thermal stability of the microcavities, it was noticed that especially the thickness of the SiO_2 layers was not completely constant over all layers. It seems that the deposition rate of the SiO_2 layer was not constant throughout the whole deposition process, even if the quartz oscillators measured a correct deposition rate during the deposition of the SiO_2 layers. Indeed, the electron beam created a crater in the crucible and there is certainly a problem with shadowing of the SiO_2 flow coming from the bottom of the crater. We carefully shifted the electron beam before the deposition of each SiO_2 layer, respectively, in order to reduce this effect.

The silicon layers are deposited from a crucible containing melted silicon, so there is no possibility for such a kind of effect as observed during the deposition of the SiO_2 layers. Indeed, no remarkable thickness variation was observed in the transmission electron microscope. Nonetheless, a densification of the layers during the annealing was observed as for the single layers in the section above.

The quality factor as shown in 4.17 (b) is the ideal value as simulated for perfectly homogeneous dielectric layers inside the cavity. In order to get an idea of the necessary precision of the deposition of SiO_2 layers, we simulated a series of spectra, reported in figure 4.19. The graph shows the influence of the irregularity of the thickness of only one single SiO_2 layer (red one) in a cavity based on two dielectric layer pairs at each side of the active layer. The quality factor Q was influenced by variations of thickness of the layers. Deviations of about 75% induce a reduction of the quality factor by a factor 2. The resonance wavelength is influenced by the variation, as well. As it can be seen, a realizable thickness accuracy of about 10% would mean a maximum reduction of the quality factor by only about 5% and a variation of the resonance wavelength of +/- 4 nm.

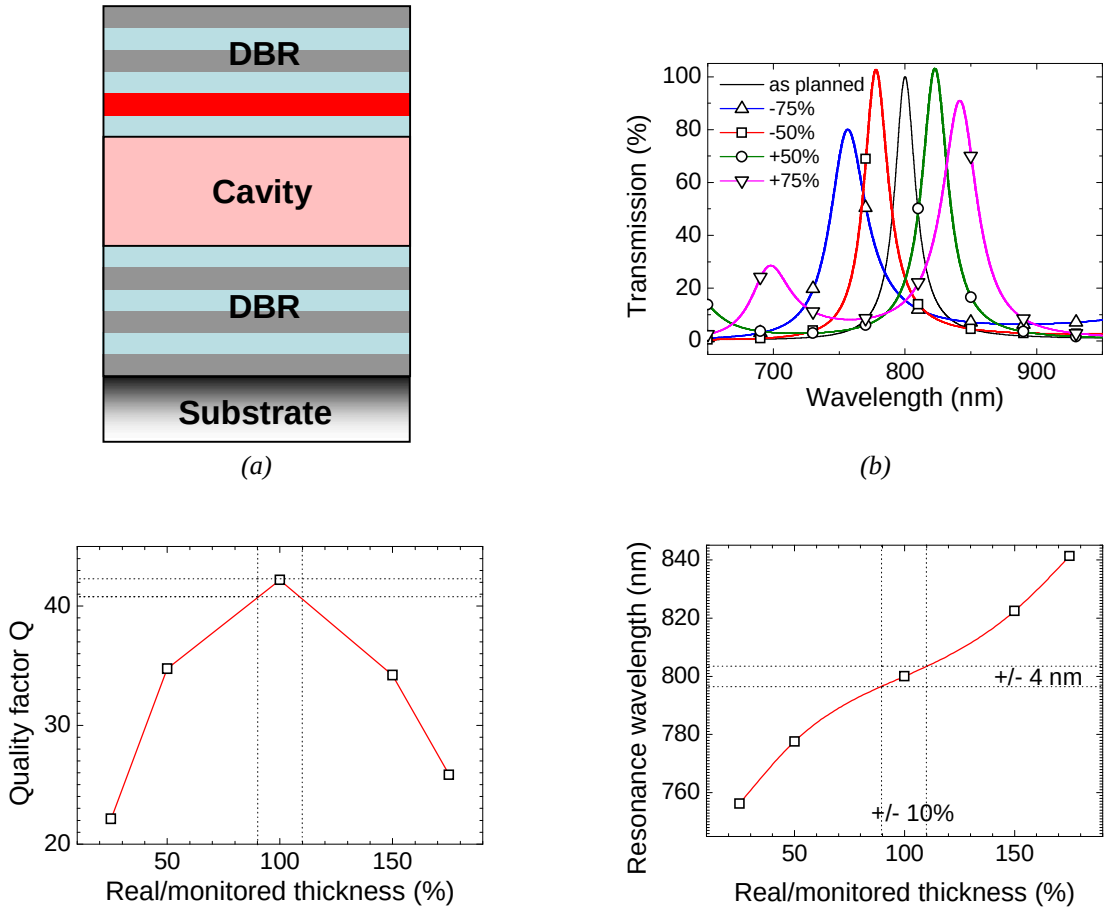

Figure 4.19: Importance of a constant SiO_2 layer thickness (a) sketch of the microcavity, the considered layer is marked in red; (b) simulated transmittance spectra as a function of the wavelength; (c) influence of the layer thickness on the quality factor; (d) influence of the layer thickness on the resonance peak.

In the same way, we simulated a series of spectra for variations of the thickness of one silicon layer (marked in red), reported in figure 4.20, which show the influence of the irregularity of the thickness of only one single silicon layer in a cavity based on two dielectric pairs at each side of the active layer. As for the SiO_2 layers, the quality factor Q was influenced by variations of thickness of the silicon layers. Deviations of about 75% induce a reduction of the quality factor that is less than the reduction induced by the variation of the SiO_2 layer. The resonance wavelength is influenced by the variation, as well. As it can be seen, a realizable thickness accuracy of about 10% would mean a maximum reduction of the quality factor of less than 5% and a variation of the resonance wavelength of +/- 10 nm.

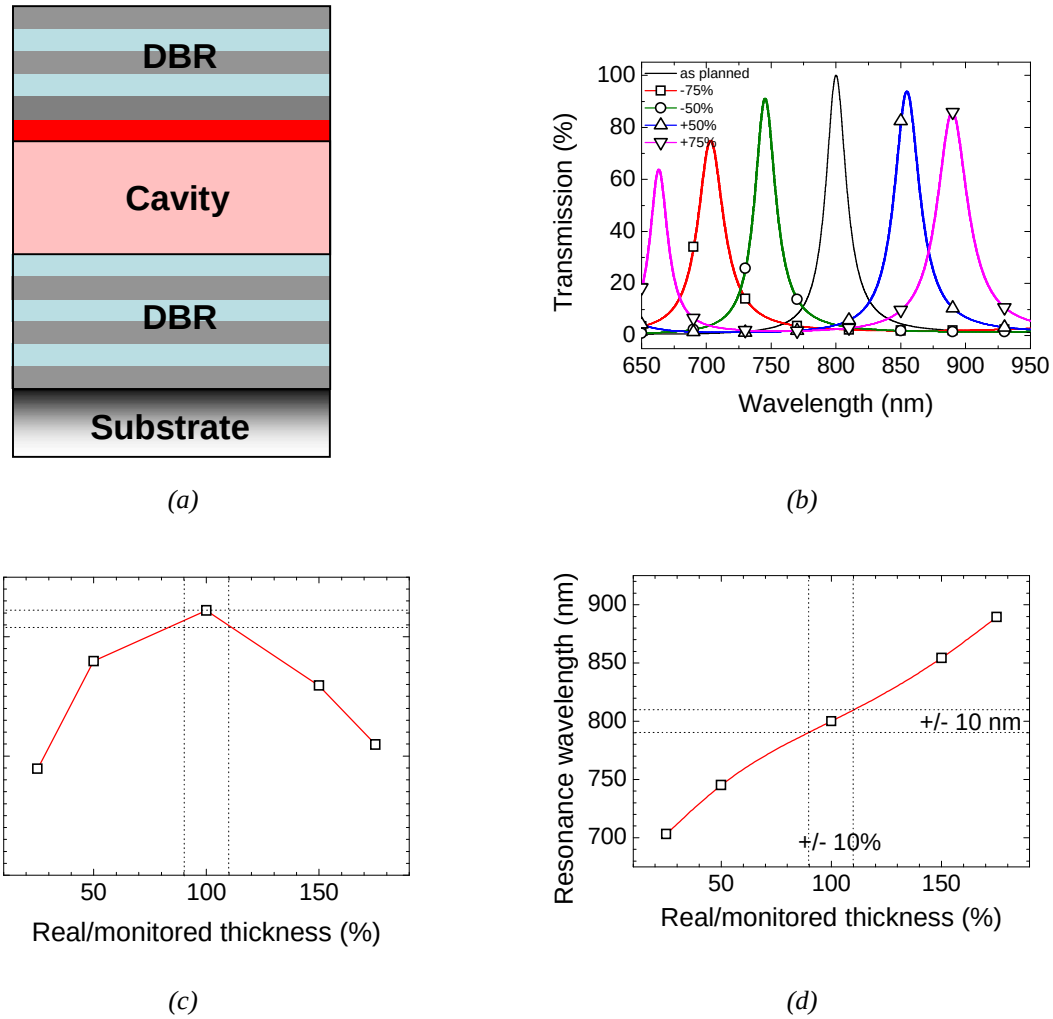

Figure 4.20: Importance of a constant silicon layer thickness (a) sketch of the microcavity, the considered layer is marked in red; (b) simulated transmittance spectra as a function of the wavelength; (c) influence of the layer thickness on the quality factor; (d) influence of the layer thickness on the resonance peak.

In summary, the quality factor and the resonance wavelength depend on the regularity of the layer thickness, but the sensibility is not dramatic since fluctuations of 10% in the thickness induce variations of a few percents in the quality factor and a shift of a few tens of nanometres in the resonance peak position.

4.5.4 Influence of the thermal annealing on the transmittance spectra of the cavity

The annealing does not only improve the adhesion and the structural stability, but also has a strong influence on the density of the films. As already shown for the case of the components as well as the distributed Bragg reflectors, the annealing induces a densification of the film and an increase of the refractive index. In this section, we will evaluate the influence of this phenomenon on the resonance peak of a microcavity.

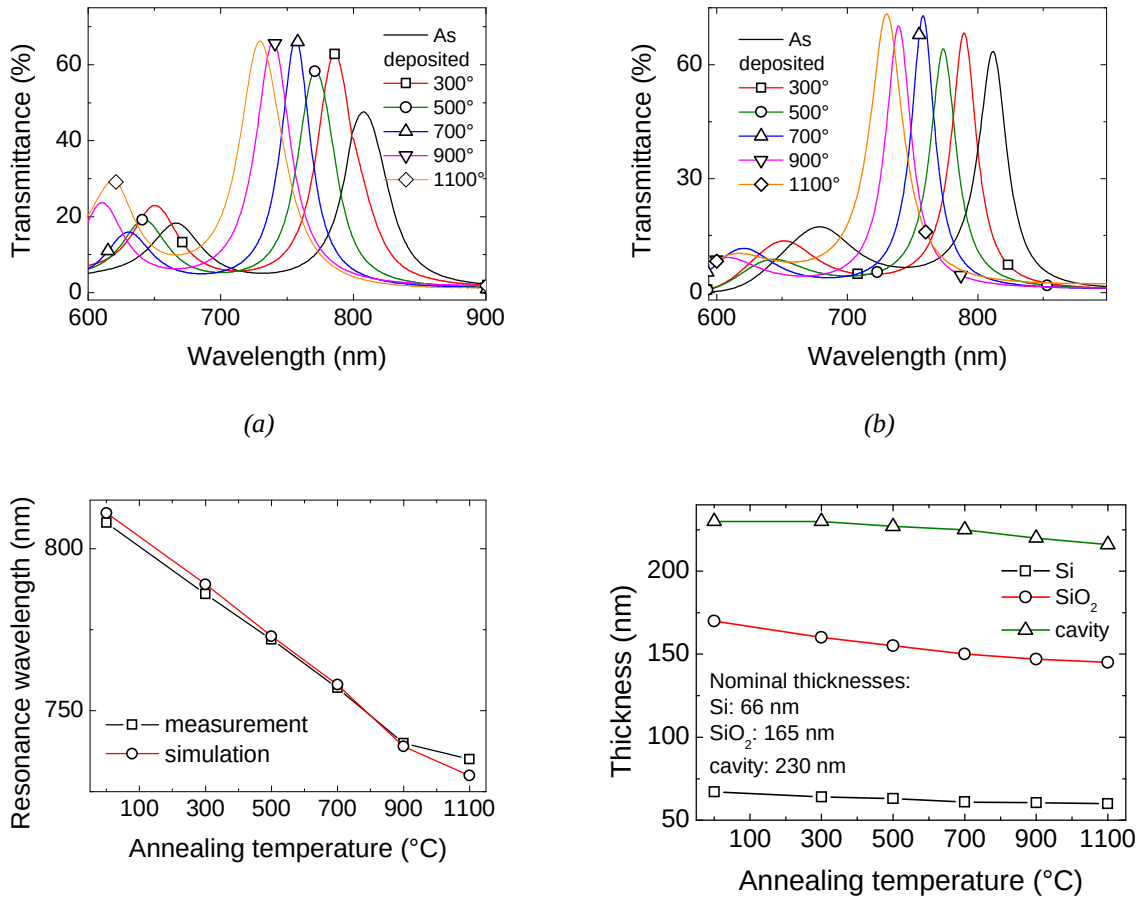

Figure 4.21: (a) Experimental transmittance spectra for different annealing temperatures; (b) simulated transmittance spectra for different annealing temperatures; (c) resonance wavelength as a function of the annealing temperature; (d) thickness as a function of the annealing temperature.

As in the case of the distributed Bragg reflector, the densification plays the leading role compared to the increase of the refractive index, and the experimental spectra show a very regular blue-shift with increasing annealing temperature. The coefficient of this blue-shift is of 0.068 nm/°C. We have tried to simulate this evolution by modifying the thickness of the layers of the distributed Bragg reflectors taking account of the evolution with annealing of the pure Si and SiO_2 layers. This evolution is shown in figure 4.21 (d). The thickness of the Si, SiO_2 and the active layer is reduced by 10, 15 and 6 %, respectively.

In summary, in this section, we investigated the influence of the annealing on the resonance peak of the cavity. As in the case of single layers and distributed Bragg reflectors, we observed a densification of the layers as well as an increase of the refractive indices. The resonance peak is blue-shifted by 0.068 nm/°C through high temperature annealing.

4.5.5 Influence of the thickness of the active layer

The thickness of the active layer, which varies with the annealing, is another important parameter that has a direct influence on the resonance wavelength, as is expressed by the Bragg condition. Figure 4.22 (a) shows the experimental transmittance spectra of four cavities that contain active layers of different thicknesses. As expected, the resonance feature red-shifts with increasing thickness (characterized by the number of SiO/SiO_2 bilayers) of the active layer (see figure 4.22 (b)).

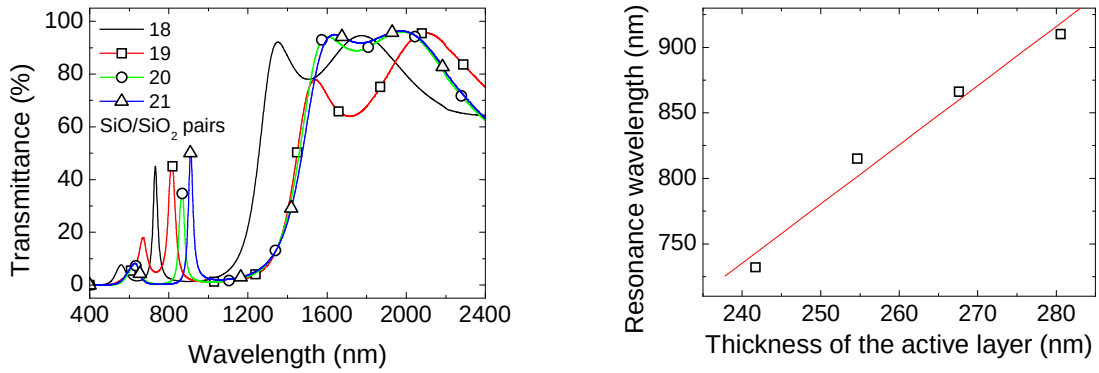

(a) *(b)*

Figure 4.22: (a) experimental transmittance spectra as a function of the wavelength. The thickness is characterized by the number of SiO/SiO_2 bilayers; (b) the resonance wavelength as a function of the thickness of the active layer.

The shift of the wavelength is of 4.5 nanometers per one deposited nanometer. This means that, e.g. a thickness deviation of about 20 nm will cause a significant shift of the resonance peak of about 90 nm. The thickness of the active layer is therefore a very important parameter for the control of the characteristics of the microcavity. This explains why it is necessary to take account of the variation of the thickness of the active layer to fit the evolution of the resonance wavelength with annealing.

4.6 Photoluminescence

4.6.1 Choice of the excitation wavelength

Usually, photoluminescence measurements on bare silicon nanocrystals are mostly done by using an excitation source in the ultraviolet range of the spectrum, as the excitation energy is higher than the gap of these nanocrystals. For example, figure 4.23 (a) shows the photoluminescence intensity at 780 nm of a reference sample containing silicon nanocrystals for the different emission lines of the mercury lamp, the photoluminescence intensities having been corrected by the relative intensities of the mercury emission lines. The photoluminescence increases when the excitation wavelength decreases and it was found to be extremely effective with an excitation at 313 nm. In fact, for the lower wavelengths, defects of the silica matrix are also excited and they participate to the luminescence at 780 nm.

For the photoluminescence experiments on silicon nanocrystals embedded in optical microcavities, an excitation in the UV risks to be inefficient, because of the strong absorption of the silicon layers and of the reflectivity of the Bragg reflectors in this spectral range as determined in the section above.

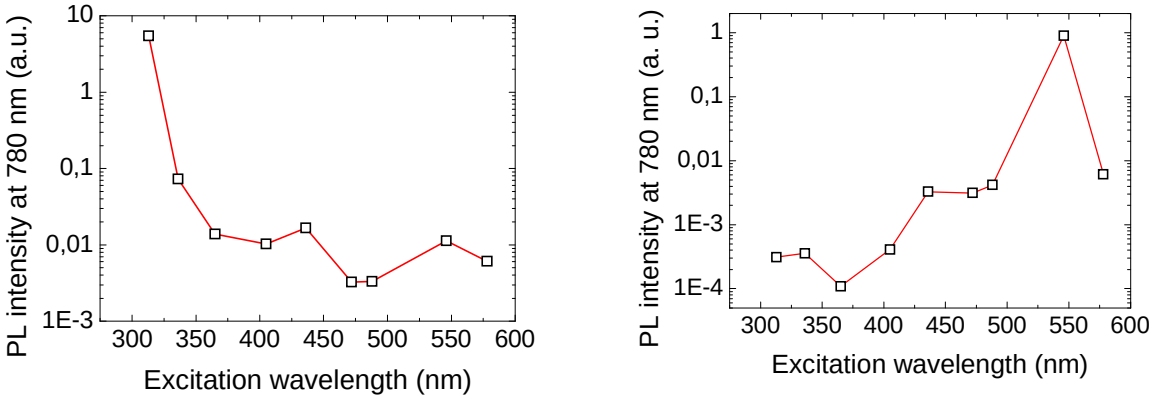

(a) *(b)*

Figure 4.23: PL intensity as a function of the excitation wavelength for (a) a reference multilayer and (b) a microcavity

Figure 4.23 (b) reports the results of the same analysis on a microcavity. For shorter wavelengths, the excitation light is absorbed by the silicon layers of the Bragg reflectors and the excitation is inefficient. The most effective emission was therefore found for an excitation wavelength of 546 nm. Higher excitation wavelengths coincide with the reflexion band of the microcavity and the excitation is reflected.

4.6.2 Microcavity with distributed Bragg reflector containing two Si/SiO_2 bilayers

Spectral selectivity of the microcavity: We use the same setup as before to analyze the spectral properties of the cavity sample. Thus, with the results of the upper section, we chose the 546 nm emission line of the mercury vapour lamp as excitation source.

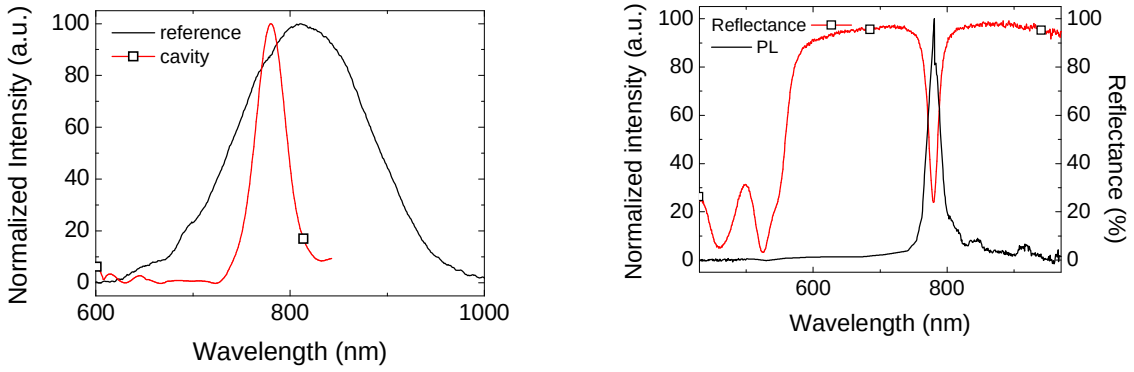

(a) *(b)*

Figure 4.24: (a) experimental photoluminescence spectra of the reference sample and the cavity, respectively; (b) normalized photoluminescence spectrum of the microcavity compared to its reflectance spectrum.

Figure 4.24 (a) reports the photoluminescence spectrum of a reference sample, i.e. an annealed multilayer containing silicon nanocrystals embedded between silica layers, as well as the photoluminescence spectrum of the cavity sample containing the same multilayer as active layer. As expected, even though the silicon nanocrystals are size controlled, the photoluminescence band, which is attributed to silicon nanocrystals is very large, of about 160 nm. It is centred at a wavelength of about 800 nm. On the contrary, the spectral line-width of the cavity was strongly reduced in comparison to the reference sample and is equal to about 25 nm. The sharpness of the spectrum can be correlated to the reflectivity spectrum of the cavity (figure 4.24 (b)), which shows a very sharp dip at 780 nm with a width equal to 25 nm. In addition, the photoluminescence signal of the cavity sample at the resonance wavelength is reduced by a factor 3 with respect to the photoluminescence signal of the reference sample.

This change in the line-width of the photoluminescence emission peak can be explained by the weak coupling between the silicon nanocrystals and the microcavity.

The change in the maximum photoluminescence emission intensity, however, depends on the strength of the coupling, described by the Purcell factor. If it is less than one, the coupling is strong enough to reduce the line-width of the photoluminescence emission, but it is too weak to increase the maximum photoluminescence emission intensity. Moreover, the absorption of the silicon layers in the distributed Bragg reflectors is high in this wavelength range. This phenomenon could contribute to a further reduction of the photoluminescence emission intensity of the silicon nanocrystals that are coupled to the cavity.

In summary, in this section, we investigated a microcavity sample by means of photoluminescence and reflectance spectroscopy. The photoluminescence line-width of the cavity sample is strongly reduced with respect to the reference sample. The photoluminescence measurement is well in agreement with the reflectance spectrum.

Spatial selectivity of the cavity: As the resonance peak depends on the optical length of the different layers of the microcavity, the analysis of the photoluminescence signal of the silicon nanocrystals was carried out as a function of the detection angle, defined as the angle between the entrance of the optical fibre and the surface normal of the sample.

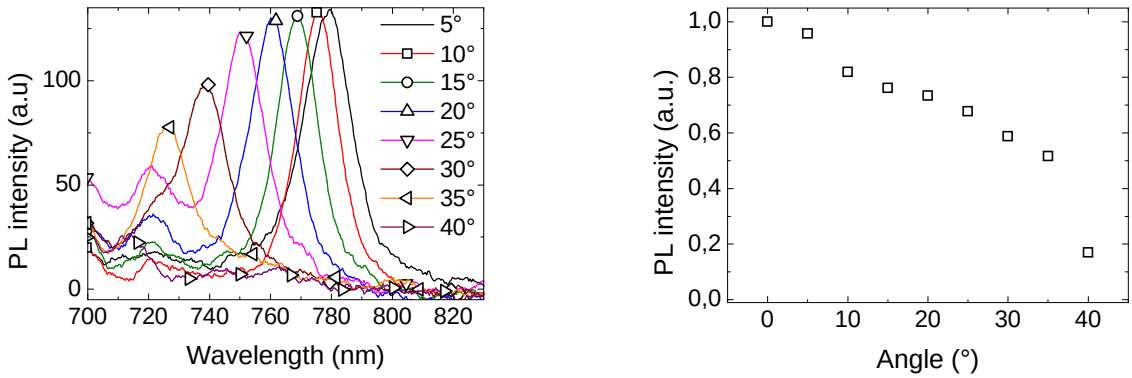

(a) *(b)*

Figure 4.25: (a) PL intensity versus the wavelength for different detection angles; (b) Evolution of the PL intensity versus the detection angle.

Figure 4.25 (a) reports the angle-resolved PL of a cavity consisting of 2 Si/SiO_2 pairs. The intensity is maximum at normal detection, but decreases rapidly as usually observed in those systems [130, 131] (see figure 4.25 (b)). We observe that, at an angle of 35°, from the surface normal the integrated intensity falls to 50% of its maximum value at normal detection.

We also observed a blue-shift of the spectra with increasing detection angle as shown in figure 4.25 (a). This is a result of the shift of the cavity mode coupled to the photoluminescence peak of the silicon nanocrystals. The wavelength shifts as a cosine of the internal cavity angle (which is equal to the observation angle) in order to fullfill the conservation of the average component of the perpendicular component of $\vec{k}$ [131]. The red line in 4.26 (a) shows a fit of this evolution by the equation

$$\lambda = \lambda_{res.} \cos\left(\sin^{-1} \frac{1}{n_a} \sin\theta_{obs} \right) \qquad (4\text{-}13)$$

where $\lambda_{res.}$ denotes the resonance wavelength, n_a the effective index of the cavity and $\theta_{obs.}$ the detection angle.

This correct behaviour of the angle-resolved photoluminescence spectra gives an indication of the good structural quality of the sample. As already mentioned in the section above, the optical density of states is modified by the microcavity. For a better understanding of the phenomenon, figure 4.26 (b) reports the polar diagram of the intensity distribution for both the reference sample (squares) and the microcavity (circles and triangles).

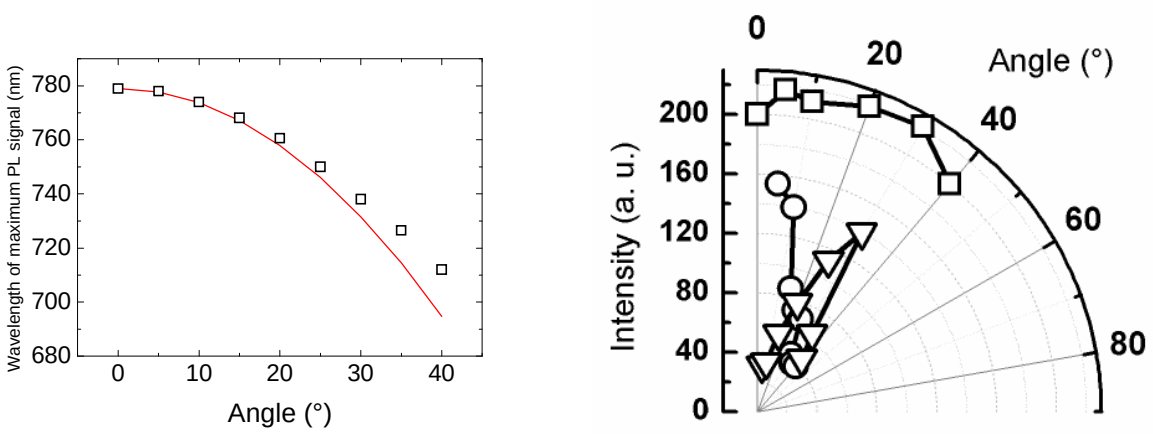

(a) *(b)*

Figure 4.26: (a) position of maximum photoluminescence intensity as a function of the detection angle ; (b) the detection wavelength is 779 nm for the reference multilayer (squares) and for the microcavity (circles), respectively The detection wavelength for the lobe at 30° was of 738 nm (triangles)

We observed a strong modification of the emission characteristic of the reference sample and the cavity, respectively. Whereas the photoluminescence intensity of the reference sample was almost isotropic, i.e. constant over the measured angle range, the photoluminescence of the cavity at the same wavelength was observable only for angles smaller than 15°. As reported by Belarouci and Gourbilleau [121] as well as Amans *et al.* [45], the lobe structure is a strong indication of the mentioned modification of the optical density of states.

In summary, in this section, we investigated the photoluminescence emission of a cavity sample by means of angle-resolved photoluminescence spectroscopy. We found that the emission wavelength is blue-shifted with increasing angle according to the dispersion relation. In addition, with increasing detection angle, the emission intensity is reduced. For the detection along the surface normal, we found an emission lobe of an aperture angle of 15°. This has been interpreted as a modification of the optical density of states from a continuum of modes towards a single permitted mode.

4.6.3 Microcavities with distributed Bragg reflectors containing three Si/SiO_2 bilayers

As observed above, two dielectric pairs are not enough to have a Purcell factor exceeding unity. Figure 4.27 (a) shows that it is possible to obtain even stable microcavities containing three Si/SiO_2 dielectric pairs at each side of the active layer. Nonetheless, the film thickness is about to be critical: it was not possible to prepare thin slices out of the as deposited film. Here we show only the TEM image of the annealed sample. It has been observed that the thickness of the SiO_2 layers was not constant from layer to layer. This can be explained by the creation of a crater in the SiO_2 crucible during the evaporation (see black circle in figure 4.27 (b)). Thus, if a quantity of SiO_2 is evaporated, the walls of the crater inhibit a homogeneous propagation of the vapour.

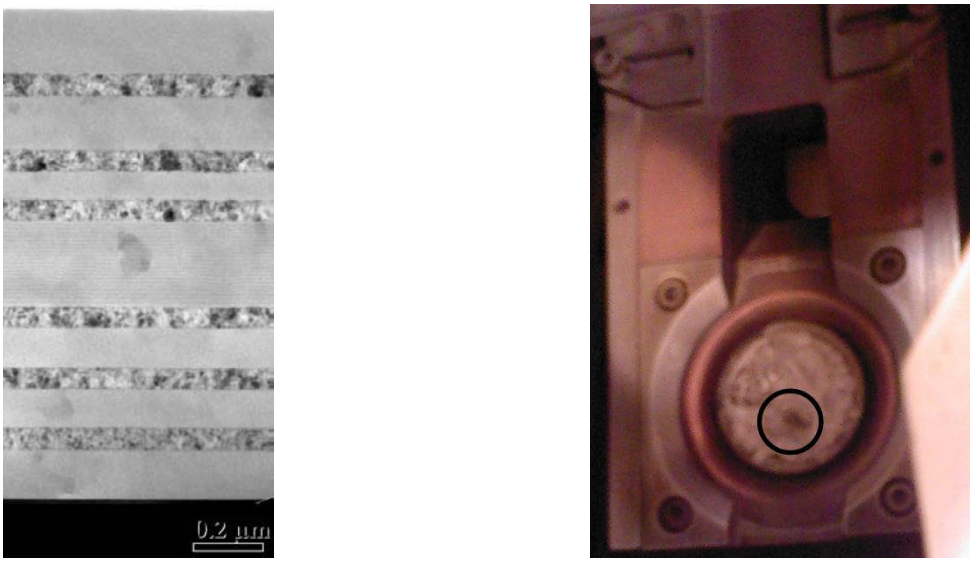

(a) *(b)*

Figure 4.27: (a) TEM image of a cavity containing three Si/SiO_2 dielectric pairs per distributed Bragg reflector; (b) Black circle: crater in the SiO_2 crucible causing inhomogeneities of SiO_2 layer thickness, e.g. in the upper SiO_2 layer of the cavity sample shown in (a).

Figure 4.28 (a) shows a reference spectrum of a multilayer sample in comparison to a cavity sample containing distributed Bragg reflectors with three dielectric layer pairs. In addition, a spectrum of a multilayer covered by a thick silicon layer is shown. The thickness of this silicon layer corresponds to three times the thickness of a silicon layer inside the distributed Bragg reflectors. The aim is to correct the spectrum for the absorption of the excitation light when it is passing through the silicon of the upper distributed Bragg reflector.

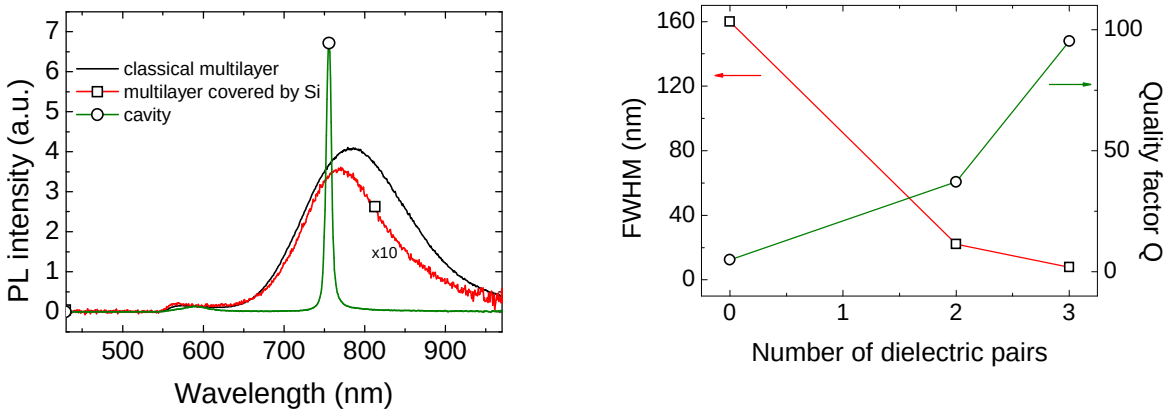

(a) *(b)*

Figure 4.28: (a) PL spectra of the multilayer, the multilayer covered by a silicon layer and the microcavity; (b) Line-width and quality factor Q as a function of the number of dielectric layers.

In the case of the cavity based on three dielectric pairs per distributed Bragg reflector, the photoluminescence intensity of the cavity sample is much stronger than the photoluminescence

intensity of the reference sample, especially of the multilayer covered by a silicon layer. The enhancement of the photoluminescence intensity is then proved in this experiment. Moreover, the photoluminescence linewidth is strongly reduced from 160 nm to 8 nm.

This result is comparable to that of Belarouci and Gourbilleau [121] who found a reduction of line-width from 250 nm to 10 nm for Si/SiO_2 microcavities containing $SRSO/SiO_2$ multilayers with distributed Bragg reflectors consisting of three dielectric pairs. They deduced a quality factor of 82, compared to 95 in our case.

Reflectivity measurements reveal a line width of even only 6 nm leading to a quality factor of 126. In order to understand the difference of this measured value to the theoretically predicted value of 245, we have to take into account the absorption in the cavity. Xu *et al.* [132] propose to attribute a quality factor to the absorption:

$$Q_{abs} = \frac{n}{2k} \tag{4-14}$$

In our case, n and k are known from section 4.3.2 to be n = 3.78 and $k=6.7\cdot10^{-3}$. This leads to an absorption related quality factor $Q_{abs.}$ of 283. So, we have for the overall quality factor:

$$\frac{1}{Q} = \frac{1}{Q_0} + \frac{1}{Q_{abs}} \tag{4-15}$$

which leads to a numerical value of 131, which is remarkably close to the value determined by reflectivity measurements.

In summary, the results obtained for cavities with distributed Bragg reflectors containing two or three bilayers, the linewidth and the quality factor are presented in figure 4.28 versus the number of dielectric bilayers. As expected, a strong increase of the quality factor is observed when the number of dielectric layer is increased. The observed effects are well in agreement with the literature values. Remaining differences between theoretical prediction and experimental results could be explained taking into account the absorption in the film.

Spatial selectivity of the cavity: The resonance peak of the cavity based on three dielectric pairs shifts as a function of the detection angle, too.

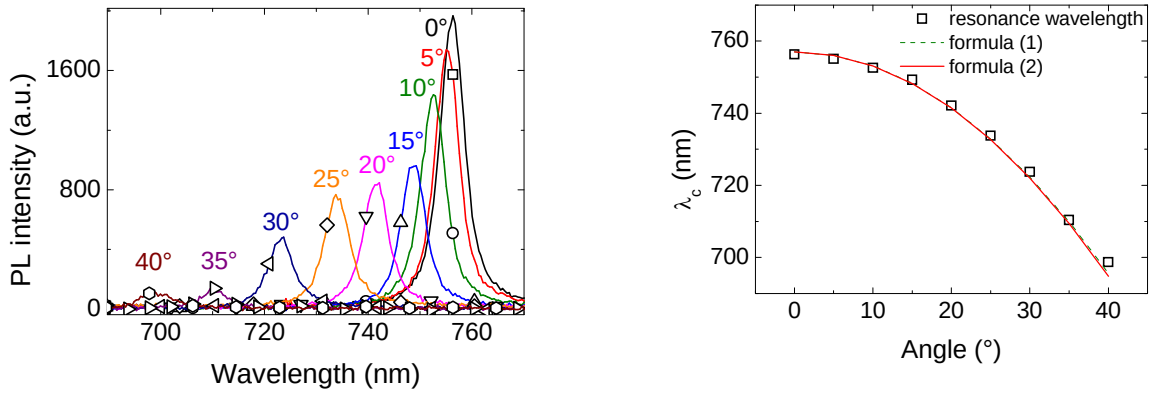

(a) *(b)*

Figure 4.29: Evolution of the PL maximum versus the detection angle. a) PL intensity as a function of the wavelength b) wavelength of the maximum as a function of the detection angle. The dotted line and the red solid line correspond to the formulas 4.1 and 4.2 given in the text

The resonance peak of the cavity based on three dielectric layers shifts as a function of the detection angle, too. Figure 4.29 (a) reports the angle resolved photoluminescence of such a cavity. We observed a blue-shift of the spectra with increasing detection angle as shown in figure 4.29 (b). The dotted line in (b) shows a fit of this evolution by the already upper mentioned equation

$$\lambda = \lambda_{res.} \cos\left(\sin^{-1} \frac{1}{n_a} \sin\theta_{obs} \right) \tag{4-16}$$

whereas the red solid line corresponds to a simplification of the upper equation [131]:

$$\lambda = \lambda_{res.} \cos\left(\frac{\theta_{obs}}{n_a} \right) \tag{4-17}$$

Apparently, even this simplification fits well the blue-shift of the resonance wavelength. As the observed wavelength does not depend on the number of dielectric pairs, figures 4.26 (a) and 4.29 (a) show almost the same blue-shift of the resonance wavelength, which is of about 60 nm in both cases. The correct behaviour of the angle-resolved photoluminescence spectra gives an indication of the good structural quality of the sample, once again.

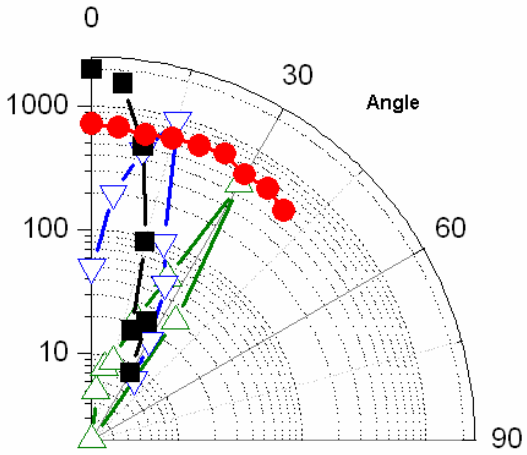

Figure 4.30: PL spectra of the microcavity as a function of the detection angle: the detection wavelength is of 779 nm (0°) for the reference multilayer and of 779 nm (0°), 749 nm (15°) and 723 nm (30°) for the microcavity, respectively.

In figure 4.30, we report the polar diagram of the intensity distribution for both the reference sample (circles) and the microcavity (squares and triangles). We observed a strong modification of the emission between the reference sample and the cavity. Whereas the photoluminescence intensity of the reference sample was almost isotropic, i.e. constant over the measured angle range, the photoluminescence of the cavity at the same wavelength was observable only for angles smaller than 15°. This lobe structure is a strong indication of the mentioned modification of the optical density of states.

In summary, we investigated in this section a microcavity based on three Si/SiO_2 dielectric pairs at each side of the resonator. An important amelioration of the emission intensity was determined with respect to the reference sample. An increased quality factor of 88 was found with respect to 26 for the cavity based on two dielectric pairs per distributed Bragg reflector. The angle-resolved photoluminescence spectroscopy confirmed the lobe structure of the emission.

4.6.4 Time resolved spectroscopy

Another definition of the Purcell factor allows us to quantify it as the ratio between the radiative lifetime of the silicon nanocrystals in a reference sample and the radiative lifetime of the silicon nanocrystals coupled to the microcavity. Thus, we performed time-resolved measurements at ambient temperature. Figure 4.26 (a) reports the reduction of the radiative lifetime of silicon nanocrystals coupled to microcavities compared to silicon nanocrystals in free space. A stretched exponential fit of the decay curves gave a decay time of 30.8 µs for silicon nanocrystals in free space compared to 23.9 µs for silicon nanocrystals coupled to microcavities. The decay times are comparable to those reported in literature as e.g. by Belarouci and Gourbilleau [121] who obtained 31.4 µs and 24.3 µs, respectively.

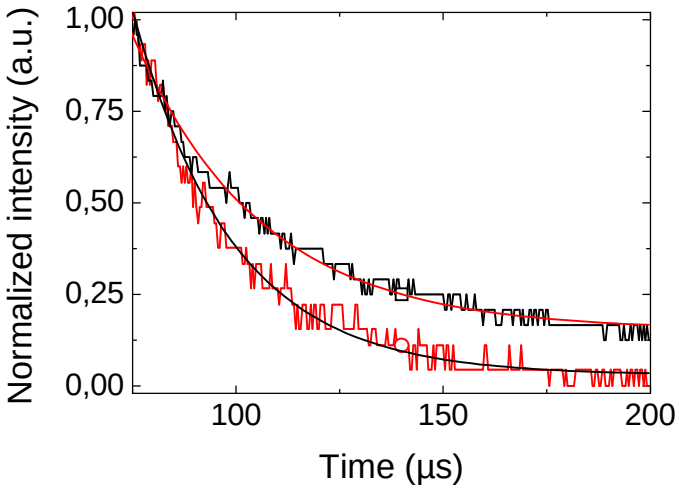

Figure 4.31: comparison of PL for Si nanocrystals and for the microcavity

Even silicon nanocrystals coupled to high-quality microdisk resonators do not show a remarkably stronger reduction of the radiative lifetime [133].

In summary, in this section, we analyzed the temporal behaviour of the photoluminescence signal arising from both reference and microcavity sample. For the cavity sample, we found a reduction of the lifetime of 22% with respect to the reference sample. This is comparable to literature values. In addition, even the time-resolved behaviour of microdisc-cavities with very high-quality factors is not very different.

4.6.5 Cavity based single dot spectroscopy

As Pitanti *et al.* [133] discuss in their article, the Purcell effect is influenced by the quality factor Q only if the linewidth of the cavity is not smaller than the linewidth of a single silicon nanocrystal. They estimate this linewidth to be of about 10 meV or 5.1 nm at 800 nm. A further increase of the Purcell effect and thus reduction of the radiative lifetime could be achieved by reducing the mode volume V and engineering of the recombination paths of the excitons.

In the following, we will give a first estimation of the photoluminescence linewidth of our silicon nanocrystals using the same formalism as used by Pitanti [49]. The commonly known formula for the Purcell factor

$$F_p = \frac{3Q(\lambda/n)^3}{4\pi^2 V} \qquad (4\text{-}12)$$

is valid only for the following simplifications:

- the linewidth of the emitter $\Delta\lambda_{em.}$ shall be smaller than the linewidth of the cavity $\Delta\lambda_{cav.}$;

- the emission wavelength has to correspond to the resonance wavelength of the microcavity;
- the emitter has to be placed at an antinode of the electric field;
- the probability of non-radiative recombination should be negligible.

As the results of this work and in literature show, silicon nanocrystals are far from being ideal light emitters. So, there are some more effects to be taken into account. Gérard [134] proposes a formula based on empirical considerations, which contains several corrective terms with respect to the ideal formula:

$$\tilde{F}_P = \frac{3}{4\pi^2}\left(\frac{\lambda}{n}\right)^3 \frac{Q_{eff.}}{V} \underbrace{\frac{\Delta\omega_c^2}{\Delta\omega_c^2 + 4(\omega-\omega_c)^2}}_{(1)} \underbrace{\frac{\left|\vec{E}(\vec{r})\right|^2}{\left|\vec{E}\right|^2_{\max.}}}_{(2)} \eta^2 \left\langle f(\omega)\right\rangle \tag{4-18}$$

where term (1) describes the spectral detuning of resonance and emitter and term (2) is a spatial correction term. η^2 describes the non-polarized emitters, $\left\langle f(\omega)\right\rangle$ the spectral resolution of the detection system and finally, $Q_{eff.}$ is the effective quality factor of the system taking into account the quality factor of the cavity and the finite linewidth of the emitters:

$$\frac{1}{Q_{eff.}} = \frac{1}{Q_{cav.}} + \frac{1}{Q_{em.}} = \frac{\Delta\lambda_{cav.}}{\lambda_{cav.}} + \frac{\Delta\lambda_{em.}}{\lambda_{em.}} \tag{4-19}$$

In our case, the influence of the spectral detuning is already taken into account in the stretched exponential function which describes the time-resolved behaviour of the system [56]. Thus, we have to consider mainly the influence of a finite linewidth of the luminescence coming from silicon nanocrystals.

Therefore, the expression simplifies to

$$\tilde{F}_P = \frac{3}{4\pi^2}\frac{\tilde{\lambda}^3}{V}\left(\frac{1}{Q_{cav.}} + \frac{\Delta\lambda_{em.}}{\lambda_{em.}}\right)^{-1} \left\langle f(\lambda)\right\rangle \tag{4-20}$$

This equation can now be transposed to an expression in $\Delta\lambda_{em.}$.

$$\Delta\lambda = \lambda\left(\frac{3}{4\pi^2\tilde{F}_P}\frac{\tilde{\lambda}^3}{V} - \frac{1}{Q_{cav.}}\right)\left\langle f(\lambda)\right\rangle \tag{4-21}$$

with

$$\tilde{F}_P = 1 + \frac{\tau_{rad}}{\tau_{free}}(\varepsilon - 1) \tag{4-22}$$

where

$$\varepsilon = \frac{\tau_{free}}{\tau_{cav}} \tag{4-23}$$

and [56]

$$\tau_{rad} = \frac{4\tau_T \tau_S}{3(\tau_T + \tau_S)} \tag{4-24}$$

where τ_T and τ_S are the triplet and singlet state of silicon nanocrystals, respectively. They represent the breakup of the degeneracy of the spin ground state in crystalline silicon. Due to electron hole interaction in confined silicon nanocrystals, this degeneracy is broken up. A triplet and a singlet state are created. Equation (4-24) results from the high temperature limit of the recombination dynamics.

The modal volume V of the microcavity can be calculated following Björk *et al.* [135] who define the radius of one single mode in the case of planar cavities as

$$a_p = \left(\frac{\lambda_{cav.} L_{cav.} \left(R_1 R_2\right)^{\frac{1}{4}}}{\pi n_{cav.} \left(1 - \left(R_1 R_2\right)^{\frac{1}{2}}\right)} \right)^{\frac{1}{2}} \approx \left(\frac{\lambda_{cav.} L_{cav.}}{\pi n_{cav.} \left(1 - \left(R_1 R_2\right)^{\frac{1}{2}}\right)} \right)^{\frac{1}{2}} \tag{4-25}$$

The formation of single, independent modes can be supposed even in a planar cavity which is not confined in the x-y-plane, if the modes are incoherent between each other.

When we consider a cylindrical mode volume of $8.35\,\tilde{\lambda}^3$, we can compute the linewidth by using the parameters which are resumed in table 4.2. For instance the spectral resolution of our spectrometer $\langle f(\omega) \rangle$ was not determined and is supposed to be unity in this calculus.

Parameter	Value	Origin
τ_{free}	30.8 µs	Time-resolved photoluminescence
$\tau_{cav.}$	23.9 µs	
τ_S	20 µs	Ref. [136]
τ_T	2 ms	
$L_{cav.}$	254 nm	Transmission electron microscopy
$\lambda_{cav.}$	756 nm	cw-photoluminescence
n_a	1.49	Bragg condition
$Q_{cav.}$	126	Reflexion spectroscopy
R_1, R_2	0.97	Simulation

Table 4.2: Parameters, which allow to estimate the linewidth of silicon nanocrystals

However the calculus gives no reasonable values as the linewidth is negative with this set of parameters. Therefore, we simulated the linewidth of the silicon nanocrystals as a function of the modal volume for different cavity quality factors. We considered both presence and absence of absorption in the thin films. Figure 4.32 shows the simulation data. The linewidth decreases as a function of the modal volume independent of the quality factor or the absorption. For low quality factors, e.g. the black line, which corresponds to the parameter set above, the linewidth decreases rapidly and turns into negative values at modal volumes smaller than the estimated modal volume in our case, which is $8.35\,\tilde{\lambda}^3$. The red curve (squares) describes the linewidth as a function of the modal volume for the same parameter set, but neglecting the absorption in the cavity. It can be seen, that for a correct estimation of the linewidth of the silicon nanocrystals, high quality factors are needed as shows the green line (circles), where the graph is linear in the region of the estimated modal volume. Considering the absorption again in the case of a quality factor of 1000, one has to note that the effective quality factor is strongly reduced.

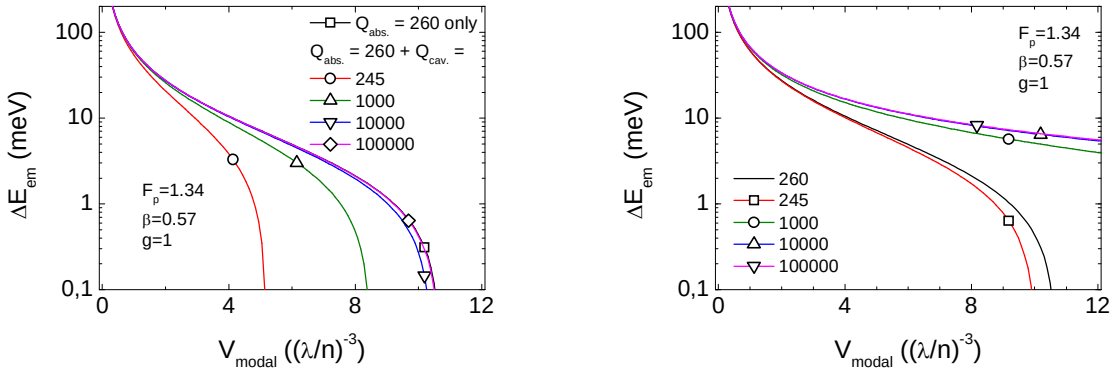

(a) *(b)*

Figure 4.32: Linewidth of silicon nanocrystals as a function of the modal volume for different quality factors in presence (a) and absence (b) of absorption.

If we consider equation (4-15), we have to note that the effective quality factor of a silicon based microcavity cannot exceed the quality factor imposed by the absorption which has a value of 260:

$$\frac{1}{Q} = \frac{1}{Q_0} + \frac{1}{Q_{abs}} \xrightarrow{Q_0 \to \infty} \frac{1}{Q_{abs}} \qquad \text{(4-15a)}$$

Thus, calculating with the quality factor $Q_{abs.}$ for our cavity, we obtain a lower limit of the linewidth of 1.5 meV. If we consider the limit of highest quality factors, the linewidth is of 8 meV.

In summary, in this section, we gave an estimation of the photoluminescence emission linewidth of silicon nanocrystals. It is between 1.5 meV and 8 meV. We deduced this range taking into account the maximum quality factor achievable with silicon based distributed Bragg reflector microcavities and an ideal system of nearly infinite quality factor. The values are in good agreement with literature [54, 133]. Nonetheless, here the limits of silicon based microcavities are shown. For a more accurate estimation it would be necessary to use less absorbing materials for the distributed Bragg reflectors.

4.7 Conclusion

In the first section, we evaluated the optical and structural properties of TiO_2, SnO_2, Si and SiO_2, as well as the SiO/SiO_2 active layer, that contains the silicon nanocrystals.

TiO_2 and SnO_2 have shown to impose too many difficulties during the fabrication process. Thus, we decided to fabricate Si/SiO_2 distributed Bragg reflector based optical microresonators, which include the silicon nanocrystals in the central layer.

For the complete and proper design, the optical properties of Si and SiO_2 have been analyzed by means of simulation of the UV-VIS-NIR transmittance spectra of the layer and of ellipsometry measurements. The obtained parameters allowed us to simulate the transmittance spectra of distributed Bragg reflectors, which have been fabricated using the obtained parameters and which have been examined by means of UV-VIS-NIR transmission spectroscopy. The comparison of simulation and experiment revealed regularity problems during the fabrication process.

In the next step, complete microcavity samples have been fabricated. They have been analyzed by means of UV-VIS-NIR transmission spectroscopy and transmission electron microscopy in order to investigate their structure and optical properties.

After this, a selective photoluminescence spectroscopy has been performed using the mercury lamp that was available in the laboratory and the most effective excitation wavelength was found to be the 546 nm line. The following comparison between the transmittance spectra and the photoluminescence spectra allowed us to indentify the resonance peak of the cavity. It was identically for both spectroscopy techniques. A measurement of resonance wavelength and linewidth revealed a quality factor of 126 for a cavity containing three Si/SiO_2 sequences at each side of the optically active layer.

The resonance peak has been analyzed by means of angle-resolved photoluminescence spectroscopy to successfully verify the origin of this peak. The evolution of the photoluminescence followed the theoretical predictions of the angular dependence of the resonance wavelength.

Time-resolved photoluminescence measurements gave a further indication of the optical coupling between silicon nanocrystals and the microcavity since the radiative lifetime inside the cavity was slightly reduced with respect to the radiative lifetime of a bare silicon nanocrystal film.

Finally, an estimation of the photoluminescence emission linewidth of silicon nanocrystals from the optical properties of the microcavity was proposed. The results are in agreement with literature but show nonetheless the limitations of microcavities based on absorbing silicon.

General Conclusion

This manuscript describes the results obtained during this PhD work. It is dedicated to the analysis of the optical properties of silicon nanocrystals. In this work, we analyzed the luminescence of silicon nanocrystals that emit light both in free space and in optically confined space.

The silicon nanocrystals are obtained by annealing a SiO_x layer. Through a demixion process that takes place during the thermal treatment, silicon-rich clusters appear in the SiO_2 matrix. The segregation follows the equation:

$$SiO_x \rightarrow \frac{x}{2} SiO_2 + \left(1 - \frac{x}{2}\right) Si$$

SiO_x/SiO_2 multilayers were also grown in order to control the average silicon nanocrystal diameters.

In the first part of this study, we try to demonstrate the possibility to isolate and to optically characterize one or few silicon nanocrystals. To reach this aim, we first try to play with the oxygen content of the SiO_x layer. Two thin films of SiO_1 and $SiO_{1.5}$ have been elaborated, and their behaviours under annealing treatments analyzed. In the two cases, the global composition of the matrix evolves towards stoechiometric silica SiO_2. Nevertheless this evolution is not complete in the case of the $SiO_{1.5}$ layer which shows a delay in the demixion process. The analysis realized with those two thin films by photoluminescence spectroscopy and Raman diffusion shows that we may have the presence of silicon clusters. The Raman spectra of those clusters show that they seem to be amorphous. The photoluminescence spectra show a weak signal located at around 750 and 900 for the as-deposited $SiO_{1.5}$ and SiO_1 samples, respectively. Nevertheless, the behaviours of the photoluminescence peaks with the analysis temperature show that is it difficult to attribute those photoluminescence signatures to silicon nanocrystal.

After a study of the different annealing conditions, and as the microstructure of those silicon nanocrystals have been studied in details in our group before, we started to analyze the silicon nanocrystals by Raman and photoluminescence spectroscopy. The photoluminescence spectra obtained for an annealing at 1100°C are typical of silicon nanoctystals. We checked this point by analyzing the evolution of the photoluminescence peaks as a function of the temperature. This evolution follows a typical Varshni law that confirms the presence of nanocrystalline silicon. Exploitable Raman spectra were only obtained for silicon nanocrystals extracted from SiO/SiO_2 layers with a SiO layer of 4 nm. Theoretical models have been developed in order to analyze the experimental spectra. The models for the photoluminescence spectra take into account phenomenological expressions for the evolution of the silicon nanocrystals band gap with their diameter and for the oscillator strength of the optical transitions. In addition, the photoluminescence model includes a Gaussian distribution of the silicon nanocrystal sizes. The model for the Raman spectra takes into account a Lorentzian function and a confinement function in the reciprocal space. Those two models give compatible results with an average silicon nanocrystal size of about 5 nm.

Once the control of the silicon nanocrystal sizes has been verified, we studied the possibility to control (and to reduce) the silicon nanocrystal surface density. We realized single SiO_x layers

sandwiched between two SiO_2 layers. This kind of sample yields the formation of a single silicon nanocrystals layer. The analysis of those samples by photoluminescence shows the presence of silicon nanocrystals for the samples made with layers of SiO_1, $SiO_{1.25}$ and $SiO_{1.5}$. The energy-filtered transmission electron microscopy analysis of the samples shows, as expected, a reduction of the surface density of the nanocrystals with the increase of the oxygen excess (a reduction of silicon content in the initial SiO_x layer). The average silicon nanocrystal diameter remains stable. In conclusion, we showed that we can play with both the silicon nanocrystal size and the silicon nanocrystal surface density.

Then, we developed lithographic processes in order to further reduce the number of silicon nanocrystals excited under the laser spot. First of all, masks were designed and transfered on an aluminium mask. The thickness of the mask has been optimized in order to be completely opaque in the range 600-900 nm, corresponding to the spectral range of the silicon nanocrystals emission. Then, we opened the holes by chemical etching, and we succeeded in obtaining apertures as small as 100 nm. We hope to excite approximately 300 silicon nanocrystals by using this kind of sample. The photoluminescence analysis realized by using a confocal microscope shows a large photoluminescence signal that decreases in intensity with the decrease of the size of the aperture in the aluminium mask.

The second part of this study is dedicated to the study of the interactions between confined light and the confined modes of the silicon nanocrystals in microcavities. The aim of this study was to control the spontaneous emission of light coming from the silicon nanocrystals. It has both fundamental interests and technical applications.

We first chose the materials we are able to grow and that are the most compatible with optical analysis. If the titanium dioxide is the most adaptated material for realizing such systems, we had many difficulties to easily elaborate stoichiometric TiO_2 layers. We chose the Si/SiO_2 doublet to realize the Bragg mirrors and the optical microcavities.

As the realization of the silicon nanocrystals needs an annealing at 1100°C, we had to study the behaviour of the different components which the Bragg mirrors and the optical microcavities are made of as a function of the annealing temperature. For analyzing of the silicon layers, we implemented two models in a simulation code with which we are able to determine the complex refractive index as a function of the wavelength. The analysis of the transmittance together with the analysis of X-ray reflectance spectra show a densification of the silicon layers with the annealing temperature. At the same time, the refractive index increases. The different parameters extracted from the fit of the transmittance spectra are close to those found in literature. The analysis of SiO_2 layers was realized by ellipsometric spectroscopy. It also shows a decrease of the SiO_2 layer thickness with the annealing temperature. In this case, the refractive index is increased, too.

The parameters deduced from the analysis of the thin films were then used in the modelling of the Bragg mirrors. First of all, a series of Bragg mirrors containing from 2 to 5 Si/SiO_2 doublets were realized and analyzed by transmittance spectroscopy in the ultraviolet-visible range. We verified with this study that the parameters deduced from the analysis of thin films were correct. This helped us to reduce the number of parameters for analyzing the Bragg mirrors.

The behaviour of the Bragg mirrors is then analyzed as a function of the annealing temperature. With the parameters deduced from the studies described above, we are able to have a good description of the evolution of the photonic band gap of the Bragg mirrors. This evolution holds together with a decrease of the thickness as well as an increase of the refractive index of the silicon and silica layers, which is of the same order of magnitude of the one observed with the thin films.

The microcavities were then studied. In our case, it is difficult to grow samples with thicknesses superior to 1 µm. We then expect to have a maximum quality factor of about 300. A first study is realized with an optical microcavity with two Si/SiO_2 Bragg mirrors. After annealing, transmission electronic microscopy reveals smooth interfaces and polycrystalline silicon inside the Bragg mirrors. Moreover, we observe that the thicknesses are not well regular along the Bragg mirrors. By modelling the influence of the layer thicknesses of the Bragg mirrors, we showed that a change of the order of 10 % is not crucial in our case.

Microcavities are then analyzed as a function of the annealing temperature. First, and as observed above, a decrease of the thicknesses of the different layers is still observed. But the important point is the observation of a strong blue-shift of the microcavity resonance peak with the annealing temperature. This shift is of about 100 nm for most of the microcavities we studied. It is consistent with the decrease of the thickness which rules out the increase of the refractive index. We have to take the shift into account in the design of the microcavities to obtain a well localized microcavity resonance peak after thermal annealing. We also studied the influence of the thickness of the microcavity on its resonance peak.

Finally, we studied the luminescence of our samples. We observed that the most efficient wavelength of light for excitation of the microcavities is 546 nm. In the case of the microcavity with two Si/SiO_2 Bragg mirrors, a strong narrowing of the emission band of the silicon nanocrystals is observed. But the enhancement of the photoluminescence signal can not be observed as the quality factor of such a microcavity is too small. For the microcavity with three Bragg mirrors, the photoluminescence signal has been compared to a sample containing multilayered silicon nanocrystals covered by a silicon layer whose thickness corresponds to the total thickness of silicon in the upper distributed Bragg reflector. Here, the photoluminescence enhancement is clearly observable and the angle-resolved photoluminescence spectra follow well the predicted dispersion relation. The evaluation of the quality factor of this sample reveals that it is smaller than the expected value because of the absorption of the silicon layer. To verify the weak coupling regime, we analyzed this sample with time-resolved photoluminescence spectroscopy. A shorter decay time is observed in the case of the microcavity in comparison with the standard silicon-nanocrystal sample. The decrease of the decay time is in the order of magnitude of the values found in literature.

Prospects

Concerning single dots spectroscopy, there is a cooperation with M. Dossot of the LCPME, Nancy, with whom we are going to inverstigate in future the samples by means of scanning near field optical microscopy and near field spectroscopy. This study will nonetheless be tricky, as the minimum surface that can be scanned is of a diameter of 50 nm. Within this surface there are still several tens of silicon nanocrystals.

So it would be very interesting to employ once again electron beam lithography to structure the active SiO_x layers: the plan would be not only to confine the silicon atoms between two layers of SiO_2 in z-direction but also confine them laterally.

The key point of the analysis presented in the fourth chapter is the value of the Purcell factor which depends on the ratio of quality factor over the modal volume. Thus, it could be interesting either to increase the quality factor or to reduce the modal volume in order to observe clear effects. To circumvent the limitations imposed by the evaporation, it could be possible to realize microcavities on fused silica with only one Bragg mirror at the substrate side of the sample and a metallic layer as a second mirror at the top of the sample. The Bragg mirror in this case could be made by the six Si/SiO_2 doublets present in the sample we studied in this work.

The second interesting point would be the reduction of the modal volume of the microcavity. As we described in this work, some people realized micropillars including optical microcavities. This work, done with III-V materials, has never been realized on silicon nanocrystals. It could be the opportunity to analyze the nature of the coupling between silicon nanocrystals and light.

Finally, we can mention the low temperature and the high power density analysis that could be realized with those samples. At low temperature, we could analyze the electronic states of the silicon nanocrystals and, for example, reach a better description of the triplet/singulet states in those nanostructures. The analysis with the excitation power density would lead to a better knowledge of the free-carrier absorption, Auger processes and non-linear effects in silicon nanocrystals.

Appendices

Appendix A – Direct simulation method

The index difference between the substrate and the deposited film is causing interferences which significantly change the actual transmission of the film. Even if from a certain point of view, these interferences are a serious handicap in obtaining the coefficient of absorption, they are of interest to calculate accurately the thickness and refractive index of the film. For this purpose it is necessary to simulate the transmission spectra. The simple expression of the transmission $T = T_0 \exp(-\alpha d)$, where α is the coefficient of absorption and film thickness is not correct in the case of measurements on thin films. We used the exact expression for the transmission of light interference effects [32,33]. This expression is valid in the case of a film deposited on a transparent substrate.

$$T = \frac{A \times \exp(-\alpha d)}{B - C \times \exp(-\alpha d) + D \times \exp(-2\alpha d)}$$

with

$A=16s(n^2+k^2)$

$B=[(n+1)^2+k^2][(n+1)(n+s^2)+k^2]$

$C=2\cos(\phi)[(n^2-1+k^2)(n^2-s^2+k^2)-2k^2(s^2+1)]-2k\sin(\phi)[2(n^2-s^2+k^2)+(s^2+1)(n^2-1+k^2)]$

$D=[(n-1)^2+k^2][(n-1)(n-s^2)+k^2]$

$\phi=4\pi nd/\lambda$, $\alpha=4\pi k/\lambda$

where n is the refractive index of the film, s the index of refraction of the substrate, α the absorption coefficient of the film, λ the wavelength, k the extinction coefficient and d the thickness of the film.

The index of refraction of the substrate is known throughout the spectral range that we used, the simulation parameters are n, α and d. To show the influence of these parameters, figure A.1 (a) shows the results of a simulation of the transmission spectrum for various thicknesses with d α, n and s constant whereas figure A.1 (b) shows simulation transmission spectra for different refractive indices with absorption coefficient and a given thickness, respectively.

The values of the index and absorption coefficient are

$$n=n_0+10^5/\lambda^2$$

$$\alpha=\exp(E/0.3)\ (E=hc/\lambda \text{ en eV})$$

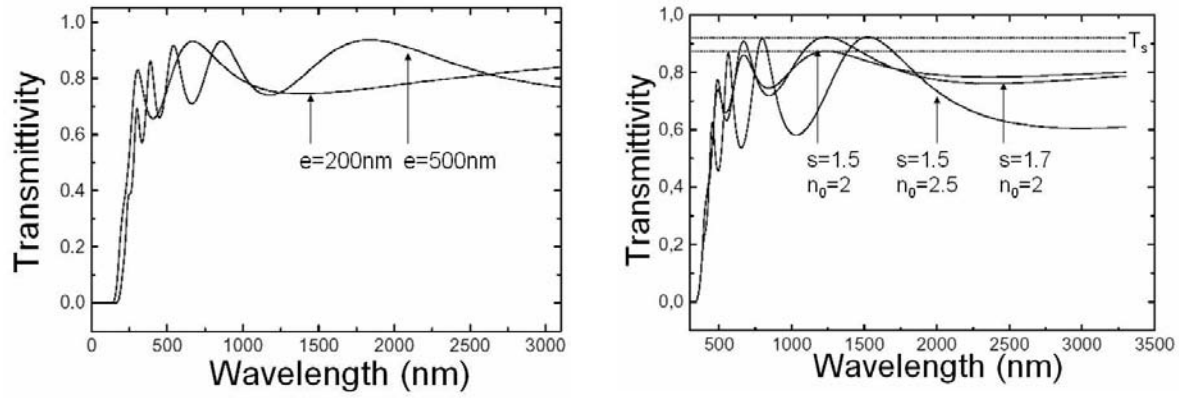

(a) *(b)*

Figure A.1: influence of (a) the thickness and (b) the refractive index of the film on simulated transmission spectra. The dotted line in b.) corresponds to the transmission of the substrate.

The thickness has an influence on the interference fringes and the intensity of transmission. The reflectance of the substrate depends on its index. So for a substrate whose index is 1.5 and 1.7, the transmitted intensity is of 92% and 87%, respectively. In the case of our substrate, the index is of 1.42 in the near infrared and thus the transmitted intensity is of 94%. The experimental spectrum provided by the device does not take into account this factor of reflection as the signal is given as a ratio of two intensities transmitted through the substrate. Before simulating the spectra, it is necessary to correct the experimental spectrum by multiplying the transmission signal provided by the device by the transmission factor

$$T_s = 2s / (s^2 + 1)$$

where s is a known function of the wavelength. The spectrum obtained by simulation takes into account the effect of this factor. The difference in refractive index between the film and the substrate has the effect of increasing the amplitude of interference. The interferences are more pronounced in the case of silicon-rich silicon oxyde as in the case of a film whose composition is close to that of silica. Like the thickness, refractive index of the film changes the interference fringe.

The index of refraction of fused silica is given by [34]

$$s^2 = 1 + \frac{0.6961663\lambda^2}{(\lambda^2 - 0.0684043^2)} + \frac{0.4079426\lambda^2}{(\lambda^2 - 0.1162414^2)} + \frac{0.8974794\lambda^2}{(\lambda^2 - 9.896161^2)}.$$

The index of the film is approached by the simple expression

$$n = n_0 + \frac{10^5 n_1}{\lambda^2} + \frac{10^9 n_2}{\lambda^4}.$$

In the near infrared, the index varies very little. In the region of strong absorption in the case of amorphous silicon, Freeman *et al.* do not use the contribution λ^4 [35]. In the case of some films, that

contribution is however necessary to obtain a good fit between the experimental spectrum and simulation, especially in the field of short wavelengths.

The optical absorption: The optical absorption of amorphous silicon and silicon oxide is related to their band structure. The steep edges of the bands of energy states extended in a crystalline material are replaced by band tails in the gap in the amorphous. The optical absorption is very different. A typical transmission spectrum of silicon oxide is shown in A.2.

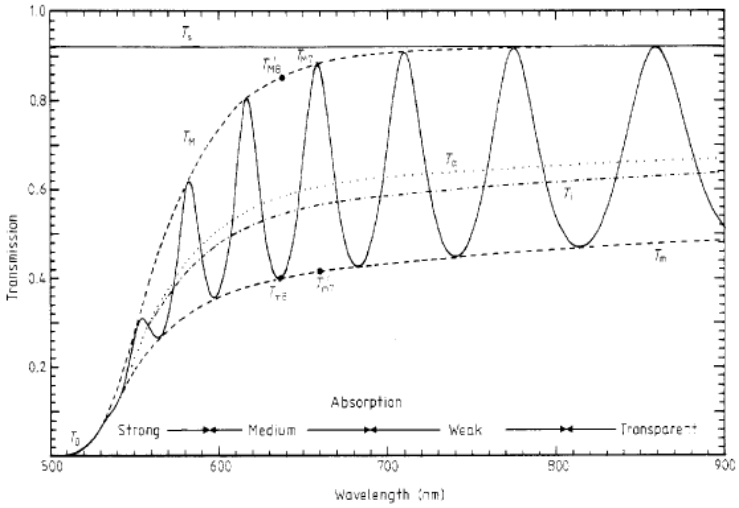

Figure A.2: Transmission spectrum of a film of silicon oxide.

We can decompose the spectrum into three regions of different absorption.

• **an area of transparency and low absorption.** It is mainly in this region that it is possible to determine by simulating the film thickness (d) and refractive index (n0), which varies little in this spectral range. This area is related to transitions involving localized defects in the gap. We do not have precise access to the absorption by transmission measurements due to the low value of α. The value of this absorption α can be obtained using the thermal deflection spectroscopy for example.

• **a region of medium absorption.** In the case of hydrogenated amorphous silicon that band is called Urbach band and corresponds to an exponential absorption [36], where α can be written $\alpha = \alpha_0 \exp(E/E_u)$. E_u is the Urbach energy which varies in a-Si: H from 60 to 120 meV using the methods of preparation of the material. In the case of our silicon oxide films, the transmission spectrum is well simulated by an exponential absorption. By analogy with a-Si: H, we use the Urbach energy as well as α_0 as simulation parameter, in this spectral range.

• **a region of strong absorption.** This region yields the value of the optical gap by the expression given by Tauc [37]. The absorption coefficient has a dependence power law and can be written $\alpha E = B (E-E_g)^2$, where E_g is the optical gap. In this region, there is a precision on the values of absorption

coefficient because the effect of the interferences is low. The values B and E_g are the simulation parameters in this spectral range.

Determination of optical constants: The values of optical constants are obtained when the simulated spectrum coincides with the experimental spectrum. Given the number of simulation parameters (thickness, three parameters for the index, four for the absorption) it is necessary to simulate the experimental spectrum with a strict procedure.

1. determining the value n_0 in the area of low absorption and thickness, the index playing on the amplitude of interference fringes and the spectral distance between two extremes and thickness on interfrange. The thickness is obtained with an accuracy of about 50 Å and the index with an error of 0.02 in this spectral range.
2. determination of n_1 with n_2 with the interference fringe as criterion, then determination of the value of the absorption in the medium absorption area and finally the absorption value in the strong absorption. The approximate value of the optical gap can also be obtained directly from the experimental spectrum, the effect of interference on the transmission being low compared to that of absorption (Figure A.3). The difference between the value of the gap obtained by the direct method and the simulation is less than 0.05 eV. The values considered in the following are still those of the simulation.

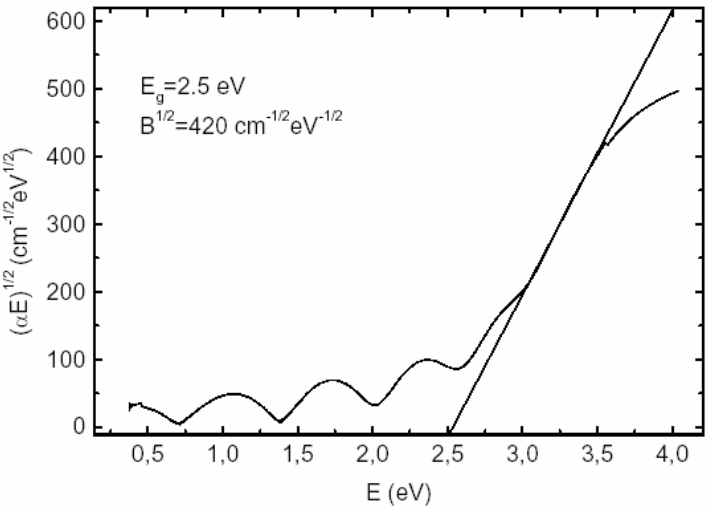

Figure A.3: Measurement of optical gap and the parameter B by direct calculation from the experimental spectrum.

Figure A.4 shows the experimental spectrum of a film of silicon oxide and the spectrum obtained by simulation. This figure shows the perfect agreement that can be achieved between the simulated spectrum and experimental spectrum.

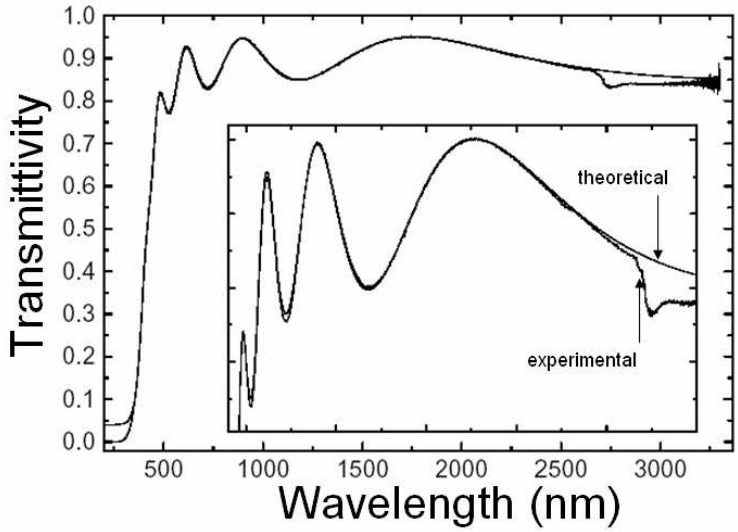

Figure A.4: Example of simulation of an experimental spectrum of silicon oxide film. (D = 5200 Å, n0 = 1.69, n1 = 0.32, α0 = 0.5 cm-1, Eu = 300 meV, B = 400 ½ ½ cm-1/2eV and Eg = 2.54 eV)

Appendix B – Swanepoel's method of envelopes

Whereas the direct calculus implicates a manual fit of the optical constants, the method being presented in the following represents a possibility to determine those constants almost automatically from a sole transmission spectrum. The method was published by Swanepoel in 1983 [58]. Its main difference from the upper treated direct calculus is the fact that this method uses the extremes of the interference fringes of the transmission spectrum to deduce the optical constants of a given thin film.

Firstly, we consider the transmission of a bare transparent, non absorbing substrate (e. g. fused silica) of finite thickness. Here the transmission is given by

$$T_s = \frac{2s}{s^2 - 1} = ¿ > s = \frac{1}{T_s} + \left(\frac{1}{T_s^2} - 1 \right)^{1/2} ,$$

s being the refractive index of the substrate.

Now, we can proceed to the description of a transparent or weakly absorbing film deposited onto the transparent substrate described above. If the difference of the refractive indices of film and substrate are high enough, reflection at the interface between film and substrate occurs and interference of transmitted and reflected light occurs, if the thickness of the film is in the order of magnitude of the wavelength of the light, as can be seen in figure A.5. In this same figure, one can distinguish three different ranges with completely different absorption properties: a zone of non-absorption or transparency at high wavelength, a zone of medium absorption and a zone of strong absorption at lower wavelengths. For each zone, one has to determine the optical constants.

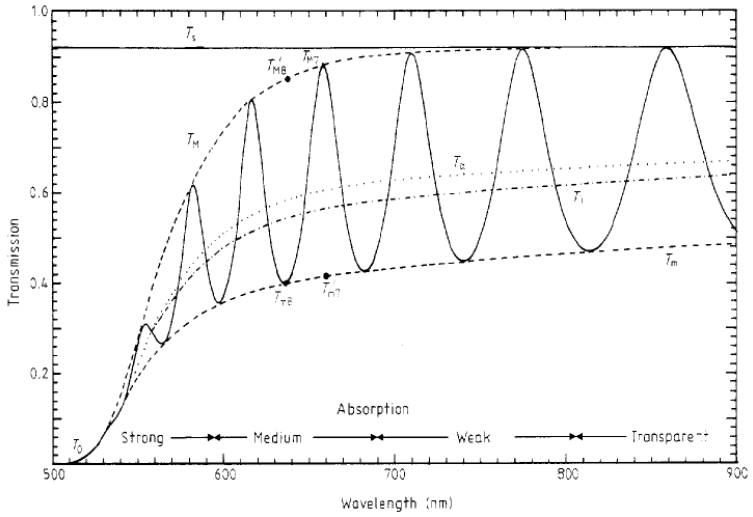

Figure B.1: Transmission spectrum of amorphous silicon as measured by Swanepoel [58]. The index contrast between air, thin film and substrate causes interference, which is at the origin of the wavy character of the transmission curve.

Zone of no absorption: In the zone of no absorption the transmission is also described by

$$T = \frac{Ax}{B - Cx\cos(\phi) + Dx^2} \tag{B.1}$$

with

$$A = 16n^2 s \qquad \phi = \frac{4\pi nd}{\lambda}$$

$$B = (n+1)^3 (n+s^2) \qquad x = e^{-\alpha d}$$

$$C = (n^2-1)^3 (n^2-s^2)$$

$$D = (n-1)^3 (n-s^2),$$

n being the refractive index of the film.

With this formula, we can describe the envelope functions for the maxima (T_M) and minima (T_m) of the spectrum by setting *cos(Φ)=1* for T_M and *cos(Φ)=-1* for T_m.

$$T_M = \frac{Ax}{B - Cx + Dx^2} \tag{B.2}$$

$$T_m = \frac{Ax}{B + Cx + Dx^2} \tag{B.3}$$

In the zone of transparency, $\alpha=0$ and $T_M = Ts$ and the envelope function of the minima is given by:

$$T_m = \frac{4n^2 s}{n^4 + n^2(s^2+1) + s^2}$$

So, knowing T_m, we can deduce *n*.

$$n_{(1)} = [M + (M^2 - s^2)^{1/2}]^{1/2} \tag{B.4}$$

where

$$M = \frac{2n_s}{T_m} - \frac{n_s^2 + 1}{2}$$

Zone of weak and medium absorption: Then, we define an area of low and medium absorption. In this region, α_0 is unequal to zero and $x < -1$. We obtain an expression independent of *x* by:

$$\frac{1}{T_m} - \frac{1}{T_M} = \frac{2C}{A}$$

Thus

$$n = [N + (N^2 - n_s^2)^{1/2}]^{1/2} \tag{B.5}$$

where

$$N = 2n_s \frac{T_M - T_m}{T_M T_m} + \frac{n_s{}^2 + 1}{2}$$

if n is known as a function of the wavelength, we can deduce x by different formulas. First, using the upper envelope T_M, we get:

$$x = \frac{E_M - [E_M^2 - (n^2-1)^3 (n^2 - n_s^4)]^{1/2}}{(n-1)^3 (n - n_s^2)} \tag{B.6}$$

with $E_M = \frac{8n^2 n_s}{T_M} + (n^2-1)(n^2 - n_s^2)$.

Or with the lower envelope T_m, we get:

$$x = \frac{E_m - [E_m^2 - (n^2-1)^3 (n^2 - n_s^4)]^{1/2}}{(n-1)^3 (n - n_s^2)} \tag{B.7}$$

with $E_m = \frac{8n^2 n_s}{T_m} - (n^2-1)(n^2 - n_s^2)$.

One can also calculate x from the equations (B.2) and (B.3). Thus, we obtain:

$$\frac{2T_M T_m}{T_M + T_m} = \frac{Ax}{B + Dx^2} \tag{B.8}$$

from which

$$x = \frac{F - [F^2 - (n^2-1)^3 (n^2 - n_s{}^4)]^{1/2}}{(n-1)^{"} (n - n_s{}^2)} \tag{B.9}$$

with $F = \frac{8n^2 n_s}{T_i}$ and $T_i = \frac{2T_M T_m}{T_M + T_m}$

Zone of strong absorption: x and n are interdependent following Kramers-Kronig relations. We can use the same formulas as in the case of weak absorption with the difference that for big α, T_m, T_M and $T_\alpha \rightarrow T_0$,

$$T_0 \approx \frac{Ax}{B}$$

$$x = \frac{(n_3{}^2 - 1)^3 (n_3 - s^2)}{16 n^2 s} T_0$$

Determination of the thickness of the film: We can determine the thickness of the film by

$$d = \frac{\lambda_1 \lambda_2}{2(\lambda_1 n_2 - \lambda_2 n_1)} \tag{B.10}$$

The indices 1 and 2 are representing two consecutive maxima or two minima. From *x* and *d*, we deduce the absorption α as follows:

$$\alpha = -\frac{\ln(x)}{d} \tag{B.11}$$

And the extinction coefficient k by:

$$k = \frac{\alpha \lambda}{4\pi} \tag{B.12}$$

Appendix C – Principle of the transfer matrix simulation method

Plane waves and Maxwell equations: Let us assume light as an electromagnetic wave which consists of an electric field $\vec{E}$ and a magnetic field $\vec{B}$. In the following, we give the Maxwell equations for electromagnetic fields in solids which describe the influence of the electromagnetic fields on the solid and vice-versa.

$$\text{div } \vec{D} = \rho \quad \text{where } \vec{D} = \varepsilon\vec{E} \qquad\qquad rot\vec{E} = -\mu_0 \frac{\partial \vec{H}}{\partial t}$$

$$\text{div } \vec{H} = 0 \quad \text{where } \vec{H} = \frac{\vec{B}}{\mu_0} \qquad\qquad \text{rot}\vec{H} = \vec{J} + \varepsilon \frac{\partial \vec{E}}{\partial t} \quad \text{where } \vec{J} = \sigma_{cond}\vec{E},$$

where $\vec{D}$ represents the electric displacement (or induction), $\vec{H}$ the magnetic excitation (or field), ρ the volume charge density, $\vec{j}$ the volume charge current density, z the dielectric permittivity, μ_0 the vacuum magnetic permeability and $\sigma_{cond.}$ the material conductivity [3].

By applying the rot operator a second time to the rot E and rot H equations, wave equations for plane electromagnetic waves can be derived from the upper mentioned Maxwell equations.

The solid state electromagnetism treats the interaction between the light and the electric charges inside the solid. The light is absorbed and emitted into several directions by moving charges. Light waves are thus transformed as they pass through a solid. In a dielectric solid, charges may be deviated from their equilibrium position by a passing wave. The deviation of positive and negative charges from each other is at the origin of a dipole. The wave equation in a dielectric lets appear the optical refraction index that fulfils the following equation that is characteristic for the solid:

$$\frac{n^2}{c^2} \cdot \frac{\partial^2 A}{\partial t^2} - \Delta A = 0 \quad \text{, where A stands for either } \vec{E} \text{ or } \vec{B}$$

The oscillating dipole created by the passing of a light wave in his turn produces a secondary radiance. The later leads to the phenomenon of absorption and thus the propagation of the wave may be altered. Particularly, one notes that – due to the refraction index – the effective velocity of the waves is slower that vacuum light speed.

At the interface between two materials of different refractive indices, the transfer of the incident light lets appear the phenomena of reflexion, transmission or absorption. The optical index may be complex, the imaginary part representing the absorption properties of the material. The complex refractive index is given in the following:

$$\underline{n} = n' + in'' = n + i\frac{\alpha}{2} \quad \text{, } \alpha \text{ representing the absorption.}$$

Notations: In the aim to determine the reflection and refraction properties of a plane wave at the interface of two different materials, we consider the boundary conditions. Those have to be written

differently corresponding to the either tangential or normal orientation of e.g. the electric field with respect to the interface. Let us start by distinguishing these two cases still noting that, for a homogeneous isotropic material, the solutions of the wave equation are planes waves that are completely described by the following relations:

$$\vec{E}(x,y,z,t) = \vec{E}_0 e^{i(\omega t - \vec{k}\cdot\vec{r})} \qquad \vec{H}(x,y,z,t) = \vec{H}_0 e^{i(\omega t - \vec{k}\cdot\vec{r})}$$

- **TE Polarization**

A TE (transverse electric) polarized wave corresponds to an electric field perpendicular to the plane of incidence. We choose as convention that the electric field is following Oy and that the magnetic field is following Ox et Oz.

$$\vec{E} = \begin{vmatrix} 0 \\ E_y \\ 0 \end{vmatrix} \quad \text{et} \quad \vec{H} = \begin{vmatrix} H_x \\ 0 \\ H_z \end{vmatrix}$$

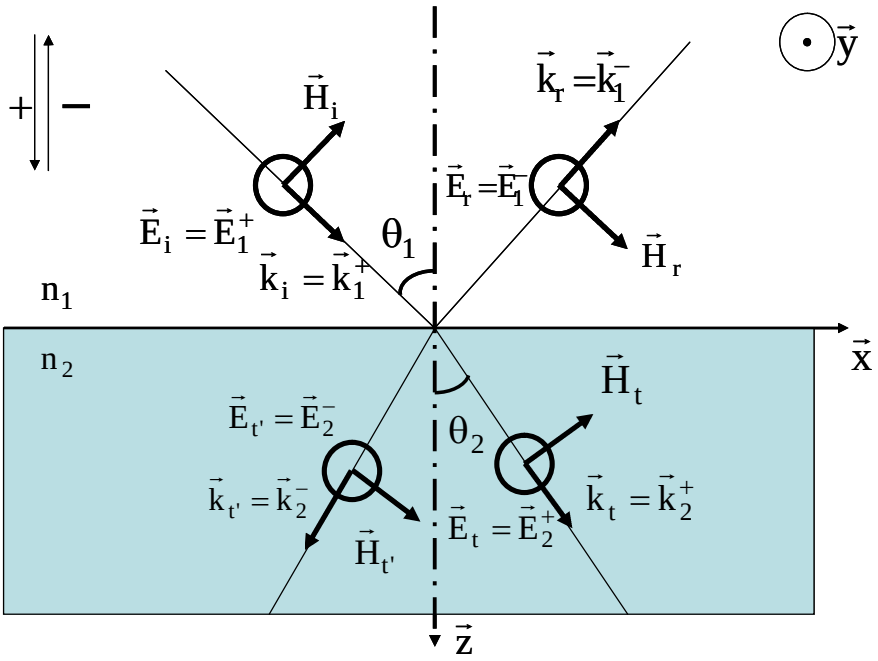

Figure C.1: TE polarized wave at the interface between two different materials

At the interface, an incident wave with the wave vector $\vec{k}_1^+$ creates an angle θ_1 with the normal in the $\vec{x}O\vec{z}$ plane. At this interface, there are two new waves to be considered: the reflected one of wave vector $\vec{k}_1^-$ and the transmitted one of wave vector $\vec{k}_2^+$. The same will be to do for each interface, if there are multiple. The indices 1 and 2 refer to the material in which the electromagnetic wave propagates and the sign indicates the direction of propagation.

- **TM Polarization**

A TM (transverse magnetic) polarized wave corresponds to a magnetic field perpendicular to the plane of incidence. By convention, the field is oriented following Oy and the electric field is following Ox and Oz.

$$\vec{E} = \begin{vmatrix} E_x \\ 0 \\ E_z \end{vmatrix} \quad \text{et} \quad \vec{H} = \begin{vmatrix} 0 \\ H_y \\ 0 \end{vmatrix}$$

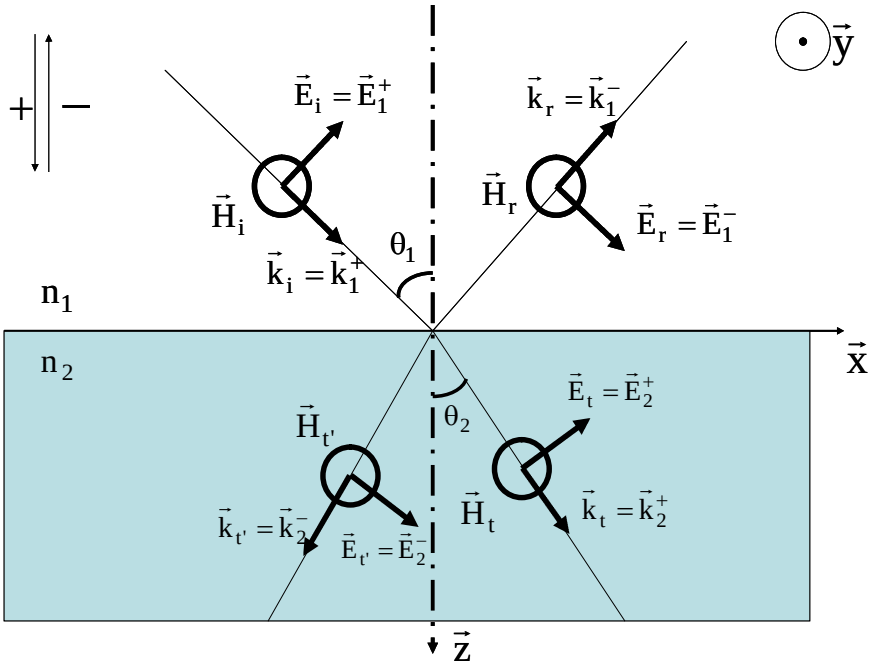

Figure C.2: TM polarized wave at the interface between two different materials

The conventions for the wave vector are the same as before.

For both incident TM and TE polarized waves, the polarization of both reflected and transmitted waves is conserved. [5]

Continuity: Light rays may be described by some empiric rules. In our case, the Descartes laws, referring to reflexion and refraction, permit to analyze these light rays at the interface between the two materials, those being characterized by their refractive index.

We consider an electromagnetic wave arriving at an interface between two materials of different refractive indices. The way of the wave follows the continuity relations, only valuable at the interface [6].

The transition conditions are specified by the Maxwell equations. They specify that

- the normal component of $\vec{E}$ is not continuous at the interface
- the tangential component of $\vec{E}$ is continuous at the interface

After having specified the continuity of the electric field at the interface, we have to consider the continuity of the magnetic field.

The continuity of the tangential component of the electric field induces the continuity of the tangential component of the magnetic field, for both TE and TM polarization.

In order to study the transmission or reflexion curves, respectively, by simulation, it is necessary to have the dispersion equations of the electromagnetic wave. The matrix formalism is well adapted to the resolution of this problem and permits to deduce the dispersion equations for our systems.

Matrix formalism

- **TE polarized wave**

In this case, $\vec{E}$ is oriented inside the plane of the interface: $\vec{E} = \begin{vmatrix} 0 \\ E_y \\ 0 \end{vmatrix}$ and thus $\vec{H} = \begin{vmatrix} H_x \\ 0 \\ H_z \end{vmatrix}$

The electric field $\vec{E}$ is written as:

$$\vec{E}_1 = (\vec{E}_1^+ e^{-in_1 k_0 \cos\theta_1 z} + \vec{E}_1^- e^{in_1 k_0 \cos\theta_1 z}).e^{i(\omega t - n_1 k_0 \sin\theta_1 x)}$$
$$\vec{E}_2 = (\vec{E}_2^+ e^{-in_2 k_0 \cos\theta_2 z} + \vec{E}_2^- e^{in_2 k_0 \cos\theta_2 z}).e^{i(\omega t - n_2 k_0 \sin\theta_2 x)}$$

Making use of the relation $\vec{H} = \frac{i\nabla \wedge \vec{E}}{\omega\mu_0}$, we deduce the magnetic field $\vec{H}$:

$$\vec{H}_x = -\frac{i}{\omega\mu_0}\frac{\partial E_y}{\partial z}\vec{x}$$

As the electric field $\vec{E}$ is purely tangential, the continuity conditions specify that its components are continuous at the interface: $\vec{E}_1 = \vec{E}_2$

From this, we deduce a first continuity equation: $\vec{E}_1^+ + \vec{E}_1^- = \vec{E}_2^+ + \vec{E}_2^-$

The continuity of $\vec{H}$ imposes that at the interface: $\vec{H}_1 = \vec{H}_2$

Thus the second continuity relation is written:

$$n_1 \cos\theta_1 (\vec{E}_1^+ - \vec{E}_1^-) = n_2 \cos\theta_2 (\vec{E}_2^+ - \vec{E}_2^-)$$

Starting from the previous continuity relations, we can deduce a matrix representation:

$$\begin{pmatrix} \vec{E}_1^{+}(z=0) \\ \vec{E}_1^{-}(z=0) \end{pmatrix} = \begin{pmatrix} \frac{n_1\cos\theta_1 + n_2\cos\theta_2}{2n_1\cos\theta_1} & \frac{n_1\cos\theta_1 - n_2\cos\theta_2}{2n_1\cos\theta_1} \\ \frac{n_1\cos\theta_1 - n_2\cos\theta_2}{2n_1\cos\theta_1} & \frac{n_1\cos\theta_1 + n_2\cos\theta_2}{2n_1\cos\theta_1} \end{pmatrix} \begin{pmatrix} \vec{E}_2^{+}(z=0) \\ \vec{E}_2^{-}(z=0) \end{pmatrix},$$

which may be rewritten as: $\begin{pmatrix} \vec{E}_1^{+}(z=0) \\ \vec{E}_1^{-}(z=0) \end{pmatrix} = \begin{pmatrix} \frac{\vec{k}_{1,z}^{+} + \vec{k}_{2,z}^{+}}{2\vec{k}_{1,z}^{+}} & \frac{\vec{k}_{1,z}^{+} - \vec{k}_{2,z}^{+}}{2\vec{k}_{0,z}^{+}} \\ \frac{\vec{k}_{1,z}^{+} - \vec{k}_{2,z}^{+}}{2\vec{k}_{1,z}^{+}} & \frac{\vec{k}_{1,z}^{+} + \vec{k}_{2,z}^{+}}{2k_{1,z}^{+}} \end{pmatrix} \begin{pmatrix} \vec{E}_2^{+}(z=0) \\ \vec{E}_2^{-}(z=0) \end{pmatrix}$

where $\begin{pmatrix} \frac{\vec{k}_{1,z}^{+} + \vec{k}_{2,z}^{+}}{2\vec{k}_{1,z}^{+}} & \frac{\vec{k}_{1,z}^{+} - \vec{k}_{2,z}^{+}}{2\vec{k}_{0,z}^{+}} \\ \frac{\vec{k}_{1,z}^{+} - \vec{k}_{2,z}^{+}}{2\vec{k}_{1,z}^{+}} & \frac{\vec{k}_{1,z}^{+} + \vec{k}_{2,z}^{+}}{2k_{1,z}^{+}} \end{pmatrix}$ is the reflexion matrix for a TE polarized wave which we denote as R_{12}, the indices corresponding to the two materials at each side of the interface.

- **TM polarized wave**

In this case, $\vec{E}$ is continuous in the plane of the interface: $\vec{E} = \begin{vmatrix} E_x \\ 0 \\ E_z \end{vmatrix}$ and $\vec{H} = \begin{vmatrix} 0 \\ H_y \\ 0 \end{vmatrix}$

The electric field $\vec{E}$ is not purely tangential, the continuity conditions ($\vec{E}_1 = \vec{E}_2$) specify that only its tangential component is continuous at the interface. From this, we obtain the first continuity equation:

$$\cos\theta_1(\vec{E}_1^{+} + \vec{E}_1^{-}) = \cos\theta_2(\vec{E}_2^{+} + \vec{E}_2^{-})$$

The continuity of $\vec{H}$ imposes that at the interface, we have: $\vec{H}_1 = \vec{H}_2$

From which results the second continuity equation: $n_1(\vec{E}_1^{+} - \vec{E}_1^{-}) = n_2(\vec{E}_2^{+} - \vec{E}_2^{-})$.

From the upper two continuity equations, we deduce the matrix form, which is as follows:

$$\begin{pmatrix} \vec{E}_1^{+}(z=0) \\ \vec{E}_1^{-}(z=0) \end{pmatrix} = \begin{pmatrix} \frac{\cos\theta_2}{2\cos\theta_1} + \frac{n_2}{2n_1} & \frac{\cos\theta_2}{2\cos\theta_1} - \frac{n_2}{2n_1} \\ \frac{\cos\theta_2}{2\cos\theta_1} - \frac{n_2}{2n_1} & \frac{\cos\theta_2}{2\cos\theta_1} + \frac{n_2}{2n_1} \end{pmatrix} \begin{pmatrix} \vec{E}_2^{+}(z=0) \\ \vec{E}_2^{-}(z=0) \end{pmatrix}$$

$$\text{or} \begin{pmatrix} \vec{E}_1^{+}(z=0) \\ \vec{E}_1^{-}(z=0) \end{pmatrix} = \begin{pmatrix} \frac{n_1\vec{k}_{2,z}^{+}}{2n_2\vec{k}_{1,z}^{+}} + \frac{n_2}{2n_1} & \frac{n_1\vec{k}_{2,z}^{+}}{2n_2\vec{k}_{1,z}^{+}} + \frac{n_2}{2n_1} \\ \frac{n_1\vec{k}_{2,z}^{+}}{2n_2\vec{k}_{1,z}^{+}} + \frac{n_2}{2n_1} & \frac{n_1\vec{k}_{2,z}^{+}}{2n_2\vec{k}_{1,z}^{+}} + \frac{n_2}{2n_1} \end{pmatrix} \begin{pmatrix} \vec{E}_2^{+}(z=0) \\ \vec{E}_2^{-}(z=0) \end{pmatrix}$$

where $\begin{pmatrix} \frac{n_1\vec{k}_{2,z}^{+}}{2n_2\vec{k}_{1,z}^{+}} + \frac{n_2}{2n_1} & \frac{n_1\vec{k}_{2,z}^{+}}{2n_2\vec{k}_{1,z}^{+}} + \frac{n_2}{2n_1} \\ \frac{n_1\vec{k}_{2,z}^{+}}{2n_2\vec{k}_{1,z}^{+}} + \frac{n_2}{2n_1} & \frac{n_1\vec{k}_{2,z}^{+}}{2n_2\vec{k}_{1,z}^{+}} + \frac{n_2}{2n_1} \end{pmatrix}$ is the reflexion matrix for a TM polarized wave, denoted R_{12} in the following. The indices correspond to the two materials at each side of the interface.

Propagation matrix

Single layer: We just treat the matrix describing the transfer from one material to another for both TE and TM polarization. Now we are interested to describe a wave passing through one of the dielectrics or even multiple layers of one material and the other. We will now deduce a complete transfer matrix, describing the fields at both interfaces and inside the thin dielectric layer.

The change over from one dielectric to the other induces a phase shift due to the propagation [5]. For both TE and TM case, the transfer matrix remains always valid.

From the upper section, we have:

$$\vec{E}_1(z) = \begin{pmatrix} \vec{E}_1^{+}(z) \\ \vec{E}_1^{-}(z) \end{pmatrix} \qquad \text{where} \qquad \vec{E}_1^{+}(z) = E_1^{+} e^{-ik_1 \cos\theta_i z} \text{ and } \vec{E}_1^{-}(z) = E_1^{-} e^{ik_1 \cos\theta_i z}$$

The transit relation of an electric wave through a layer of thickness *e* is thus written:

$$\begin{pmatrix} \vec{E}_1^{+}(z) \\ \vec{E}_1^{-}(z) \end{pmatrix} = \begin{pmatrix} e^{ik_1 \cos\theta_i e} & 0 \\ 0 & e^{-ik_1 \cos\theta_i e} \end{pmatrix} \begin{pmatrix} \vec{E}_1^{+}(z+e) \\ \vec{E}_1^{-}(z+e) \end{pmatrix}$$

with $\begin{pmatrix} e^{ik_1 \cos\theta_i e} & 0 \\ 0 & e^{-ik_1 \cos\theta_i e} \end{pmatrix}$ as the propagation matrix, denoted T_α, with α as the number of the layer.

Multiple layers: Finally, in order to calculate the complete transfer matrix in the case of multiple layers, it is sufficient to multiply to each other the reflexion and propagation matrices which permits to associate the incident wave to the outgoing one [5]. E. g., for a succession of *n* thin layers of refractive index n_α and thickness e_α, with an incident TE polarized wave, we get:

$$\begin{pmatrix} \vec{E}_i^{+}(0) \\ \vec{E}_i^{-}(0) \end{pmatrix} = R_{i1}T_1R_{12}T_2R_{21}T_1R_{12}T_2.....R_{.s}T_s\ R_{si} \begin{pmatrix} \vec{E}_s^{+}(Z) \\ \vec{E}_s^{-}(Z) \end{pmatrix}$$

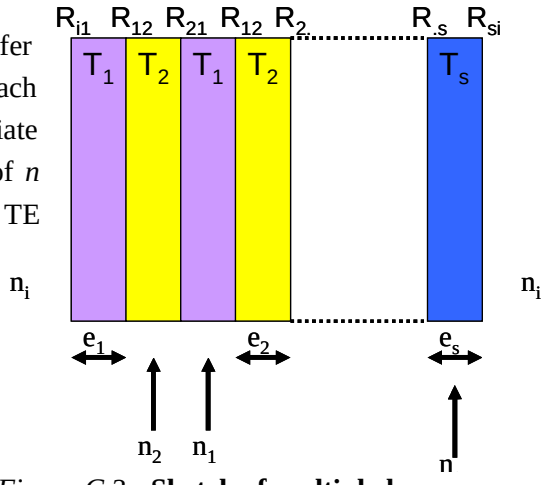

Figure C.3: **Sketch of multiple layers**

where: *i* represents the initial medium

s the substrate

$$Z = \sum_{\alpha=1}^{s} e_\alpha \ .$$

The complete transfer matrix is denoted M:

$M = R_{i1}T_1R_{12}T_2R_{21}T_1R_{12}T_2.....R_sT_s\ R_{si}$.

Reflexion and transmission: The determination of the transfer matrix permits to calculate the amplitude of reflexion and transmission coefficients.

For TE or TM waves, we obtain $r = \frac{M(1,2)}{M(1,1)} = \frac{M(2,1)}{M(2,2)}$ and $t = \frac{1}{M(1,1)} = \frac{1}{M(2,2)}$

From this, we can deduce the reflexion and transmission coefficients as a function of energy:

$R = |r|^2 = rr^*$ and $T = |t|^2 \frac{n_2 \cos\theta_2}{n_1 \cos\theta_1}$

In the following, we only present transmission spectra. The reflexion spectra can be deduced using the relation $R + T = 1$.

Optical absorption: As described in part I, the band structure of silicon induces an optical absorption. The abrupt band edges of the extended energy states in a crystalline solid are replaced by band tails present in the forbidden gap of an amorphous solid. The optical absorption is thus very different from the crystalline case. In figure A.9, we present a typical transmission spectrum of silicon oxyde.

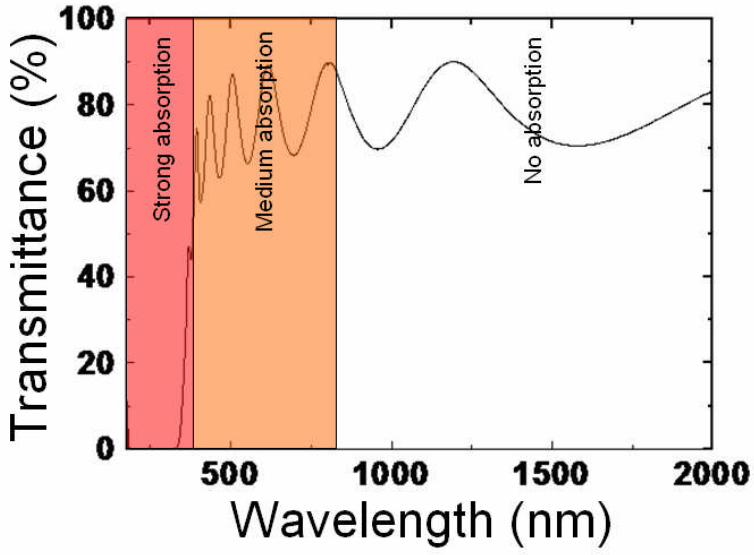

Figure C.4: Transmission spectrum of a thin layer of silicon oxide showing different absorption regimes [7]

The spectrum can be sub-divided in three intervals of different absorption:

- Zone of strong absorption: (from $\lambda = 200\ nm$ *to* $\lambda = 520\ nm$). In this zone, the absorption can be written as given by Tauc : $\alpha = (B \cdot \frac{(E - E_g)^2}{E})$ where E_g represents the optical gap anf B the Tauc energy.
- Zone of middle absorption: (from $\lambda = 500\ nm$ *to* $\lambda = 2000\ nm$) in the case of amorphous hydrogenated silicon, this zone is called Urbach band and the absorption is written as: $\alpha = \alpha_0 e^{(\frac{E}{E_u})}$ where E_u is the Urbach energy.
- Zone of transparency or weak absorption: (from $\lambda = 2000\ nm$ *to* $\lambda = 3300\ nm$) this band is related to the lack of permitted optical transition or at least a very weak concentration of defects that have optically active energy levels inside the band gap. Because of the small value of α in this zone, we can't measure the absorption precisely. However, it is possible to determine refractive index and thickness of the layer.

The substrates used in this study are made of fused silica. Their advantage is a very low absorption over the whole spectral range that is analyzed. The dispersion relation of the refractive index of these substrates is perfectly known:

$$n_s^2 = 1 + \frac{0.6961663\lambda^2}{(\lambda^2 - 0.0684043^2)} + \frac{0.4079426\lambda^2}{(\lambda^2 - 0.1162414^2)} + \frac{0.8974794\lambda^2}{(\lambda^2 - 9.896161^2)}$$ (with the wavelength λ in µm)

As it shows figure A.10, this theoretical value fits very well to the experimentally determined value.

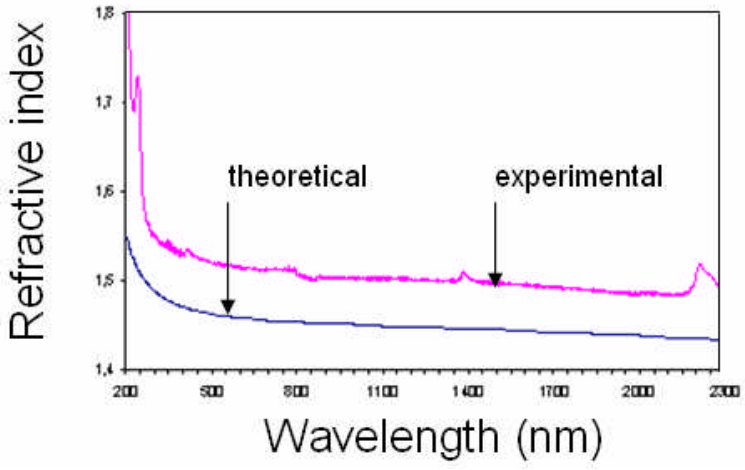

Figure C.5: Comparison of refractive indices determined by either simulation or measurement

The offset between theoretical and experimental values is of 0.05. This seems quite reasonable.

Finally, the refractive index of the thin films deposited onto the substrates is given by:

$$n = n_0 + \frac{10^5 n_1}{\lambda^2} + \frac{10^9 n_2}{\lambda^4}.$$

Bibliography

[1] L.T. Canham, Appl. Phys. Lett. **57** 1046 (1990)

[2] A.G. Cullis, L.T. Canham, and P.D.J. Calcott, J. Appl. Phys., **82** 909 (1997)

[3] S. Godefroo, M. Hayne, M. Jivanescu, A. Stesmans, M. Zacharias, O. I. Lebedev, G. Van Tendeloo and V. V. Moshchalkov, Nature Nanotechnology **3**, 174 (2008)

[4] S. Munekuni, T. Yamanaka, Y. Shimogaichi, R. Tohmon, Y. Ohki, K. Nagasawa, and Y. Hama. J. Appl. Phys., **68** 1212 (1990)

[5] G. Pacchioni and G. Ierano. Phys. Rev. B, **57**(2), 818 (1998)

[6] S.M. Prokes. Appl. Phys. Lett., **62** 3244 (1993)

[7] C. Delerue, G. Allan, and M. Lannoo. Phys. Rev. B, **48**(15) 11024 (1993)

[8] K. Leung and KB Whaley. Phys. Rev. B, **56**(12) 7455 (1997)

[9] M.V. Wolkin, J. Jorne, P.M. Fauchet, G. Allan, and C. Delerue. Phys. Rev. B, **82** (1) 197 (1999)

[10] J. Heitmann, F. Müller, L. Yi, M. Zacharias, D. Kovalev, and F. Eichhorn; Phys. Rev. B, **69** (19) 195309 (2004)

[11] F. Iacona, G. Franzò, and C. Spinella. J. Appl. Phys., **87** 1295 (2000)

[12] P. Allongue, V. Costa Kieling, and H. Gerisher, Electrochim. Acta **40**, 1353 (1997)

[13] Y. H. Xie, W. L. Wilson, F. M. Ross, J. A. Mucha, E. A. Fitzgerald, J. M. Macaulay and T. D. Harris, J. Appl. Phys. **71**, 2403 (1992)

[14] A. Bsiesy, J. C. Vial, F. Gaspard, R. Herino, M. Ligeon, F. Muller, R. Romestain, A. Wasiela, A. Halimaoui, and G. Bomchil, Surf. Sci. **254**, 195 (1991)

[15] J. Linnros, N. Lalic, A. Galeckas, and V. Grivickas, J. Appl. Phys. **86**, 6128 (1999)

[16] M. Molinari, PhD thesis, Université Henri Poincaré, Nancy 1 (2002)

[17] D. J. Lockwood, Z. H. Lu, and J.-M. Baribeau, Phys. Rev. Lett. **76**, 539 (1996)

[18] V. Ioannou-Sougleridis, A. G. Nassiopoulou, T. Ouisse, F. Bassani, and F. A. d'Avitaya, Appl. Phys. Lett. **79**, 2076 (2001)

[19] M. Zacharias, J. Heitmann, R. Scholz, U. Kahler, M. Schmidt, and J. Blasing, Appl. Phys. Lett. **80**, 661 (2002).

[20] B. Garrido Fernandez, M. Lopez, C. Garcia, A. Perez-Rodriguez, J. R. Morante, C. Bonafos, M. Carrada, and A. Claverie, J. Appl. Phys. **91**, 798 (2002)

[21] T. Shimizu-Iwayama, N. Kurumado, D. E. Hole, and P. D. Townsend, J. Appl. Phys. **83**, 6018 (1998)

[22] H. Rinnert, PhD thesis, Université Henri Poincaré, Nancy 1, (1999)

[23] S. Hayashi, T. Nagareda, Y. Kanzawa, and K. Yamamoto, Japanese J. Appl. Phys. **32**, 3840 (1993)

[24] L. Tsybeskov, K. D. Hirschman, S. P. Duttagupta, M. Zacharias, P. M. Fauchet, J. P. McCaffrey, and D. J. Lockwood, Appl. Phys. Lett. **72**, 43 (1998)

[25] M. Zacharias and P. Streitenberger, Phys. Rev. B **62**, 8391 (2000)

[26] V. Vinciguerra, G. Franzo, F. Priolo, F. Iacona, and C. Spinella, J. Appl. Phys. **87**, 8165 (2000)

[27] O. Jambois, H. Rinnert, X. Devaux, and M. Vergnat ; J. Appl. Phys. **100**, 123504 (2006)

[28] J. -Y. Marzin, J. -M. Gérard, A. Izraël, D. Barrier and G. Bastard; Phys. Rev. Lett. **73**, 716 (1994)

[29] M. Bayer, O. Stern, P. Hawrylak, S. Fafard and A. Forchel; Letters to Nature, **405** 923 (2000)

[30] J. Valenta, Book Chapter of "Towards the First Silicon Laser"; NATO Science Series II: Mathematics, Physics and Chemistry; Ed. L. Pavesi, S.V. Gaponenko L. Dal Negro, Kluwer Academic Publishers (2003)
[31] I. Sychugov, R. Juhasz, J. Valenta, M. Zhang, P. Pirouz and J. Linnros; Appl. Surf. Sci. **252** 5249 (2006)
[32] J. Valenta, R. Juhasz and J. Linnros; J. Lumin. **98** 15 (2002)
[33] I. Sychugov, R. Juhasz, J. Valenta and J. Linnros; Phys. Rev. Lett. **94** 087405 (2005)
[34] T. Takagahara; J. Lumin. **70** 129 (1996)
[35] J. Valenta, N. Lalic, J. Linnros; Appl. Phys. Lett. **84** 9 (2004)
[36] S. Yasin, M.N. Khalid, J.H. Rice, R.A. Taylor; Microelectron. Eng. **73–74** 762 (2004)
[37] C. Dumas, J. Grisolia, L. Ressier, A. Arbouet, V. Paillard, G. Ben Assayag, A. Claverie, M. A. F. van den Boogaart and J. Brugger; Phys. Stat. Sol. (a) **204**, No. 2, 487 (2007)
[38] A. Arbouet, M. Carrada, F. Demangeot, V. Paillard, G. BenAssayag, C. Bonafos, A. Claverie, S. Schamm, C. Dumas, J. Grisolia, M.A.F. Van den Boogaart, J. Brugger and L. Doeswijk; J. Lumin. **121** 340 (2006)
[39] S. Haroche, D. Kleppner; Physics Today, p.24 (01/1989)
[40] H. Benisty, H. De Neve, C. Weisbuch; IEEE J. Quant. Elec. **34** p.1612 (1998)
[41] M. Purcell; Phys. Rev. **69**, 681 (1946)
[42] J.-M. Lourtioz, H. Benisty, V. Berger, J.-M. Gérard, D. Maystre, A. Tchelnokov; Ed. Lavoisier Hermès Science, Paris (2003)
[43] K. J. Vahala ; Nature **424** 839 (2003)
[44] F. Iacona, G. Franzò, E. Ceretta Moreira, D. Pacifici, A. Irrera and F. Priolo; Mat. Sci. Eng. C **19**.377 (2002)
[45] D. Amans, S. Callard, A. Gagnaire, and J. Joseph; J. Appl. Phys. **95** 9 5010 (2004)
[46] M. Pelton, C. Santori, J. Vučković, B. Zhang, G. S. Solomon, J. Plant, and Y. Yamamoto; Phys. Rev. Lett. **89**, 233602 (2002)
[47] R.-J. Zhang, S.-Y. Seo, A. P. Milenin, M. Zacharias and U. Gösele; Appl. Phys. Lett. **88**, 153120 (2006)
[48] R.D. Kekatpure and M.L. Brongersma ; Phys. Rev. A **78**, 023829 (2008)
[49] A. Pitanti, PhD thesis, Università degli studi di Trento (2010)
[50] A. Pitanti, M. Ghulinyan, D. Navarro-Urrios, G. Pucker and L. Pavesi ; Phys. Rev. Lett. **104** 103901 (2010)
[51] J. M. Gérard and B. Gayral ; J. Lightwave Technol. **17** 2089 (1999)
[52] T. J. Kippenberg, A. L. Tchebotareva, J. Kalkman, A. Polman and K. J. Vahala; Phys. Rev. Lett. **103** 027406 (2009)
[53] A. M. Beltaos and A. Meldrum; J. Lumin. **126** 606 (2007)
[54] A. Meldrum, P. Bianucci and F. Marsiglio; Opt. Express **18** 10 10230 (2010)
[55] M. Vergnat; PhD thesis, Université Henri Poincaré, Nancy 1 (1988)
[56] O. Jambois; PhD thesis, Université Henri Poincaré, Nancy 1 (2005)
[57] J.C. Manifacier, J. Gassiot, and J. Fillard; J. Phys. E **9**, 1002 (1976)
[58] R. Swanepoel; J. Phys. E **16**, 1214 (1983)
[59] F. Iacona, G. Franzo, and C. Spinella, J. Appl. Phys. **87**, 1295 (2000)
[60] V. Vinciguerra, G. Franzò, F. Priolo, F. Iacona, and C. Spinella, J. Appl. Phys. **87**, 8165 (2000)

[61] C. Bonafos, B. Garrido, M. Lopez, A. Perez-Rodriguez, J. R. Morante, Y. Kihn, G. Ben Assayag, and A. Claverie, Mat. Sci. Eng. B **69**, 380 (2000)
[62] C. Bonafos, B. Colombeau, A. Altibelli, M. Carrada, G. Ben Assayag, B. Garrido, M. López, A. Pérez-Rodríguez, J. R. Morante and A. Claverie; Nucl. Instrum. Meth. B **178**, 17 (2001)
[63] A. Morimoto, H. Noriyama, and T. Shimizu; Japanese J. Appl. Phys. **26**, 22 (1986)
[64] Z. Iqbal and S. Veprek; Journal de Physique C: Physique de l'Etat Solide **15**, 377 (1982)
[65] P. G. Pai, S. S. Chao, Y. Takagi, and G. Lucovsky, J. Vac. Sci. Technol. A **4**, 689 (1986)
[66] S.Y. Lin ; J. Appl. Phys. **82**, 5976 (1997)
[67] Z. Jing, J.L. Whitten, and G. Lucovsky; Phys. Rev. B **45**, 13978 (1992)
[68] M. Zacharias, H. Freistedt, F. Stolze, T.P. Drüsedau, M. Rosenbauer, and M. Stutzmann; J. Non-Cryst. Solids **164**, 1089 (1993)
[69] W. Weber ; Phys. Rev. B **15**, 4789 (1977)
[70] J.D. Joannopoulos, and W.B. Pollard; Solid State Commun. **20**, 947 (1976)
[71] P.E. Meek; Philos. Mag. **33**, 897 (1976)
[72] N. Ishii, M. Kumeda, and T. Shimizu; Solid State Commun. **50**, 367 (1984)
[73] M. Marinov, and N. Zotov; Phys. Rev. B **55**, 2938 (1996)
[74] F. Wooten, K. Winer, and D. Weaire; Phys. Rev. Lett. **54**, 1392 (1985)
[75] R. Alben, D. Weaire, J.E. Smith and M.H. Brodsky; Phys. Rev. B **11**, 2271 (1975)
[76] H. Richter, Z.P. Wang and L. Ley; Solid State Commun. **39**, 625 (1981)
[77] I.H. Campbell and P.M. Fauchet; Solid State Commun. **58**, 739 (1986)
[78] J. Zi, K. Zhang and X. Xie; Phys. Rev. B **55**, 9263 (1996)
[79] J.Zi, H. Büsher, C. Falter, W. Ludwig, K. Zhang and X. Xie; Appl. Phys. Lett. **69**, 200 (1996)
[80] D. Kovalev, H. Heckler, G. Polisski and F. Koch; phys. stat. sol. (b) **215**, 871 (1999)
[81] L. Pavesi and M. Ceschini; Phys. Rev. B **48**, 23 (1993)
[82] V. A. Belyakov, V. A. Burdov, R. Lockwood, and A. Meldrum; Adv. Opt. Techn. 279502 (2008)
[83] M. Zacharias, J. Heitmann, R. Scholz, U. Kahler, M. Schmidt and J. Bläsing; Appl. Phys. Lett. **80**, 4 (2002)
[84] T. Z. Lu, M. Alexe, R. Scholz, V. Talalaev, R. J. Zhang, and M. Zacharias; J. Appl. Phys. **100**, 014310 (2006)
[85] N. Gisin and R. Thew; Nature Photonics **1**, 165 (2007)
[86] I .Sychugov, R. Juhasz, A. Galeckas, J. Valenta and J. Linnros; Opt. Mater. **27** 973 (2005)
[87] H. Rinnert, O. Jambois, M. Vergnat and M. Molinari; Opt. Mat. **27**, 983 (2005)
[88] U. Kahler and H. Hofmeister; Appl. Phys. A **74**, 13 (2002)
[89] G. Wora Adeola; Thèse de doctorat, Université Henri Poincaré, Nancy 1 (2007)
[90] H. Rinnert, M. Vergnat and G. Marchal; Mat. Sci. Eng. B**69–70** 484 (2000)
[91] P. G. Pai, S. S. Chao, Y. Takagi, and G. Lucovsky, J. Vac. Sci. Technol. A **4**, 689 (1986)
[92] S.Y. Lin. J. Appl. Phys.; **82**, 5976 (1997)
[93] H.Z. Song, X.M. Bao, NS Li, and X.L Wu.; Appl. Phys. Lett.; **72** 356 (1998)
[94] H. Nishikawa, E. Watanabe, D. Ito, Y. Sakurai, K. Nagasawa, and Y. Ohki; J. Appl. Phys. **80**, 3513 (1996)
[95] M. Kalceff and M. Phillips; Phys. Rev. B **52**, 3122 (1995)
[96] S. M. Prokes, W. E. Carlos, S. Veprek, and C. Ossadnik; Phys. Rev. B **58**, 15632 (1998)

[97] J. Y. Jeong, S. Im, O. M. S., H. B. Kim, K. H. Chae, C. N. Whang, and J. H. Song; J. Lumin. **80**, 285 (1999)
[98] M. Zhu, Y. Han, R. B. Wehrspohn, C. Godet, R. Etemadi, and D. Ballutaud; J. Appl. Phys. **83**, 5386 (1998)
[99] B. Hinds, F. Wang, D. Wolfe, C. Hinkle, and G. Lucovsky; J. Vac. Sci. Tech. B **16**, 2171 (1998)
[100] J. Knights, R. Street, and G. Lucovsky; J. Non-cryst. Solids 35 & 36, 279 (1980)
[101] Y. Kanzawa, S. Hayashi, and K. Yamamoto; J. Phys.: Cond. Mat. **8**, 4823 (1996)
[102] G. Allan, C. Delerue, and M. Lannoo; Phys. Rev. Lett. **78**, 3161 (1997)
[103] P. Calcott, K. Nash, L. Canham, M. Kane, and D. Brumhead; J. Phys.: Cond. Mat. **5,** L91 (1993)
[104] V. Lehmann and U. Gösele; Appl. Phys. Lett. **58**, 856 (1991)
[105] F. Galeener and A. Geissberger; Phys. Rev. B. **27**, 6199 (1983)
[106] C. Itoh and K. T. dn N. Itoh; J. Phys. C: Solid State Physics **21**, 4693 (1988)
[107] P. Miska *et al. submitted to* J. Phys. Chem. US
[108] C. Meiers, A. Gondorf, S. Lüttjohann and A. Lorke; J. Appl. Phys. **101**, 103112 (2007).
[109] C. Delerue, G. Allan and M. Lannoo; Phys. Rev. B **48**, 11024 (1993)
[110] G. Faraci, S. Gibiliso, P. Russo, A. R. Pennisi and S. La Rosa, Phys. Rev. B **73**, 033307 (2006)
[111] H. Rinnert and M. Vergnat, J. Lumin. **113**, 64 (2004)
[112] O. Jambois, H. Rinnert X. Devaux and M. Vergnat ; J. Appl. Phys. **100**, 123504 (2006)
[113] L. Pavesi, L. Dal Negro, C. Mazzoleni, G. Franzo and F. Priolo, Nature **408**, 440 (2000)
[114] P. G. Han, Z. Y. Ma, Z. Y. Xia, D. Y. Chen, D. Y. Wei, B. Qian, W. Li, J. Xu, X. F. Huang, K. J. Chen and D. Feng, Nanotechnology **18**, 255703 (2007)
[115] R. Pässler, Solid State Electron. **39**, 1311 (1996)
[116] Y. Kanemitsu, H. Uto and Y. Masumoto, T. Matsumoto, T. Futagi and H. Mimura, Phys. Rev. B **48**, 2827 (1993)
[117] A. Wellner, V. Paillard, C. Bonafos, H. Coffin, A. Claverie, B. Schmidt and K. H. Heinig, J. Appl. Phys. **94**, 5639 (2003)
[118] T. Aguirov, T. Mchedlidze, M. Kittler, R. Röver, B. Berghohh, M. Först and B. Spangenberg; Appl. Phys. Lett. **89**, 3157 (2006)
[119] A. Palandre; Thèse de doctorat; Université Catholique de Louvain (2004)
[120] M. Grün; Master thesis, Université Henri Poincaré, Nancy I and Universität Saarbrücken (2007)
[121] A. Belarouci and F. Gourbilleau; Appl. Phys. B: Lasers O., **88** (2), pp. 237 (2007)
[122] Rabaste, S., Bellessa, J., Brioude, A., Bovier, C., Plenet, J.C., Brenier, R., Marty, O., Mugnier, J.; Thin Solid Films, **416** (1-2), pp. 242 (2002)
[123] Lim, H.J., Ryu, B.Y., Ryu, J.I., Jang, J.; Thin Solid Films, **289** (1-2), pp. 227 (1996)
[124] Handbook of optical constants of solids, volume 1, Edited by Edward D.Palik, 1998 Elsevier
[125] Fogal et al. Solid State Commun. **120** (2001) 429
[126] Orapunt, F. and O'Leary, S. K.; Appl. Phys. Lett. **84**, 523 (2004)
[127] Lim, H.J., Ryu, B.Y., Ryu, J.I., Jang, J.; Thin Solid Films, **289** (1-2), pp. 227 (1996)
[128] Zanatta, A. R. and Chambouleyron, I.; Phys. Rev. B **53,** 3833 (1996)
[129] G. Almuneau; PhD thesis, Université Montpellier II (198)
[130] A. Tredicucci, Y. Chen, V. Pellegrini and C. Deparis, Appl. Phys. Lett. **66** (1995) 2388
[131] H. A. Lopez and P. Fauchet, Appl. Phys. Lett. **77** 3704 (2000)
[132] T. Xu, S. Yang, S. Selvakumar, V. Nair, and H.E. Ruda; Phys. Rev. B **75**, 125104 (2007)

[133] A. Pitanti, M. Ghulinyan, D. Navarro-Urrios, G. Pucker and L. Pavesi; Phys. Rev. Lett. **104**, 103901 (2010)
[134] J. M. Gérard in Single Quantum Dots: Fundamentals, Applications and New Concepts, edited by P. Michler, Springer (2003)
[135] G. Björk, H Heitmann and Y. Yamamoto; Phys. Rev. A **47**, 4451 (1993)
[136] M. Dovrat, Y. Goshen, J. Jedrzejewski, I. Balberg, and A. Sa'ar; Phys. Rev. B **69**, 155311 (2004)

Résumé

Ce travail de thèse concerne la réalisation et l'analyse des propriétés optiques de nanocristaux de silicium. Ces objets de taille nanométrique possèdent des propriétés optiques remarquables, en particulier de photoluminescence. Les propriétés de confinement quantique qui les caractérisent permettent d'obtenir un signal de luminescence intense dans le domaine du visible. Des composants optoélectroniques et photoniques ont été envisagés à base de nanocristaux de silicium. Les raisons physiques du fort signal de luminescence en revanche sont encore mal comprises.

Les nanocristaux de silicium sont élaborés par évaporation. L'élaboration et le recuit thermique de multicouches SiO/SiO_2 permet d'obtenir des nanocristaux de silicium de diamètre moyen bien contrôlé. Ceux-ci sont issus de la démixtion de la couche de SiO selon la réaction $SiO_x \rightarrow Si + SiO_2$. Le contrôle du diamètre des nanocristaux de silicium permet de maîtriser la région spectrale de luminescence dans la région du visible.

La première partie de ce travail de thèse vise à isoler un ou quelques nanocristaux de silicium. L'objectif est de remonter à la largeur homogène de ces nano-objets. Dans un premier temps, une étude centrée sur le matériau SiOx est réalisée afin de réduire la densité surfacique de nanocristaux de silicium. Dans un deuxième temps, des moyens de lithographie ultime sont mis en œuvre afin de réaliser des masques percés de trous de diamètres de l'ordre de la centaine de nanomètre. Des expériences de spectroscopie optique sont réalisées sur ces systèmes.

La deuxième partie de ce travail vise à contrôler l'émission spontanée de lumière issue des nanocristaux de silicium. Ceci se fait en couplant les modes électroniques aux modes optiques confinés d'une microcavité optique. Le manuscrit détaille les moyens développés afin d'obtenir une micocavité optique dont les modes optiques puissent se coupler efficacement aux nanocristaux de silicium. Les propriétés optiques de ces systèmes sont finalement analysées.

Mots clés : nanocristaux de silicium, SiO_x, spectroscopie optique, lithographie électronique, nanocristal isolé, microcavité optique, couplage optique